University of Burgos

Department of Civil Engineering

Numerical models for simulating hydrogen diffusion and embrittlement in high strength steels

Andrés Díaz Portugal

Supervisor: Jesús Manuel Alegre Calderón

This dissertation is submitted for the degree of

Doctor of Philosophy

Burgos October 2017

Acknowledgements

To my supervisor, Jesús Manuel Alegre, for guiding me on the steps to follow in this difficult research line, for trusting in my ability to carry out this work, for always wanting to undertake new projects and, especially, for his friendship and good humour.

To Iván Cuesta for his absolute dedication, his wise advices, his help in this research and for making daily work really gratifying.

To the University of Burgos and, in particular, to the Area of Continuum Mechanics where the work environment has been the best that one could imagine for this pre-doctoral stage.

To Emilio Martinez-Pañeda, for his help in the numerical part of this thesis, but, above all, for expanding my vision on hydrogen diffusion phenomena, embrittlement, and plasticity.

To Zhiliang Zhang, for giving me the opportunity to be part of his Nanomechanical Lab during three months and for guiding me in my research. To all the NTNU's colleagues and friends in Trondheim, especially to Haiyang for his help and dedication.

To colleagues I have met at conferences, for awakening my interest in material modelling from the most diverse approaches, and for all their contributions.

To the financial support from the Ministry of Economy and Competitiveness of Spain through grant MAT2014-58738-C3 To the Junta of Castile and Leon through project BU053U16 and pre-doctoral grant EDU/1006/2015.

To my friends, for encouraging me to do this work, for cheering me up in the worst moments and for making all of these years a really exciting stage of my life.

Principally, I want to thank my grandparents, my parents and my sister. I am grateful to you for your support, your trust, for being a good example and also for your patience with me. Thank you for always being there.

Abstract

This thesis presents and discusses hydrogen diffusion modelling as a first step in predicting and mitigating hydrogen-assisted fracture. Hydrogen embrittlement is a common phenomenon that degrades metals and alloys, and related failures are usual in industry. However, the relationship between hydrogen and the transition from ductile to brittle modes of fracture is not entirely clear. Even though mechanism operating at nano and microscales are not yet completely understood, it has been proved that embrittlement is proportional to hydrogen concentration within a metal. Therefore, the present work has the objective of establishing, validating, implementing and analysing a consistent numerical model for hydrogen diffusion, in a Continuum Mechanics framework by means of a Finite Element software.

Diffusion phenomena are reviewed and particularised on hydrogen transport in metals. In particular, a "two-level" model, considering trapping effects explicitly, is chosen in order to simulate hydrogen diffusion near a crack tip. Strain and stress fields present in a crack or notch are connected with hydrogen diffusion; additionally, hydrogen promotes a local softening, a dilatation and a reduction in cohesive energy so a coupled behaviour between diffusion, elasto-plasticity and damage must be considered.

Finally, numerical models for diffusion are applied to fracture modelling in a Cohesive Zone Model approach and a notched tensile test is simulated, demonstrating that the combination of diffusion with damage models might predict brittle fracture. Vessels storing hydrogen are also simulated with the purpose of finding hydrogen distributions near stress concentrators; influence of cyclic loads and compressive residual stresses is also evaluated in these deposits.

Contents

Contents vii
List of Figures xi
List of Tables xv
Nomenclature 17
Chapter 1 Introduction 21
1.1 Motivation 21
1.2 Research objectives 24
1.3 Document structure 26
Chapter 2 Review on hydrogen diffusion modelling 29
2.1 Introduction 29
2.2 Multiscale approach 31
2.3 Diffusion phenomena 33
2.3.1 Einstein equation for brownian motion 34
2.3.2 Diffusion as a random walk 34
2.3.3 Landscape of potential energies 35
2.3.4 Transition rate 40
2.3.5 Driving force and flux 43
2.4 Interstitial Solid Solutions 45
2.4.1 Chemical potential 46
2.4.2 Chemical activity 51
2.4.3 Equilibrium between sites 51
2.4.4 Stress state 52
2.5 Two-level continuum model 53
2.5.1 Interstitial flux 54
2.5.2 Chemical potential 55
2.5.3 Mass balance 55
2.5.4 Trapping influence 56
2.6 Coupled diffusion 65
2.6.1 Local softening 65

2.6.2 Lattice dilatation 66
2.7 Summary 68
Chapter 3 Implementation of hydrogen diffusion and embrittlement modelling 69
3.1 Introduction 69
3.2 Implemented diffusion equations 73
3.2.1 Flux between trapping sites 73
3.2.2 Mass balance: general governing equation 75
3.2.3 Simplified governing equation 75
3.2.4 Oriani's equilibrium 76
3.2.5 Plastic strain influence 77
3.3 Boundary conditions 77
3.4 Coupled diffusion 79
3.4.1 Hydrogen induced softening 79
3.4.2 Hydrogen induced dilatation 80
3.5 Informed cohesive model 80
3.5.1 Traction – Separation Law 80
3.5.2 Hydrogen influence 83
3.5.3 Triaxiality influence 84
3.6 Implementation in ABAQUS through user subroutines 85
3.6.1 Diffusion equations 86
3.6.2 Coupling equations 88
3.6.3 Boundary conditions 90
3.6.4 Multi-trapping effects 90
3.6.5 Kinetic equations 91
3.6.6 Cohesive element behaviour 92
3.7 Validation of subroutines for diffusion 92
3.7.1 Parameters 93
3.7.2 Geometry and boundary conditions 94
3.7.3 Results 97
Chapter 4 Numerical simulation of hydrogen diffusion near a crack tip 101
4.1 Introduction 101
4.2 Materials and geometry 103
4.3 Simulation of coupled effects 103
4.3.1 Dilatation 104
4.3.2 Hardening/Softening 106
4.4 Flux between trapping sites 107
4.5 Boundary conditions 110

4.6 Kinetic reconsideration of trapping 112
4.7 Multi-trapping effects 118
4.7.1 Equilibrium 118
4.7.2 Non-equilibrium 124
4.8 Conclusions 129
Chapter 5 Simulation of hydrogen and triaxiality effects in notched specimens 131
5.1 Introduction 131
5.2 Materials and procedures 132
5.3 Hydrogen diffusion model 134
5.4 Results and discussion 138
5.5 Conclusions 145
Chapter 6 Application to a pressure vessel considering cyclic loading 147
6.1 Introduction 147
6.2 Hydrogen diffusion model 148
6.3 Modelling 148
6.3.1 Material characterization 148
6.3.2 Diffusion parameters 149
6.3.3 Thickness design 150
6.3.4 Vessel 152
6.3.5 Cyclic load 152
6.4 Results and discussion 152
6.5 Conclusions 159
Chapter 7 Assessment of residual stress effects in a pressure vessel 161
7.1 Introduction 161
7.2 Hydrogen diffusion model 163
7.2.1 Parameters and boundary concentration 163
7.2.2 Hydrogen trapping 165
7.3 Vessel modelling 166
7.3.1 Vessel without defects 168
7.3.2 Notched vessel 171
7.4 Results and discussion 172
7.5 Conclusions 181
Chapter 8 Conclusions and future work 183
8.1 Conclusions 183
8.1.1 Hydrogen diffusion near a crack tip 184
8.1.2 Hydrogen Assisted Fracture modelling 185
8.1.3 Diffusion in high pressure vessels for H_2 storage 186

8.2 Future work 187
8.2.1 Numerical implementation 187
8.2.2 Experimental work 190
References 191

List of Figures

Figure 2-1. Multiscale approaches (blue) and its respective computational methods (brown). Boxes on the left correspond to a continuum scale while boxes on the right are related to the atomic scale. 32

Figure 2-2. Potential energy of a metal lattice along a certain *x* direction 37

Figure 2-3. Potential energy distribution and degeneracy of the well points in different configurations (R Kirchheim, 1982). 38

Figure 2-4. Hop between two different sites A y B. 42

Figure 2-5. Comparison between different expressions for $N_T(\varepsilon^p)$ found in literature. 60

Figure 3-1. Diagram of the modelling approach and relationship between the physical phenomena and the numerical problem. 70

Figure 3-2. Continuum and cohesive element responses. 81

Figure 3-3. Coupling scheme between diffusion and elasto-plastic response. 89

Figure 3-4 Boundary layer geometry with symmetry boundary condition and far-field displacements. 96

Figure 3-5 Mesh detail in a crack tip with initial radios of $b_0/2$ and hydrogen concentration C_b in the boundary. 96

Figure 3-6. Hydrogen lattice concentration at 130 s. 98

Figure 3-7. Hydrogen lattice concentration with and without plastic strain rate. Comparison with reference (A. Krom et al., 1999)(dashed lines). 98

Figure 3-8. Hydrogen concentration in trapping sites. Comparison with reference (A. Krom et al., 1999)(dashed blue lines). 99

Figure 4-1 Hydrogen lattice concentration at 130 s with and without dilatation parameter λ. Comparison with reference (Taha & Sofronis, 2001)(green solid line). 105

Figure 4-2 Hydrogen lattice concentration with softening ($\xi = -2.04\times10^6$) and hardening ($\xi = 2.04\times10^6$) effects. 106

Figure 4-3. Potential energy trace and energetic relationships between trapping sites (*T*) and lattice sites (*L*). 108

Figure 4-4. Hydrogen concentration at 130 s in trapping sites (C_T) and lattice sites (C_L) with and without considering flux between traps with binding energy E_b = 60 kJ/mol. 109

Figure 4-5. Hydrogen concentration at 130 s in trapping sites (C_T) and lattice sites (C_L) with and without considering flux between traps with binding energy E_b = 10 kJ/mol. 110

Figure 4-6. Hydrogen concentration in lattice sites with stress-dependent boundary condition. Comparison with reference (Di Leo & Anand, 2013). 111

Figure 4-7. Hydrogen concentration in lattice sites after 0.13 and 1.3 seconds for Eb = 60 kJ/mol. Comparison between equilibrium and kinetic formulations. 113

Figure 4-8. Hydrogen concentration in trapping sites after 0.13 and 1.3 seconds for Eb = 60 kJ/mol. Comparison between equilibrium and kinetic formulations. 113

Figure 4-9. Hydrogen concentration in lattice sites after 0.13 and 1.3 seconds for Eb = 20 kJ/mol. Comparison between equilibrium and kinetic formulations. 114

Figure 4-10. Hydrogen concentration in trapping sites after 0.13 and 1.3 seconds for Eb = 20 kJ/mol. Comparison between equilibrium and kinetic formulations. 114

Figure 4-11. Binding energy influence on hydrogen concentration in lattice sites after 1.3 seconds. 115

Figure 4-12. Hydrogen concentration in lattice sites after 0.13 and 1.3 seconds for Eb = 60 kJ/mol. Comparison between equilibrium and kinetic formulations for initially empty traps ($\theta T, 0 = 0$). 116

Figure 4-13. Influence of vibration frequencies on hydrogen concentration in lattice sites after 0.13 and 1.3 seconds for E_b = 40 kJ/mol. 117

Figure 4-14 Influence of vibration frequencies on hydrogen concentration in trapping sites after 0.13 and 1.3 seconds for E_b = 40 kJ/mol. 118

Figure 4-15. Hydrogen concentration in lattice sites after 0.13 and 1.3 seconds. Comparison between the single-trap model (with E_b = 60 kJ/mol) and multi-trap model (with E_b^d = 30 kJ/mol and E_b^{gb} = 60 kJ/mol). 119

Figure 4-16. Hydrogen concentration in trapping sites after 1.3 seconds. Comparison between the single-trap model with E_b = 60 kJ/mol) and multi-trap model (with E_b^d = 30 kJ/mol and E_b^{gb} = 60 kJ/mol). 120

Figure 4-17. Influence of $N_T(\varepsilon^p)$ expression on hydrogen concentration in lattice sites for the single-trap model (with E_b = 60 kJ/mol). 121

Figure 4-18. Influence of $N_T(\varepsilon^p)$ expression on hydrogen concentration in trapping sites for the single-trap model (with E_b = 60 kJ/mol). 121

Figure 4-19. Influence of $N_T(\varepsilon^p)$ expression on hydrogen concentration in lattice sites for the multi-trap model (with E_b^d = 30 kJ/mol and E_b^{gb} = 60 kJ/mol).. 122

Figure 4-20. Binding energy influence for the multi-trap model on hydrogen concentration in lattice sites. 123

Figure 4-21. Binding energy influence for the multi-trap model on hydrogen concentration in trapping sites. 123

Figure 4-22. Influence of vibration frequency for hydrogen concentration in lattice sites after 1.3 seconds. Comparison between equilibrium and kinetic formulations. 124

Figure 4-23. Influence of vibration frequency for hydrogen concentration in trapping sites after 1.3 seconds. Comparison between equilibrium and kinetic formulations. 125

Figure 4-24. Hydrogen concentration in lattice sites after 0.13 and 1.3 seconds. Comparison between multi-traps models with equilibrium and non-equilibrium considerations with E_b^d = 30 kJ/mol and E_b^{gb} = 60 kJ/mol. 126

Figure 4-25. Hydrogen concentration in trapping sites after 0.13 and 1.3 seconds. Comparison between multi-traps models with equilibrium and non-equilibrium considerations with E_b^d = 30 kJ/mol and E_b^{gb} = 60 kJ/mol. 126

Figure 4-26. Hydrogen concentration in lattice sites after 0.13 and 1.3 seconds. Comparison between multi-traps models with equilibrium and non-equilibrium considerations with E_b^d = 60 kJ/mol and E_b^{gb} = 30 kJ/mol. 127

Figure 4-27. Hydrogen concentration in trapping sites after 0.13 and 1.3 seconds. Comparison between multi-traps models with equilibrium and non-equilibrium considerations with E_b^d = 60 kJ/mol and E_b^{gb} = 30 kJ/mol. 127

Figure 4-28. Hydrogen concentration in lattice sites after 0.13 and 1.3 seconds. Comparison between multi-traps models with equilibrium and non-equilibrium considerations withE_b^d = E_b^{gb} = 45 kJ/mol. 128

Figure 4-29. Hydrogen concentration in trapping sites after 0.13 and 1.3 seconds. Comparison between multi-traps models with equilibrium and non-equilibrium considerations with E_b^d = E_b^{gb} = 45 kJ/mol. 128

Figure 5-1. NRB dimensions. 134

Figure 5-2. Scheme of the two-step simulation: firstly a mechanical and diffusion coupled analysis is performed and then an informed CZM analysis. 138

Figure 5-3. Hydrostatic pressure at the beginning of load for r = 0.25 mm. (note that $p = -\sigma_h$) 139

Figure 5-4. Equivalent stress at the beginning of load for r = 0.25 mm. 140

Figure 5-5. Triaxiality and coverage distribution in the notch root section with increasing load for r = 0.25 mm. 140

Figure 5-6. Notch radius effect on maximum triaxiality and hydrogen coverage. 141

Figure 5-7. Stress-strain curve for different notch radii without cohesive elements. 142

Figure 5-8. Stress-strain curve for different notch radii with cohesive elements 143

Figure 5-9. Stress-strain curve for r = 0.25 mm: triaxiality H, and coverage influence. 144

Figure 5-10. Stress-strain curve for r = 0.25 mm: α influence. 144

Figure 6-1. Hydrogen distribution C_L and C_T in the symmetry axis. 153

Figure 6-2. Hydrogen distribution in lattice sites near the notch tip. 154

Figure 6-3. C_L at crack tip boundary (dashed red line) and maximum C_L (solid blue line) for R = 1.0 155

Figure 6-4. CL at crack tip boundary (dashed red line) and maximum C_L (solid blue line) for R = 0.714 and $tcycle$ = 300 s 156

Figure 6-5. C_L at crack tip boundary (dashed red line) and maximum C_L (solid blue line) for R = 0.5 and $tcycle$ = 300 s 157

Figure 6-6. C_L at crack tip boundary (dashed red line) and maximum C_L (solid blue line) for R = 0.5 and $tcycle$ = 30 s 158

Figure 7-1. Internal pressure history. 167

Figure 7-2. Hoop stress σ_θ along the vessel thickness depending on the autofrettage pressure. Dashed lines represent residual stress and solid lines represent the hoop stress during the service life. 170

Figure 7-3. Hydrostatic stress σ_h along the vessel thickness depending on the autofrettage pressure. Dashed lines represent residual stress and solid lines represent the hoop stress during the service life. 171

Figure 7-4. Geometry and hydrostatic stress during service for p_a = 140 MPa. Detail shows notch geometry and mesh for L_n = 0.5 mm. Note that here compressive stresses are positive (i.e. $p = -\sigma_h$) 172

Figure 7-5. Lattice hydrogen concentration and total hydrogen concentration near the notch root for: (a) L_n = 0.1 mm and Eb = 30 kJ/mol; (b) L_n = 0.1 mm and E_b = 60 kJ/mol; (c) LL_n = 0.9 mm and E_b = 30 kJ/mol; (d) L_n = 0.9 mm and E_b = 60 kJ/mol. 174

Figure 7-6. C_{tot}^{max} response surface for E_b = 30 kJ/mol. 180

Figure 7-7. C_{tot}^{max} response surface for E_b = 45 kJ/mol. 180

Figure 7-8. C_{tot}^{max} response surface for E_b = 60 kJ/mol. 181

List of Tables

Table 2-1. Binding energies (or detrapping activation energies in brackets) for different types of trapping sites. References collected by Song, 2014. 64

Table 3-1. Chronological compilation of works modelling hydrogen diffusion near a crack tip using a Modified Boundary Layer approach and considering trapping sites in diffusion equations. 72

Table 3-2. Analogy between variables in heat transfer and diffusion. 87

Table 3-3. Elasto-plastic and diffusion parameters (from reference (Sofronis & McMeeking, 1989)). 93

Table 3-4. Maximum displacements in the far field contour, correspondent to a load of K_I = 89.2 MPa$\sqrt{\text{m}}$. 95

Table 4-1. Coupling parameters. 104

Table 5-1. AISI 4130 steel: mechanical parameters. 133

Table 5-2. AISI 4130 steel: hydrogen related parameters (San Marchi & Somerday, 2008). 133

Table 6-1. Allowable composition range (wt%) for AISI 4130 steel (San Marchi & Somerday) 149

Table 6-2. Mechanical parameters for AISI 4130 steel. 149

Table 6-3. Diffusion parameters for AISI 4130 steel. 150

Table 6-4. Minimum thickness required considering different approaches. 152

Table 7-1. Diffusion parameters for AISI 4130 steel. 164

Table 7-2. Mechanical parameters for AISI 4130 steel. 166

Table 7-3. Variable parameter range in the interval [-1, 1]. 175

Table 7-4. Design of experiments performed forE_b = 30 kJ/mol. 176

Table 7-5. Design of experiments performed for E_b = 45 kJ/mol. 177

Table 7-6. Design of experiments performed for E_b = 60 kJ/mol. 178

Table 7-7. Coefficients of the functions $f(L_n, p_a)$. 179

Nomenclature

D	diffusivity, diffusion coefficient
D_L	diffusivity in the ideal lattice without defects
D_{eff}	effective diffusivity
B	mobility coefficient
T	temperature
C	hydrogen concentration (hydrogen per unit volume)
C_i	hydrogen concentration in *i* –sites (hydrogen per unit volume)
C_T^i	hydrogen concentration in trapping sites of *i*-type
C_b	hydrogen concentration in the boundary
C_{eq}	equilibrium hydrogen concentration at a given fugacity or pressure
c	hydrogen concentration (in hydrogen atoms per metal atoms)
γ	geometrical factor for random diffusion
E	energy of a potential well
E_0	energy of a potential well in a perfect lattice
E_t	energy of a potential well in a defect
$g(E)$	degeneracy of energy states E
E_a	activation energy (for diffusivity or hop frequency)
a	hop distance or lattice constant
$\Gamma_{i\to j}$	hop frequency of hydrogen atoms from sites *i* to sites *j*
$\Omega_{i\to j}$	frequency of hop attempt form sites *i* to sites *j*
$E_{i\to j}$	energy barrier (activation energy) from sites *i* to sites *j*

K_{ij}	equilibrium constant for the exchange between *i* and *j* sites.
ω_{0i}	vibration frequency of hydrogen atom in sites *i*
N	number of sites where a hydrogen atom might be located (per volume unit)
N_i	number of *i*-sites where a hydrogen atom might be located (per volume unit)
N_L	number of lattice sites (per volume unit)
N_T	number of trapping sites (per volume unit)
N_T^i	number of trapping sites of *i*-type (per volume unit)
E_b	binding energy of a defect (potential well)
K_T	equilibrium constant for trapping sites
$\mathbf{J}_i$	flux vector of *i*-component (or hydrogen located in *i*-sites)
$\mathbf{F}_j$	thermodynamic force vector
L_{ij}	Onsager coefficients for *i*-component and *j*-force.
$\mathbf{v}_j$	drift velocity (drifted diffusion)
μ	chemical potential
μ_i	chemical potential of *i*-component (or hydrogen located in *i*-sites)
μ_i^0	chemical potential of *i*-component in the standard state
μ_b	chemical potential in the boundary
f_{H_2}	fugacity of gaseous hydrogen
p^0	hydrogen pressure in the standard state
θ	hydrogen occupancy (fraction of sites occupied by hydrogen)
θ	hydrogen coverage (occupancy of surface sites)
θ_i	hydrogen occupancy in *i*-sites
$\bar{V}_H$	partial molar volume
$\boldsymbol{\sigma}$	Cauchy stress tensor
σ_h	hydrostatic stress
σ_e	Von Mises equivalent stress
H	local triaxiality

ε^p	equivalent plastic strain
ρ	dislocation density
E	Young's modulus (elastic modulus)
ν	Poisson coefficient
σ_0	yield stress (before plastic straining)
σ_{ys}	yield stress (including hardening/softening)
ξ	parameter considering hydrogen-induced softening or hardening
D_{ij}	component *ij* in the deformation rate tensor
ε^t	hydrogen-induced dilatational true strain
e_{vol}^t	hydrogen-induced volumetric engineering strain
Δv	volume change for each introduced hydrogen atom
Ω	mean volume of a metal atom
λ	dilatational parameter ($\Delta v/\Omega$)
K	hydrogen solubility
Ψ	potential function defining a Traction – Separation Law
Δ_n	normal separation between element faces
Δ_t	tangential separation between element faces
δ_n	critical separation for the normal mode
δ_t	critical separation for the tangential mode
T_n	traction in the normal direction
T_t	traction in the tangential direction
σ_{max}	critical traction for the normal mode
τ_{max}	critical traction for the tangential mode
ϕ_n	fracture energy for the normal mode
ϕ_t	fracture energy for the tangential mode
α	shape parameter for the normal Traction –Separation Law
h	characteristic length of cohesive elements
K_I	stress intensity factor in mode I

p_a	autofrettage pressure in a vessel
p_w	working pressure in a vessel
r_o	outer radius of a vessel
r_i	inner radius of a vessel
t_w	outer radius of a vessel
σ_θ^*, σ_r^*, σ_z^*	elastic hoop, radial and axial stress
σ_θ, σ_r, σ_z	hoop, radial and axial stress distribution

SUBSCRIPTS

L	lattice or interstitial sites
T	trapping sites

Chapter 1 Introduction

In this Chapter, the problem of hydrogen-metal interaction is exposed in its context and some examples of application are shown. Once the problem has been motivated, research objectives are enlisted and the document structure is summarised.

1.1 Motivation

Hydrogen embrittlement is a common phenomenon which degrades metals (Barnoush, 2011; Bernstein, 1970; Delafosse & Magnin, 2001; Gangloff & Somerday, 2012; Hirth, 1980; Lynch, 2007; Oriani, 1978). A reduction in mechanical properties of metals and alloys occurs due to the inclusion of hydrogen as an impurity.

Over the past hundred years many failures have been documented in metals that can be attributed to hydrogen damage. Avoiding the presence of hydrogen is extremely difficult in certain situations: hydrogen is a corrosion by-product in humid and sour environments (Kittel, Smanio, Fregonese, Garnier, & Lefebvre, 2010); For example, numerous failures attributed to hydrogen assisted cracking have been documented in pipelines transporting natural gas or oil (Hadianfard, 2010). Such petrochemical products typically contain H_2S which promote an aggressive environment in which hydrogen is produced and diffuses through the metal causing embrittlement. For this reason, API pipeline X – grades steels have been thoroughly investigated and tested in hydrogen environments (e.g. X42 (Bueno, Moreira, & Gomes, 2014); X60, X80 and X100 (Hardie, Charles, & Lopez, 2006)). Additionally, cathodic protection, sometimes used in order to avoid corrosion, for example in buried pipes or in marine environments, results in hydrogen production which can produce unexpected failures (Shipilov & Le May, 2006; Zhenqian, Zhiling, Chun, & Shuangping, 2015). Similarly, hydrogen absorption might occur in parts that have been plated electrolytically (Devanathan, Stachurski, & Beck, 1963). Tanner documented failures of

cadmium plated head cap screws during service and attributed them to hydrogen embrittlement (Tanner, 1992).

Welding processes may also introduce significant amounts of hydrogen and promote failure (Moon, Lee, Kim, Kim, & Kim, 2003). Hydrogen is supplied by materials in the electrode coating, in the flux or in the shielding gas, as well as by the moist environment (Dayal & Parvathavarthini). This hydrogen insertion added to the usual presence of residual stresses in the weld frequently causes Hydrogen Assisted Cracking (Pardal et al., 2013).

In recent decades, since hydrogen has been proposed as a promising energy carrier, the interest in the interaction between hydrogen and diverse types of materials for hydrogen storage has increased. Several methods of storing hydrogen have been proposed (Zhou, 2005): liquid hydrogen at cryogenic temperatures, by physisorption, as a metal hydride and in gaseous state at high pressures, e.g. at 35 up to 75 MPa (Zheng et al., 2012). The last is the least expensive and consist in storing H_2 in pressure vessels made of alloys or composite materials. However, although H_2 containers have been built for more than a century, embrittlement of the used alloys still is a problem. The explosion of some iron bottles storing gaseous hydrogen in an airship in 1894 (Boellinghaus, Holtappels, Mair, & Grunewald, 2014) might be regarded as one of the first failure cases of hydrogen containers documented.

Currently, selection of suitable components for hydrogen service simply discriminates between especially susceptible alloys (high strength steels, and nickel alloys) and alloys hardly affected (austenitic stainless steels and aluminium alloys), as the Standard ANSI/CSA CHMC 1-2014 defines (Moriconi, Hénaff, & Halm, 2014). Such distinction has an empirical basis but lacks a consistent microstructural and physical explanation.

In the manufacturing of high pressure vessels, compressive residual stresses are usually introduced. It has been demonstrated that compressive residual stresses improve fatigue life, however, some methods (autofrettage, swaging, etc.) produce the yielding of the inner core of the vessel. This yielding reduces some mechanical properties of the vessel (Alegre, Bravo, & Preciado, 2007). It is thus necessary to find a balance between the compressive stresses and the plastic strain. Son et al. (Son & Chang, 2012; Son, Hong, & Chang, 2012) investigated the effect of autofrettage in a pressure vessel for hydrogen storage. The vessel was made of composite layers and an aluminium liner. Discussion on hydrogen content was neglected

there since the aluminium liner is expected to minimise hydrogen diffusion. However, vessels without aluminium or austenitic steel liner, e.g. Type I tanks made of high strength steels, do not keep hydrogen from diffusing along the whole thickness and embrittlement might occur.

Hydrogen in solid solution interacts with the crystal lattice, thereby modifying the mechanical properties of the metal or alloy. Furthermore, the interaction of hydrogen with lattice defects, such as vacancies, dislocations, grain boundaries or inclusions, also plays a crucial role. Progress must be made towards a greater understanding of these phenomena comprising various scales with the objective of predicting and preventing the failure of industrial components subjected to hydrogen embrittlement. Therefore, also the assessment of hydrogen embrittlement must move towards a physical-based numerical modelling of the metal-hydrogen system.

Even if the embrittlement phenomenon involves fracture at low strains, surface morphologies usually show small dimples (Beachem, 1972; Birnbaum & Sofronis, 1994). Thus, even though fracture looks brittle from a macroscopic point of view, a significant plastic process is happening in the crack tip (Oriani & Josephic, 1974). There is agreement about the hydrogen induced dislocation mobility (Birnbaum & Sofronis, 1994), which, in the end, causes strain localization and failures that seem brittle at a higher scale. Moreover, from atomistic calculations, it has been shown that hydrogen reduces the cohesive energy as it weakens the metallic bonding (Jiang & Carter, 2004). However, it is not clear which one is predominant in each specific situation or if there are more mechanisms involved (Lynch, 2007). Thus, hydrogen embrittlement modelling is a challenging matter due to numerical issues as well as uncertainties in the micro-mechanisms operating.

Since hydrogen atom diffuses rapidly due to its small size, time-scale and the possibility of delayed effects are crucial in the interaction between metallic lattice and the inserted hydrogen atom. The number of hydrogen atoms in a region will be directly related to the local response of the metal; then, hydrogen concentration is usually the variable sought when embrittlement wants to be predicted or prevented.

Modelling is even more complex since hydrogen transport through the metallic matrix and the material response are not decoupled. Stress and strain modify crystal morphology and its

defects, affecting thus hydrogen diffusion, while, at the same time, hydrogen is influencing dislocation movement and metallic bonding. Coupled effects are critical in fracture because stress concentrators might promote hydrogen accumulation. Therefore, hydrogen diffusion near a crack tip must be simulated and, with this objective, robust numerical models must be established and verified.

1.2 Research objectives

The framework for this thesis is the simulation of hydrogen embrittlement processes. However, due to the complexity of these phenomena, only the initial phase in embrittlement modelling will be studied: hydrogen transport within metals. Nevertheless, a coupled response of the material and cohesive models modified by hydrogen concentration will also be introduced. Therefore, the main goal of the work will be the numerical modelling of hydrogen diffusion.

Finding a balance between physically-based models (which have many parameters difficult to find empirically) and phenomenological models (which, in contrast, are not based in the real mechanisms) is also an objective sought.

As a more practical aspect of this thesis, the established models will be finally applied in the simulation of hydrogen diffusion in vessels. The objective is not to design a real deposit but to demonstrate how the particularities of the stress state present in a vessel affect hydrogen diffusion and its accumulation around stress concentrators. The relationship between internal pressure in the vessel, stress state, and hydrogen entry phenomena is also intended to be clarified.

The specific objectives of this thesis are:

- Contextualising hydrogen embrittlement as an important issue in material modelling and highlighting its importance for fracture prevention.
- Reviewing extensively and critically the existing numerical models for hydrogen diffusion in metals, especially in steels. The following aspects are discussed:

- Microstructural defects as trapping sites. Consideration of hydrogen different sites in the mass balance.
- Hydrogen hops between different sites giving a kinetic formulation for trapping phenomena
- Thermodynamic equilibrium between trapped hydrogen and hydrogen located in interstitial sites.
- Stress state influence and hydrogen accumulation in tensile regions.
- Relationship between plastic deformation and crystallographic defects.
- Boundary conditions, emerging from the adsorption/absorption processes occurring at the metal surface.

- Presenting a numerical strategy for the implementation of diffusion models in a Finite Element code, including:
  - Analogy between hydrogen diffusion and heat transfer. This strategy can be extended to other phenomena like thermal softening or thermal-induced dilatation.
  - Modelling in ABAQUS by means of the available user subroutines (in brackets) modifying:
    - Balance equations, considering the possible trapping sites (UMATHT).
    - Hydrogen fluxes, including drift terms depending on the hydrostatic stress gradient (UMATHT).
    - State variables: plastic strain, hydrostatic stress, etc. (USDFLD).
    - Boundary conditions: non-uniform and stress dependent (DISP).
    - Hardening/softening (UHARD).
    - Hydrogen-induced dilatation (UEXPAN)
  - Modification of Cohesive Zone Models, specifically of Traction-Separation Law, by hydrogen concentration and local triaxiality using:
    - A two-step simulation (diffusion + crack propagation)
    - A user-defined element (UEL subroutine)

- Numerical simulation of hydrogen embrittlement in notched tensile specimens of a high strength steel
    - Analysis of hydrogen and triaxiality influence on damage initiation
    - Discussion on the Traction-Separation Law capability of simulating the shift from ductile to brittle failure.
- Numerical simulation of hydrogen diffusion through a vessel wall of a high strength steel
    - Analysis of diffusion near a stress concentrator
    - Simulation of cyclic loads and its effects on hydrogen diffusion
    - Assessment of residual stress influence on hydrogen concentration at equilibrium

Beyond the numerical study and simulations, a primary, even though more abstract, goal will be to describe the uncertainties and knowledge gaps present in research on hydrogen diffusion and embrittlement. The aim is to clarify the future challenges in this field, to emphasize the need for a multidisciplinary study and to delimitate the possibilities of the current models.

1.3 Document structure

Following this introductory chapter, the dissertation structure is:

- **Chapter 2. Review on hydrogen diffusion modelling** In this chapter, diffusion fundamentals are exposed in a didactic way, reviewing the main equations modelling this phenomenon in various scales: from the atomic perspectives to the continuum equations in which FEM codes are based. The vast part of this Chapter is extracted from the paper “A review on diffusion modelling in hydrogen related failures” published in the journal *Engineering Failure Analysis*.

- **Chapter 3. Implementation of hydrogen diffusion and embrittlement modelling.** Taking the previous chapter as a starting point, governing equations for hydrogen

diffusion in metals, specifically steels, are shown. Hydrogen concentrations are treated separately depending on the sites in which they are located (lattice or trapping sites). A critical review of the milestones in this research field is carried out. After that, a consistent model is presented, which is used afterwards in the diffusion simulations made in Chapter 4 to Chapter 7. In Section 3.5. a methodology aiming at modelling fracture with cohesive elements is presented, in which hydrogen content and local triaxiality influence the fracture process. Section 3.6. includes the details for the numerical implementation by means of user subroutines in the commercial FE code ABAQUS. Finally, diffusion model implementation is validated with some results from literature.

- **Chapter 4. Numerical simulation of hydrogen diffusion near a crack tip.** In this chapter, the main objective of the dissertation thesis is partially covered: the simulation and analysis of hydrogen diffusion near a crack tip. With this purpose, the previously presented model variants, e.g. realistic boundary conditions or multi-trapping effects, are evaluated and a parametric study is made. This Chapter is based on the research paper "Coupled hydrogen diffusion simulation using a heat transfer analogy" published in the journal *International Journal of Mechanical Sciences*.

- **Chapter 5. Simulation of hydrogen and triaxiality effects in notched specimens.** This Chapter is dedicated to simulating hydrogen-assisted fracture of notched specimens employing the informed-cohesive model presented in Section 3.5 after finding hydrogen local concentrations considering equilibrium. This Chapter is based on the research paper "Numerical simulation of hydrogen embrittlement and local triaxiality effects in notched specimens" published in the journal *Theoretical and Applied Fracture Mechanics*.

- **Chapter 6. Application to a pressure vessel considering cyclic loading.** Here, the implemented subroutine considering fugacity and stress effects on the boundary conditions is used to obtain hydrogen concentrations near a notch in a pressure vessel. Frequency and load amplitude effects are also analysed. This Chapter is based on the

conference paper “Hydrogen transport modelling near a crack tip in a pressurized tank” published in the journal *Procedia Engineering*.

- **Chapter 7. Assessment of residual stress effects in a pressure vessel.** Hydrogen diffusion is analysed near a notch in a pressure vessel storing H_2, which has been subjected to an autofrettage process. Relationship between hydrogen concentration, compressive residual stress and plastic strain is evaluated. This simulation represents an industrial application of the presented numerical methodology. This Chapter is based on the research paper “A methodology for the numerical assessment of autofrettage influence on hydrogen content near a notch in a 4130 steel pressure vessel” published in the journal *Theoretical and Applied Fracture Mechanics*.

- **Chapter 8. Conclusions and future work.** In the last Chapter of this thesis, the most important drawn conclusions are summarised both for the followed methodology and for the found results. Finally, the possible future steps in this research are anticipated.

Chapter 2 Review on hydrogen diffusion modelling

In this Chapter, the need of hydrogen diffusion modelling is highlighted as a first step in the numerical characterisation and prevention of hydrogen embrittlement. Interstitial solid state diffusion can be described as a random phenomenon, however there will be also some drift forces biasing this behaviour so a modification in Fick's laws is needed. The potential energy landscape of the metal lattice characterises the influence of imposed fields and microstructural defects in transport kinetics. Thus, considering the chemical potential as a driving force, the physical basis of diffusion will be translated into continuum equations. Finally, the two-level models that take into account lattice and trapping sites for hydrogen will be reviewed in this Chapter.

2.1 Introduction

Usually, the interaction of metal-hydrogen is divided into two parts: transport phenomena (absorption and diffusion) and damage mechanisms. Both phenomena are related, but in this Chapter only the mathematical models that try to establish constitutive equations of diffusion are reviewed. The ultimate aim of diffusion modelling is to obtain concentration profiles to predict where and how the fracture will begin or where the more severe damage will occur. In any case, a consistent theory of diffusion and the influence of the stress-strain fields on it will not only produce more accurate concentration profiles, but it will result in a better understanding of the damage micro-mechanisms.

The objective of this review is to develop a simplified continuum level model from the general physics fundamentals. Firstly, the multiscale and multidisciplinary character of materials science is underlined and in particular that of hydrogen embrittlement.

Later, mass transport is physically explained and the interstitial diffusion mechanism is explained as a random motion at the atomic level.

Next, the importance of characterising the energy landscape of the metal lattice is shown and what the factors are that influence the energy state of an inserted hydrogen atom. Spatial variations in such free potential energy are discussed as a driving force. This leads to defining and characterizing the chemical potential as a continuum function. In order to consider all the effects in a single driving force, one must know how the chemical potential changes with the variation of concentration and stress state. These functions can be found using thermodynamic properties and statistical physics. Chemical equilibrium or, alternatively, kinetic relationships between components or between sites are also discussed.

Then, through appropriate simplifications, the physical concepts exposed are related to the continuous diffusion models that are most commonly used in finite element simulations. These are models that consider only two types of sites for hydrogen: interstitial sites and microstructural traps.

Finally, the coupled nature of diffusion is briefly reviewed from a numerical point of view. The equations presented are related to damage micro-mechanisms involved. In this sense, hydrogen embrittlement is explained by a great number of theories but two of them are the most developed: HEDE (Hydrogen enhanced decohesion) in which hydrogen expands the matrix and so the cohesion and the fracture energy are reduced (Gerberich & Chen, 1975; R. A. Oriani & Josephic, 1974; Steigerwald, Schaller, & Troiano, 1960) and HELP (Hydrogen locally enhanced plasticity) in which hydrogen favours the mobility of dislocations which implies local plasticity even if there is a macroscopically brittle failure (Birnbaum & Sofronis, 1994; Lufrano, Sofronis, & Birnbaum, 1996, 1998). Furthermore, in some metals, dissolved atomic hydrogen can establish bonds with the metal element. Thus, the resulting hydrides can also produce embrittlement (Lufrano et al., 1998; Owen & Scott, 1972) but these considerations are beyond the scope of this review where only the situations in which hydrogen is in a solution are considered.

2.2 Multiscale approach

In materials science there is often, unfortunately, a gap between the different approaches modelling the same fact; nevertheless, in recent years the need of a multiscale approach in modelling has been emphasised (Horstemeyer, 2010; Risto, 2002). Diffusion and hydrogen embrittlement are not exceptions.

Regarding the hydrogen transport, diffusion has usually been a phenomenological science based on the laws of Fick and Arrhenius. Because both classical theories and quantum physics agree in these behaviours, researchers can find unprofitable to follow a quantum approach (A. M. Stoneham, 1978).

However, due to the nature of the metals, quantum physics and solid state physics have become increasingly important in the field of metallurgy and in the prediction of properties of such materials. In addition, with regard to hydrogen diffusion, quantum effects are not always negligible because the small size and mass of the hydrogen atom causes that it cannot be treated as a classical particle (Paxton, 2014).

For example, a quantum phenomenon that can alter the prognosis made by classical physics in terms of mass transport is tunnelling (A. Stoneham, 1972a, 1972b; K. Yu & Klinger, 1974). Diffusion in this case is not thermally activated and thus an Arrhenius-based approach would be wrong.

At the atomic level, metallic bonding properties vary due to the insertion of hydrogen. Besides, at microscopic scale, the interaction of hydrogen with certain defects such as dislocations must be also considered.

In this sense, the presumed absence of a single mechanism to explain hydrogen embrittlement is remarkable: models that may seem contradictory at the continuum level, such as decohesion (HEDE) versus localized plasticity (HELP) should be explained at the microscopic or even atomic level.

Therefore, even if diffusion can be described by a continuum description in a first approximation, the micro-mechanisms of damage must count with the interaction of hydrogen with crystal defects.

Furthermore, the amplitude of scales is not only dimensional but also temporary. Diffusion involves jumps occurring in femtoseconds, but the evolution of the whole system can last for months or years and affect the durability or integrity of a component in its service life.

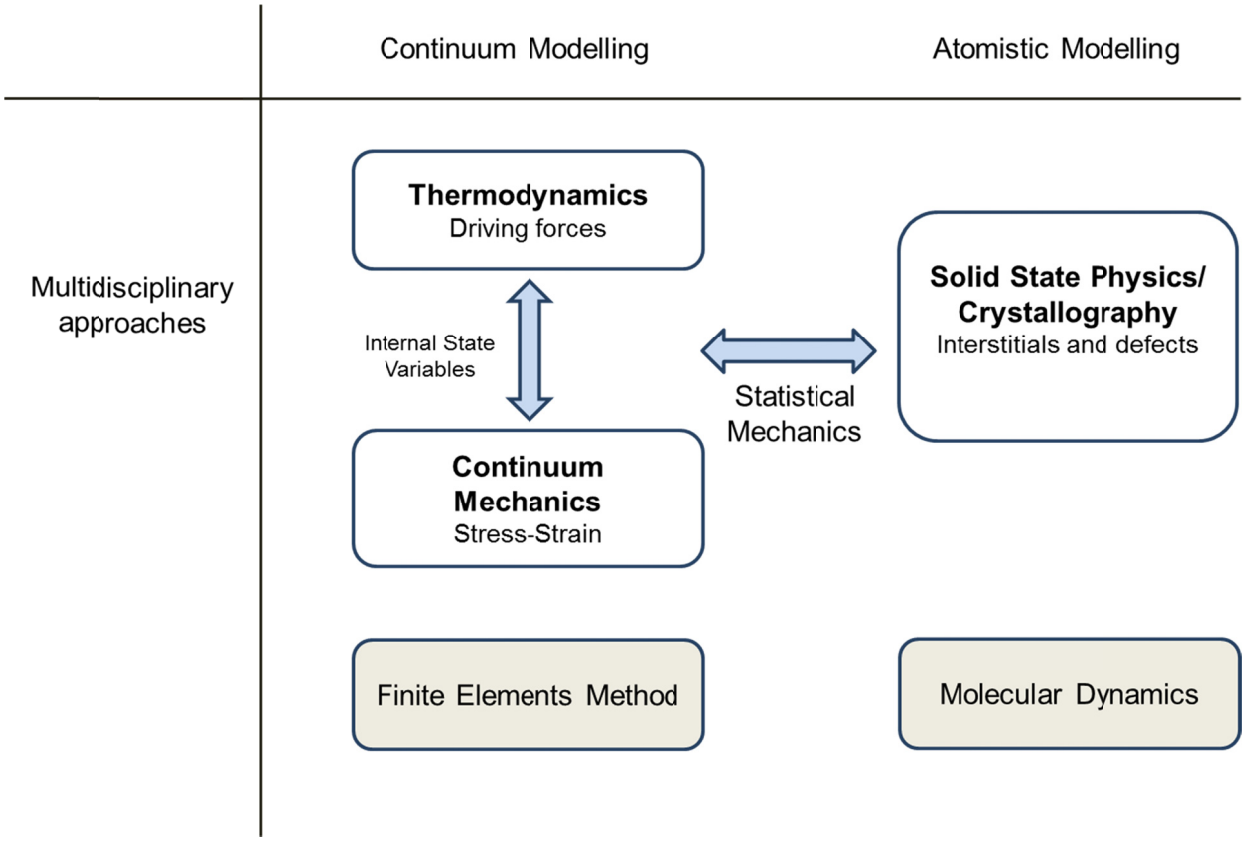

Figure 2-1. Multiscale approaches and its respective computational methods (brown). Boxes on the left correspond to a continuum scale while boxes on the right are related to the atomic scale.

There is also a gap between scales in the computational methods used to simulate these phenomena. Continuum mechanics use finite element simulation as the main tool. Its handicap arises when it is required to model small regions like crack tips where, as noted, atomic phenomena are important. Finite element methods are also limited when the material is not homogeneous and there are defects altering the behaviour, as it occurs in the diffusion of hydrogen.

On the other hand, the atomistic approach utilizes molecular dynamics whose disadvantage is that only small regions and short time windows can be modelled [30]. Still, this computational tool is useful for finding properties of metals and their interaction with

hydrogen. In the context of transport phenomena, due to the random walk nature of diffusion, the Monte Carlo method is usually applied (R. Kirchheim, 1987; R. Kirchheim & Stolz, 1987).

The present review consists in the following conceptual scheme: an understanding of the diffusion phenomenon as a random jump at atomic level that, due to the interstitial solution properties, is translated into driving forces associated with macroscopic thermodynamic magnitudes. This means that, although the review aims at putting the focus on the modelling of continuous, previously the basics of diffusion will be presented in connection with solid state physics (Figure 2-1). It is also shown how statistical mechanics serve as a bridge between the two scales.

It is noteworthy that not only the interstitial transport must be described; hydrogen entry at surfaces plays a key role. When adsorption/absorption occurs in aqueous media, an electrochemical approach should be considered. Thus, in many processes of interest in the degradation of metals by hydrogen, electrochemistry is an indispensable science (Beck, Bockris, McBreen, & Nanis, 1966; Bockris & Subramanyan, 1971; Liu, Atrens, Shi, Verbeken, & Atrens, 2014).

2.3 Diffusion phenomena

Basically, diffusion is a mass transport from one region to another caused by concentration gradients. The flux of particles in a mixture tends to a dispersion of the components until the complete mixing is achieved. This fact was first observed in fluids and later in solids (Mehrer & Stolwijk, 2009). Chronologically, the Fick's phenomenological approach of preceded the study of molecular diffusion, but in the subsequent development of models the opposite path is followed.

2.3.1 Einstein equation for brownian motion

In his work on Brownian movement (Einstein, 1906), Albert Einstein presented a kinetic theory explaining the randomness in the motion of particles in suspension observed by Robert Brown. A relation between the diffusion coefficient D, the temperature T and the fluid viscosity is found: it is called Stokes-Einstein relation. More generically, a mobility coefficient B is defined that in the case of Brownian motion would depend on the viscosity and particle size:

$$D = Bk_BT \tag{2.1}$$

Such generic equation is called Einstein-Smoluchowski relation. Although supposedly Brownian motion only refers to fluids, an analogy with crystalline solids can be made since diffusion has also the random walk as a basis (Schubert, 2005).

However, the causes of this random motion are different: classical Brownian motion is produced by collisions of pollen particles with fluid molecules whereas interstitial solid diffusion is caused by the vibrations of the interstitial impurity and its random jump to a neighbour site.

2.3.2 Diffusion as a random walk

In order to prove the randomness of diffusion, it is supposed a certain hydrogen mass M deposited at $x = 0$ in a unidimensional path. Initially, it is assumed that each hydrogen atom has the same opportunities to make a jump to the left than to the right. The atoms that make many more steps towards one side than towards the other side will move away very much from the origin. However, most of atoms make approximately the same number of hops to the right than to the left. This leads to the hypothesis that the distribution will approach, as the number of steps increases, to a normal distribution. The randomness leading to such distribution is what is known as Gaussian White Noise. In fact, the differential equation that represents Fick's second law can be easily solved (Crank, 1979) obtaining:

$$C(x,t) = \frac{M}{2\sqrt{\pi Dt}}\exp\left(-\frac{x^2}{4Dt}\right) \tag{2.2}$$

It is proved that $C(x,t)/M$ approaches a normal distribution centred in the origin, i.e. with a mean value of $\mu = 0$, and with a variance of $\sigma^2 = 2Dt$. Therefore Fick's law is compatible with a random movement. Actually, the diffusion equations are a particularization of the Fokker-Planck equation governing the evolution of a stochastic event such as Brownian motion (Altenberger, 1978) or, in this case, the interstitial solid diffusion. Drift forces are also included in the Fokker-Planck equation (Tsallis & Bukman, 1996).This deviation is discussed in section 3.5.

It is important to highlight, that the standard deviation depends on time: the more time elapses the distribution will be "extended". Knowing the properties of a normal distribution, σ^2 is the expected value of the square of the distance to the mean. Therefore, on average, the square of the displacement ε of an atom is expected to be (Einstein, 1906):

$$\varepsilon^2 = 2Dt \tag{2.3}$$

The expression is only valid for the one-dimensional diffusion. Generically, instead of a factor of 2, a γ coefficient that takes into account the geometry can be included. For instance, for the three-dimensional case, $\gamma = 6$.

While the movement of a single particle in a given time may thus be described with the concept of random motion, it is not possible to tell in which direction it will move in that time (Crank, 1979). However, considering no longer a particle but a large set of particles distributed in a region, random motion will result statistically in a net flux from regions of high concentration to regions of low concentration; this fact occurs simply because there are more molecules in the area of high concentration.

2.3.3 Landscape of potential energies

From this perspective, diffusion is the balance of hops between the different sites where the hydrogen atom can stay. In the diffusion equations position is a continuous magnitude, but metals have a crystalline structure so those sites correspond to the unoccupied spaces at atomic level and the equilibrium position of an atom is actually a discrete variable.

As a result of the interatomic attractions generated by the metal lattice, sites where hydrogen tends to stay correspond to areas of low potential energy. Interatomic potentials are usually treated as a two-body problem; however, an impurity in a metal crystal is a many-body problem. In order to solve this difficulty, there are different approaches that derive analytic potentials from semi-empirical quantum-mechanics arguments.

Among them there is the Embedded Atom Method (EAM) developed by Daw and Baskes that allows to find the interatomic potential and to characterize the influence of defects and impurities in metals (Daw & Baskes, 1983; Daw & Baskes, 1984).

Some works (X. Zhang, Peng, & Lu, 2010; Zhao & Lu, 2011) perform a multiscale modelling considering two regions: an interior zone where Quantum Mechanics (QM) calculations are done including Density Functional Theory (DFT) and an outer region where Molecular Mechanics (MM)calculations are performed with the EAM. An interaction energy must be included in order to couple the two scales (QM/MM). This procedure is a tool for obtaining preference sites and energy distributions.

Thus, analysing the diffusion in certain orientation x, the potential trace $V(x)$ will have some well points where the hydrogen atom can be placed and saddle points to be overcome in the hop between neighbour sites.

Diffusion is a thermally activated process, i.e. energy is needed to overcome the saddle, at most of the temperatures of interest in industrial and technological processes. However, as discussed in paragraph 2, an effect called quantum tunnelling has been found in which the hydrogen atom can move to an adjacent site through the barrier with less energy than expected. Because this phenomenon occurs only at extremely low temperatures (Grabert & Wipf, 1990), this behaviour is neglected from now onwards, only considering the thermally activated nature of diffusion. Nonetheless, even at room temperature, when tunnelling is not the predominant mechanism, Katzarov et al. demonstrate, using the path integral theory, that quantum effects play a crucial role in hydrogen diffusion (Katzarov, Pashov, & Paxton, 2013).

When there is an ideal crystal lattice, the depths of the wells will be repeated periodically according to a pattern dependent on the orientation. However, the potential distribution might be modified in two ways [39]. Firstly, when other potential field $\phi(x)$ is imposed:

$$V(x) = V_0(x) + \phi(x) \tag{2.4}$$

Where $V_0(x)$ is the potential trace of the perfect lattice, i.e. without defects. For example, the stress state can be regarded as a potential field superimposed.

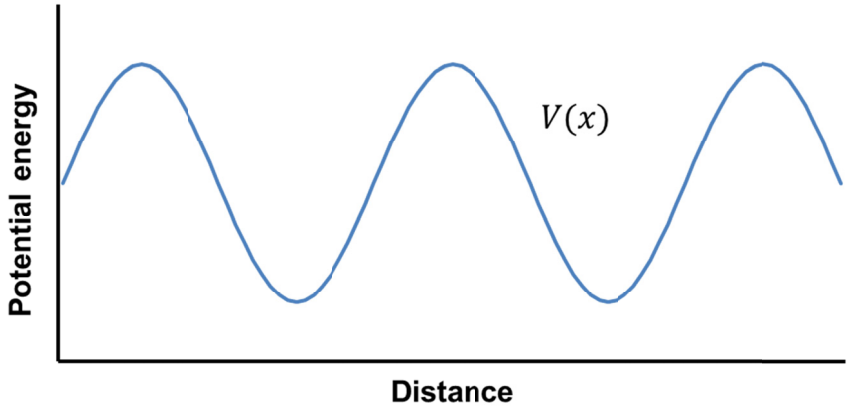

Figure 2-2. Potential energy of a metal lattice along a certain *x* direction

Secondly, when there are defects in the metal lattice: these places are broader and therefore the hydrogen present in them is less attracted; thus, the well point is deeper and the retention of the hydrogen atom is stronger. Hydrogen may be in different lattice imperfections (e.g. inclusions, vacancies, dislocations, grain boundaries, second phases, etc) called microstructural traps (G. M. Pressouyre, 1980). The two main effects, as it will be seen in the following sections, are an increase in apparent solubility and a decrease in the apparent diffusivity (A. M. Krom & A. Bakker, 2000).

When the potential trace is not uniform, the jump is biased towards directions of lower potential energy and thus it is not completely random. Actually, during the interstitial diffusion metal atoms move locally distorting the matrix, and therefore, each jump is never a complete stochastic event independent from the previous ones. In order to expect this independence, the matrix relaxation should be much faster than the time it takes a hop (Kehr, 1978).

Following Kirchheim's work (R Kirchheim, 1982), a way of characterizing the state of a crystal imperfection is to describe the energy distribution. The potential wells correspond to the energy states E in Figure 2-3. Degeneracy of each state, $g(E)$, i.e., the number of times it is repeated on the total, may range from perfect crystal to amorphous state. In the first case, it is called one-level system since all potential wells have the same energy E_0. One kind of trap can be added with energy E_t less than E_0; in this two-level system degeneracy of each level obviously depends on the concentration of traps. The extreme case is the amorphous state; although it is difficult to represent the distribution of defects, one can consider that degeneracy follows a Gaussian distribution, being the most probable energy state that of the ideal interstitial site.

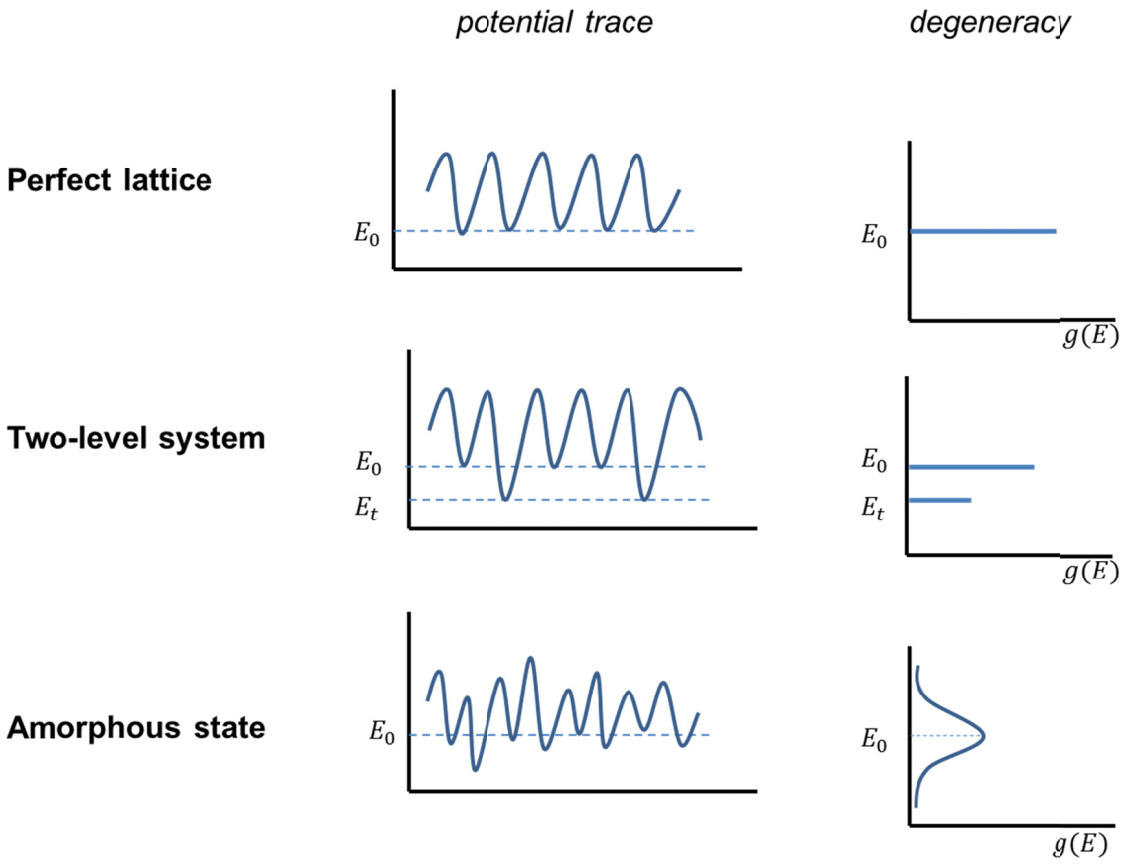

Figure 2-3. Potential energy distribution and degeneracy of the well points in different configurations (R Kirchheim, 1982).

In order to characterize the energy levels associated with different type of traps, there are different experimental techniques: one of the most used is Thermal Desorption Spectroscopy (TDS) (M Nagumo, Takai, & Okuda, 1999; Takai, Yamauchi, Nakamura, & Nagumo, 1998) in which trapping energies are closely related to the temperature at which the rate of desorbed hydrogen is greater. Isothermal methods such as electrochemical permeation might also be used to find the energies associated with traps if a number of tests at different temperatures are made (Oudriss, Creus, Bouhattate, Conforto, et al., 2012).

Such techniques have their limitations and with them it is challenging to obtain accurate values of binding energies for each type of trap because in the same specimen simultaneous effects of different traps occur (Maroef, Olson, Eberhart, & Edwards, 2002). Besides, by a well potential it is only possible to characterize the ideal vacancies or substitutional impurities. Most of the real traps have instead an associated distribution of energy wells and saddle points. Therefore, comparison of the experimental values with atomistic calculations (e.g. semiempirical potential in the above-mentioned EAM) will be crucial for better energy characterization of the traps in each specific situation.

Energy distributions has been can be calculated by the EAM for different systems, e.g. for hydrogen in body-centered-cubic iron (Wen, Xu, Fukuyama, & Yokogawa, 2001). In that work of Wen et al., calculated binding energies of dislocations and vacancies are in agreement with experimental values.

Grain boundaries (GB) are particularly complex because they not only act as trapping sites but they constitute accelerated diffusion paths or short-circuits (A Barnoush, 2011). However, knowledge and energy characterization of both phenomena are still limited.

In nickel grain boundaries, Oudriss et al. studied these double effect (Oudriss, Creus, Bouhattate, Savall, et al., 2012) and concluded that trapping phenomena are predominant in GB in which there is a large density of dislocations and vacancies, whereas in the high-angle random boundaries hydrogen diffusion is accelerated (Oudriss, Creus, Bouhattate, Conforto, et al., 2012).

Furthermore, the influence of hydrogen on grain boundary decohesion plays a fundamental role in intergranular fracture modelling (Alvaro, Thue Jensen, Kheradmand, Løvvik, & Olden, 2015).

2.3.4 Transition rate

Considering the metal lattice as a discrete space of sites, each jump is the step of a random walk with a length equal to the distance a between two adjacent well points. In addition, the frequency of jump, i.e. the transition rate, will be the inverse magnitude of the time elapsed in a single step: $\Gamma = 1/t$. Starting from here, it is possible to reach numeric expressions of the diffusion coefficient.

2.3.4.1 Hop between equal sites

When all sites are equal, i.e. matrix without defects or one-level system, and there is no interaction between interstitial hydrogen atoms because the concentration is very low and all neighbour sites are empty, a single jumping frequency can be defined by means of an Arrhenius law. The exponential term indicates the probability of thermal energy exceeding the diffusion barrier; in other words, a thermally-activated jump with E_a is considered:

$$\Gamma = \Gamma_0 \exp\left(-\frac{E_a}{k_B T}\right) \tag{2.5}$$

The pre-exponential factor Γ_0 depends on the vibration frequency of the hydrogen atom, sometimes taken as the Debye frequency within the metal lattice and hence a quantum problem that is not reviewed here. This fact is related with tunnelling or delocalization. Therefore, deviation from the expected $-T^{-1}$ dependence of diffusion coefficient occurs at low temperatures (Hirth, 1980). Wimmer et al. obtain temperature-dependent diffusion coefficients in nickel from ab initio computations considering all vibrational terms (Wimmer et al., 2008). The pre-exponential factor is also greatly isotope dependent (Schaumann, Völki, & Alefeld, 1970).

The activation energy of a single hop is the difference between the well point and the saddle point that should be overcome in the direction of the jump. Most times, its value is fitted by

empirical values of the diffusion coefficient. However, there exist elastic models able to calculate the diffusion barrier assuming a lattice elastic expansion (Ferro, 1957). However, with ε equal to the interatomic distance a:

$$D = \frac{1}{\gamma} a^2 \Gamma_0 \exp\left(-\frac{E_a}{k_B T}\right) \tag{2.6}$$

An Arrhenius type expression is obtained for D:

$$D = D_0 \exp\left(-\frac{E_a}{k_B T}\right) \tag{2.7}$$

2.3.4.2 Hop between different sites

More generically, following Toribio and Kharin's work (Toribio & Kharin, 2015), it must be assumed that the jump occurs between different sites and even that the neighbour sites may already be occupied. The kinetics of mass exchange between two adjacent places, for instance A and B, can be described by the frequency $\Gamma_{A\to B}$ in which the hop from A to B occurs:

$$\Gamma_{A\to B} = \Omega_{A\to B} Y_B \tag{2.8}$$

It is equal to the frequency $\Omega_{A\to B}$ in which the jump is attempted, multiplied by the probability that the jump is effective Y_B. The first term depends on the vibration frequency ω_{0A} of the particle in A and the activation energy $E_{A\to B}$ acting as a barrier between A and B:

$$\Omega_{A\to B} = \omega_{0A} \exp\left(-\frac{E_{A\to B}}{k_B T}\right) \tag{2.9}$$

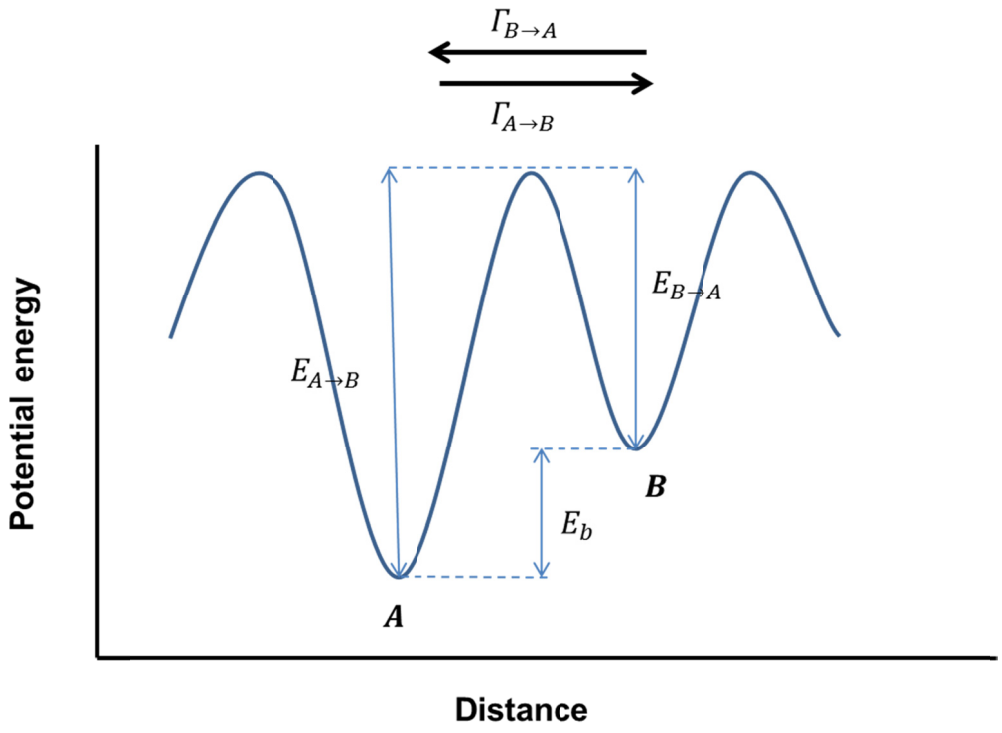

Figure 2-4. Hop between two different sites A y B.

The probability that the jump is effective Y_B is equal to the probability of finding a B-type site (N_B/N) multiplied by the probability that it is empty ($1-\theta_B$). Where N_B is the number of B-type sites; N the total sites and θ_B the occupancy of this kind of sites. Numerically:

$$Y_B = \frac{N_B}{N}(1-\theta_B) \tag{2.10}$$

In these cases where there are two states the transition rate is not symmetrical and thus it will be an activation energy in each direction. The difference between both is called binding energy E_b and characterizes each trap in relation with interstitial ideal sites. Some authors consider that it is an inherently negative energy (Sofronis & McMeeking, 1989); nevertheless, in the present work E_b is assumed as a positive value. Because the transition rate is asymmetrical, the diffusion coefficient is specific for each pair. In addition, each hydrogen trap may be classified as reversible or irreversible depending on the activation energy needed to remove hydrogen from there.

2.3.5 Driving force and flux

In classical physics, a force is any magnitude capable of modifying the momentum of a particle or system. Knowing that in the fluids there is an analogy between the Transport Phenomena (Bird, Stewart, & Lightfoot, 2007), i.e. momentum transfer, heat transfer and mass transfer, a force will also represent any agent capable of modifying the amount of energy or matter.

Momentum transfer has as driving force in a fluid the velocity gradient, which constitutes Newton's law relating the shear stress with such gradient and through the a coefficient called viscosity.

Analogically, there is the Fourier's law for heat transfer and Fick's law for mass diffusion. Focusing on diffusion, Fick's law assumes that the flux $\mathbf{J}_i$ of particles of a component i is proportional to the concentration gradient ∇C_i. This proportionality allows defining the diffusivity or diffusion coefficient D with units of type m^2/s. The negative sign indicates that transport is produced from high to low concentrations:

$$\mathbf{J}_i = -D\nabla C_i \tag{2.11}$$

Exchange of matter will happen until thermodynamic equilibrium is reached. This equilibrium is characterized by the absence of variations in different thermodynamic quantities. This condition does not always mean an absence of concentration gradients (Gorban, Sargsyan, & Wahab, 2011). Onsager uses this fact to include the diffusion in the context of non-equilibrium thermodynamics (Onsager, 1931a, 1931b):

$$\mathbf{J}_i = \sum_j L_{ij}\mathbf{F}_j \tag{2.12}$$

Where the component i suffers a flux due to the different driving forces $\mathbf{F}_j$ (each one defined as a vector). The matrix L_{ij} contains the corresponding coefficients. Moreover, each driving force defines a scalar potential in the classical form:

$$\mathbf{F}_j = -\nabla V_j \tag{2.13}$$

In other words, the thermodynamic equilibrium may be defined as the absence of gradients on the potential of these forces. Usually, the driving forces are caused by variations in chemical potential μ_k of the components, in temperature T, in pressure P, and in other external potentials. For example, transport due to temperature gradients is called Soret effect or thermophoresis; osmosis is explained by the pressure gradient; or if the external potential is due to electrostatic forces, the expression obtained is the Nernst-Planck equation.

When several of these processes occur at the same time, in order to consider a less complex approach, it is taken into account that all driving forces can be reduced into gradients of chemical potential (Wijmans & Baker, 1995). Thus, a flux of particles of component i will be created:

$$\mathbf{J}_i = -\sum_k L_{ik} \nabla \mu_k \tag{2.14}$$

When there is a multicomponent solution, the terms $k \neq i$ are designated as cross coefficients because they weight the influence of a component in the transport of the other.

A different approach consist in establishing that hydrogen flux is equal to the contribution of all the jumps ($\Gamma_{A\to B}$) passing through a particular surface. Using Fourier series, flux vector can be expressed at a given point (Toribio & Kharin, 2015). This approach is more physical-based, but it is mathematically more complex than the phenomenological Onsager expression.

As noted, Fick's laws have a random distribution as numerical solution. This occurs when the only driving force is the concentration gradient. However, when the jump is not completely random, diffusion deviates from Fick's first law. This deviation can be described by a drift flux that is equal to the concentration multiplied by a quantity called drift velocity v_j, which is always associated with a driving force. It is assumed that there is only one component and thereby the subscript i is removed:

$$\mathbf{J} = -D\nabla C + \mathbf{v}_j C \tag{2.15}$$

$$\mathbf{J} = \mathbf{J}_{random} + \mathbf{J}_{drift} \tag{2.16}$$

Following Teorell's formula, a relation between the velocity and the driving force is obtained through the associated mobility B defined above.

$$\mathbf{v}_j = B\mathbf{F}_j \tag{2.17}$$

Although drift velocity and drift flux were initially defined for drag forces occurring in fluids due to advection, i.e., due to the bulk transport of the media, it is also applicable in rigid solids considering other phenomena that cause deviation of random motion. In addition, this double flux term also serves to explain the Kirkendall effect (Danielewski & Wierzba, 2010).

Nevertheless, the approach based on the equation 14 allows to include both random effects and the deviation from them in the chemical potential as the only driving force. In this case, the flux is:

$$\mathbf{J} = BC\mathbf{F}_j = -\frac{D}{k_B T} C\nabla\mu \tag{2.18}$$

where the mobility is considered as expressed before. It could be shown how, for dilute solutions, substituting the value of the chemical potential as a function of concentration $\mu = \mu(C)$ Fick's first law is finally obtained.

2.4 Interstitial Solid Solutions

For the purpose of modelling the continuum, it must be found an accurate function of the chemical potential μ. Then, a flux tending to equalize the chemical potentials until equilibrium is established.

There is a different thermodynamic approach that explains the random phenomena like Brownian motion considering that the main driving force is an entropy gradient (Neumann, 1980). As a conclusion drawn in section 3.2, random motion of a certain mass tends to a normal distribution in unidimensional diffusion; in this probabilistic context, the normal distribution maximizes entropy. Consequently, both approaches must be equivalent.

2.4.1 Chemical potential

As noted, hydrogen atoms tend to stay in places of low potential free energy. From fundamental thermodynamic relations the chemical potential is defined as a molar free energy. Considering the Helmholtz free energy:

$$\mu_i = \left(\frac{\partial F}{\partial n_i}\right)_{T,V,n_{j\neq i}} \tag{2.19}$$

But the most common conditions in engineering are those of constant pressure and temperature. In that case the Gibbs free energy is used:

$$\mu_i = \left(\frac{\partial G}{\partial n_i}\right)_{P,T,n_{j\neq i}} \tag{2.20}$$

As seen in section 3.3, the potential energy landscape characterizes diffusion at the atomic level. Making the necessary corrections, microscopic properties of the lattice should be translated into macroscopic features (thermodynamic potentials). The tool that bridges the gap between both scales is provided by statistical mechanics.

Alternatively, through an atomic approach, Venturini et al. (Venturini, Wang, Romero, Ariza, & Ortiz, 2014) define a particle chemical potential that may vary from particle to particle, thus it is not a uniform field. In such a case, driving forces and linear kinetics are considered discrete.

In this review, a continuum model is pursued so the main objective is to find a relationship between chemical activity expressed by the chemical potential and concentration, or equivalently, between chemical potential and occupancy.

2.4.1.1 Statistical Mechanics

Entropy can be divided into a configurational part S^c, dependent on the "order" of the particles, and a non-configurational part S^{nc}. Configurational entropy follows Boltzmann law depending on the number of possible microstates W:

$$S^c = k_B \ln W \tag{2.21}$$

Possible microstates are calculated by means of combinatory as a function of the number of particles n and the number of possible sites N:

$$W = \frac{N!}{n!\,(N-n)!} \tag{2.22}$$

Using, as it is usually done in statistical physics, Stirling's approximation, and an expression for the chemical potential is obtained (Fukai, 2006). Defining a dimensionless concentration called occupancy $\theta = n/N$:

$$\mu = \mu^{nc} + k_B T \ln\left(\frac{\theta}{1-\theta}\right) \tag{2.23}$$

If only the configurational entropy is considered, the model is called quasi-regular solution (Lumsden, 1952; Lupis & Elliott, 1967; R. B. McLellan, 1972). In this case, $\mu^{nc} = \mu^0$ is the molar enthalpy.

The next step is to take into account the interaction energy between pairs of atoms (Guggenheim & McGlashan, 1951): solute-site (H-S), solute-solute (H-H) and site-site (S-S). The total energy E_k is the sum over all possible pairs. In that term the coordination number of interstitial sites is also included, depending on the type of cell (R. B. McLellan, 1972). Because there is an energetic degeneracy dependent on the configuration of the sites, the canonical ensemble is used, whose partition function Z is:

$$Z = \sum_k g(E_K) \exp\left(-\frac{E_k}{k_B T}\right) \tag{2.24}$$

where the summation is made over each of the possible configurations k and $g(E_K)$ is the degeneracy of each one. From this partition function, it can be found the Helmholtz free energy F:

$$F = -k_B T \ln Z \tag{2.25}$$

There are two possibilities to calculate the partition function: zeroth order or first order treatment. In the first case it is considered that the atoms are randomly distributed in the interstitial sites so the sum of all states is replaced by a single degenerate state (Alex & McLellan, 1970).

Actually, each interstitial solute atom restricts to a number of neighbour sites to be occupied. It is what is called quasi-chemical or first-order treatment (R. B. McLellan & Dunn, 1969). In this approach, therefore, the entropy is not completely random. Now it is not possible to suppose a single degenerate state and the expression for degeneracy will be much more complex.

In both cases, however, there is a term independent on occupancy, μ^0; another term associated with the number of possible microstates and finally a more or less extensive sequence of terms that depend on configuration k, on occupancy and on the interaction energy between hydrogen atoms ε_h:

$$\mu = \mu^0 + k_B T \ln\left(\frac{\theta}{1-\theta}\right) + f(k, \theta, \varepsilon_h) \tag{2.26}$$

A similar result is given by Christensen et al. (Christensen, Stoltze, Jacobsen, & Nrskov, 1990) for the chemical potential of hydrogen in Palladium. Performing a thermodynamic analysis, available sites are considered in contact with an hydrogen reservoir (J. R. Lacher, 1937; John R. Lacher, 1937).

2.4.1.2 Fermi-Dirac distribution

Hydrogen in a metal lattice follows Fermi-Dirac statistics because each energy state can be occupied only by an atom and therefore an analogy with the Pauli exclusion principle can be established. The probability that the E_i level is occupied by a hydrogen atom corresponds to the Fermi-Dirac distribution:

$$p_i = \frac{1}{1 + \exp\left(\frac{E_i - \mu}{k_B T}\right)} \tag{2.27}$$

Equivalence between the chemical potential and the Fermi energy is assumed, although this is physically arguably [68]. The total occupancy will be:

$$\theta = \sum_i p_i g_i \tag{2.28}$$

Where is g_i the degeneracy of the energy state E_i, i.e. the density of site energies (DOSE) (Reiner Kirchheim, 1988). For an interstitial solid solution, being N_i the total number of sites of type i, degeneracy means the normalized number of such sites:

$$g_i = \frac{N_i}{\sum N_i} \tag{2.29}$$

If the energy levels are very close, occupancy and degeneracy can be expressed in a continuous manner:

$$\theta = \int_{-\infty}^{+\infty} \frac{g(E)}{1 + \exp\left(\frac{E - \mu}{k_B T}\right)} dE \tag{2.30}$$

Therefore, from the Fermi-Dirac distribution and considering an expression of $g(E)$ it is possible to find the relationship between the occupancy and the chemical potential. The energy E corresponds to the well points of the potential energy trace (Figure 2-3).

Degeneracy has a different expression depending on whether one considers the perfect crystal, with certain defects or completely amorphous. There will be considered only extreme cases.

In the former case, a lattice without defects represents a completely degenerate state in which the distribution of sites follows the Dirac delta function (Reiner Kirchheim, 1988). The potential well is constant and equal to E_0.

$$g(E) = \delta(E - E_0) \tag{2.31}$$

Solving the corresponding integral (substituting eq. 31 in 30) and isolating the chemical potential, a similar expression is obtained where the term μ^0 is equivalent to the energy of a potential well in the ideal matrix, E_0.

$$\mu = E_0 + k_B T \ln\left(\frac{\theta}{1-\theta}\right) \tag{2.32}$$

For the latter case, the amorphous state, it is almost impossible to know the real distribution of defects and therefore the energy states distribution. Nevertheless, the amorphous state can be characterized as a deviation from the perfect crystal, i.e. with a mean value of E_0, following a normal distribution. Kirchheim (Reiner Kirchheim, 1988) makes some simplifications in order to solve the integral and obtains for high temperatures and low concentrations:

$$\mu = E_0 - \frac{\sigma^2}{4k_B T} + k_B T \ln\theta \tag{2.33}$$

This expression tends to that of an ideal dilute solution ideal. The less irregular the crystal is (less deviation σ^2 from perfect lattice) the more ideal behaviour will have.

2.4.1.3 Corrections

As it was said in section 3.3., potential energy trace can be derived from ab initio calculations based on solid state physics and quantum physics. However, the potential free energy of the

system includes not only the lattice energy generated by the interatomic forces; vibrational and thermal effects must also be taken into account (Anderson, 1989).

Therefore, when theoretical calculations of the chemical potential are compared with experimental results, two corrections should be introduced. The first correction is made by a phonon term or zero-point energy (Hao et al., 2012; Jiang & Carter, 2004). The second one is a correction due to the thermal electronic excitations (Christensen et al., 1990).

2.4.2 Chemical activity

Chemical activity can be defined through the chemical potential:

$$\mu = \mu^0 + k_B T \ln a \tag{2.34}$$

In this expression the chemical potential in a reference state μ^0 corresponds to that of an activity equal to unity. Taking into consideration the forms of the chemical potential previously found, Henry's law and ideal behaviour are satisfied only for a dilute solution, i.e. $\theta \ll 1$.

Interaction effects between hydrogen atoms, non-configurational entropy excess and corrections by zero point energy and thermal excitations will be neglected hereinafter. And therefore, the chemical potential of a component i (disregarding the stress state) will be:

$$\mu_i = \mu_i^0 + k_B T \ln \frac{\theta_i}{1 - \theta_i} \tag{2.35}$$

2.4.3 Equilibrium between sites

As said in sections 3.3 and 3.4, there are various kinds of sites that can be seen as two different species. An exchange of matter between them, characterized by its energy relationship, is established. In a physicochemical approach, reaction between the hydrogen atoms (H) and the empty sites (V) of each state is assumed and therefore a law of mass action can be used (R Kirchheim, 1982)

$$H_A + V_B \rightleftarrows V_A + H_B \tag{2.36}$$

When the reaction, that is, the exchange between A and B reaches equilibrium, a constant can be defined. Concentrations of empty and filled sites are here expressed in terms of the number of particles n_i and the number of each type of site N_i:

$$K_{AB} = \frac{N_A - n_a}{N_B - n_B} \cdot \frac{n_B}{n_A} \tag{2.37}$$

Expressed in terms of occupancy, $\theta_i = n_i/N_i$, Oriani's equilibrium (R. A. Oriani, 1970) equation is obtained:

$$\frac{\theta_B}{1-\theta_B} = \frac{\theta_A}{1-\theta_A} K_{AB} \tag{2.38}$$

The value of the equilibrium constant follows an Arrhenius law. This can be proved because in equilibrium between both species, their chemical potentials are equal. Therefore, with equations (35) and (38) and imposing $\mu_A = \mu_B$:

$$K_{AB} = \exp\left(-\frac{\mu_B^0 - \mu_A^0}{k_B T}\right) \tag{2.39}$$

The difference between the potential in the standard state of both species can be seen as the enthalpy of formation of a reaction. In the context of diffusion affected by microstructural traps, this enthalpy is called the binding energy between the two sites: $E_b = \mu_B^0 - \mu_A^0$. As mentioned above, binding energy is used in this research work to characterise crystal defects with positive values; that means: $E_b = \mu_T^0 - \mu_L^0 > 0$ and $K_T = \exp(E_b/RT)$.

2.4.4 Stress state

Aiming at describing the evolution of the metal-hydrogen system, a thermodynamically consistent approach is necessary. It must take into account the balance (momentum, mass, energy) and the irreversibility of processes (dissipation and entropy) (Di Leo & Anand, 2013; Gurtin, Fried, & Anand, 2010). However, because this review focuses on transport models, only the possible influences of the stress state in the chemical potential are considered since this function represents the diffusion driving force.

In a lattice subjected to a traction stress state, the sites will be wider and hence the chemical potential will be lower. In different thermodynamic studies on stressed solids (A. G. McLellan, 1970) it has been found:

$$\mu(\sigma_h) = \mu(\sigma_h = 0) - \sigma_h \bar{V}_H \tag{2.40}$$

This means that the energy of interaction of hydrogen atoms with the stress field only depends on the diagonal terms of the stress tensor, $\sigma_h = \frac{1}{3}(\sigma_{11} + \sigma_{22} + \sigma_{33})$ and on the hydrogen partial molar volume $\bar{V}_H$.

Here, only spherical distortion is considered. However, depending on the type of lattice there will be a greater or lesser anisotropy that causes non-symmetrical distortion (Hirth, 1980). In this case, the distortion is tetragonal and the off-diagonal stress terms are also important (T.-Y. Zhang & Hack, 1999).

Interaction energy can also be calculated for a dislocation stress field interacting with an hydrogen atoms atmosphere (Robertson, 2001; Sofronis & Birnbaum, 1995). This approach is fundamental in localized plasticity theories.

2.5 Two-level continuum model

With the aim of implementing a transport model in a finite element code, usually some simplifications are made. Thus, models that consider two types of sites are reviewed: lattice sites (subscript L) and trapping sites (subscript T). Therefore, it is a two-level model with the energy degeneracy shown schematically in Figure 2-3 and all the lattice defects have the same binding energy. This is an idealization since there always are various types of traps in any metallic bulk. To extend the equations presented below for a model with more than one type of traps, the concentration of each kind of trap and their respective exchange kinetics equation must be introduced in the global mass balance (Leblond & Dubois, 1983a, 1983b; Turnbull, 2015; Van Leeuwen, 1974).

Another simplification is to consider that all the saddle points have the same energy for the entire crystal. Therefore, a single activation energy is considered for interstitial diffusion D_L. Furthermore, this diffusivity is considered independent of concentration.

For convenience, hereinafter the more usual nomenclature in bibliography will be used. Energies are usually expressed per mol so the universal constant R is included. In addition, the occupation θ_i in each kind of site i represents the relationship between the hydrogen concentration C_i and the concentration N_i of this type of site.

2.5.1 Interstitial flux

It is assumed, by definition, that traps are isolated from each other (Di Leo & Anand, 2013). Thus $\mathbf{J}_T = 0$ and only the interstitial flux is considered. Another interpretation (Toribio & Kharin, 2015) consists of neglecting flux between traps only if the jump between the two places is unlikely: when there are few traps or when excessive energy is required; in this case need not be considered isolated traps. Anyway, taking the interstitial flux (18), the total hydrogen flux is:

$$\mathbf{J} = -\frac{D_L}{RT} C_L \nabla \mu_L \tag{2.41}$$

This means that only interstitial diffusion is considered and the trapping influence is taken into account as a reaction between the two species.

Assuming $\mathbf{J}_T = 0$ is a problematic simplification even though most of the numerical simulations in literature include it. In situations where many dislocations (for example in a crack tip due to the high level of plasticity) or in grain boundaries, there will be a large accumulation of trapping sites and therefore traps cannot be considered isolated. Simulations that take into account such fluxes in balance equations should be implemented in the future.

2.5.2 Chemical potential

Despite being the chemical potential gradient which governs diffusion, equations are traditionally expressed in terms of a more familiar physical variable: concentration. The simplification made here is to consider a dilute solution, i.e., low occupancy: $\theta_L \ll 1$. Thus, with (35) and (49) the chemical potential is:

$$\mu_L = \mu_L^0 + RT \ln \theta_L - \sigma_h \bar{V}_H \tag{2.42}$$

Substituting equation (41) into (42) and operating, flux is obtained as a concentration function:

$$\mathbf{J} = -D_L \nabla C_L + \frac{D_L}{RT} C_L \bar{V}_H \nabla \sigma_h \tag{2.43}$$

It can be observed how, analogically to (15), (16) and (17), a random term and a drift flux have been obtained. The drift force is here the hydrostatic stress gradient.

2.5.3 Mass balance

Mass conservation implies that the variation of hydrogen concentration in the total volume must be equal to the flux through the surface containing it. Numerically:

$$\frac{\partial}{\partial t} \int_V (C_L + C_T) dV + \int_S \mathbf{J}_L \cdot \mathbf{n} \, dS = 0 \tag{2.44}$$

Substituting (43) in (44) and using the divergence theorem, this balance represents a modified form of the second Fick's law.

$$\frac{\partial C_T}{\partial t} + \frac{\partial C_L}{\partial t} - \nabla \cdot (D_L \nabla C_L) + \nabla \cdot \left(\frac{D_L C_L \bar{V}_H}{RT} \nabla \sigma_h \right) = 0 \tag{2.45}$$

This constitutive equation of diffusion must be solved by a numerical method such as the finite element method. To do this, it must be assumed a relationship between C_L and C_T. Different models present a correspondent meaning of the term $\partial C_T / \partial t$ quantifying the

kinetics of exchange between interstitial sites and traps. All models reviewed are isothermal, i.e., there are no temporal or spatial temperature variations.

2.5.4 Trapping influence

Depending on the considered relationship between traps and interstices, a different numerical expansion of $\partial C_T/\partial t$ is obtained.

2.5.4.1 Effective diffusivity

One of the first attempts, if not the first, to develop a finite element simulation of a two-level diffusion was made by Sofronis and McMeeking (Sofronis & McMeeking, 1989). The general transport equation (45) can be rewritten:

$$\left(\frac{\partial C_T}{\partial C_L}+1\right)\frac{\partial C_L}{\partial t}-\nabla\cdot(D_L\nabla C_L)+\nabla\cdot\left(\frac{D_L C_L \overline{V}_H}{RT}\nabla\sigma_h\right)=0 \tag{2.46}$$

It is possible to define an effective diffusion coefficient representing the delay in diffusion produced by trapping:

$$D_{eff}=D_L\frac{1}{1+\partial C_T/\partial C_L} \tag{2.47}$$

Finally, the general equation used by Sofronis and McMeeking has the form:

$$\frac{D_L}{D_{eff}}\frac{\partial C_L}{\partial t}=\nabla\cdot(D_L\nabla C_L)+\nabla\cdot\left(\frac{D_L C_L \overline{V}_H}{RT}\nabla\sigma_h\right) \tag{2.48}$$

In their work, Oriani's equilibrium is assumed. Deriving from (38) and with $\theta_L \ll 1$:

$$D_{eff}=D_L\frac{C_L}{C_L+C_T(1-\theta_T)} \tag{2.49}$$

Sometimes, the concepts of effective and apparent diffusivity are used as synonyms. However, in the present dissertation effective diffusivity D_{eff} is concentration-dependant and a local magnitude whereas apparent diffusivity is an empirically coefficient obtained from the empirical fitting of permeation or desorption tests [Carneiro Filho; etc.].

The concept underlying the permeation test is simple: evaluating the time that hydrogen takes to diffuse through a thin layer of metal. With this purpose, (Devanathan et al., 1963) proposed an set of two cells: a charging cell in which hydrogen is produced and absorbed in the entry surface of the thin metallic specimen and an oxidation cell in which hydrogen atoms that have reached the exit side of the membrane are oxidised. Hydrogen flux on the exit side might be recorded since it is proportional to the oxidation current density. This test is standardised by the ISO 17081:2014 *Method of measurement of hydrogen permeation and determination of hydrogen uptake and transport in metals by an electrochemical technique*. The output flux rises after the first atoms reach the exit surface and stabilises at a certain time. The final flux is called steady state flux j_∞.

Parameters are obtained by numerical fitting techniques; an analytical expression of the permeation transient flux must be then analysed. In order to obtain these equations, some simplifications are considered. In addition, a proper selection of boundary conditions must be made to reflect the real permeation behaviour. Boundary conditions are the mathematical translation of the physical phenomena implied in hydrogen uptake, i.e. during adsorption and absorption processes. Permeation tests are usually carried out by electrochemical means. As it is mentioned in the previous section, a realistic generalised boundary condition is not usually taken into account in the electrochemical permeation. Nevertheless, hydrogen absorption in a gaseous H_2 environment can be more easily modelled using Sievert's law.

2.5.4.2 Plastic strain influence

From the previous model, Krom et al. (A. Krom, R. Koers, & A. Bakker, 1999) consider the plastic strain rate. Applying the chain rule, an additional term is included:

$$\frac{\partial C_T}{\partial t} = \frac{\partial C_T}{\partial C_L}\frac{\partial C_L}{\partial t} + \frac{\partial C_T}{\partial N_T}\frac{dN_T}{d\varepsilon_p}\frac{\partial \varepsilon^p}{\partial t} \tag{2.50}$$

Oriani's equilibrium is again assumed obtaining:

$$\frac{\partial C_T}{\partial t} = \frac{C_T(1-\theta_T)}{C_L}\frac{\partial C_L}{\partial t} + \theta_T\frac{dN_T}{d\varepsilon_p}\frac{\partial \varepsilon^p}{\partial t} \tag{2.51}$$

The number of traps N_T is not a characteristic value of the matrix and is very difficult to determine because of the large variety of microstructural defects that can be included under this category. However, various investigations have shown that the trap population is associated with dislocation density and depends on the level of plastic strain.

Despite the usual employment of expressions relating N_T with ε^p, it should be noted that this is an important simplification: the number of traps depends not only on dislocations as there will be other types of traps: grain boundaries, vacancies, inclusions, etc.

Number of trapping sites N_T could depend on many microstructural factors: grain size (Oudriss, Creus, Bouhattate, Conforto, et al., 2012), grain boundary misorientation (Oudriss, Creus, Bouhattate, Savall, et al., 2012), density of inclusions , etc. But the importance of hydrogen diffusion in a crack tip has led to many authors to relate N_T with the equivalent plastic strain ε^p. From a crystallographic point of view, an individual trap might be assumed for each atomic plane intersected by a dislocation. Sofronis et al. (Sofronis, Liang, & Aravas, 2001) calculate the number of traps from the dislocation density ρ (m/m^3), and the lattice parameter a (m):

$$N_T = \sqrt{2}\frac{\rho}{a} \tag{2.52}$$

For the dislocation density, those authors use an empirical expression of $\rho(\varepsilon^p)$:

$$\rho = \begin{cases} \rho_0 + \gamma\varepsilon^p, & \varepsilon^p < 0.5 \\ 10^{16}, & \varepsilon^p \geq 0.5 \end{cases} \tag{2.53}$$

where ρ_0 is the dislocation density without plastic deformation and γ is an empirical constant, so there is a lack of physical meaning. This could be improved by taking dislocation density-based constitutive models as a link between dislocation evolution and macroscopic response. Kocks-Mecking model (Mecking & Kocks, 1981), later developed by Estrin (Estrin, 1996), shows the following relationship between dislocation density and equivalent plastic strain:

$$\frac{d\rho}{d\varepsilon^p} = k_1\sqrt{\rho} - k_2\rho \tag{2.54}$$

where k_1 is associated with dislocation storage, and k_2 with dislocation annihilation by recovery. Actually, k_2 depend on ε^p rate, but assuming that it is also constant and solving the differential equation (2.57(2.57), the following relationship is obtained:

$$\rho(\varepsilon^p) = \left[\frac{k_1}{k_2} + \left(\sqrt{\rho_0} - \frac{k_1}{k_2}\right)\exp\left(-\frac{1}{2}k_2\varepsilon^p\right)\right]^2 \tag{2.55}$$

Here, according to Horstemeyer et al. , ρ only includes the Statistically Stored Dislocations (SSD). If Geometrically Necessary Dislocations (GND) are to be introduced, grain boundary effects (Oudriss, Creus, Bouhattate, Conforto, et al., 2012) and Strain Gradient Plasticity (SGP) (Martínez-Pañeda, del Busto, Niordson, & Betegón, 2016; Martínez-Pañeda & Niordson, 2016) should be discussed.

Oudriss et al. (Oudriss, Creus, Bouhattate, Conforto, et al., 2012) have found that N_T decreases with grain size in polycrystalline nickel. As a first approximation they assumed that N_T is due to geometrically necessary dislocations (GND), because the density of GND decreased as the grain size increased. But the difference between experimental N_T and calculated N_T^{GND} indicates that vacancies played a crucial role in trapping.

Dislocations are not immobile defects and, additionally, an hydrogen enhanced mobility has been found, establishing the HELP theory. From the previously defined transport model, Dadfarnia et al. (Mohsen Dadfarnia, Martin, Nagao, Sofronis, & Robertson, 2015) have implemented the mobility of dislocations by means of a drift term consisting of an hydrogen flux associated with mobile dislocations. This term includes dislocation mobility in transport models but does not consider how this mobility is enhanced by hydrogen. Moreover, Zhang et al. (X. Zhang et al., 2010) found by way of quantum and molecular mechanics simulations that dislocations and stacking faults can promote the so-called “pipe diffusion” creating short-circuits for hydrogen.

Anyway, permeation tests with different levels of cold working have revealed that plastic strain delays diffusion, therefore it might be a measure of the trap density. With the values of

the effective diffusivity it is possible to fit an empirical relationship $N_T(\varepsilon^p)$ (Dietzel, Pfuff, & Juilfs, 2006; Juilfs, 2002; A. J. Kumnick & H. H. Johnson, 1980).

A commonly used result is the obtained by Kumnick and Johnson (A. J. Kumnick & H. H. Johnson, 1980) by permeation tests in alpha iron with different levels of equivalent plastic strain. Their results are fitted into the following expression (Sofronis & McMeeking, 1989):

$$\log N_T = 23.26 - 2.33 \exp(-5.5\varepsilon^p) \tag{2.56}$$

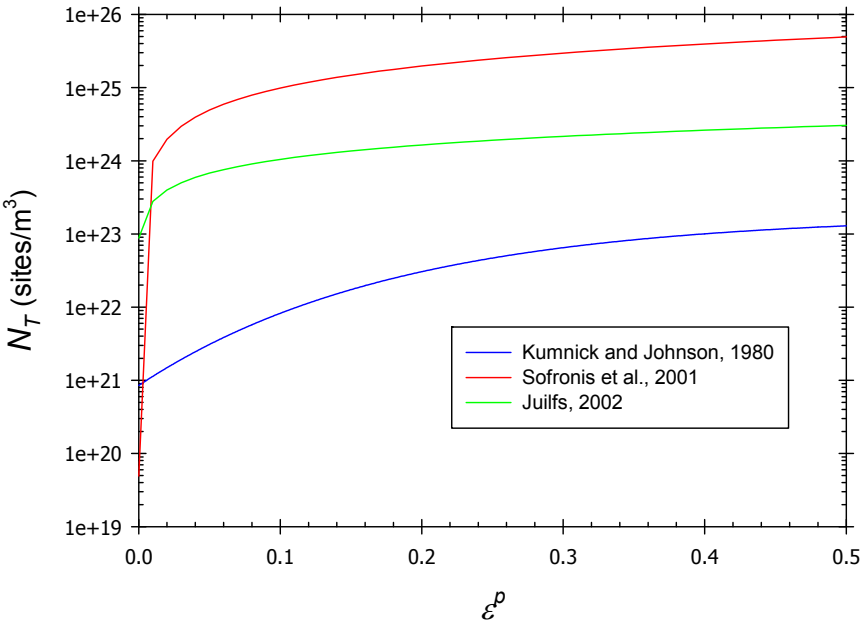

Figure 2-5. Comparison between different expressions for $N_T(\varepsilon^p)$ found in literature.

Comparing three empirical expressions found in literature for BCC iron (Figure 2-5), it is observed that there is a considerable difference between them but the tendency of the curve is similar. It raises from values about 10^{20} sites/m^3 and stabilizes at a plastic deformation of approximately 50%. Tests have been made for different types of steel so comparison should be taken with caution.

2.5.4.3 Non equilibrium

Another option is to consider the influence of strain rate but assuming the formulation of McNabb and Foster (McNabb & Foster, 1963), like in the simulation made by Kanayama et. al. (Kanayama, Ndong-Mefane, Ogino, & Miresmaeili, 2009). In this review, however, the development of Krom and Baker (A. M. Krom & A. Bakker, 2000) is followed where the parameters are dimensionally consistent.

A general expression for $\partial C_T/\partial t$ must be found when Oriani's equilibrium is not satisfied. The variation of concentration in traps can be expressed as the total jumps from L to T minus the total jumps from T to L. Depending on the asymmetric transition rate, it can be expressed:

$$\frac{\partial C_T}{\partial t} = C_L \Gamma_{L\to T} - C_T \Gamma_{T\to L} \tag{2.57}$$

Krom and Bakker assume that the total number of interstitial sites is much greater than the total number of traps $N_L \gg N_T$ and, additionally, that there is a low occupancy $\theta_L \ll 1$, resulting in:

$$\frac{\partial C_T}{\partial t} = \Omega_{L\to T}\theta_L N_T(1-\theta_T) - \Omega_{T\to L} C_T \tag{2.58}$$

Where the frequencies of jump attempt depends on the activation energy E_a and on the binding energy E_b:

$$\Omega_{L\to T} = \omega_{0L} \exp\left(-\frac{E_a}{k_B T}\right) \tag{2.59}$$

$$\Omega_{T\to L} = \omega_{0T} \exp\left(-\frac{E_b + E_a}{k_B T}\right) \tag{2.60}$$

Or, if the number of trapping sites is not constant:

$$\frac{\partial C_T}{\partial t} = N_T \frac{\partial \theta_T}{\partial t} + \theta_T \frac{\partial N_T}{\partial t} \tag{2.61}$$

where:

$$\frac{\partial \theta_T}{\partial t} = \Omega_{L\to T}\theta_L(1-\theta_T) - \Omega_{T\to L}\theta_T \tag{2.62}$$

Then, Equation (2.61) might be expressed as:

$$\frac{\partial C_T}{\partial t} = N_T[\Omega_{L\to T}\theta_L(1-\theta_T) - \Omega_{T\to L}\theta_T] + \theta_T \frac{dN_T}{d\varepsilon^p}\frac{\partial \varepsilon^p}{\partial t} \tag{2.63}$$

It is worth mentioning that, when traps can be assumed as irreversible because they represent deep potential wells, i.e. $E_{T\to L}$ is very high, then $\Omega_{T\to L} \approx 0$. Therefore, once these traps are saturated during diffusion, transport equations are independent of C_T.

In equilibrium, $\partial C_T/\partial t = 0$, representing a relationship between the parameters:

$$\frac{\Omega_{L\to T}}{\Omega_{T\to L}} = \frac{\theta_T}{\theta_L(1-\theta_T)} = K_T \tag{2.64}$$

This means that Oriani's equilibrium is a particular case of the more general kinetic formulation. Local equilibrium is usually considered in diffusion models due to its numerical simplicity, nonetheless this assumption is not valid when changes in lattice hydrogen concentrations are so fast that trapped hydrogen is not able to achieve the condition represented in Equation (2.38) (R. A. Oriani, 1970). Oriani's hypothesis must be carefully held when kinetics might predominate, especially when defects with high binding energy exist (R. A. Oriani, 1970; Thompson, Bernstein, & Swanson, 1982).

At constant temperature, it is not easy to obtain activation energies of diffusion or the capture and release of hydrogen from trapping sites, due to the thermally activated nature of those physical processes. Thermal Desorption Spectroscopy is a technique in which hydrogen content evolution is analysed in ramping temperature conditions. However, temperature changes, especially at high heating rates, invalidate the thermodynamic equilibrium assumption (Ebihara, Kaburaki, Suzudo, & Takai, 2009)., making thus even more complicated the mathematical solution of the problem. Oriani's equilibrium, which relates concentration in trapping sites univocally with that in lattice sites, must be replaced by the

equations from the work of McNabb and Foster in which the change of hydrogen concentration in trapping sites is introduced as in Equation (2.58).

The hydrogen analyser monitories the hydrogen flux escaping the specimen as a function of time. Resultant curves have some characteristic peaks showing when the desorption hydrogen from a specific site is maximum. At different heating rates ϕ, those peaks appear at different temperatures T_p; the relationship between those variables has been proposed by Choo and Lee 1:

$$\frac{\partial \ln(\phi/T_p^2)}{\partial(1/T_p)} = -\frac{E_a}{R} \tag{2.65}$$

Thus, plotting the inverse of the temperature against $\ln(\phi/T_p^2)$, activation energies correspondent to each possible site for hydrogen might be found through the slope of this plot. However, when the influence of other magnitudes on the TDS profiles need to be found, e.g. density of trapping sites, rate constants or other parameters describing kinetics of hydrogen transport, a numerical approach should be followed. Binding energy of each kind of trap might be found as the difference between the activation energy to escape from the trap and the diffusion activation energy. Some trap binding energies collected by Song, 2014 are presented in Table 2-1.

It must be noted that kind of traps show too much scatter in the empirical binding energies. For instance, grain boundaries have been found to have an activation energy of 17 kJ/mol, while other authors cite grain boundaries as irreversible traps, e.g. Dadfarnia et al., 2011, use 58.6 kJ/mol as binding energy. Dislocations also are expected to have an uncertain binding energy ranging from 20 to 60 kJ/mol.

Table 2-1. Binding energies (or detrapping activation energies in brackets) for different types of trapping sites. References collected by Song, 2014.

Type of trap	Binding energy	Reference
grain boundary	(17)	(Choo & Lee, 1982)
grain boundary	45, 47	(Ono & Meshii, 1992)
grain boundary	59	(Asaoka, Lapasset, Aucouturier, & Lacombe, 1978)
grain boundary, dislocation	(22)	(F. G. Wei, Hara, & Tsuzaki, 2004)
dislocation	25	(R. A. Oriani, 1970)
dislocation	36	(Hill & Johnson, 1959)
dislocation	59	(A. J. Kumnick & H. H. Johnson, 1980)
dislocation	(27)	(Choo & Lee, 1982)
surface	71	(Chornet & Coughlin, 1972)
Fe oxide interface	(51, 70)	(K. Y. Lee, Lee, & Kim, 1984)
AlN interface	65	(Podgurski & Oriani, 1972)
MnS interface	(72)	(J. L. Lee & Lee, 1983)
Al_2O_3 interface	(79)	(J.-L. Lee & Lee, 1986)
substitutional Ti	(22)	(G. Pressouyre & Bernstein, 1978)
TiC interface	(95)	(G. Pressouyre & Bernstein, 1978)
TiC interface	(86)	(F. G. Wei et al., 2004)
TiC interface	(87)	(H. G. Lee & Lee, 1984)
TiC interface (semicoherent)	(50)	(F. G. Wei et al., 2004)
NbC interface	(63-68)	(Wallaert, Depover, Arafin, & Verbeken, 2014)
NbN interface	(100-143)	(Wallaert et al., 2014)

2.6 Coupled diffusion

The modelling of hydrogen damage and the discussion between localized plasticity and decohesion are beyond the scope of this review. However, it is essential to bear in mind that transport phenomena are determined by the stress-strain state. This can also be observed in a multiscale approach: at mircostructural level, the crystal lattice is modified due to stress fields and therefore the energy states and microscopic interaction forces drift the diffusion; at continuous level, thermodynamic variables that phenomenologically describe transport are influenced by the elasticity and plasticity.

Based on the theoretical framework developed by Coleman and Noll (Coleman & Noll, 1963), some authors (Di Leo & Anand, 2013; Gurtin et al., 2010) define the influence of mass transport in continuum mechanics through some internal state variables. Energy balance and entropy imbalance will lead to dissipation expressions for describing the evolution of the system in a thermodynamically consistent way. However, here the coupling of diffusion is described with a simplified treatment: on one hand with the alteration of the chemical potential by distortion (see section 4.4) and on the other by modifying the constitutive elasto-plastic equation introducing hydrogen concentration. In this sense, from advances Sofronis et al. (Birnbaum & Sofronis, 1994; Liang & Sofronis, 2003; Liang, Sofronis, & Aravas, 2003; Lufrano et al., 1998; Taha & Sofronis, 2001) is usually considered a double effect of hydrogen:

2.6.1 Local softening

Increasing mobility of dislocations, hydrogen induces a softening. This results in a reduction in resistance to local plastic flow σ_{ys} (Kotake, Matsumoto, Taketomi, & Miyazaki, 2008; Liang & Sofronis, 2003; Liang et al., 2003; Miresmaeili, Ogino, Nakagawa, & Kanayama, 2010)

$$\sigma_{ys} = \sigma_0(c)F(\varepsilon_P) \tag{2.66}$$

Where $F(\varepsilon_P)$ is the strain hardening function; $\sigma_0(c)$ the yield strength before hardening and with an hydrogen concentration c (measured in H atoms per metal atom); and $\sigma_0 = \sigma_0(0)$ is

the yield strength in the absence of hydrogen. Softening can be assumed linear with a parameter $\xi < 1$.

$$\sigma_0(c) = [(\xi - 1)c + 1]\sigma_0 \tag{2.67}$$

Notably, according to Sofronis et al., although plastic flow will always be microscopically reduced, it may be increased macroscopically so a hardening produced by hydrogen will be observed. Either behaviour depends on the stress level, temperature, surface damage due to the electrolytic charging, etc. (Hirth, 1980; Kimura & Matsui, 1987; Matsui, Kimura, & Moriya, 1979; R. A. Oriani, 1983). Once again, consistency between scales is required.

2.6.2 Lattice dilatation

Hydrogen produces a lattice dilatation (Liang & Sofronis, 2003; Liang et al., 2003; Lufrano et al., 1998; Taha & Sofronis, 2001) which can be expressed by adding a term D_{ij}^t to the total deformation rate tensor D_{ij} (besides the plastic and elastic part):

$$D_{ij} = D_{ij}^e + D_{ij}^p + D_{ij}^t \tag{2.68}$$

This term (Lufrano et al., 1998) can be written in terms of true strain ε^t associated with that dilatation and the Kronecker delta δ_{ij}:

$$D_{ij}^t = \frac{\partial \varepsilon^t}{\partial t}\delta_{ij} \tag{2.69}$$

δ_{ij} is the Kronecker delta and $\dot{\varepsilon^t}$ is the deformation due to expansion. However, the usual expression (Peisl, 1978) relates dilatational engineering strain e_{vol}^t, i.e. volumetric true strain, with concentrations c and c_0, local and initial respectively, present in the metal (measured in H atoms per metal atom):

$$e_{vol}^t = (c - c_0)\frac{\Delta v}{\Omega} \tag{2.70}$$

Possible hydride formation of hydrides has not been considered here. In addition, Δv is the volume change for each introduced hydrogen atom (related to the partial molar volume: $\Delta v = \bar{V}_H / N_A$, being N_A Avogadro's number) and Ω is the mean volume Ω of a metal atom.

This engineering volumetric strain e_{vol}^{t} needs to be transformed in a linear true strain. Considering that dilatation produces an equal strain in the three principal directions, it is finally obtained:

$$D_{ij}^{t} = \frac{\partial}{\partial t}\left\{\ln\left[1 + \frac{(c - c_0)}{3}\frac{\Delta v}{\Omega}\right]\right\}\delta_{ij} \tag{2.71}$$

Zhang and Hack (T.-Y. Zhang & Hack, 1999) discuss the situations where deformation is not only dilatational but there is a tetragonal distortion.

Considering this double hydrogen effect, and substituting the found expressions for D_{ij}^{p} and D_{ij}^{t} depending on concentration, the constitutive equation obtained is of the form:

$$\dot{\sigma} = f(D_{ij}) \tag{2.72}$$

Summing up, hydrogen transport depends on the equivalent plastic strain and the hydrostatic stress, which leads to claim that it is a coupled problem and its resolution should be an iterative process.

Despite present coupled models include total concentration in elasto-plastic equations (57) (62), this is arguably. Lattice sites are distorted by hydrogen in a different way than trapping sites, as well as local softening mainly depends on hydrogen interaction with dislocations. Therefore, an atomistic approach should enrich continuum elaso-plastic equations in order to incorporate a different hydrogen influence depending on where it is.

Apart from hydrogen transport, fracture modelling using Cohesive Zone Models (Olden, Thaulow, Johnsen, & Østby, 2007) also will use a hydrogen concentration modifying the parameters of the constitutive law, particularly the traction-separation law (Alvaro et al., 2015).

There is also an effect of hydrogen on dislocation nucleation (Afrooz Barnoush & Vehoff, 2010) so ductile continuum damage models, e.g. Gurson model (Gurson, 1977), might incorporate hydrogen concentration as a parameter (Grange, Besson, & Andrieu, 2000).

Although these numerical models pay attention to diffusion in a crack tip within the context of fracture mechanics, comparison with experimental values is very problematic because it is not easy to measure a hydrogen concentration so localized. Promising methods are Secondary

Ion Mass Spectrometry (SIMS) (Brass, Chene, & Boutry-Forveille, 1996; Mao & Li, 1998) and Micro-Print Technique (Kawamoto et al., 2009).

2.7 Summary

The present Chapter has tried to show how diffusion is a random phenomenon at the atomic level when the thermodynamic potentials are uniform. Nevertheless, when there is an imposed tensional field, for example, or when the crystal lattice defects act as retention sites, the usual Fick laws must be modified.

In that approach, the gradient of the chemical potential is considered as the driving force of diffusion. Its expression depending on the hydrogen occupation can be found through the partition function in the context of statistical mechanics. Fermi-Dirac distribution and degeneracy of the existing defects can be also used to find that expression.

Moreover, thermodynamic studies of stressed solids define how the chemical potential is modified by a given stress state in the metallic bulk. It will be essential in the future to describe better the anisotropic distortion of the cells.

Finally, mass balance equations representing the modified Fick's second law are obtained. Each model must consider a kinetic relationship between traps and interstitial sites so all models that are reviewed here are called two-level models. When Oriani's equilibrium is not applicable, the generic kinetic formulation of McNabb and Foster must be used.

To sum up, hydrogen transport at continuous level is a multidisciplinary and multiscale phenomenon. In this review Chapter, it has been tried to recapitulate the underlying physics fundamentals and to translate them into some constitutive equations that will allow a more accurate and consistent numerical simulation.

Chapter 3 Implementation of hydrogen diffusion and embrittlement modelling

In this Chapter, diffusion equations are particularised for the two-level model differentiating between trapping sites and lattice sites, following Sections 2.5 and 2.6. Constant concentration boundary condition is revisited and modified to consider hydrostatic stress. In addition, hydrogen embrittlement modelling with cohesive elements is presented here. Numerical implementation by means of User Subroutines in ABAQUS is also described in the present Chapter. Finally, subroutines for diffusion are validated comparing results with those obtained in literature.

3.1 Introduction

The first requirement for embrittlement to occur is that there must be a source of hydrogen in contact with a metal. The steps of insertion of hydrogen into the metal are the following:

- Physical transport (in a gaseous or aqueous medium) to the surface of the metal.
- Physical adsorption: there is a contact between the metal and the source of hydrogen.
- Chemical adsorption (and desorption):
    - in gaseous H_2, the molecule must be dissociated.
    - in aqueous media, hydrogen reduction occurs through a cathodic reaction.
- Absorption: the hydrogen adsorbed on the surface enters the metallic volume.
- Diffusion: concentration gradients cause transport of internal hydrogen.

Transferring the physical-chemical steps into a numerical model, diffusion might be associated to a differential balance equation while absorption-adsorption might be linked to

its surface boundary condition. Both steps are equally important in determining the hydrogen content present in the specimen, component or vessel possibly subjected to embrittlement.

PDE are based on the operating physical phenomena. The set of equations chosen with the aim of simulating the actual behaviour of the system must fulfil the following conditions: (i) being accurate enough to predict the real response of the material/component; (ii) being simple enough to implement in a FEM with a limited number of unknowns variables and a limited number of material parameters, permitting thus the empirical fitting with experimental results.

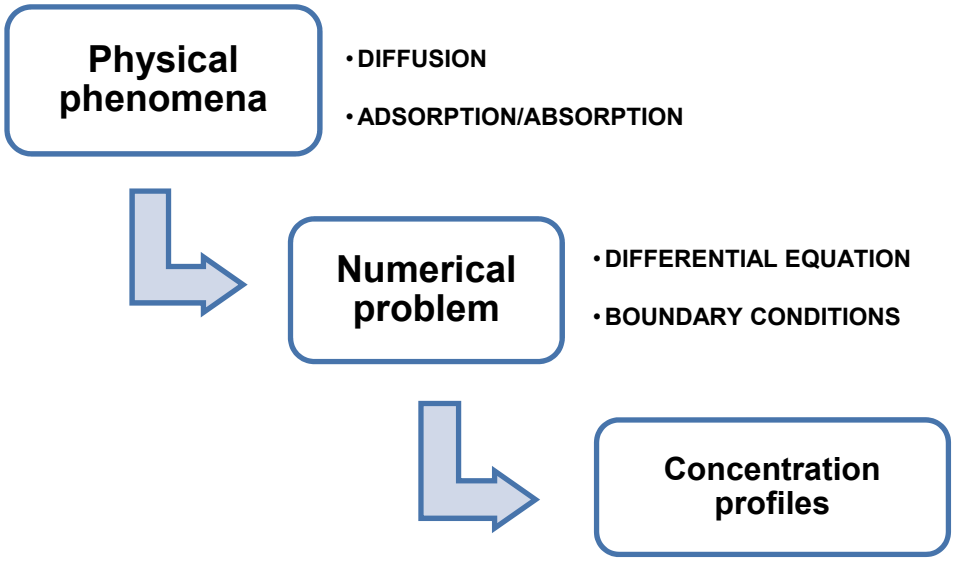

Figure 3-1. Diagram of the modelling approach and relationship between the physical phenomena and the numerical problem.

The corresponding boundary conditions are fundamental as they act as a bridge between numerical modelling and environmental conditions. Hydrogen activity near the metallic surface and subsurface must be better known and implemented in the transport models. The present work does not focus on these surface conditions.

It should be emphasized another simplification assumed in the numerical models used here: temperature will be considered in all of them as constant over time and uniform over the volume in which diffusion takes place.

Taking the Section 2.5 as a starting point, a numerical methodology will be established in the present Chapter, in Continuum Mechanics framework and with the objective of a FEM implementation. First, a chronological recompilation of pioneering works and milestones on hydrogen diffusion modelling near a crack tip is presented in Table 3-1. All of these works have simulated a crack by means of a Modified Boundary Layer approach.

Starting from the paper of Sofronis & McMeeking,, 1989, and considering the trapping effects, the following breakthroughs might be highlighted (in bold letters):

- Turnbull et al., 1997: consideration of McNabb and Foster equations and a generalised boundary conditions emerging from the absorption/adsorption reactions in the crack surface.
- Krom et al., 1999: consideration of the rate of trap creation dN_T/dt , which might be related to the plastic strain rate.
- Taha & Sofronis, 2001: inclusion of a volumetric deformation due to the hydrogen-induced dilatation.
- Sofronis et al., 2001: modification of hardening law by the local concentration in order to translate the HELP theory to a local softening.
- Kanayama et al., 2009: reconsideration of the Krom et al. results, but with the McNabb and Foster kinetic formulation.
- Dadfarnia et al., 2011: implementation of various kinds of traps in the diffusion governing equation: grain boundaries N_T^{GB} (strong traps), dislocations N_T^d (weak traps and the density depends on plastic strain) and carbides N_T^C (very weak traps).
- Di Leo & Anand, 2013: modelling realistic boundary conditions considering a constant chemical potential $\mu_b = cte$**,** which might be translated to a stress-dependent boundary concentration.
- Dadfarnia et al., 2015: inclusion of mobile dislocation effects on diffusion by means of a drift flux term $\mathbf{J}^d$.

Table 3-1. Chronological compilation of works modelling hydrogen diffusion near a crack tip using a Modified Boundary Layer approach and considering trapping sites in diffusion equations.

Reference	Sites	Trapping sites	Coupled effects	Equilibrium	Boundary Conditions
Sofronis & McMeeking 1989	N_L and N_T	$N_T = N_T(\varepsilon^p)$	-	Oriani	$C_b = cte$
Turnbull et al. 1997	N_L and N_T	$N_T = cte$	-	**McNabb and Foster**	**Generalised flux**
Krom et al. 1999	N_L and N_T	$N_T = N_T(\varepsilon^p)$ $\boldsymbol{dN_T/dt}$	-	Oriani	$C_b = cte$
Taha & Sofronis 2001	N_L and N_T	$N_T = N_T(\varepsilon^p)$ dN_T/dt	**Dilatation**	Oriani	$C_b = cte$
Sofronis et al. 2001	N_L and N_T	$N_T = N_T(\varepsilon^p)$	**Local softening**	Oriani	$C_b = cte$
Kanayama et al. 2009	N_L and N_T	$N_T = N_T(\varepsilon^p)$ dN_T/dt	-	**McNabb and Foster**	$C_b = cte$
Dadfarnia et al. 2011	N_L, $\boldsymbol{N_T^d}$, $\boldsymbol{N_T^{GB}}$ **and** $\boldsymbol{N_T^C}$	$N_T^d = N_T(\varepsilon^p)$ dN_T/dt	-	Oriani	$C_b = cte$
Di Leo & Anand 2013	N_L and N_T	$N_T = N_T(\varepsilon^p)$ dN_T/dt	-	Oriani	$\boldsymbol{\mu_b = cte}$
Dadfarnia et al. 2015	N_L	$N_T = N_T(\varepsilon^p)$ dN_T/dt $\mathbf{J}^d$	-	Oriani	$C_b = cte$

3.2 Implemented diffusion equations

Hydrogen Assisted Cracking must be modelled in a continuous scale in order to handle the stress-strain fields. For this reason, diffusion equations describing hydrogen transport are usually based on a phenomenological approach in which vector fluxes and mass balances are defined over the material domain (Díaz, Alegre, & Cuesta).

Hydrogen atoms promote decohesion, modify dislocation motion and alter material properties in many different ways. In addition, the stress-strain field influences hydrogen transport by means of two phenomena: hydrostatic stress, which produces lattice dilatation so hydrogen will tend to reach expanded sites, and plastic strain, which increases the amount of crystal defects creating trapping sites.

The latter phenomenon is crucial in a crack tip where plastic strain is highly localized. This is why hydrogen diffusion models consider a two-level approach as if there were two different chemical components. That is to say hydrogen might be localized in lattice sites (L subscript) or trapping sites (T subscript). Taking Chapter 2 as a starting point, governing equations used in simulations will be presented now.

3.2.1 Flux between trapping sites

As it was noted, hydrogen diffusion models in metals usually consider two types of sites. Within the framework of non-equilibrium thermodynamics, mass fluxes derived from Onsager relationships are taken into account (Onsager, 1931a, 1931b). Even though mass concentration is the sought variable, chemical potential gradients $\nabla\mu_j$ represent the thermodynamic driving force which produces diffusion. Onsager coefficients L_{ij} denote the action of force j on component i; negative sign indicates that the net movement of i-type hydrogen atoms , i.e. hydrogen flux J_i, occurs from high to low chemical potential regions:

$$\mathbf{J}_i = -\sum_{j=1}^{n} L_{ij}\nabla\mu_j \tag{3.1}$$

Particularly, for the two-level diffusion model accounting for lattice and trapping sites, fluxes might be expressed in a matrix form:

$$\begin{bmatrix}\mathbf{J}_L\\ \mathbf{J}_T\end{bmatrix}=\begin{bmatrix}L_{LL} & L_{LT}\\ L_{TL} & L_{TT}\end{bmatrix}\begin{bmatrix}\nabla\mu_L\\ \nabla\mu_T\end{bmatrix} \tag{3.2}$$

However, it is usually assumed that the gradient of μ_L does not affect the flux between trapping sites and the gradient of μ_T does not affect the flux between lattice sites. Cross-terms are thus neglected, $L_{LT}=L_{TL}=0$, so:

$$\mathbf{J}_L=-L_{LL}\nabla\mu_L \tag{3.3}$$

$$\mathbf{J}_T=-L_{TT}\nabla\mu_T \tag{3.4}$$

Onsager coefficients are related to the Einstein equation of diffusion,

$$L_{LL}=\frac{D_L}{RT}C_L \tag{3.5}$$

$$L_{TT}=\frac{D_T}{RT}C_T \tag{3.6}$$

where D_L is the lattice diffusivity, D_T is the diffusivity between trapping sites, C_L and C_T are the hydrogen concentrations in lattice and trapping sites respectively, R is the universal constant of gases and T is the absolute temperature.

Additionally, chemical potential can be expressed in terms of hydrogen concentration. More precisely, it is related to occupancy of *i*-sites $\theta_i=C_i/N_i$, where N_i is the concentration of *i*-sites. From interstitial solid solutions thermodynamic theory, chemical potential usually comprises a term depending on configurational entropy, thus on occupancy, and another term μ_i^0 which express the chemical potential in the standard state. Influence of stress state is considered by means of a purely dilatational term, therefore a term is added consisting of hydrostatic stress $\sigma_h=\frac{1}{3}trace(\boldsymbol{\sigma})$ multiplied by the partial molar volumen of hydrogen inside the metal $\overline{V}_H$. In the present work, it has been assumed, as it was by Di Leo et al. (Di Leo & Anand, 2013), that the chemical expansion is the same for lattice sites and trapping sites:

$$\mu_L = \mu_L^0 + RT \ln \frac{\theta_L}{1-\theta_L} - \bar{V}_H \sigma_h \tag{3.7}$$

$$\mu_T = \mu_T^0 + RT \ln \frac{\theta_T}{1-\theta_T} - \bar{V}_H \sigma_h \tag{3.8}$$

Substituting (3.5), (3.6), (3.7) and (3.8) into (3.3) and (3.4) gives:

$$\mathbf{J}_L = D_L \frac{C_L}{1-\theta_L}\left(\frac{\nabla C_L}{C_L} - \frac{\nabla N_L}{N_L}\right) + \frac{D_L}{RT} C_L \bar{V}_H \nabla \sigma_h \tag{3.9}$$

$$\mathbf{J}_T = D_T \frac{C_T}{1-\theta_T}\left(\frac{\nabla C_T}{C_T} - \frac{\nabla N_T}{N_T}\right) + \frac{D_T}{RT} C_T \bar{V}_H \nabla \sigma_h \tag{3.10}$$

3.2.2 Mass balance: general governing equation

In order to relate fluxes, which are established due to the chemical potential gradient, with concentration variation, a mass balance is required. Assuming no internal sources of hydrogen, the variation of total hydrogen concentration in a volume V must be equal to the flux through the surrounding surface S of such a volume:

$$\frac{\partial}{\partial t}\int_V (C_L + C_T) dV = -\int_S (\mathbf{J}_L + \mathbf{J}_T) \cdot \mathbf{n}\, dS \tag{3.11}$$

Surface is orientated outwards, so negative sign means that positive fluxes represent hydrogen exit from the volume.

3.2.3 Simplified governing equation

These expressions are usually simplified considering the following facts:

- Interstitial sites concentration is assumed constant: $\nabla N_L = 0$. This is arguably because as traps are created the number of interstitial sites could be modified.

- In many alloys, especially in bcc lattices, it is expected low occupancy $\theta_L \ll 1$ because $N_L \gg C_L$. However, θ_L may not be small in FCC metals (Toribio & Kharin, 2015).

- Mobility between trapping sites, or equivalently diffusion coefficient, is considered near zero: $D_T \approx 0$, because traps are not connected or becuase their deep potential energy well prevents hydrogen from diffusing, i.e. $\Delta E_{TT} \gg 1$. This will be discussed in detail in Section 4.4.

Assuming these simulifications, fluxes might be expressed as follows:

$$\mathbf{J}_L = D_L \nabla C_L + \frac{D_L}{RT} C_L \bar{V}_H \nabla \sigma_h \tag{3.12}$$

$$\mathbf{J}_T = 0 \tag{3.13}$$

According to divergence theorem, equation (3.11) can be expressed:

$$\frac{\partial}{\partial t} \int_V (C_L + C_T) dV = - \int_V \nabla \cdot \mathbf{J}_L \, dV \tag{3.14}$$

The balance equation to be solved is then:

$$\frac{\partial C_L}{\partial t} + \frac{\partial C_T}{\partial t} + \nabla \cdot \mathbf{J}_L = 0 \tag{3.15}$$

3.2.4 Oriani's equilibrium

Having two unknowns (C_L and C_T), both variables should be connected using kinetic or thermodynamic assumptions. Equilibrium between the traps and interstitial sites is considered, i.e. $\mu_L = \mu_T$, which leads to the so-called Oriani's equilibrium (R. A. Oriani, 1970):

$$\frac{\theta_T}{1 - \theta_T} = \frac{\theta_L}{1 - \theta_L} K_T \tag{3.16}$$

Where $K_T = \exp(E_b/RT)$ and the binding energy, is defined as the difference $\mu_T^0 - \mu_L^0$. When thermodynamic equilibrium cannot be assumed, McNabb and Foster (McNabb & Foster, 1963) formulation must be included in diffusion equations. Operating in Equation (3.16) wih the assumption that $\theta_L \ll 1$, C_T might be expressed in terms of lattice concentration C_L:

$$C_T = \frac{N_T}{1 + \frac{N_L}{C_L K_T}} \tag{3.17}$$

3.2.5 Plastic strain influence

As seen in Subsection Plastic strain influence2.5.4.2, a plastic strain rate term emerges when the chain rule is applied to the variation in hydrogen concentration in trapping sites. If equilibrium is considered:

$$\frac{\partial C_T}{\partial t} = \frac{C_T(1-\theta_T)}{C_L}\frac{\partial C_L}{\partial t} + \theta_T \frac{dN_T}{d\varepsilon_p}\frac{\partial \varepsilon^p}{\partial t} \tag{3.18}$$

In contrast, when McNabb and Foster equations are used:

$$\frac{\partial C_T}{\partial t} = \Omega_{L\to T}\theta_L N_T(1-\theta_T) - \Omega_{T\to L} C_T + \theta_T \frac{dN_T}{d\varepsilon^p}\frac{\partial \varepsilon^p}{\partial t} \tag{3.19}$$

3.3 Boundary conditions

Different expressions of hydrogen flux as a boundary condition have been discussed, especially when hydrogen is inserted electrochemically (Falkenberg, Brocks, Dietzel, & Scheider, 2010; Liu et al., 2014; Turnbull, 2015) with a particular application for permeation modelling. Turnball et al. (Turnbull, 2015) underline that the entering flux depends also on hydrostatic stress. In the case of hydrogen concentration as a boundary condition, this also can be shown. Assuming a balance between the diatomic hydrogen gas at the surface and the hydrogen atom in solution inside the metal (Marchi, Somerday, & Robinson, 2007):

$$\frac{1}{2}H_2 \leftrightarrow H \tag{3.20}$$

From this equilibrium, the following relation between chemical potential must be met:

$$\frac{1}{2}\mu_{H_2} = \mu_H \tag{3.21}$$

Where chemical potential of hydrogenous gas μ_{H_2} depends on its chemical activity or its fugacity f_{H_2} (Di Leo & Anand, 2013):

$$\mu_{H_2} = \mu_{H_2}^0 + RT \ln\left(\frac{f_{H_2}}{p^0}\right) \tag{3.22}$$

Chemical potential of hydrogenous gas in the standard state (p^0 = 1 atm and T = 25ºC) is zero: $\mu_{H_2}^0$ = 0; therefore p^0 might be omitted provided fugacity is expressed in atmospheres. Electrolytic charging of hydrogen is equivalent to gaseous charging if both methods produce the same fugacity; in electrolytic charging fugacity depends on overpotential (Liu et al., 2014) while in gaseous charging fugacity depends on pressure (Marchi et al., 2007).

Substituting (3.22) in equation (3.21), it can be concluded that chemical potential of hydrogen in solution in the boundary ($x \in \mathcal{B}$) follows the expression:

$$\mu_H(x \in \mathcal{B}) = RT \ln\left(\sqrt{\frac{f_{H_2}}{p^0}}\right) \tag{3.23}$$

It is supposed that this hydrogen atom is placed in a lattice site, i.e. $\mu_H = \mu_L$; thus with equation (3.7), and assuming again low occupancy, $\theta_L \ll 1$, a boundary concentration is obtained:

$$C_L(x \in \mathcal{B}) = \frac{N_L}{\sqrt{p^0}} \exp\left(-\frac{\mu_L^0}{RT}\right) \exp\left(\frac{\bar{V}_H \sigma_h(x \in \mathcal{B})}{RT}\right) \sqrt{f_{H_2}} \tag{3.24}$$

This expression might be grouped in the Sievert's law form, with solubility K and fugacity instead of pressure. The boundary concentration $C_{L,b} = C_L(x \in \mathcal{B})$ is then:

$$C_{L,b} = K \sqrt{f_{H_2}} \tag{3.25}$$

Terms included in solubility demonstrate that it follows an Arrhenius law and it should be expressed in units of concentration divided by pressure (e.g. at·m^{-3}·MPa$^{-1/2}$). It is also crucial

to note that apparent solubility increases with hydrostatic stress due to the lower chemical potential in regions under tension. If equivalent concentration C_{eq} included in the previous simulations is only considered in the unstressed state (with solubility $K_{\sigma_h=0}$), then the realistic boundary condition should be:

$$C_{L,b} = C_{eq} \exp\left(\frac{\bar{V}_H \sigma_{h,b}}{RT}\right) \tag{3.26}$$

3.4 Coupled diffusion

Transport equations include stress-strain variables; hydrostatic stress and equivalent plastic strain is this case. Similarly, constitutive elasto-plastic equations which model material behaviour might be influenced by *internal variables*, e.g. hydrogen concentration. Two phenomena are usually included in this coupled response: hydrogen induced dilatation and hydrogen induced softening.

3.4.1 Hydrogen induced softening

Following Sofronis' works, local flow stress is modelled as a function of total concentration c In the implemented model in this thesis, the factor ξ is taken following Kotake et al. (Kotake et al., 2008). Last multiplying term represents a hardening exponential function where σ_0 is the initial yield stress, E is the Young modulus, ε^p the equivalent plastic strain and n the hardening exponent:

$$\sigma_0(c) = [\xi c + 1]\sigma_0 \left(1 + \frac{E}{\sigma_0}\varepsilon^p\right)^n \tag{3.27}$$

Depending on the specific conditions, ξ might be a softening parameter ($\xi < 0$) or a hardening parameter ($\xi > 0$). An experimental fitting is recommended due to the lack of physical base of this parameter.

3.4.2 Hydrogen induced dilatation

If only a pure dilatational distortion of the metal lattice is considered, a volumetric strain is introduced (Lufrano et al., 1998):

$$e_{vol}^{t} = (c - c_0)\frac{\Delta v}{\Omega} \tag{3.28}$$

With c and c_0, local and initial concentrations respectively (measured in H atoms per metal atom); and where, Δv is the volume change for each introduced hydrogen atom and Ω is the mean volume of a metal atom. As it was show in Subsection 2.6.2, a term in the deformation rate tensor might be included to account for this effect. Inserting a parameter $\lambda = \Delta v/\Omega$ and considering every variable constant respect to time, except concentration c, dilatational rate tensor takes the form:

$$D_{ij}^{t} = \frac{\lambda}{3 + \lambda(c - c_0)}\frac{\partial c}{\partial t}\delta_{ij} \tag{3.29}$$

3.5 Informed cohesive model

3.5.1 Traction – Separation Law

While a continuum element response is described in terms of a stress-strain curve, the cohesive element is governed by the relationship between the traction vector and the separation between its faces (Elices, Guinea, Gómez, & Planas, 2002) as show in Figure 3-2. In the present work, both normal and tangential tractions and separations are considered in the Finite Element implementation.

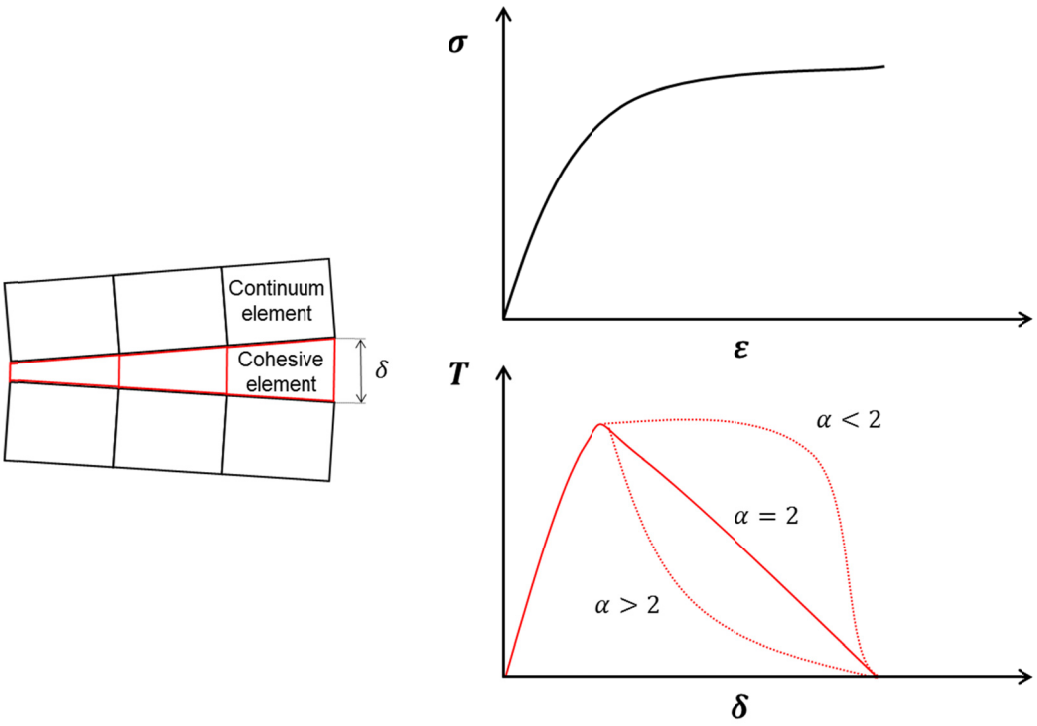

Figure 3-2. Continuum and cohesive element responses.

Damage initiates when traction reaches a critical stress. Then, damage evolves following the predefined TSL up to a critical displacement value. A complete damaged cohesive element provokes the creation of a new surface between two continuum elements and thus it might be regarded as a crack initiation criterion. There are dozens of proposed TSL's (Park & Paulino, 2013): triangular, polynomial, trapezoidal, etc. In the CZM framework, TSL with a triangular shape are usually used to reproduce brittle behaviour, whereas trapezoidal TSL are used to model ductile crack propagation. Figure 3-2 plots a trapezoidal Traction-Separation curve.

However, here the PPR (Park, Paulino and Roesler) formulation is chosen for the TSL. PPR model has the advantage of being a potential-based cohesive model. In addition, it might simulate the shift from ductile to brittle behaviour not only by means of a fracture energy lowering, but also locally modifying the shape of the TSL taking advantage of the "shape parameters".

Equations (3.30) to (3.32) are extracted from the work of the cited authors (Park, Paulino, & Roesler, 2009) and their original formulation is maintained to avoid confusion. The TSL

proposed by these three authors has the advantage of being potential-based, being the potential Ψ as a function of normal and tangential separation Δ_n, Δ_t:

$$\Psi(\Delta_n, \Delta_t) = \min(\phi_n, \phi_t) + \left[\Gamma_n \left(1 - \frac{\Delta_n}{\delta_n}\right)^{\alpha} \left(\frac{m}{\alpha} + \frac{\Delta_n}{\delta_n}\right)^{m} + \langle \phi_n - \phi_t \rangle\right] \times \left[\Gamma_t \left(1 - \frac{|\Delta_t|}{\delta_t}\right)^{\beta} \left(\frac{n}{\beta} + \frac{|\Delta_t|}{\delta_t}\right)^{n} + \langle \phi_t - \phi_n \rangle\right] \tag{3.30}$$

where $\langle \cdot \rangle$ is the Macauley bracket, ϕ_n and ϕ_t are the normal and tangential fracture energies; Γ_n and Γ_t are two energy constants; α and β are the two shape parameters aforementioned, and m and n are non-dimensional exponents.

Cohesive response is governed by this potential and elements are completely damaged when the separations reach a critical value: δ_n for the normal and δ_t for the tangential separation. As seen in Equation (3.30) there is a coupling between tangential and normal modes so this formulation could be used to model mixed mode. Tractions are found differentiating the potential with respect to the correspondent separation:

$$T_n(\Delta_n, \Delta_t) = \frac{\Gamma_n}{\delta_n}\left[m\left(1 - \frac{\Delta_n}{\delta_n}\right)^{\alpha} \left(\frac{m}{\alpha} - \frac{\Delta_n}{\delta_n}\right)^{m-1} - \alpha\left(1 - \frac{\Delta_n}{\delta_n}\right)^{\alpha-1} \left(\frac{m}{\alpha} + \frac{\Delta_n}{\delta_n}\right)^{m}\right] \times \left[\Gamma_t \left(1 - \frac{|\Delta_t|}{\delta_t}\right)^{\beta} \left(\frac{n}{\beta} + \frac{|\Delta_t|}{\delta_t}\right)^{n} + \langle \phi_t - \phi_n \rangle\right] \tag{3.31}$$

$$T_t(\Delta_n, \Delta_t) = \frac{\Gamma_t}{\delta_t}\left[n\left(1 - \frac{|\Delta_t|}{\delta_t}\right)^{\beta} \left(\frac{n}{\beta} + \frac{|\Delta_t|}{\delta_t}\right)^{n-1} - \beta\left(1 - \frac{|\Delta_t|}{\delta_t}\right)^{\beta-1} \left(\frac{n}{\beta} + \frac{|\Delta_t|}{\delta_t}\right)^{n}\right] \times \left[\Gamma_n \left(1 - \frac{\Delta_n}{\delta_n}\right)^{\beta} \left(\frac{m}{\alpha} + \frac{\Delta_n}{\delta_n}\right)^{m} + \langle \phi_n - \phi_t \rangle\right] \frac{\Delta_t}{|\Delta_t|} \tag{3.32}$$

Importance of mixed-mode lies in the fact that normal TSL depends on tangential damage and vice versa. Maximum tractions correspond to the cohesive strengths $\max[T_n(\Delta_n, 0)] = \sigma_{max}$ and $\max[T_t(0, \Delta_t)] = \tau_{max}$ while the area under each curve corresponds to the fracture energies ϕ_n and ϕ_t. The shape of normal traction-separation curve depends on the parameter α: when α tends to 1, a trapezoidal law is obtained while $\alpha > 2$ corresponds to a polynomial law.

3.5.2 Hydrogen influence

From first principle calculations, many authors have demonstrated a cohesive energy reduction promoted by hydrogen (Alvaro et al., 2015; Jiang & Carter, 2004). Atomistic simulations might reproduce bulk or grain boundary decohesion. Expressions can be fitted between hydrogen concentration and fracture energy. Serebrinsky et al. (Serebrinsky, Carter, & Ortiz, 2004), from the experiments performed by Jiang and Carter (Jiang & Carter, 2004), correlate the hydrogen coverage θ in a grain boundary with the cohesive energy ϕ:

$$\phi(\theta) = \phi(0)[1 - 1.0467\,\theta + 0.1687\,\theta^2] \tag{3.33}$$

Some authors (Gobbi, Colombo, & Vergani, 2016; Moriconi et al., 2014; Olden, Thaulow, Johnsen, Østby, & Berstad, 2008) have used this expression in a Cohesive Zone Model, assuming the same reduction in the area under the TSL. However, the transferability from atomic scales to a crack tip is challenging.

Haiyang et al. (H. Yu, Olsen, Alvaro, et al., 2016) follow a different approach: tensile test of notched round bars from (Wang, Akiyama, & Tsuzaki, 2005) are simulated and numerical results are fitted to the experiment. Considering the same shape and critical displacement for the TSL in every cohesive element, they found a reduction in maximum traction as a function of hydrogen lattice concentration. Without more evidence, here the reduction expressed in Equation (3.33) is taken for $\phi_n(\theta)$ and also for $\phi_t(\theta)$. It is also assumed that neither σ_{max} nor τ_{max} depend on hydrogen in the PPR Traction Separation Law.

TSL shape and parameters can also be obtained from Representative Volume Element simulations, considering an internal void or not. Ahn et al. (Ahn, Sofronis, & Dodds, 2007)

include local softening and hydrogen-induced dilatation in the constitutive response of the material and they found a reduction in maximum traction as well as in the dissipated fracture energy. Results indicate that void growth and coalescence, leading to plastic instabilities, are affected by triaxiality and by the hydrogen-induced softening.

It is well known that fracture energy does not only depend on material or environmental variables like hydrogen or temperature, there is also a constraint effect due to the triaxiality of the stress state. Plastic strain is limited in situations of high triaxiality and, as a consequence, ductility is limited. This is the reason why triaxiality shifts failures from ductile to brittle nature. Within the framework of CZM, the traction separation law describing damage must be modified to account for triaxiality.

3.5.3 Triaxiality influence

Fracture in specimens with high triaxiality is more brittle. Local triaxiality H is defined as the ratio between hydrostatic stress σ_h and Von Mises equivalent stress σ_e in each material point,

$$H = \frac{\sigma_h}{\sigma_e} \tag{3.34}$$

Hydrostatic stress has been already defined; Von Mises equivalent stress is defined as:

$$\sigma_e = \sqrt{\frac{3}{2}\mathbf{S}:\mathbf{S}} \tag{3.35}$$

where $\mathbf{S}$ is the deviatoric stress tensor:

$$\mathbf{S} = \boldsymbol{\sigma} - \sigma_h \mathbf{I} \tag{3.36}$$

being $\boldsymbol{\sigma}$ the Cauchy stress tensor and $\mathbf{I}$ the identity tensor. Simulating Representative Volume Elements (RVE), some authors have obtained the influence of triaxiality on the TSL.

The size of this volume appears as a characteristic length in the expression. Results obtained by Anvari et al. (Anvari, Scheider, & Thaulow, 2006) are used. Maximum traction and cohesive energy also depends on yield strength σ_0:

$$\sigma_{max} = [1.1\ln(H) + 2.1]\sigma_0 \tag{3.37}$$

$$\frac{\phi_n(0)}{h} = 1.43\ H^{-1.36}\sigma_0 \tag{3.38}$$

where h is the characteristic length of the RVE. In the present simulation, h is assumed as the cohesive element length. It could be possible to obtain similar expression for shear loads in a RVE simulation but in a tensile test in which mode I predominates this influence might be neglected. Ahn, Liang et al, have found similar expressions considering hydrogen and triaxiality effects at the same time; however, they only take into account Hydrogen Enhanced Localized Plasticity (HELP) mechanism and they introduce a phenomenological softening parameter ξ is the which is hard to assess physically.

Local triaxialiy is obtained in the Coupled Temperature-Displacement analysis in Abaqus and then the correspondent TSL is assigned at each cohesive element.

3.6 Implementation in ABAQUS through user subroutines

Due to the scarce versatility allowed by mass diffusion analysis in Finite Element commercial codes, some authors have used the analogy comparing heat transfer and diffusion for numerical implementation (Falkenberg et al., 2010; Kim, Oh, Kim, Yoon, & Ma, 2012; Oh, Kim, & Yoon, 2010).

Transport phenomena are described by similar balance equations and fluxes. Particularly, momentum exchange is studied in viscous fluids, energy exchange in heat transfer analysis and mass exchange in diffusion processes (Bird et al., 2007). This work puts the focus on the analogy between the last two phenomena. ABAQUS is the commercial software used, so different subroutines are written in order to modify the thermal analysis and obtain concentration distributions in Finite Element simulations. Barrera et al. (Barrera, Tarleton, Tang, & Cocks, 2016) have recently discussed the numerical details for the implementation of this thermal analogy, improving the numerical procedure previously proposed by Oh et al. (Oh et al., 2010). Regarding diffusion equations, a consistent approach with (Barrera et al.,

2016) is followed in the next section although here the coupling effects and the boundary conditions are modelled in a different way.

3.6.1 Diffusion equations

The energy balance for a solid stationary (Bird et al., 2007) is analogous to equation (3.11). ABAQUS consider the balance in the following form:

$$\int_V \rho \frac{\partial \widehat{U}}{\partial t} dV = \int_S \mathbf{q} \cdot \mathbf{n}\, dS + \int_V r\, dV \tag{3.39}$$

$$\rho \frac{\partial \widehat{U}}{\partial t} + \nabla \cdot \mathbf{q} = \mathbf{0} \tag{3.40}$$

Heat flux $\mathbf{q}$ depends on the temperature gradient according to Fourier's law. And $\widehat{U}$ is the internal energy per unit mass. An internal heat source or sink r might be added. This term might be translated to a mass source or sink in diffusion modelling. If density is set equal to one, total hydrogen concentration might be regarded as the internal energy per unit mass. Both are the conserved quantities in the global balance. This fact was already noted by Barrera et al. (Barrera et al., 2016): the analogous variable to the internal energy $\widehat{U}$ is total concentration C, and not the chemical potential as was suggested by Oh et al. (Oh et al., 2010).

At constant pressure, a relationship between the variation of that energy and temperature can be defined as specific heat capacity c_P:

$$d\widehat{U} = c_p dT \tag{3.41}$$

Analogically the term D_L/D_{eff} relates dC with dC_L, but in this case the plastic strain rate term has also been included. Because both factors depend on hydrogen concentrations, a UMATHT subroutine is used. In addition to the increment of internal energy $d\widehat{U}$, the variation with temperature, $d\widehat{U}/dT$, must be also defined for convergence purposes in a UMATHT subroutine. The increment introduced in the code is:

$$dC = \left(1 + \frac{\partial C_T}{\partial C_L}\right) dC_L + \theta_T \frac{dN_T}{d\varepsilon^p} d\varepsilon^p \tag{3.42}$$

Diffusivity in Fick's first law correspond to conductivity in Fourier's law, but this is not important since fluxes are completely redefined following equations (3.9) and (3.10) or (3.11), (3.12) and (3.13). Table 3-2 summarizes analogies between variables.

Table 3-2. Analogy between variables in heat transfer and diffusion.

Heat transfer	**Diffusion**
Internal energy per unit mass: $\widehat{U}$	Total concentration: C
Heat flux: **q**	Mass flux: **J**
Temperature: T	Concentration in lattice sites: C_L
Specific heat capacity: c_p	D_L/D_{eff}
Density: ρ	1

Within the UMATHT interface, it is not necessary to explicitly calculate the gradient ∇C_L as its analogous variable DTEMDX is already available. However, as shown before, hydrogen flux always depends on the hydrostatic stress gradient. The user subroutine USDFLD allows to access the value of the hydrostatic stress at the integration points of an element $[\sigma_h]_{el}$. Then, the 2D gradient of hydrostatic stress at any point $[\nabla\sigma_h]_{x,y}$ is obtained by means of the gradient matrix [**B**]:

$$[\nabla\sigma_h]_{x,y} = [\mathbf{B}][\sigma_h]_{el} \tag{3.43}$$

In the performed simulations elements with four integration points have been used, so there are four values in the vector $[\sigma_h]_{el}$ and four shape functions N_i. Thus, equation (3.43) might be rewritten as:

$$\begin{bmatrix} \frac{\partial \sigma_h}{\partial x} \\ \frac{\partial \sigma_h}{\partial y} \end{bmatrix}_{x,y} = \begin{bmatrix} \frac{\partial N_1}{\partial x} & \frac{\partial N_2}{\partial x} & \frac{\partial N_3}{\partial x} & \frac{\partial N_4}{\partial x} \\ \frac{\partial N_1}{\partial y} & \frac{\partial N_2}{\partial y} & \frac{\partial N_3}{\partial y} & \frac{\partial N_4}{\partial y} \end{bmatrix} \begin{bmatrix} \sigma_{h,1} \\ \sigma_{h,2} \\ \sigma_{h,3} \\ \sigma_{h,4} \end{bmatrix}_{el} \tag{3.44}$$

In order to obtain the derivatives of the shape functions included in [**B**], the inverse of the Jacobian matrix $[\mathbf{J}]^{-1}$, must be used:

$$\begin{bmatrix} \frac{\partial N_1}{\partial x} \\ \frac{\partial N_1}{\partial y} \end{bmatrix} = [\mathbf{J}]^{-1} \begin{bmatrix} \frac{\partial N_1}{\partial \xi} \\ \frac{\partial N_1}{\partial \eta} \end{bmatrix} \tag{3.45}$$

This Jacobian matrix corresponds to the transformation from global to natural coordinates, i.e. the mapping from the global system (x, y) to the isoparametric system (ξ, η):

$$[\mathbf{J}] = \begin{bmatrix} \frac{\partial x}{\partial \xi} & \frac{\partial y}{\partial \xi} \\ \frac{\partial x}{\partial \eta} & \frac{\partial y}{\partial \eta} \end{bmatrix} = \begin{bmatrix} \sum_{i=1}^{4} \frac{\partial N_i}{\partial \xi} x_i & \sum_{i=1}^{4} \frac{\partial N_i}{\partial \xi} y_i \\ \sum_{i=1}^{4} \frac{\partial N_i}{\partial \eta} x_i & \sum_{i=1}^{4} \frac{\partial N_i}{\partial \eta} y_i \end{bmatrix} \tag{3.46}$$

For the generalised fluxes –equations (3.9) and (3.10)– the determination of ∇C_T and $\nabla \varepsilon_p$ is also required so a similar procedure is followed there, once the values at integration points are known.

3.6.2 Coupling equations

Coupled effects on hydrogen diffusion explained on Section 3.4 are usually inserted by means of a UMAT in ABAQUS. Here, for the sake of simplicity, the analogy with heat transfer is exploited again. The advantage is that constitutive elasto-plastic equations have not to be modified and tangent stiffness matrix has not to be recalculated as it is in other works (Kotake et al., 2008; Miresmaeili et al., 2010). In an incremental form, deformation rate term due to hydrogen dilatation can be expressed:

$$\Delta\varepsilon_{ij}^{t} = \frac{\lambda}{3+\lambda(c-c_0)}\Delta c\delta_{ij} \tag{3.47}$$

This reminds a thermal expansion strain considered purely dilatational $\Delta\varepsilon_{ij}^{T}$, which is introduced in ABAQUS by means of UEXPAN subroutine.

$$\Delta\varepsilon_{ij}^{T} = \alpha(T)\Delta T\delta_{ij} \tag{3.48}$$

Therefore a coefficient alpha is redefined as:

$$\alpha(c) = \frac{\lambda}{3+\lambda(c-c_0)} \tag{3.49}$$

On the other hand, local softening is modelled taking advantage of UHARD subroutine where yield stress may be redefined by the user as a function of plastic strain and temperature, in this case plastic strain and concentration.

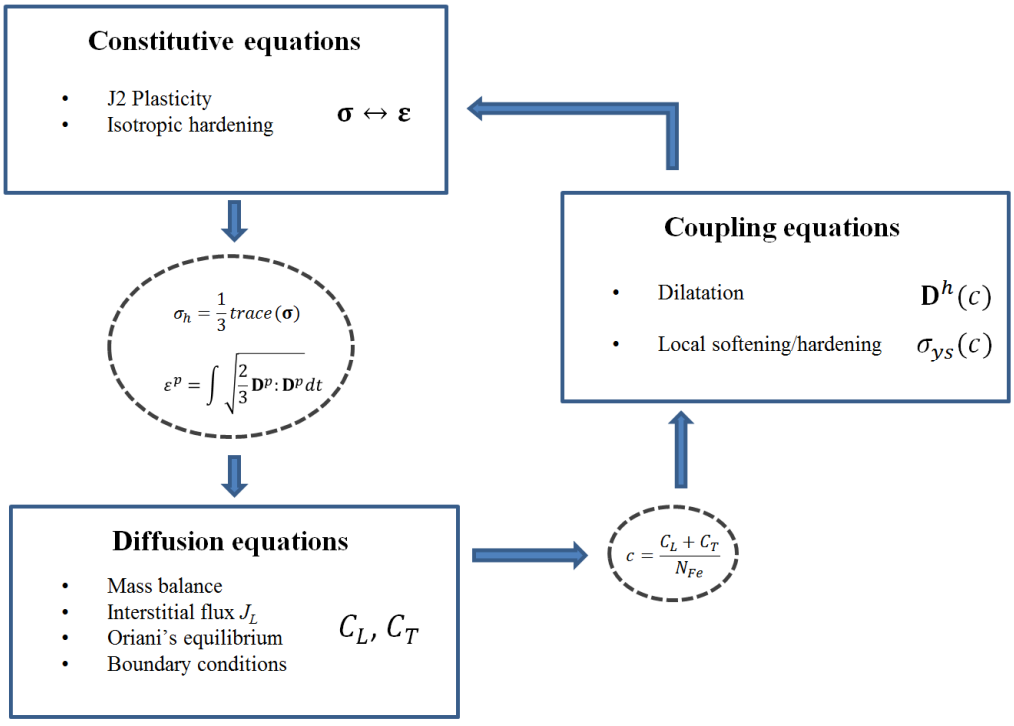

Figure 3-3. Coupling scheme between diffusion and elasto-plastic response.

3.6.3 Boundary conditions

In this model two approaches are merged: the implementation of appropriate boundary conditions according to equation (3.26), and the use of the heat transfer analogy described in previous sections. To this end, in addition to the previously mentioned subroutines, a DISP subroutine is used, allowing one to enter a user-defined boundary condition. DISP works with nodal values while the hydrostatic stress is calculated at the integration points, so an interpolation should be performed by means of the shape functions in order to get $\sigma_h(x \in \mathcal{B})$.

3.6.4 Multi-trapping effects

When more than a single kind of trap is included in the mass balance, the variation of each concentration, $\partial C_T^i/\partial t$ must be included in the governing equation:

$$\sum_i \frac{\partial C_T^i}{\partial t} + \frac{\partial C_L}{\partial t} - \nabla \cdot (D_L \nabla C_L) + \nabla \cdot \left(\frac{D_L C_L \overline{V}_H}{RT} \nabla \sigma_h \right) = 0 \tag{3.50}$$

If Oriani's equilibrium is considered:

$$\sum_i \frac{\partial C_T^i}{\partial t} = \sum_i \frac{C_T^i \left(1 - \theta_T^i\right)}{C_L} \frac{\partial C_L}{\partial t} + \sum_i \theta_T^i \frac{dN_T^i}{d\varepsilon_p} \frac{\partial \varepsilon^p}{\partial t} \tag{3.51}$$

It must be noted that density of some kind of trap might be independent on plastic strain, so $dN_T^i/d\varepsilon_p = 0$ and its contribution in the last term disappears. Following the analogy with the heat transfer, the terms that must be introduced in the UMATHT subroutine are:

$$\Delta C = \left(1 + \frac{C_T^i (1 - \theta_T^i)}{C_L}\right) \Delta C_L + \sum_i \theta_T^i \frac{dN_T^i}{d\varepsilon_p} \Delta \varepsilon^p \tag{3.52}$$

When thermodynamic equilibrium is not applicable, the first right-term in equation (3.51) cannot be expressed as a function of $\partial C_L/\partial t$. Then, McNabb and Foster equations must be included:

$$\sum_i \frac{\partial C_T^i}{\partial t} = \sum_i N_T^i \frac{\partial \theta_T^i}{\partial t} + \sum_i \theta_T^i \frac{dN_T^i}{d\varepsilon_p} \frac{\partial \varepsilon^p}{\partial t} \tag{3.53}$$

In that case, obtaining an expression for $\partial C_T / \partial C_L$ is more complex. Thus, there might be convergence difficulties. In the UMATHT, it has been implemented the following increment of total concentration, i.e. the analogous internal energy increment:

$$\Delta C = \Delta C_L + \sum_i N_T^i \Delta \theta_T^i \sum_i \theta_T^i \frac{dN_T^i}{d\varepsilon_p} \Delta \varepsilon^p \tag{3.54}$$

3.6.5 Kinetic equations

McNabb and Foster equation is implemented in ABAQUS in the occupancy form. That is:

$$\frac{\partial \theta_T}{\partial t} = \Omega_{L \to T} \theta_L (1 - \theta_T) - \Omega_{T \to L} \theta_T \tag{3.55}$$

Occupation in trapping sites must be integrated when McNabb and Foster equations are considered. Here, an explicit scheme is used to find trap occupancy and a smaller time increment is considered following (Kanayama et al., 2009):

$$(\theta_T)_{n+\frac{1}{m}} = (\theta_T)_n + [\Omega_{L \to T} (\theta_L)_n [1 - (\theta_T)_n] - \Omega_{T \to L} (\theta_T)_n] \, \Delta\tau \tag{3.56}$$

where the time increment in the ABAQUS analysis, Δt, is divided in $m > 1$ subincrements of $\Delta\tau$ duration ($\Delta t = m\Delta\tau$). Subscript n indicates the current increment, and $n + 1$ the next one. This scheme is coded in UMATHT subroutine, where the mass balance and the flux equations must be defined using the heat transfer analogy previously presented. Then, the occupation increment for each kind of trap which must be included in equation (3.54) is:

$$\Delta \theta_T = [\Omega_{L \to T} \theta_L [1 - (\theta_T)_n] - \Omega_{T \to L} (\theta_T)_n] \, \Delta t \tag{3.57}$$

When the time increment Δt is high in comparison with hop frequencies, some numerical instabilities might appear since the real trapping and release phenomena are not accurately modelled. In addition, an initial condition for trap occupancy must be given, being a fundamental parameter in the first increments of diffusion simulations. This initial $\theta_{T,0}$ is

implanted using a SDVINI subroutine, which can be used to initialise solution-dependent state variables.

3.6.6 Cohesive element behaviour

Complex expressions for the TSL usually require writing a user element, which is the purpose of the UEL subroutine in the Finite Element commercial code Abaqus. For the PPR model, the UEL is available for educational purposes (Park & Paulino, 2012) for 2D and 3D elements. In the present work, some modifications have been introduced in the 2D code originally developed by Park and Paulino (Park & Paulino, 2012). The original 2D code has nine input parameters: fracture energies ϕ_n, ϕ_t; maximum tractions σ_{max}, τ_{max}; shape parameters α, β; slope parameters λ_n, λ_t; and the 2D thickness. The thickness is not required here as the code has been modified to account for axisymmetric elements. Interface areas associated with each material point have been calculated for the axisymmetric model.

Considering the values of these eight parameters and the proper boundary conditions, Γ_n, Γ_t, m and n are found. In addition, the fracture energies ϕ_n, ϕ_t and maximum tractions σ_{max}, τ_{max} are introduced as a function of hydrogen coverage and/or triaxiality, as it is shown in the next sections. UEL access to the file written in a previous Coupled Temperature-Displacement analysis, in which, for different coordinates (in the notch section) and for various times of simulations, H and θ have been stored.

3.7 Validation of subroutines for diffusion

Diffusion near a crack tip is simulated following the pioneering work of Sofronis and McMeeking (Sofronis & McMeeking, 1989). In order to validate the heat transfer subroutine, the following scenarios are considered:

- Diffusion general equation without plastic strain rate. Results are then compared with those of Sofronis and McMeeking (Sofronis & McMeeking, 1989).
- Diffusion general equation with plastic strain rate. Results are then compared with those of Krom et al. (A. Krom et al., 1999).

3.7.1 Parameters

The simulated material is bcc iron as it is was chosen by Sofronis & McMeeking in its pioneer work and afterwards reproduced by many authors. Therefore, all simulation parameters are obtained from such reference (Sofronis & McMeeking, 1989).

It is worth mentioning that N_L has been obtained assuming the usual density and atomic weight of iron (ρ_{Fe} = 7.87 g/cm^3, A_{Fe} = 55.845 g/mol) and a parameter β = 6 which means that, in a bcc lattice, there are six interstitial sites for each iron atom.

$$N_L = \beta N_{Fe} = \beta \frac{\rho_{Fe} N_A}{A_{Fe}} \tag{3.58}$$

Binding energy of 60 kJ/mol represents an irreversible trap if the limit proposed by (R. A. Oriani, 1970) is taken into account. However, this limit depends on kinetics of diffusion and on temperature in particular.

Table 3-3. Elasto-plastic and diffusion parameters (from reference (Sofronis & McMeeking, 1989)).

E (MPa)	207000
ν	0.3
σ_0 (MPa)	250
n	0.2
D_L (mm^2/s)	0.0127
N_L (sites/mm^3)	5.09×10^{20}
$\overline{V}_H$ (mm^3/mol)	2000
E_b (kJ/mol)	60

Classical J2 plasticity and isotropic hardening is considered. Elasto-plastic material behaviour is modelled by a power law (A. Krom et al., 1999), being the relationship between uniaxial stresses and strains $\sigma - \varepsilon$:

$$\varepsilon = \begin{cases} \dfrac{\sigma}{E} & \varepsilon \leq \dfrac{\sigma_0}{E} \\ \dfrac{\sigma_0}{E}\left(\dfrac{\sigma}{\sigma_0}\right)^{1/n} & \varepsilon > \dfrac{\sigma_0}{E} \end{cases} \tag{3.59}$$

where E is the Young's modulus, σ_0 the yield strength and n the hardening coefficient. Table 3-3 shows the material parameters both mechanical and related to diffusion. The expression $N_T = N_T(\varepsilon^p)$ is fitted from the permeation tests performed by Kumnick and Johnson (A. J. Kumnick & H. H. Johnson, 1980) above mentioned, with N_T in units of number of traps per cubic meter.

Environmental parameters are: a temperature of 300 K and the hydrogen concentration in the boundary highlighted in Figure 3-5,Figure 3-5 Mesh detail in a crack tip with initial radios of $b_0/2$ and hydrogen concentration C_b in the boundary. which is equal to an equilibrium concentration C_{eq} = 2.08×10^{12} H atoms/mm^3 (Sofronis & McMeeking, 1989); this is a very low concentration, as it is expected in an iron-hydrogen system, corresponding in weight parts per million to C_{eq} = 4.424×10^{-4} wppm.

3.7.2 Geometry and boundary conditions

Plane strain conditions in which the plastic zone is confined (yielding small scale) are simulated. Therefore Liner Elastic Fracture Mechanics are applied. With the aim of reproducing the stress state in a crack tip, the finite model is replaced by an "infinite" material and a "semi-infinite" crack; correspondent displacements (in a remote radius) are imposed as boundary conditions. This is the so-called "Modified Boundary Layer approach". Plane strain conditions lead to the following displacements u_x in x direction and u_y in y direction:

$$\begin{cases} u_x(R,\theta) = K_I \dfrac{1+\nu}{E}\sqrt{\dfrac{R}{2\pi}}\cos\left(\dfrac{\theta}{2}\right)\left[2-4\nu+2\sin^2\left(\dfrac{\theta}{2}\right)\right] \\ u_y(R,\theta) = K_I \dfrac{1+\nu}{E}\sqrt{\dfrac{R}{2\pi}}\sin\left(\dfrac{\theta}{2}\right)\left[4-4\nu+2\cos^2\left(\dfrac{\theta}{2}\right)\right] \end{cases} \tag{3.60}$$

where the outer radius is R = 0.15 m and θ is the angle in radians from the crack plane of crack (Figure 3-4Figure 3-4 Boundary layer geometry with symmetry boundary condition and far-field displacements.). Load, and therefore the stress state, increases from 0 to its maximum value K_I = 89.2 $\sqrt{\text{m}}$ during the first 130 seconds of simulation. Thereafter, it remains constant until 1419 hours. Substituting for this load in equation (3.60), maximum displacements applied each 7.5º in ABAQUS simulations are shown in Table 3-4.

Table 3-4. Maximum displacements in the far field contour, correspondent to a load of K_I = 89.2 MPa$\sqrt{\text{m}}$.

$\boldsymbol{\theta}$ (°)	$\boldsymbol{u_x(mm)}$	$\boldsymbol{u_y(mm)}$	$\boldsymbol{\theta}$ (°)	$\boldsymbol{u_x(mm)}$	$\boldsymbol{u_y(mm)}$
0	0.06924422	0	97.5	0.11017486	0.12563035
7.5	0.06983487	0.00457722	105	0.10848229	0.14137688
15	0.0715759	0.00942315	112.5	0.10495987	0.15708354
22.5	0.07437574	0.01479426	120	0.09953857	0.17240586
30	0.07808586	0.02092304	127.5	0.09221322	0.18698991
37.5	0.08250657	0.02800721	135	0.08304358	0.20048493
45	0.08739501	0.0362002	142.5	0.07215301	0.21255591
52.5	0.09247474	0.0456035	150	0.05972471	0.22289566
60	0.09744679	0.05626093	157.5	0.04599569	0.23123597
67.5	0.10200156	0.06815526	165	0.03124869	0.23735733
75	0.10583123	0.08120716	172.5	0.01580233	0.24109697
82.5	0.10864218	0.09527664	180	1.4846E-17	0.24235478
90	0.11016688	0.11016688			

Initial crack tip radius is equal to the half of initial crack opening $b_0/2 = 0.01$ mm (Figure 3-5). As $R \gg b_0/2$, remoteness of applied displacements is ensured. Regarding the mesh, it has been refined in this work respect original references (Di Leo & Anand, 2013; A. Krom et al., 1999; Sofronis & McMeeking, 1989) in order to better capture all phenomena occurring in the crack tip. To do this, geometry is divided in two parts: until 0.05 mm from the crack tip, the side of the elements is a regular dimension (about 0.0025 mm), from there that dimension grows radially by a factor of 1.29 (Figure 3-4). This procedure results in a total of 4073 nodes and 1308 elements CPE8RT type (quadrilateral elements for plane strain, 8 nodes with reduced formulation and used for heat transfer).

Besides imposed displacements, symmetry must be considered as another boundary condition restricting the movement perpendicular to the plane of symmetry (Figure 3-4). A boundary concentration equal to equilibrium hydrogen lattice concentration $C_b = C_{eq}$ is also imposed in the crack face (Figure 3-5 in blue).

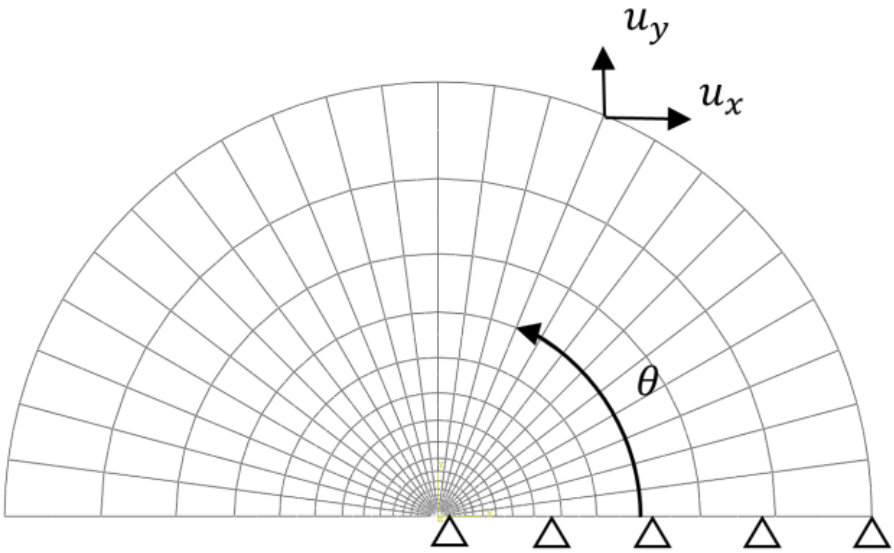

Figure 3-4 Boundary layer geometry with symmetry boundary condition and far-field displacements.

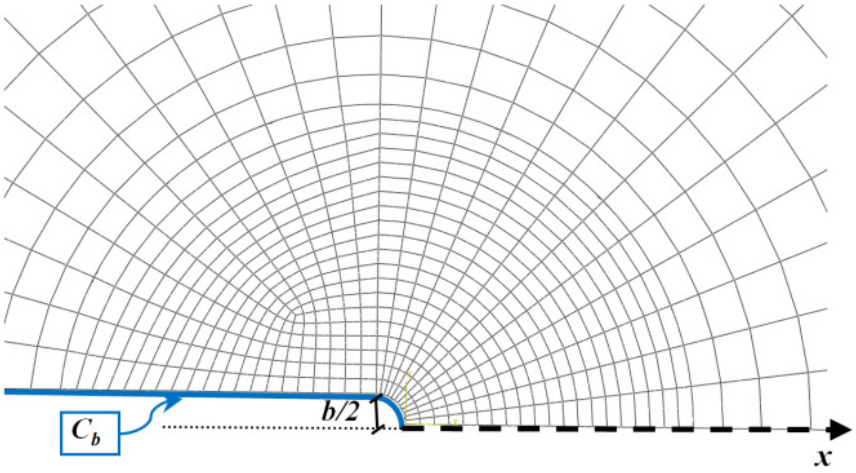

Figure 3-5 Mesh detail in a crack tip with initial radios of $b_0/2$ and hydrogen concentration C_b in the boundary.

3.7.3 Results

Hydrogen lattice distribution follows that of the hydrostatic stress, as expected, reaching the peak concentration at approximately 0.07 mm from the crack tip (Figure 3-6).

Plotting concentration profiles with and without plastic strain rate (last term in Equation (3.18)), along the x axis (normalized by the crack tip tip opening displacement b) in the crack plane, results perfectly fit those of Krom et al. (A. Krom et al., 1999), as seen in Figure 3-7. Small differences in crack tip are due to refining the mesh. Therefore, UMATHT subroutine is regarded as a valid method for simulating hydrogen transport near a crack tip. As Krom et al. (A. Krom et al., 1999) demonstrated, considering plastic strain rate $\partial\varepsilon^p/\partial t$ results in a greater concentration C_L at 130 s while it does not alter distribution at 1419 h.

Once C_L is known, hydrogen concentration in traps C_T is obtained through equation (3.17). At the crack tip ($x = 0$), trapped hydrogen is about 86 times greater than C_{eq} (Figure 3-8) so it has a much greater weight in the total concentration ($C = C_L + C_T \approx C_T$). This is due to the large plastic deformation levels in the crack tip. Contrasting with interstitial hydrogen, hydrogen distribution in traps at 130 s nearly corresponds with that of the steady state at 1419 hours. It has to be noted that the plotted x/b range is greater in Figure 3-7 (0.0 to 5.0) than in Figure 3-8 (0.0 to 1.5) so direct visual comparison can be misleading.

Comparing the results obtained by means of the implemented model, described in sections 3.2 and 3.6.1, with those from the references, it might be concluded that the numerical implementation has been validated

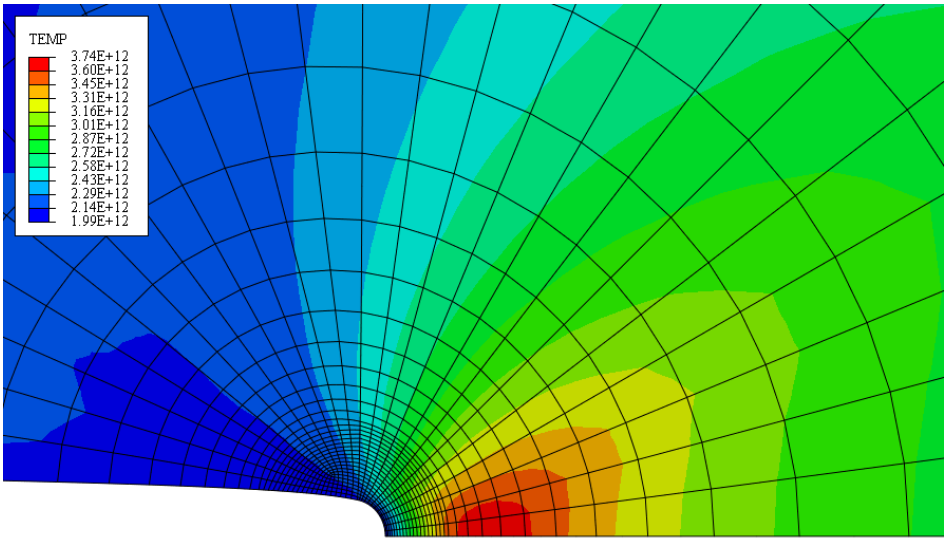

Figure 3-6. Hydrogen lattice concentration at 130 s.

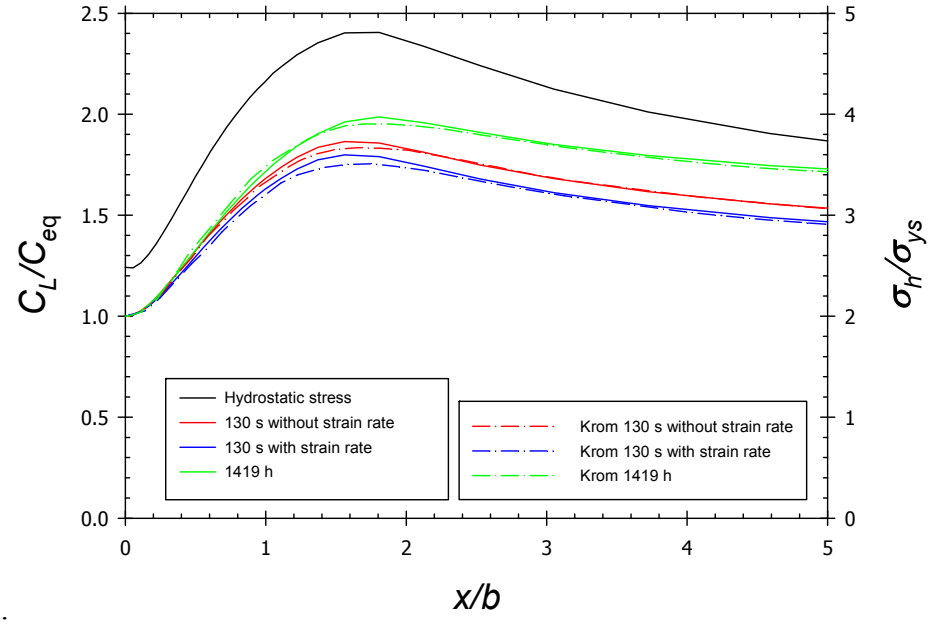

Figure 3-7. Hydrogen lattice concentration with and without plastic strain rate. Comparison with reference (A. Krom et al., 1999)(dashed lines).

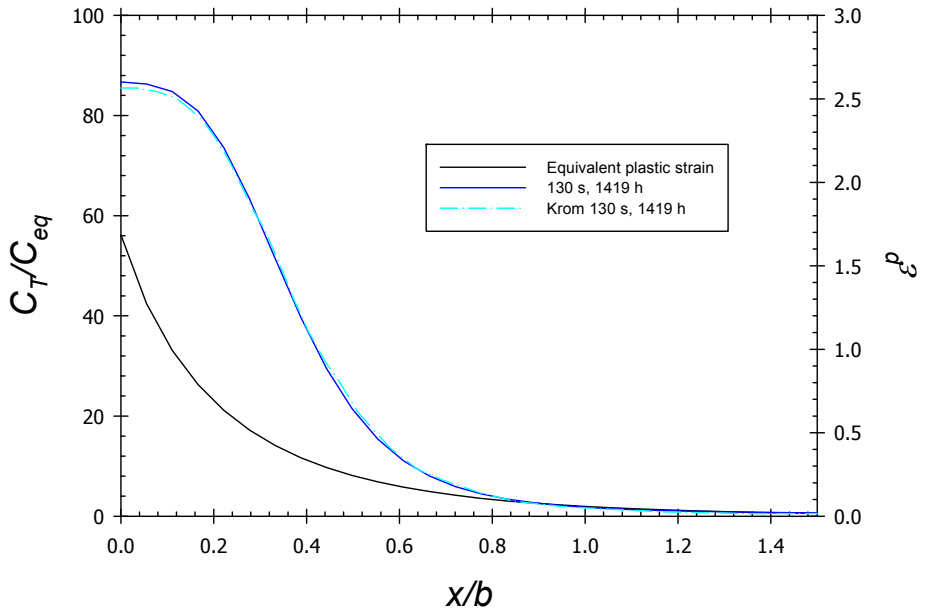

Figure 3-8. Hydrogen concentration in trapping sites. Comparison with reference (A. Krom et al., 1999)(dashed blue lines).

.

Chapter 4 Numerical simulation of hydrogen diffusion near a crack tip

In this Chapter, crack tip diffusion simulations are carried out following the Modified Boundary Layer approach, with the geometry and original parameters from Sofronis & McMeeking, 1989. However, here some modifications and improvements of diffusion models are evaluated: coupled effects, consideration of flux between traps, realistic boundary conditions, kinetic formulation and the inclusion of various types of trapping sites.

4.1 Introduction

Simulations of Hydrogen Assisted Cracking (HAC) in metals and alloys include hydrogen concentration as a crucial variable. With this objective, phenomenological diffusion models that consider chemical potential gradients as the driving force for diffusion are included. Equations are then modified to include the influence of the stress-strain state and trapping.

A crack tip, whose field of stresses and displacements is described by Fracture Mechanics, is modelled while diffusion equations are implemented through subroutines in the commercial program ABAQUS by means of the analogy between diffusion equations and heat transfer, as shown in Chapter 3. Effects of trapping on hydrogen transport are then discussed. Moreover, hydrogen induces a lattice dilatation and a modification of the local plastic flow; this coupled behaviour is also modelled through the heat transfer analogy. Finally, stress-dependent boundary conditions are implemented, representing hydrogen entry in a more realistic way.

In addition to the coupling effects and the realistic boundary conditions, thermodynamic equilibrium is reconsidered and kinetic equations, first proposed by McNabb and Foster, are

implemented. The influence of non-equilibrium consideration on crack tip diffusion is analysed in 4.6 and in 4.7.2. Sub-section 4.7 is meant to evaluate the two-level model extension including more than one kind of trap.

Modelling the interaction between hydrogen and the material in a crack tip is essential, because hydrogen drastically affects fracture behaviour. So damage models, both continuous damage models and cohesive models, must incorporate a new variable: hydrogen concentration. This work aims to contribute to this first step in the hydrogen embrittlement modelling, i.e. to predict accurate hydrogen distributions near a crack tip.

With this objective, diffusion equations are derived from Fick's laws which describe the hydrogen flux due to a concentration gradient. Trapping is considered within this model in an explicit form in such a way that diffusion variables (concentration, occupancy, chemical potential and flux) are distinguished depending on whether hydrogen is in a lattice or a trapping site. These equations are also modified by the stress-strain field.

In order to properly include hydrogen trapping, there is currently no commercial Finite Element software in which these equations are implemented by default. It has been necessary, therefore, to develop a subroutine based on the analogy between diffusion and heat transfer, as exposed in Section 3.6. This procedure has been verified by simulating hydrogen diffusion near a crack tip with a Modified Boundary Layer (MBL) approach, using the same geometry and parameters as those first proposed by Sofronis and McMeeking (Sofronis & McMeeking, 1989) for hydrogen in iron. This simulation has been repeatedly revisited in literature for the sake of comparison, and some improvements have been made: the inclusion of a plastic strain rate (A. Krom et al., 1999), the consideration of coupled diffusion (Lufrano et al., 1998; Sofronis et al., 2001), stress-state dependent boundary conditions (Di Leo & Anand, 2013), kinetic exchange between trapping and lattice sites in non-equilibrium situations (McNabb & Foster, 1963), and the consideration of more than a single kind of trap (M. Dadfarnia, Sofronis, & Neeraj, 2011). All of these improvements are discussed in the present Chapter and are implemented in Finite Element simulations following the analogy between diffusion and heat transfer. Emphasis is also put on the range of validity of the simplification usually assumed in diffusion models.

4.2 Materials and geometry

The same material and load parameters than in Section 3.7.1 and 3.7.2 have been chosen for the sake of comparison with the previously mentioned works. Modified Boundary Layer geometry is also the same.

4.3 Simulation of coupled effects

Geometry, diffusion parameters and loads are the same that those of the previous Chapter. Only coupling Equations (3.27) and (3.29) modify the transport model in this Subsection. With the meaning above mentioned, volume change for each introduced atom Δv is related to the partial molar volume: $\Delta v = \bar{V}_H / N_A$, being N_A Avogadro's number. The mean volume of an iron atom Ω is the inverse of the iron atom concentration N_{Fe}. Hydrogen concentrations, c and c_0, are expressed in total H atoms per metal atom; consequently, they must be expressed in terms of lattice and trap concentration in order to couple the transport equations:

$$c = \frac{C_L + C_T}{N_{Fe}} \tag{4.1}$$

Additionally, initial concentration in the unstressed state is taken as the equilibrium concentration per metal atom: $c_0 = C_{eq}/N_{Fe}$.

Local softening parameter ξ is difficult to interpret because it does not have physical meaning. From Kotake et al. (Kotake et al., 2008), $1 + \xi$ factor can be seen as how much the yield stress increases (or decreases if $\xi < 0$) when the normalised concentration has reached its maximum, i.e. $c = 1$. However, this maximum concentration is difficult to reproduce experimentally so in this work the equilibrium concentration is the reference value. For example, it is supposed that at C_{eq} yield stress has been reduced by 5%. Then:

$$\xi c_0 + 1 = 0.95 \tag{4.2}$$

Thus with $c_0 = 2.447\times10^{-8}$ atH/atFe, coupling parameter is $\xi = -2.04\times10^{6}$

Table 4-1. Coupling parameters.

Δv (atH mm^3)	3.3211×10^{-21}
Ω (mm^3/atFe)	1.1764×10^{-20}
λ	0.2826
c_0 (atH/atFe)	2.4469×10^{-8}
ξ	-2.04×10^{6}; 0; $+2.04\times10^{6}$

Three scenarios are simulated:

- Hydrogen does not affect plastic flow, thus $\xi = 0$ and only dilatation is considered.
- At equilibrium concentration, C_{eq} = 2.08×10^{12} atH/mm^3, yield stress is reduced by 5%, corresponding to $\xi = -2.04\times10^{6}$ which indicates local softening.
- At equilibrium concentration, C_{eq} = 2.08×10^{12} atH/mm^3, yield stress is increased by 5%, corresponding to $\xi = +2.04\times10^{6}$ which indicates local hardening.

4.3.1 Dilatation

Following the MBL approach, the work of Taha and Sofronis (Taha & Sofronis, 2001), usually cited in hydrogen diffusion modelling papers, is taken for the sake of comparison.

However, only dilatation is considered by these authors, i.e. $\xi = 0$. Therefore, simulation with $\xi = 0$ and $\lambda = 0.2816$ has been performed and hydrogen concentration in lattice sites is plotted (solid line with red crosses in Figure 4-1) and compared with (Taha & Sofronis, 2001) (green solid line in Figure 4-1). The obtained small deviation between the present study and the reference is attributed to numerical implementation and meshing differences.

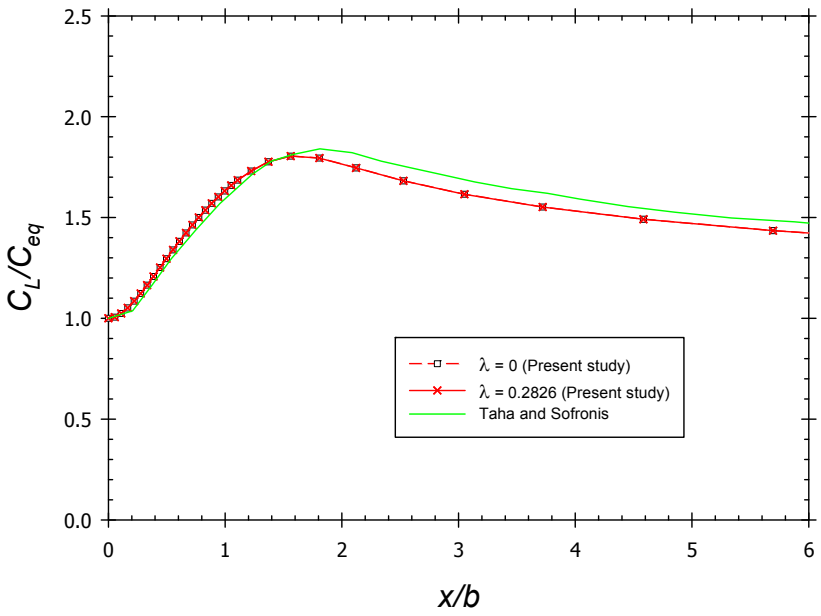

Figure 4-1 Hydrogen lattice concentration at 130 s with and without dilatation parameter λ. Comparison with reference (Taha & Sofronis, 2001)(green solid line).

Results also show that dilatation does not modify hydrogen concentration distribution as results considering $\lambda = 0.2816$ coincide with $\lambda = 0$, i.e. hydrogen induced dilatation strain does not affect hydrogen transport. This was expected because hydrogen has a low solubility in iron so parameters λ and c_0 are too low. In the case of high solubility systems (e.g. Niobium), as demonstrated by some authors (Lufrano et al., 1998), dilatation significantly alter hydrogen transport.

Keeping $\lambda = 0.2816$, higher equilibrium concentrations C_{eq} have been simulated, leading to higher c_0 parameters; there are not changes in C_L distributions in any case (solid line with red crosses in Figure 4-1 is always found). This means that even under extreme conditions (very high H_2 fugacity in gaseous charging (Marchi et al., 2007) or high overpotential in electrochemical charging (Liu et al., 2014)) hydrogen dilatation may be neglected in transport simulations.

However, it has been taken into account that for high equilibrium concentrations, lattice occupancy approximates to one: $\theta_L \approx 1$, i.e. $C_{eq} = N_L$, so simplifications made in Section 3.2.3., i.e. $\theta_L \ll 1$, are not consistent and results might not be accurate; in any case, these

extreme high values of lattice occupancy are nearly impossible to find experimentally in steel due to its low solubility, so it is presumed that dilatation can be always neglected.

4.3.2 Hardening/Softening

Considering plastic flow modified by hydrogen concentration, lattice hydrogen concentrations are plotted (Figure 4-2). Enhanced softening ($\xi = -2.04\times10^6$) results in a minor hydrostatic stress distribution and thus a smaller hydrogen lattice concentration.

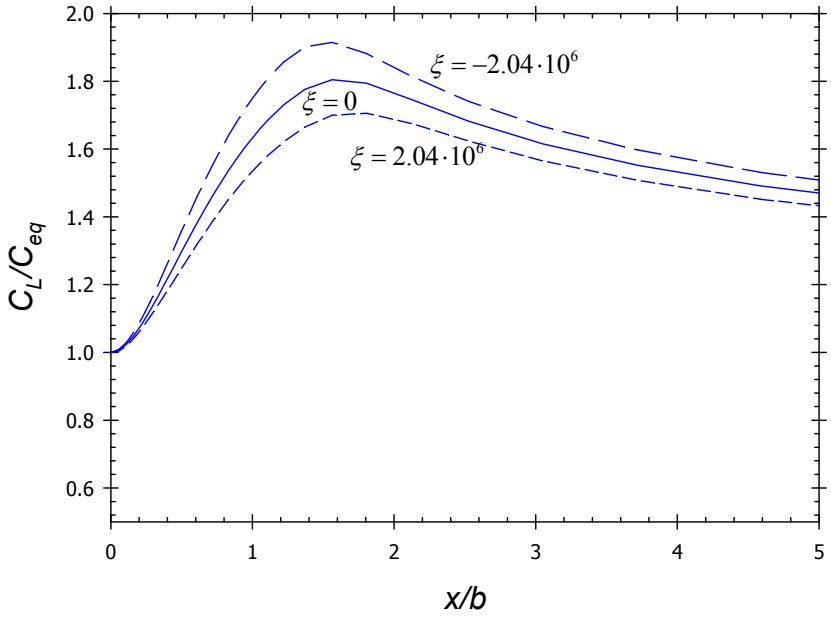

Figure 4-2 Hydrogen lattice concentration with softening ($\xi = -2.04\times10^6$) and hardening ($\xi=2.04\times10^6$) effects.

Results are qualitatively discussed because they lack empirical base. Hardening or softening parameter ξ should be experimentally fitted. Atomistic simulations of dislocation interactions with hydrogen could also lead to a better understanding of this microscale phenomenon.

4.4 Flux between trapping sites

One of the simplifications assumed was that $\mathbf{J}_T = 0$. In a crack tip, it is arguably whether traps are isolated amongst each other or not, so simulation with all of the parameters shown in 3.7 is performed again, but this time considering flux between traps different from zero, according to Equation (3.9). It is important to note that in the gradient of the number of trapping sites, a plastic strain gradient appears. For example, if the Kumnick and Johnson expression is considered:

$$\nabla N_T = 29.51\, N_T \nabla \varepsilon^p \exp(-5.5\varepsilon^p) \tag{4.3}$$

In the present work, classical theory of plasticity is assumed, however, considering plastic strain gradients could lead to implementing the gradient-enhanced local hardening predicted by Strain Gradient Plasticity (SGP) (Fleck & Hutchinson, 1993; Hutchinson, 2000). Moreover, the role played by Geometrically Necessary Dislocations (GND) associated with these gradient theories in hydrogen trapping is still not well understood. Taking into account SGP in hydrogen diffusion near a crack tip (Martínez-Pañeda et al., 2016) could represent a breakthrough for Hydrogen Assisted Cracking modelling (Turnbull, 2015).

To account for $\mathbf{J}_T$, diffusivity between trapping sites must be included. Diffusion coefficient between two different sites, *i* and *j,* has the following expression:

$$D_{ij} = \omega_{0i} l_{ij}^2 \exp\left(-\frac{\Delta E_{ij}}{RT}\right) \tag{4.4}$$

Assuming the same pre-exponential factor, i.e. the same frequency of vibration and the same hopping length, an energetic relation might be established: $\Delta E_{TT} - \Delta E_{LL} = E_b$ (Figure 4-3). Saddle points in the potential energy distribution are supposed constant.

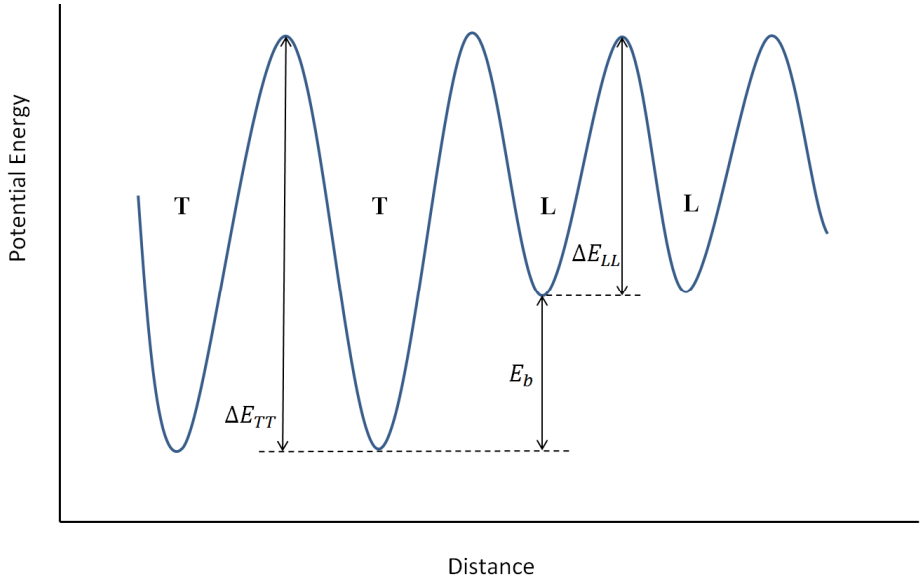

Figure 4-3. Potential energy trace and energetic relationships between trapping sites (T) and lattice sites (L).

From Equations (3.7) and (3.8), and considering $\mu_L = \mu_T$,, the binding energy E_b defines the equilibrium constant $K_T = \exp(E_b/RT)$. Diffusivities might be related as follows:

$$D_{TT} = \frac{D_{LL}}{K_T} \tag{4.5}$$

And the subscripts are simplified as: $D_{TT} = D_T$ and $D_{LL} = D_L$. With the binding energy E_b = 60 kJ/mol and D_L = 0.0127 mm^2/s chosen from reference (Sofronis & McMeeking, 1989), D_T = 4.53×10^{-13} mm^2/s. Results in Figure 4-4 compare simulation without considering $\mathbf{J}_T$ (at 130 s from Figure 3-7 and Figure 3-8) with indicate that flux between trapping sites can be neglected so the simplification made before is valid. However, this validity has to be connected to specific parameters, in this case with a high binding energy and its consequent very low D_T.

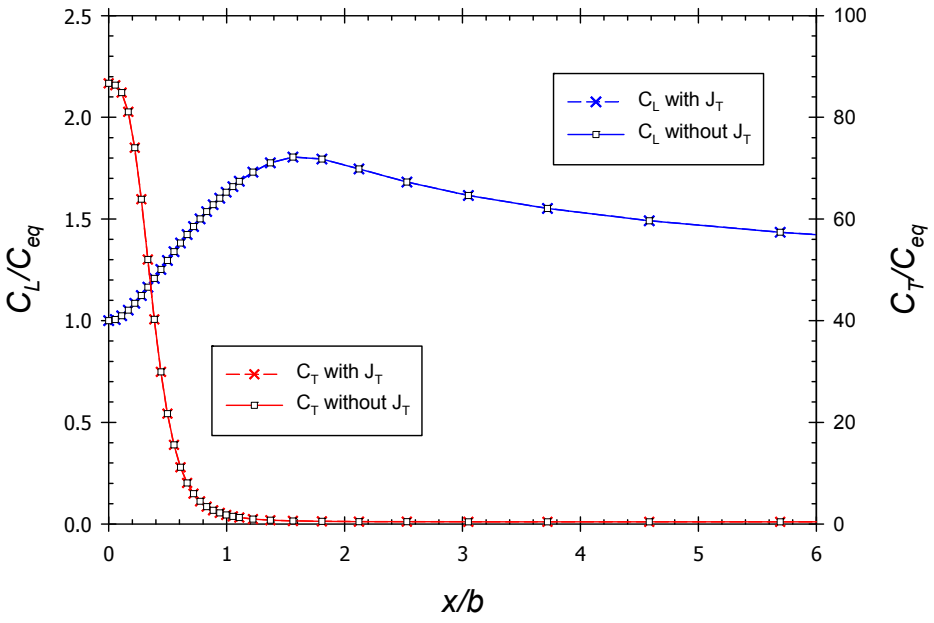

Figure 4-4. Hydrogen concentration at 130 s in trapping sites (C_T) and lattice sites (C_L) with and without considering flux between traps $\mathbf{J}_T$ with binding energy E_b = 60 kJ/mol.

If the simulation is repeated only decreasing the absolute value of the binding energy from 60 kJ/mol to 10 kJ/mol, the diffusivity D_T increases exponentially ($D_T = 2.3\times10^{-4}$ mm^2/s) , but as Oriani's equilibrium has been supposed, hydrogen concentration in trapping sites is nearly zero C_T (Figure 4-5). Therefore, results of concentration change respect Section 4.2 but flux between traps might be neglected again.

It must be concluded that, even though binding energy is an influential parameter, remoteness of trapping sites between them is the crucial factor when considering flux $\mathbf{J}_T$ (Toribio & Kharin, 2015). In order to assume that traps are not connected, the ratio between N_T and N_L must be considered. If the number of traps is high compared with the number of interstices, the crystal has many defects and $\mathbf{J}_T$ cannot be neglected; this approach could explain the accelerated diffusion or "pipe diffusion" found in grain boundaries (Oudriss, Creus, Bouhattate, Conforto, et al., 2012) or dislocation cores (X. Zhang et al., 2010).

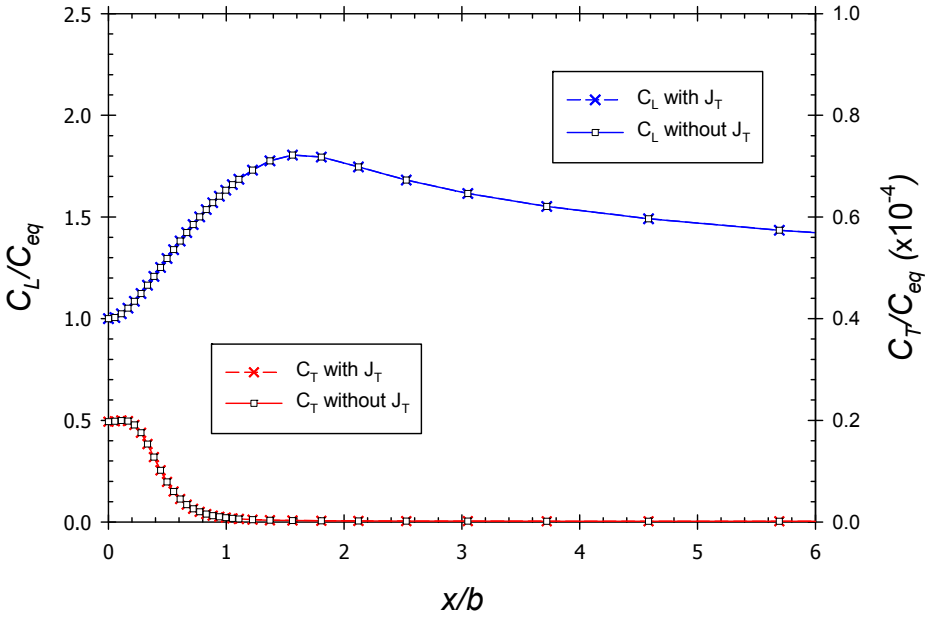

Figure 4-5. Hydrogen concentration at 130 s in trapping sites (C_T) and lattice sites (C_L) with and without considering flux between traps $\mathbf{J}_T$ with binding energy E_b = 10 kJ/mol.

Toribio and Kharin (Toribio & Kharin, 2015) discuss the generalised model and the particular simplifications from discrete random walking principles. Therefore, fluxes include explicitly the jump success probability from two different places. However, comparison with phenomenological models based on Onsager's approach presents several difficulties. For instance, parameters L_{ij} can be related to diffusivites D_{ij}, as made in equations (3.5) and (3.6), from atomistic arguments in solid solutions (Choudhury et al., 2011). More effort to bridge both approaches must be made.

4.5 Boundary conditions

Previously only simulations with a constant hydrogen concentration C_{eq} in the crack tip have been shown. Referenced works (Di Leo & Anand, 2013; A. Krom et al., 1999; Sofronis & McMeeking, 1989; Taha & Sofronis, 2001) also include an insulated situation, equivalent to a zero flux perpendicular to the boundary (*zero flux boundary condition*). Here, a stress-dependent boundary concentration is implemented following this expression:

$$C_{L,b} = C_{eq} \exp\left(\frac{\bar{V}_H \sigma_h}{RT}\right) \tag{4.6}$$

Di Leo and Anand (Di Leo & Anand, 2013) realised that analytic solution of diffusion in steady state, i.e. when fluxes definitely become zero, follows this expression but simulations made by several authors (e.g. Sofronis and McMeeking (Sofronis & McMeeking, 1989), Krom et al. (A. Krom et al., 1999), etc.) did not. The reason is because stress state must be included in the boundary condition. Di Leo and Anand consider hydrogen chemical potential as the finite element unknown variable, instead of hydrogen lattice concentration, so equation (4.6) is their boundary condition.

Hydrogen diffusion near a crack tip is simulated again without coupling effects and with the parameters of Table 3-3 but now with the stress-dependant boundary concentration.

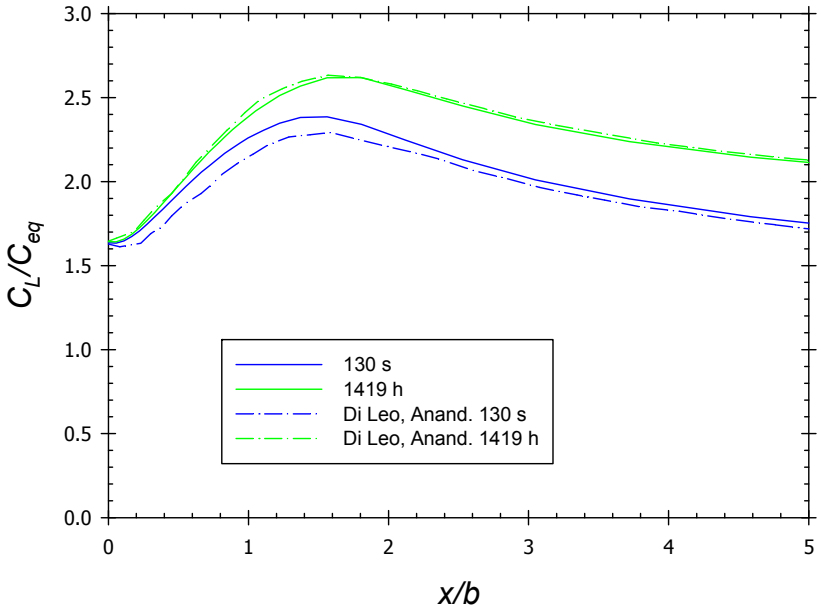

Figure 4-6. Hydrogen concentration in lattice sites with stress-dependent boundary condition. Comparison with reference (Di Leo & Anand, 2013).

Results (Figure 4-6) agree perfectly for 1419 hours and with a slight deviation for 130 seconds with those obtained by Di Leo and Anand. The most remarkably conclusion is that there is a considerable increase in hydrogen lattice concentration compared to simulations

that do not consider stress state in the boundary conditions. Moreover, hydrogen distribution at 1419 hours perfectly matches with analytical solution of the steady state.

4.6 Kinetic reconsideration of trapping

Kanayama et al., 2009, found that considering kinetic effects, i.e. the adoption of McNabb and Foster equations, is only necessary for very short diffusion times. Then, a shorter total time of 1.3 s is simulated onwards. This means that the maximum load, $K_I = 89.2$ MPa$\sqrt{\text{m}}$ is reached after 1.3 s. The parameters that are kept constant are:

- $\omega_{0L} = \omega_{0T} = 10^{12}$ s^{-1}
- E_a = 6.88 kJ/mol (activation energy for $L \rightarrow T$ is assumed equal to diffusion activated energy from Sofronis & McMeeking, 1989).

First of all, the influence of binding energy is evaluated. Figure 4-7 and Figure 4-8 show hydrogen distribution in the crack direction for a binding energy of defects equal to 60 kJ/mol. In Figure 4-7, a small difference might be seen after 0.13 seconds when McNabb and Foster (non-equilibrium) equations are considered. However, for the hydrogen concentration in trapping sites, plotted in Figure 4-8, no influence is noted. The decrease in C_L occurring at the end of the load, 1.3 seconds, is due to the plastic strain rate term: lattice sites are depleted because of the high strain rate and the high binding energy considered for dislocations.

Nevertheless, when the same simulation is repeated changing only E_b from 60 to 20 kJ/mol, lattice sites depletion is not observed in Figure 4-9 whereas a very great difference between equilibrium and non-equilibrium models (Figure 4-10) is found. This implies the non-validity of Oriani's expression for weak traps since capture and release occur so fast that there is no enough time to reach equilibrium.

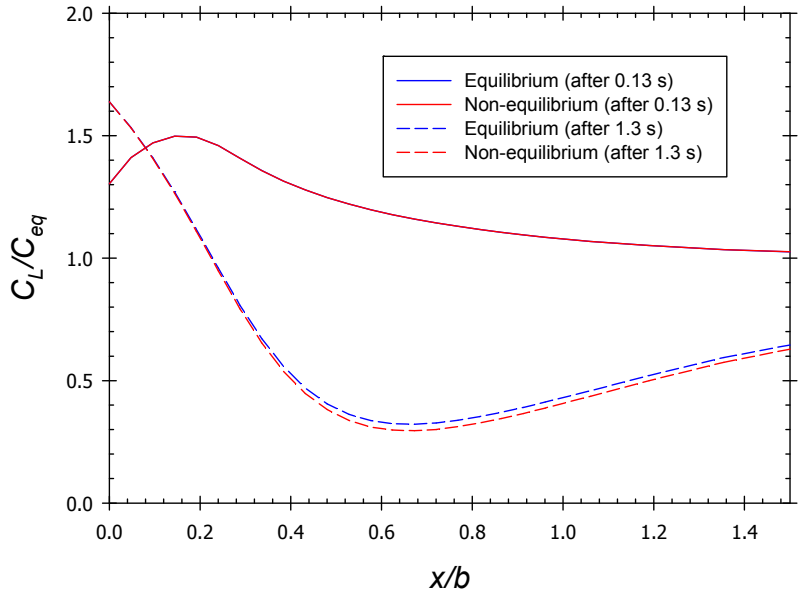

Figure 4-7. Hydrogen concentration in lattice sites after 0.13 and 1.3 seconds for E_b = 60 kJ/mol. Comparison between equilibrium and kinetic formulations.

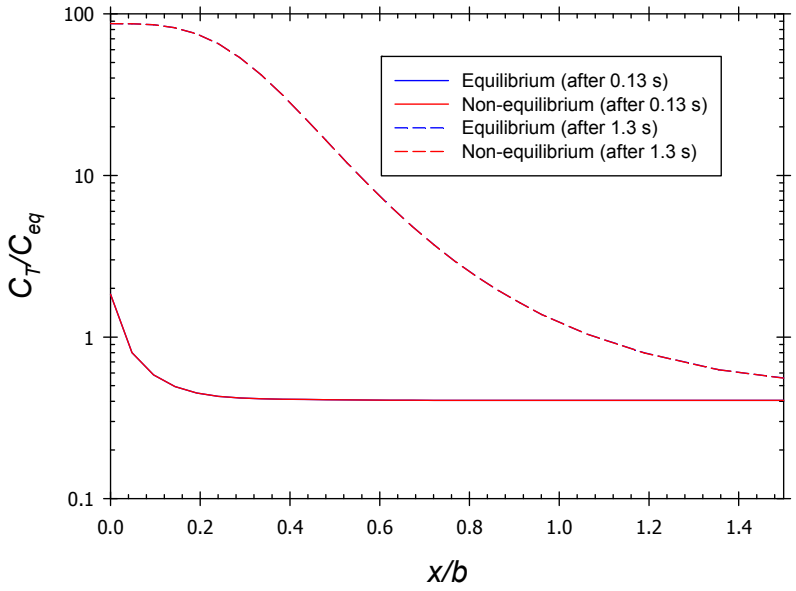

Figure 4-8. Hydrogen concentration in trapping sites after 0.13 and 1.3 seconds for E_b = 60 kJ/mol. Comparison between equilibrium and kinetic formulations.

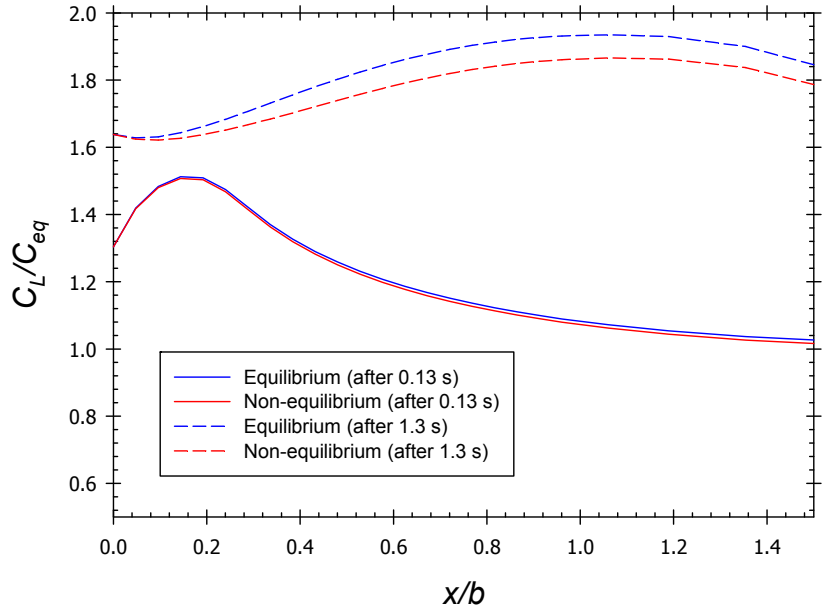

Figure 4-9. Hydrogen concentration in lattice sites after 0.13 and 1.3 seconds for E_b = 20 kJ/mol. Comparison between equilibrium and kinetic formulations.

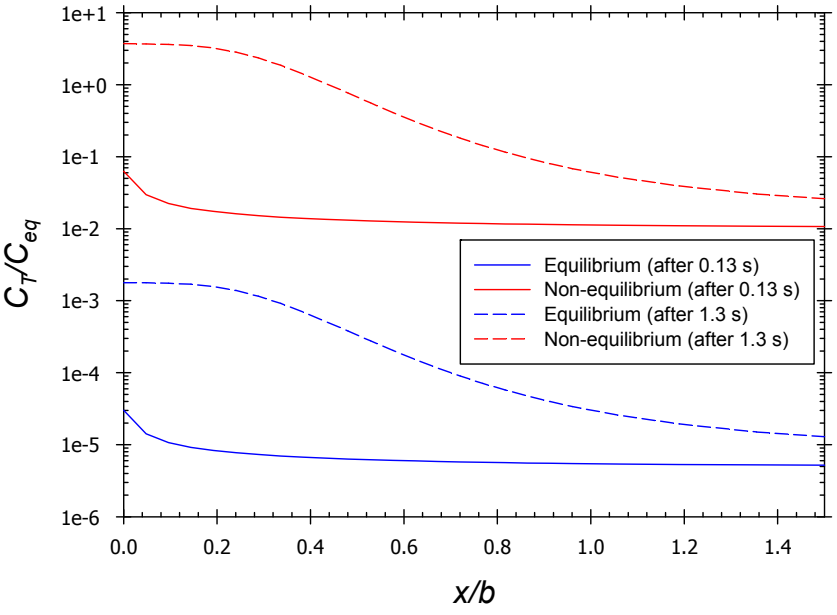

Figure 4-10. Hydrogen concentration in trapping sites after 0.13 and 1.3 seconds for E_b = 20 kJ/mol. Comparison between equilibrium and kinetic formulations.

As it was expected, a lower binding energy of defects leads to a lower concentration in trapping sites. Figure 4-11 shows the binding energy influence in C_L: for E_b = 60 kJ/mol, lattice sites are depleted after 1.3 s due to the rapid creation of traps, while for E_b = 20 kJ/mol, the peak in C_L corresponding to the hydrostatic maximum is present.

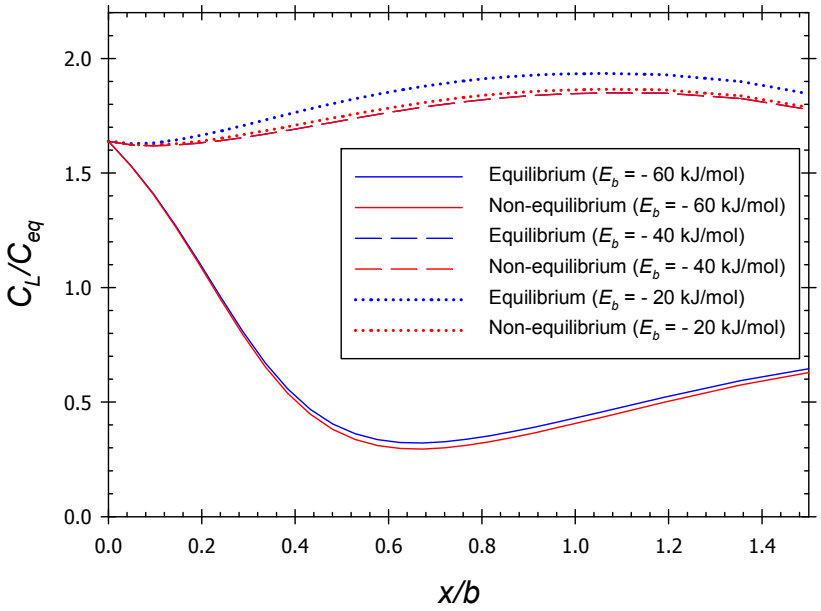

Figure 4-11. Binding energy influence on hydrogen concentration in lattice sites after 1.3 seconds.

These results should change for different conditions. When the kinetic model initiates from equilibrium, a deviation from this equilibrium hardly occurs. For this deviation, a sudden change (e.g. a temperature ramp in TDS tests) should be introduced. However, when simulations are repeated starting with a trapping occupation equal to zero (even though there is a uniform $C_{L,0}$), hydrogen capture in trapping sites has a greater effect. In addition, since the initial θ_T equals zero, the plastic strain rate effect is zero until the traps are filled in the "non-equilibrium" model.

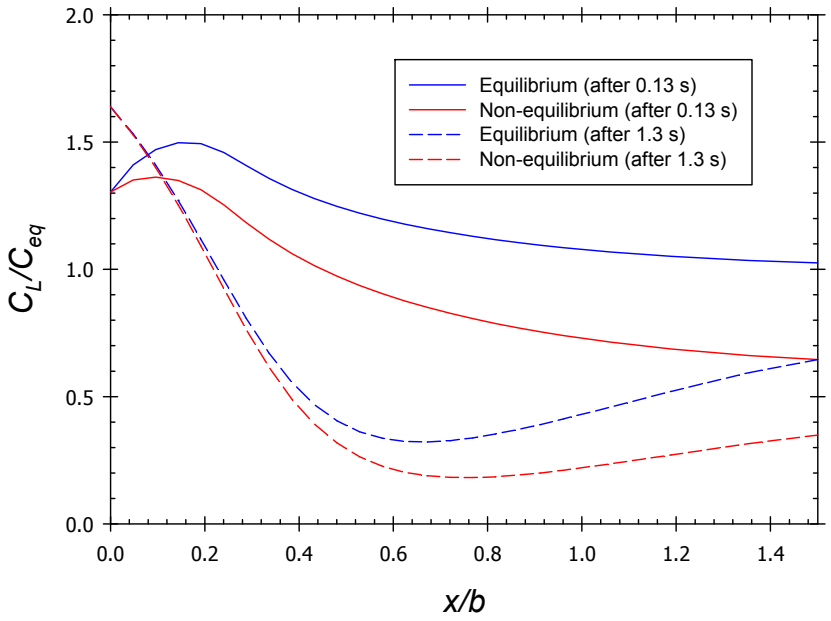

Figure 4-12. Hydrogen concentration in lattice sites after 0.13 and 1.3 seconds for E_b = 60 kJ/mol. Comparison between equilibrium and kinetic formulations for initially empty traps ($\theta_{T,0} = 0$).

Turnbull et al., 1997, state that the value of the constants ω_{0L} and ω_{0T} (in the original paper k_0 and p_0) has little influence on results for hydrogen diffusion simulations, only the ratio k_0/p_0 must be constant. That fact would mean that the vibration frequencies are not critical in hydrogen diffusion and trapping. However, Legrand et al., 2015 have simulated TDS profiles considering different vibration frequencies for hydrogen depending whether it is located in a trapping site or in a lattice site.

In Figure 4-13 and Figure 4-14, different values for frequencies are simulated for a single kind of trapping defect with E_b = 40 kJ/mol. The following conclusions might be drawn for lattice hydrogen distribution:

- after 0.13 seconds, C_L distribution is independent of ω_{0L} and ω_{0T} values.
- after 1.3 seconds,
  - C_L shows a peak, correspondent to the hydrostatic stress peak, when $\omega_{0L} = \omega_{0T}$. This peak is slightly higher for $\omega_{0L} = \omega_{0T} = 10^6$ s^{-1} than for $\omega_{0L} = \omega_{0T} = 10^{12}$ s^{-1}

- C_L decreases for a high ratio ω_{0L}/ω_{0T}.

And, evaluating trapped hydrogen distribution at 0.13 and 1.3 seconds:

- C_T is higher for $\omega_{0L} > \omega_{0T}$ than for $\omega_{0L} = \omega_{0T}$.
  - No differences are observed between $\omega_{0L} = 10^{12}$ s^{-1}, $\omega_{0T} = 10^{6}$ s^{-1} and $\omega_{0L} = 10^{12}$ s^{-1}, $\omega_{0T} = 10^{9}$ s^{-1}
- In contrast with C_L distribution, C_T is slightly higher for $\omega_{0L} = \omega_{0T} = 10^{6}$ s^{-1} than for $\omega_{0L} = \omega_{0T} = 10^{12}$ s^{-1}.

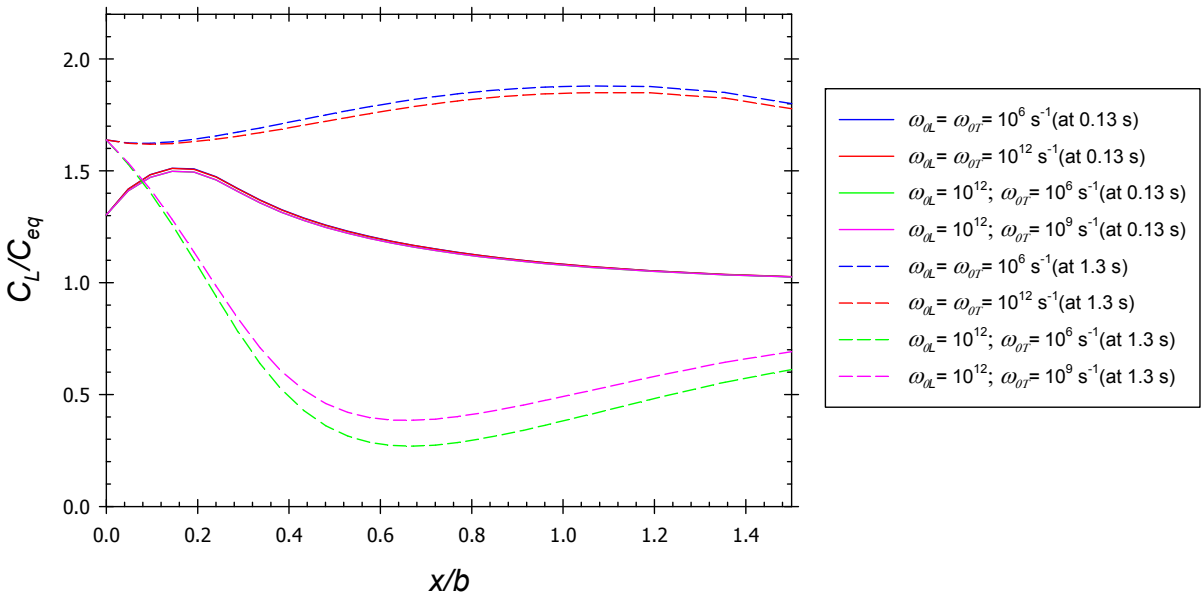

Figure 4-13. Influence of vibration frequencies on hydrogen concentration in lattice sites after 0.13 and 1.3 seconds for E_b = 40 kJ/mol.

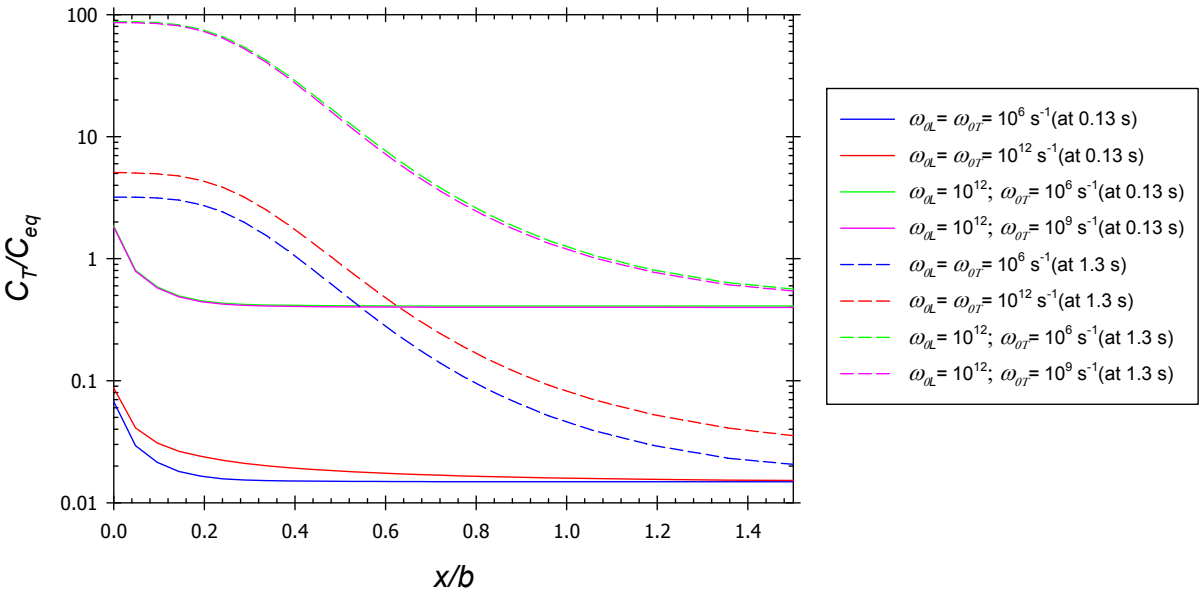

Figure 4-14 Influence of vibration frequencies on hydrogen concentration in trapping sites after 0.13 and 1.3 seconds for E_b = 40 kJ/mol.

4.7 Multi-trapping effects

4.7.1 Equilibrium

When various kinds of traps are to be included in the numerical model, a density for each one must be given: N_T^i. Here, the approach followed by Dadfarnia et al., 2011 is used, and the number of traps associated to dislocations N_T^d is related to the equivalent plastic strain by means of the expression presented in Section 2.5.

If only one type of trap is included in the governing equations, as made in previous sections, and the density is related to plastic strain, it is assumed that defects correspond to dislocations. Here, trapping sites in grain boundaries are assumed to be uniform and constant over time, and related to the number of lattice sites, as in Dadfarnia et al., $N_T^{gb} = 10^{-6} N_L$. Binding energies are assumed to be E_b^d = 30 kJ/mol and E_b^{gb} = 60 kJ/mol, because, in literature, grain boundaries are usually classified as irreversible traps for hydrogen.

Results in Figure 4-15 show how the inclusion of a second type of trap, grain boundaries in this case, affects hydrogen distribution. At the beginning of diffusion, i.e. at 0.13 seconds, the multi-trap model predicts a lower concentration in lattice sites because grain boundaries have a high binding energy and hydrogen is strongly trapped. However, after 1.3 seconds, trap density N_T in the single-trap model has increased due to its dependence on plastic straining and the binding energy considered is equal to 60 kJ/mol. Thus, interstitial sites are depleted, giving a lower concentration C_L.

Strong trapping in grain boundaries is demonstrated in results plotted in Figure 4-16, in which the multi-trap model predicts that dislocations are almost empty and high hydrogen concentrations in grain boundaries, approximately $C_T \approx 250\, C_{eq}$, due to the high binding energy of this kind of defects and the high number of traps, $N_T^{gb} = 10^{-6} N_L = 5.09\times10^{14}$ traps/mm^3. Note that y-axis in Figure 4-16 is in logarithmic scale.

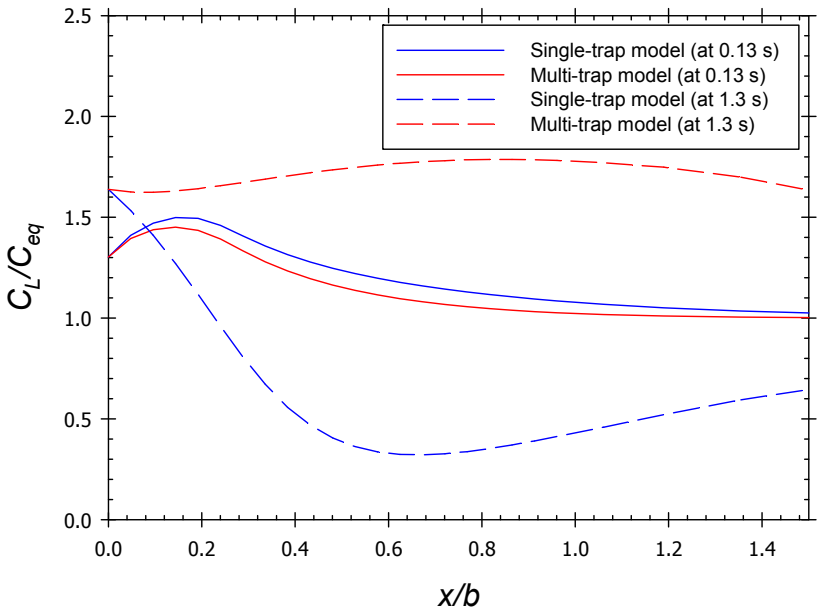

Figure 4-15. Hydrogen concentration in lattice sites after 0.13 and 1.3 seconds. Comparison between the single-trap model (with E_b = 60 kJ/mol) and multi-trap model (with E_b^d = 30 kJ/mol and E_b^{gb} = 60 kJ/mol).

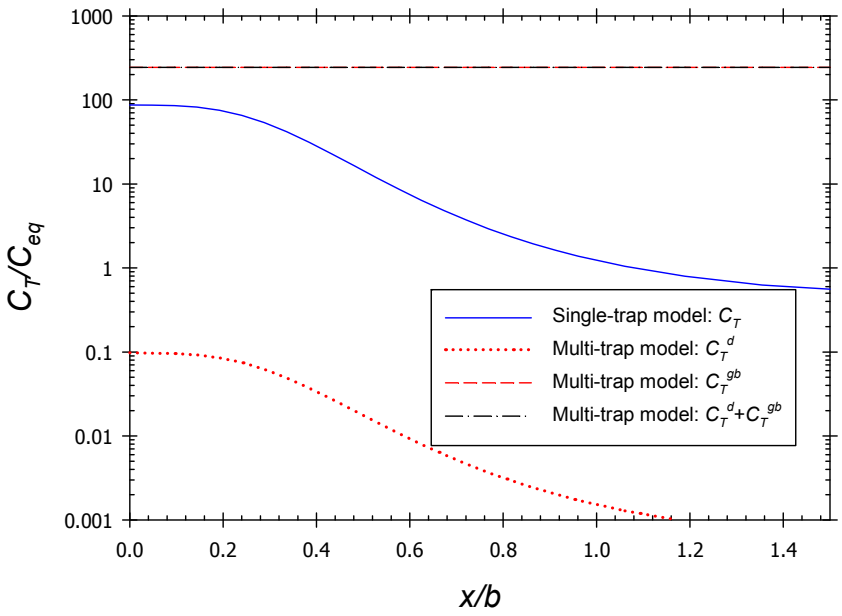

Figure 4-16. Hydrogen concentration in trapping sites after 1.3 seconds. Comparison between the single-trap model with E_b = 60 kJ/mol) and multi-trap model (with E_b^d = 30 kJ/mol and E_b^{gb} = 60 kJ/mol).

Until now all simulations performed with the single-trap model have considered Kumnick and Johnson expression in order to implement the $N_T - \varepsilon^p$ dependence. However, as shown in Figure 2-5, considering the dislocation density approach, the parameters mentioned in (2.53), a number of traps N_T of about 10^{25} traps/m^3 (i.e. 10^{16} traps/mm^3) is predicted, almost three orders higher than the expression (2.56). This fact is confirmed, for E_b = 60 kJ/mol, in Figure 4-17 where the interstitial hydrogen concentration is lower for Sofronis et al. expression because the greater presence of defects. In Figure 4-18, it is shown, as expected, how the very high dislocation density considered (red lines) promotes very high concentrations in trapping sites.

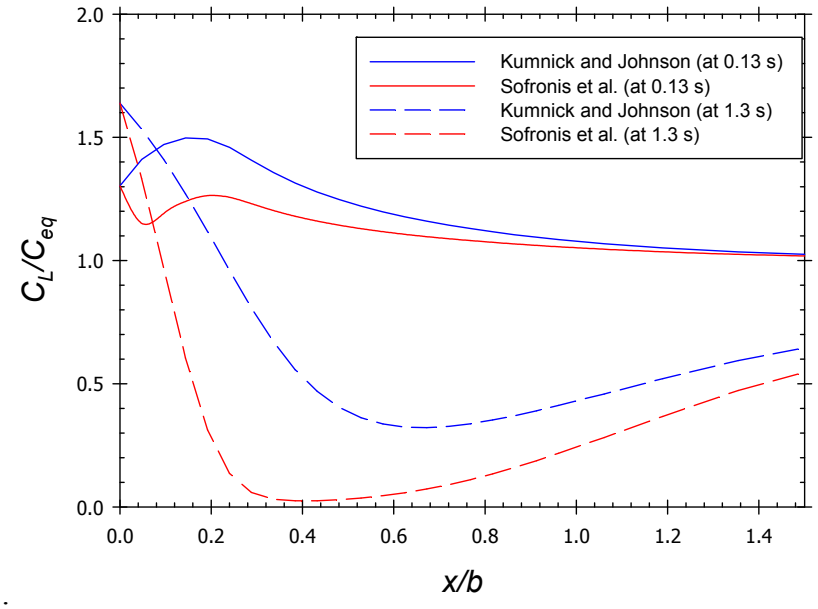

Figure 4-17. Influence of $N_T - \varepsilon^p$ expression on hydrogen concentration in lattice sites for the single-trap model (with E_b = 60 kJ/mol).

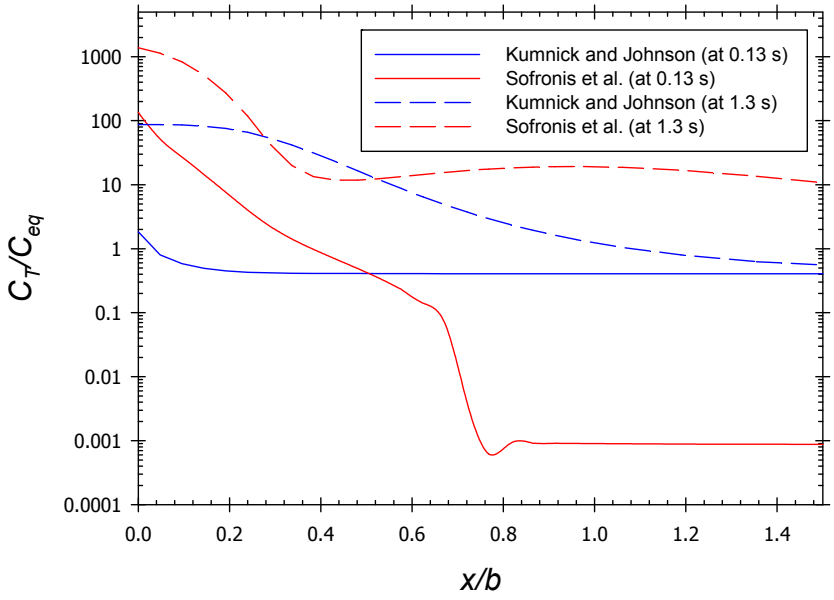

Figure 4-18. Influence of $N_T - \varepsilon^p$ expression on hydrogen concentration in trapping sites for the single-trap model (with E_b = 60 kJ/mol).

Nevertheless, when the $N_T - \varepsilon^p$ influence is reassessed, this time for the multi-trap model and assuming, as in Dadfarnia et al., 2011, E_b^d = 30 kJ/mol and E_b^{gb} = 60 kJ/mol, a small difference is found in C_L (Figure 4-19) between Kumnick & Johnosn and Sofronis et al. expressions.

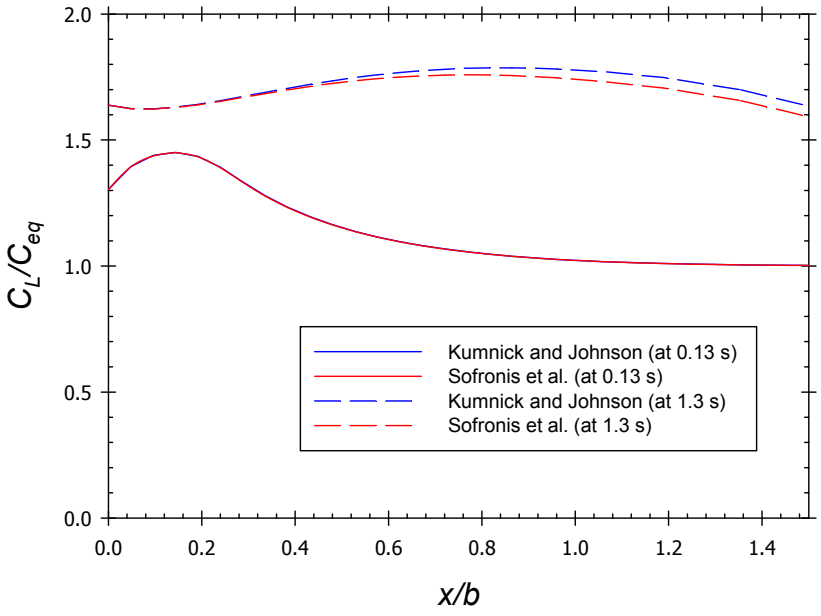

Figure 4-19. Influence of $N_T - \varepsilon^p$ expression on hydrogen concentration in lattice sites for the multi-trap model (with E_b^d = 30 kJ/mol and E_b^{gb} = 60 kJ/mol)..

As it has been shown in Table 2-1, there is a great scatter between binding energies empirically obtained for different crystal defects. That is why is so important to perform a parametric study of the binding energy influence on results. Assuming N_T^d from Equation (2.53) and a constant grain boundary trap density, $N_T^{gb} = 10^{-6} N_L$, Figure 4-20 and Figure 4-21 plot hydrogen distributions for different combinations of binding energies.

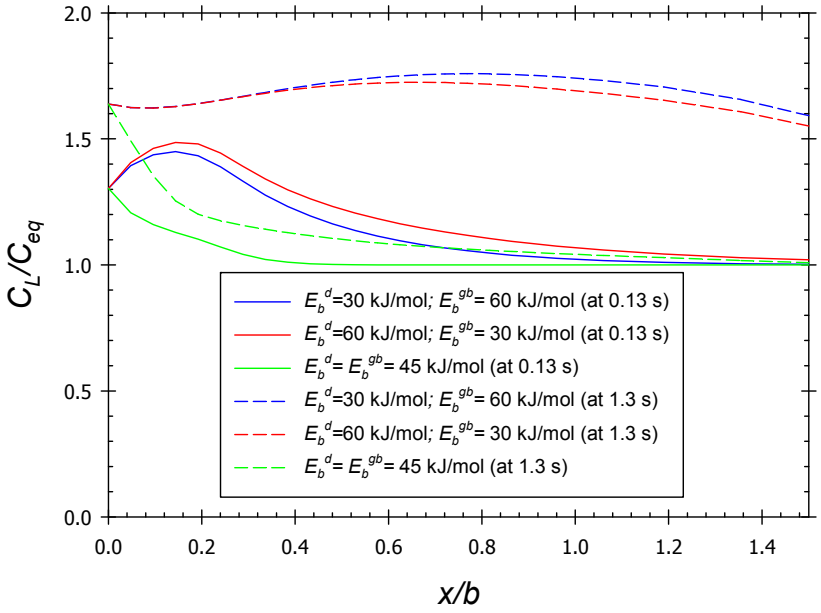

Figure 4-20. Binding energy influence for the multi-trap model on hydrogen concentration in lattice sites.

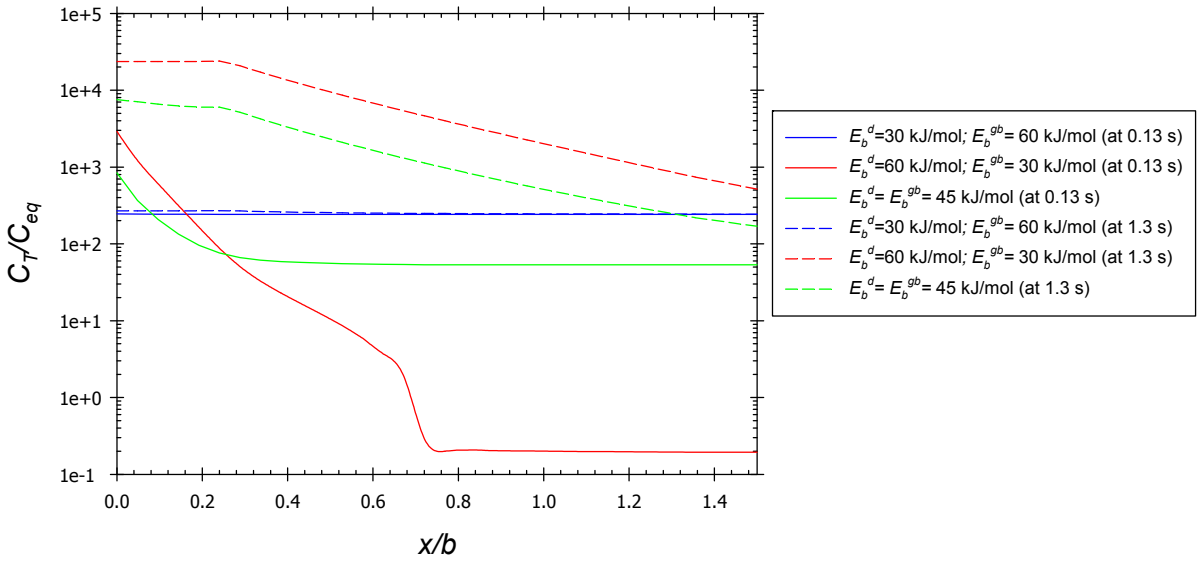

Figure 4-21. Binding energy influence for the multi-trap model on hydrogen concentration in trapping sites.

4.7.2 Non-equilibrium

Frequency effects are analysed again, this time for the multi-trap model, considering McNabb and Foster formulation, i.e. non-equilibrium. A higher trapped hydrogen concentration is present due to the grain boundary effects. Therefore, capture of hydrogen in grain boundaries and release of hydrogen from lattice and dislocation sites occur really fast. For high vibration frequencies (>10^9 s^{-1}), there are numerical instabilities. In order to avoid them, small sub-increments must be chosen for the time-integration of trap occupancies. Hydrogen concentration in lattice sites predicted by non-equilibrium assumption differs substantially in the multi-trap simulation (Figure 4-22). In one hand, small influence of frequency (ω_0 = 10^6 s^{-1} versus ω_0 = 10^8 s^{-1}) is observed for C_L at 1.3 s, i.e. at the end of the load; on the other hand, for C_T in Figure 4-23, the simulation with ω_0 = 10^8 s^{-1} approximates the equilibrium distribution. This means that hydrogen kinetic exchange between lattice and trapping sites occur faster so thermodynamic equilibrium is practically reached.

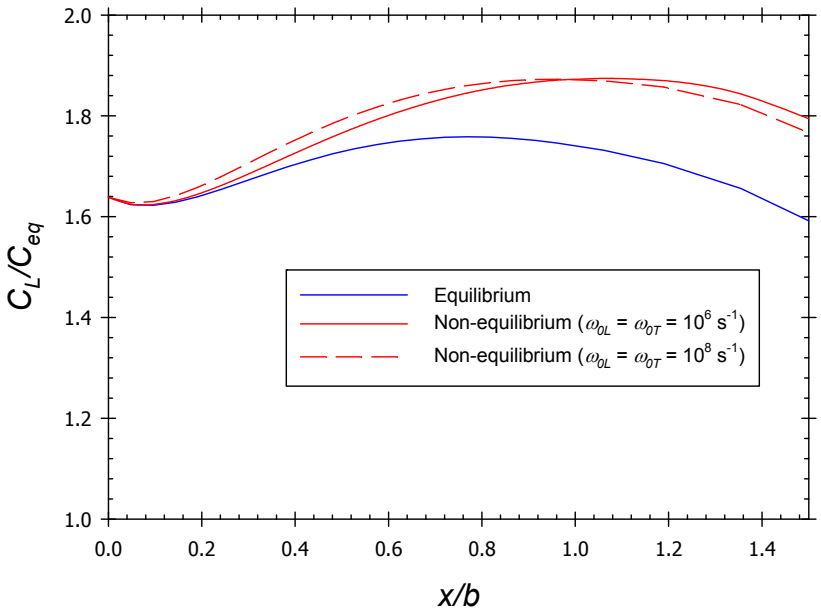

Figure 4-22. Influence of vibration frequency for hydrogen concentration in lattice sites after 1.3 seconds. Comparison between equilibrium and kinetic formulations.

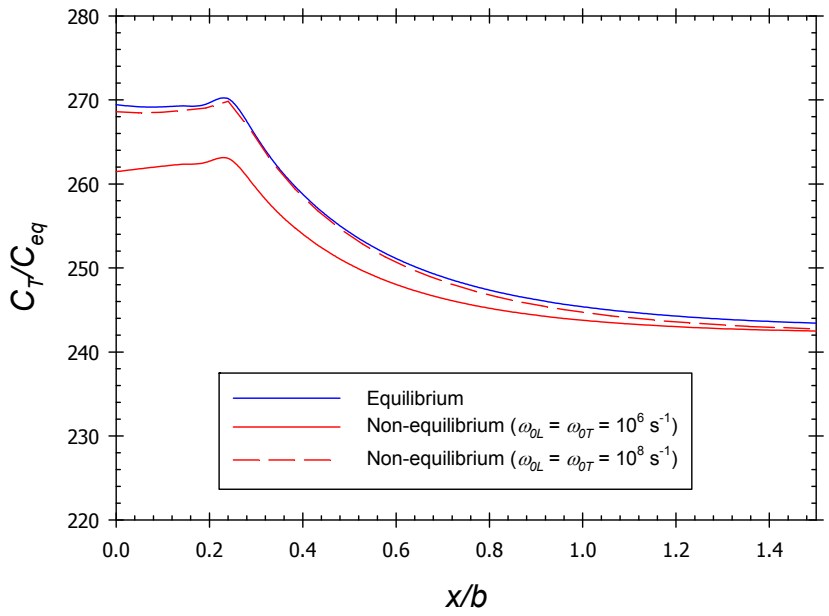

Figure 4-23. Influence of vibration frequency for hydrogen concentration in trapping sites after 1.3 seconds. Comparison between equilibrium and kinetic formulations.

As made in the previous subsection 4.7.1, binding energy influence is also assessed for the kinetic model. The following combinations of binding energy are simulated and plotted:

- E_b^d = 30 kJ/mol and E_b^{gb} = 60 kJ/mol(Figure 4-24 for C_L and Figure 4-25 for C_T)
- E_b^d = 60 kJ/mol and E_b^{gb} = 30 kJ/mol (Figure 4-24 for C_L and Figure 4-27 for C_T)
- E_b^d = 45 kJ/mol and E_b^{gb} = 45 kJ/mol(Figure 4-28 for C_L and Figure 4-29 for C_T)

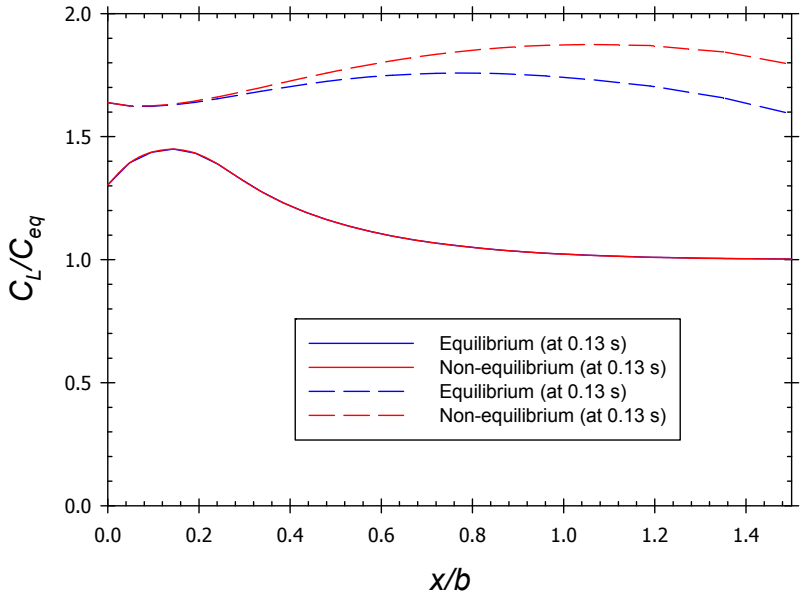

Figure 4-24. Hydrogen concentration in lattice sites after 0.13 and 1.3 seconds. Comparison between multi-traps models with equilibrium and non-equilibrium considerations with E_b^d = 30 kJ/mol and E_b^{gb} = 60 kJ/mol.

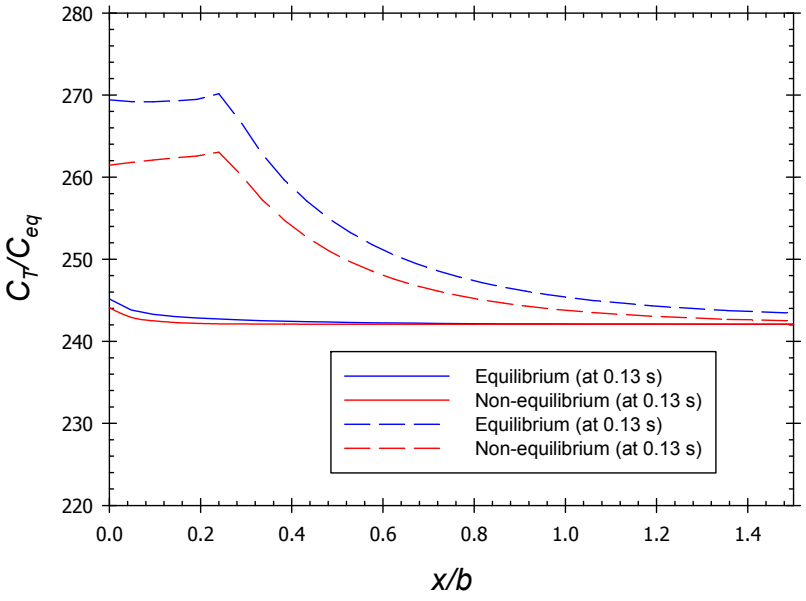

Figure 4-25. Hydrogen concentration in trapping sites after 0.13 and 1.3 seconds. Comparison between multi-traps models with equilibrium and non-equilibrium considerations with E_b^d = 30 kJ/mol and E_b^{gb} = 60 kJ/mol.

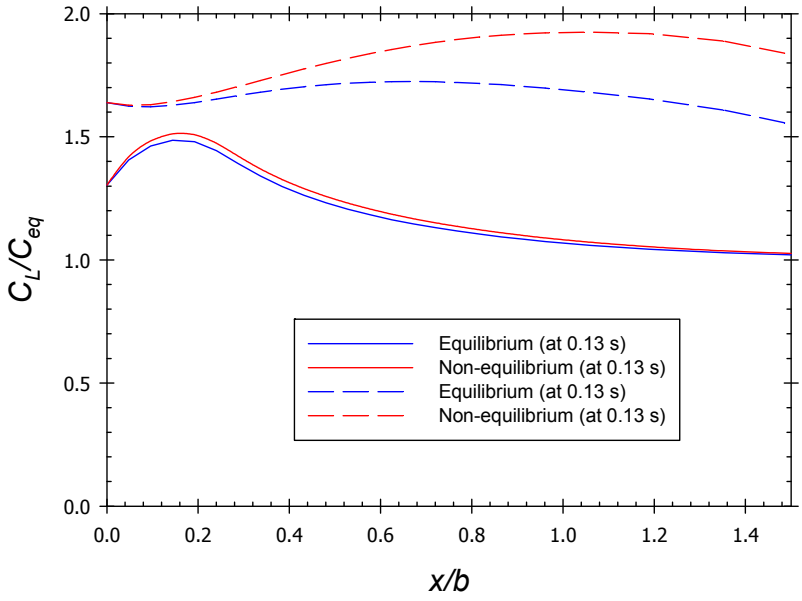

Figure 4-26. Hydrogen concentration in lattice sites after 0.13 and 1.3 seconds. Comparison between multi-traps models with equilibrium and non-equilibrium considerations with E_b^d = 60 kJ/mol and E_b^{gb} = 30 kJ/mol.

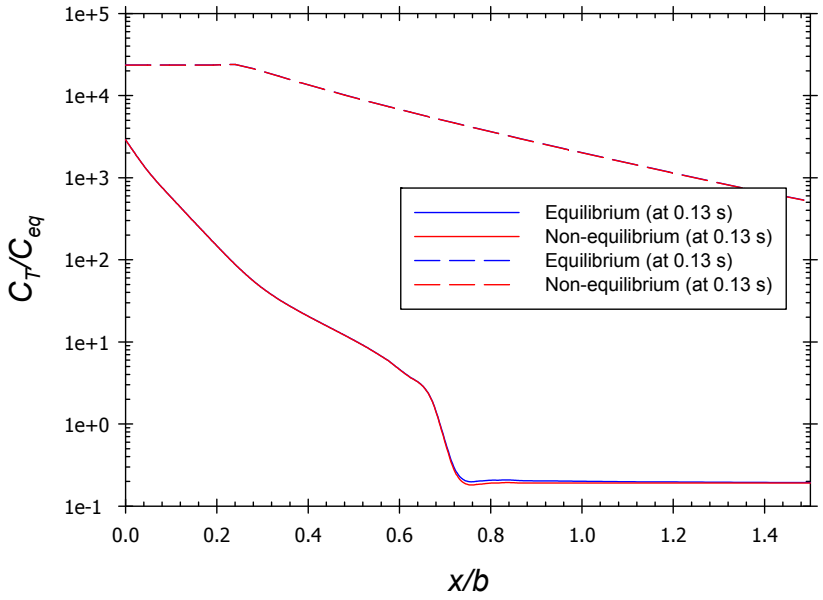

Figure 4-27. Hydrogen concentration in trapping sites after 0.13 and 1.3 seconds. Comparison between multi-traps models with equilibrium and non-equilibrium considerations with E_b^d = 60 kJ/mol and E_b^{gb} = 30 kJ/mol.

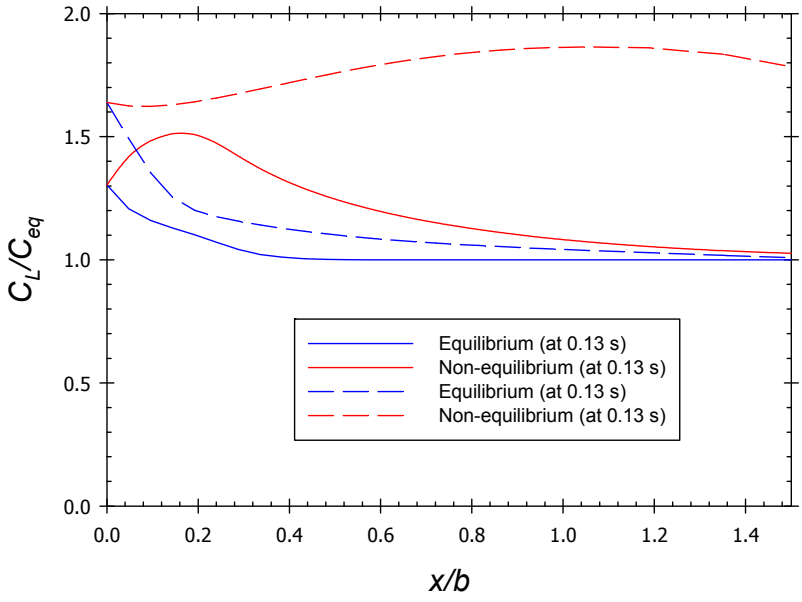

Figure 4-28. Hydrogen concentration in lattice sites after 0.13 and 1.3 seconds. Comparison between multi-traps models with equilibrium and non-equilibrium considerations with $E_b^d = E_b^{gb} = 45$ kJ/mol.

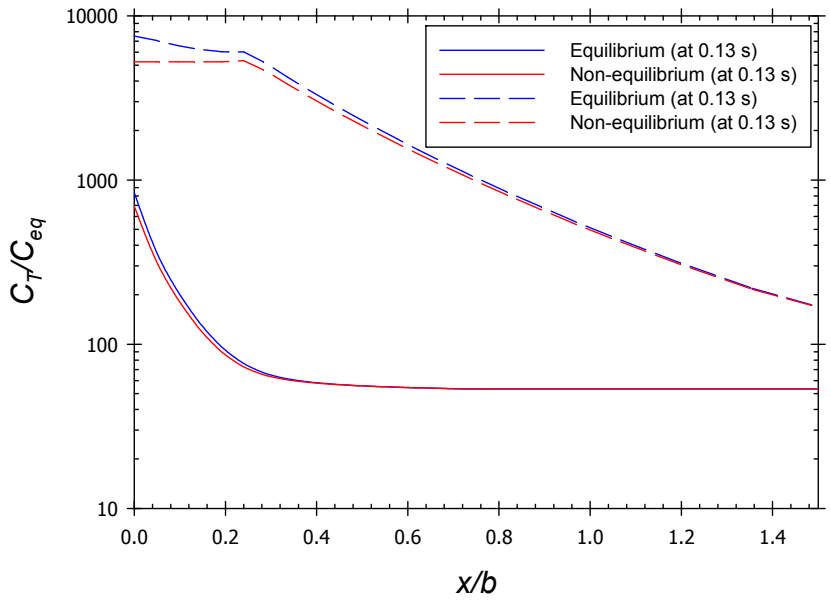

Figure 4-29. Hydrogen concentration in trapping sites after 0.13 and 1.3 seconds. Comparison between multi-traps models with equilibrium and non-equilibrium considerations with $E_b^d = E_b^{gb} = 45$ kJ/mol. .

As seen in Figure 4-28, the highest difference between equilibrium and kinetic considerations for the hydrogen concentration in lattice sites is observed when both binding energies, i.e. grain boundaries and dislocations energies, are equal, i.e. in the third simulated situation $E_b^d = E_b^{gb}$ = 45 kJ/mol.

When dislocations are assumed to have high binding energy, as in the second situation, E_b^d = 60 kJ/mol and E_b^{gb} = 60 kJ/mol (Figure 4-24 for C_L and Figure 4-27 for C_T), concentration in trapping sites is found to be 2.3×10^4 times C_{eq}, i.e. $C_T \approx 4.78\times10^{16}$ hydrogen atoms per mm^3, which corresponds to 10.2 wppm. Therefore, strong trapping in dislocations might be a possible explanation for embrittlement even at very soft environmental conditions, i.e. for very low equilibrium concentrations.

4.8 Conclusions

The same results as references (Di Leo & Anand, 2013; A. Krom et al., 1999; Sofronis & McMeeking, 1989; Taha & Sofronis, 2001) were obtained in crack tip through the boundary layer approach. Interstitial hydrogen concentration has a peak, about 1.5 to 2 times the boundary concentration, due to the hydrostatic stress peak at a certain distance from the crack tip. However, consideration of traps associated with plastic strain causes hydrogen concentration in trapping sites to show a maximum of approximately 80 times C_{eq} just at the crack tip. The location of critical hydrogen concentration is crucial in order to pinpoint the Fracture Process Zone.

In addition, implementation of the plastic strain rate term in UMATHT subroutine confirms the results of Krom et al. (A. Krom et al., 1999): the velocity at which traps are created influences the concentration for short times, but it does not alter the hydrogen distribution in the steady state. When loading rates are very high, thermodynamic equilibrium proposed by Oriani might not be fulfilled, and thus a kinetic formulation for the exchange between traps and lattice sites must be used.

Flux between traps is neglected, as in the revisited literature, and this assumption is verified numerically, as it has been confirmed that for the parameters used by Sofronis and

McMeeking for alpha iron (Sofronis & McMeeking, 1989), $\mathbf{J}_T$ is insignificant. For traps with high binding energy, diffusivity between trapping sites always has a very low value (irreversible traps), while for traps with low binding energy, Oriani's balance predicts very low concentrations in trapping sites; in both cases $\mathbf{J}_T$ is nearly zero. However, the concept of proximity or remoteness should be explicitly included when discussing whether flux between traps occurs or not.

It is also essential to know how the hydrogen concentration influences the elasto-plastic material response, i.e. the so-called coupled diffusion. By means of subroutines that continue with the heat transfer analogy (UEXPAN and UHARD), coupled diffusion has been implemented more easily without directly rewriting the material constitutive equations and its tangent stiffness. It has been concluded that dilation in alpha iron is negligible even for very high concentrations which only occur under extreme conditions. Nevertheless, for other metals and lattice arrangements, dilatation modelling might be unavoidable, especially in those metals that form hydrides.

Hydrogen influence on plastic flow cannot be easily modelled, since each particular situation may lead to either a local softening or a local hardening. The coupling parameter ξ would be best interpreted from a microstructural point of view; to this end, interaction of hydrogen with dislocations should be better understood.

Besides the coupling of diffusion, boundary conditions are crucial in simulation results. However, they have been usually overlooked, and little attention is paid to its stress state dependence. In this thesis, from the expression of a chemical potential constant at the boundary, a hydrogen concentration dependent on hydrostatic stress has been implemented as a boundary condition.

Chapter 5 Simulation of hydrogen and triaxiality effects in notched specimens

In this Chapter, a Cohesive Zone Model approach is used to simulate fracture initiation in notched specimens. Hydrogen embrittlement is reproduced by means of the informed-cohesive model presented in Chapter 3, in which local triaxiality and hydrogen concentration promote a reduction in cohesive energy. The expected fracture at lower strains in tensile tests, due to the presence of hydrogen, is evaluated here.

5.1 Introduction

As it has been mentioned previously, hydrogen embrittlement micro-mechanisms are not yet completely understood. However, strain localization and decohesion seem to be usually accelerated by hydrogen, which might cause brittle fracture. With the aim of predicting those failures, the local interaction between notch fracture mechanics and hydrogen diffusion is analysed in this Chapter. As the stress-strain state affects hydrogen diffusion, a great hydrogen concentration is expected in the vicinity of a notch. Additionally, the level of constraint affects plastic localization. In the present Chapter, the effect of the notch radius as an indicator of triaxility and stress concentration on hydrogen diffusion is studied. Moreover, damage evolution is implemented with cohesive elements along the notch tip plane using the Traction – Separation Law proposed by Park, Paulino and Roesler (PPR) and presented in Section 3.5.1. Cohesive energy and critical separation depend on hydrogen content but also on triaxiality, i.e. on the notch radius. In order to reproduce a brittle behaviour at the macroscopic scale, tensile tests of Notched Round Bars with different notch radii are

simulated in a high-pressure hydrogen environment. The competition and/or synergy between constraint and hydrogen embrittlement are discussed.

Susceptibility to Hydrogen Embrittlement can be tested in a laboratory with different standardised specimens: tensile, compact tension, three-point bending, etc. Hydrogen effects on smooth specimens in tensile tests are not very significant; however, for notched bars failures occur at much lower strains (Wang et al., 2005). This fact indicates an important synergy between notch fracture mechanics and hydrogen damage. Here a Notched Round Bar (NRB) in a tensile test is simulated in order to assess the hydrogen influence on fracture and the effect of the notch radius.

To account for crack propagation and final fracture, a damage model must be also included (Pineau, Benzerga, & Pardoen, 2016). Cohesive Zone Model (CZM) is a numerical technique that allows the creation of new surfaces. A Traction-Separation Law (TSL) governs the cohesive element response. Considering that hydrogen reduces cohesive energy, the area under the TSL might be modified to account for this effect. In the performed simulations of notched specimens, cohesive response is informed by a previous hydrogen diffusion analysis. Additionally, the TSL could also be influenced by local triaxiality. Cohesive elements are versatile because they can simulate brittle failures as well as ductile fracture. In the present work, the TSL proposed by Park, Paulino and Roesler (Park et al., 2009) has been chosen and its adaptability to model the shift from ductile to brittle failure is discussed.

5.2 Materials and procedures

As mentioned above, hydrogen embrittlement must be considered for H_2 pressure vessel design. Some steels, such as high strength steels (HSS), are susceptible to this kind of failure. Nevertheless, the use of HSS is often very convenient in order to reduce vessel thickness and weight, especially at high internal pressures.

Steel candidates for H_2 storage include the Cr-Mo family because it has a good combination of strength and toughness. AISI steels like 4130, 4340 and 4135 have been extensively studied and tested under hydrogen conditions. For low temperature of tempering, they can

reach a very high yield strength. Due to the wide range of these strengths, here a value of σ_0 = 1000 MPa is chosen just for the numerical assessment. Elasto-plastic response is assumed to follow a power law and simulated mechanical parameters are and shown in Table 5-1, with typical steel parameters while hydrogen related parameters are shown in Table 5-2.

Table 5-1. AISI 4130 steel: mechanical parameters.

E (MPa)	207000
ν	0.3
σ_0 (MPa)	1000
n	0.05

Table 5-2. AISI 4130 steel: hydrogen related parameters (San Marchi & Somerday, 2008).

D_L (mm^2/s)	0.0141
K (wppm·MPa$^{-1/2}$)	0.011
$\overline{V}_H$ (mm^3/mol)	2000
E_b (kJ/mol)	60

Notched round bars (NRB) might be used to calibrate the Traction – Separation Law in Cohesive Zone Modelling (Cornec, Scheider, & Schwalbe, 2003). The specimen is simulated with the following dimensions: length l = 60 mm, nominal diameter: d = 10 mm, diameter at notch: d_n = 4 mm. Three different notch radii are chosen to analyse the effect on hydrogen related fracture: r = 0.25, 0.50 and 1.00 mm. A Slow Strain Rate Test (SSRT) is considered so the dynamic effects are neglected.

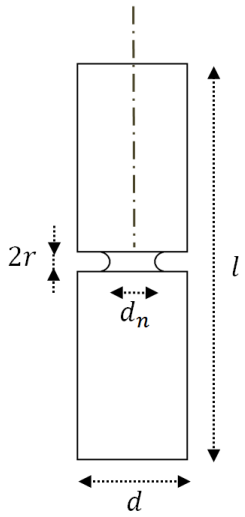

Figure 5-1. NRB dimensions.

Shape and slope parameters are kept constant with the following values: α = 2.0, β = 1.1, λ_n = λ_t = 0.1. The election of slope parameters is related to convergence issues while the influence of α on the results will also be discussed. It is worth noting that even if all of the mentioned parameters are included in the simulation, those corresponding to tangential mode are trivial because in the simulated tensile test fail occurs under mode I.

Cohesive elements have 4 nodes, and its initial length is equal to 0.025 mm, corresponding to the characteristic length h in the triaxiality-dependent cohesive energy, as shown in equation (3.38). With this length, the notch plane comprises 80 cohesive elements aimed at modelling crack propagation. Discussion about mesh dependency is out of the scope of this work, however some authors have discussed about size effects, length of the cohesive process zone and intrinsic material length in the CZM framework (Harper & Hallett, 2008; Turon, Dávila, Camanho, & Costa, 2007).

5.3 Hydrogen diffusion model

As here the test is simulated in a hydrogen chamber and at slow strain rate, diffusion is assumed to be faster than straining. Therefore, hydrogen concentrations are considered in equilibrium and there is no actual transient diffusion analysis; instead, the current hydrogen distribution is directly related to the present stress-strain state (Liang, Ahn, Sofronis, Dodds Jr, & Bammann, 2008).

Even in an equilibrium analysis, hydrogen is trapped in crystal defects like grain boundaries, inclusions, vacancies or dislocations. Two kinds of hydrogen concentrations are thus considered: hydrogen in lattice sites C_L and in trapping sites C_T (Sofronis & McMeeking, 1989). Assuming that the only significant flux is created between lattice sites, this vector $\mathbf{J}_L$ is proportional to a parameter called diffusivity D_L, to the lattice hydrogen concentration C_L and to the gradient of chemical potential μ_L. Operating, the flux equation emerges:

$$\mathbf{J}_L = D_L \nabla C_L + \frac{D_L}{RT} C_L \bar{V}_H \nabla \sigma_h \tag{5.1}$$

Hydrostatic stress is defined as the trace of the Cauchy stress tensor:

$$\sigma_h = \frac{1}{3} trace(\boldsymbol{\sigma}) \tag{5.2}$$

Positive σ_h indicates a tensile region, i.e. a lower chemical potential and a higher concentration in comparison with the stress-free lattice. The importance of this stress-dependency is vital in the vicinity of a notch. Even when the flux becomes zero, hydrogen concentration is not uniform if a stress-state is present. Making $\mathbf{J}_L$= 0 and operating, an exponential term is revealed, and hydrogen concentration in lattice sites might be expressed as:

$$C_L = C_{L,0} \exp\left(\frac{\bar{V}_H \sigma_h}{RT}\right) \tag{5.3}$$

where $C_{L,0} = C_L(\sigma_h = 0)$ is the concentration of hydrogen in the unstressed lattice, which can be obtained through Sievert's Law (Di Leo & Anand, 2013):

$$C_{L,0} = K\sqrt{p_{H_2}} \tag{5.4}$$

This value is related to the hydrogen pressure in the chamber, i.e. p_{H_2}= 20 MPa, and the selected solubility; thus, $C_{L,0}$ = 0.051 wppm.

As mentioned above, hydrogen might also be trapped in special sites. Even though hydrogen flux is neglected in traps, there is a kinetic relationship with lattice hydrogen. Crystal defects

mean a deep potential well in relation to the ideal lattice sites; the occupancy of both kinds of sites might be related if a thermodynamic equilibrium is considered:

Oriani first considered this expression (R. A. Oriani, 1970). E_b is the binding energy characterizing the trap; for high values of E_b hydrogen is irreversibly retained. Assuming low lattice occupancy $\theta_L \ll 1$ and operating, hydrogen concentration in trapping sites might be expressed as:

$$C_T = \frac{N_T}{1 + \frac{N_L}{C_L \exp\left(\frac{E_b}{RT}\right)}} \tag{5.5}$$

Here, the expression found by Kumnick and Johnson (A. J. Kumnick & H. H. Johnson, 1980) for the dependence $N_T(\varepsilon^p)$ is used. Equations (5.1) to (5.5) are implemented and solved in ABAQUS using a Heat Transfer analysis and a UMATHT subroutine, taking advantage of the analogy between heat transfer and diffusion (Díaz, Alegre, & Cuesta, 2016). Once the equilibrium concentrations C_L and C_T are obtained, the role of each one in a damage model is controversial:

- Lattice hydrogen reduces cohesive forces between slip systems. Hence cleavage should be expected.
- Hydrogen is segregated in grain boundaries so intergranular decohesion might occur.
- Hydrogen near dislocations, weakly trapped, is supposed to promote strain localization and hence embrittlement.
- On the other hand, irreversible traps might mitigate embrittlement by reducing the available amount of lattice hydrogen (M. Dadfarnia et al., 2011).

Then, hydrogen must be discriminated depending on the location and its contribution to damage. Here, for the sake of simplicity, total concentration is considered in a non-dimensional magnitude c:

$$c = \frac{C_L + C_T}{N_{Fe}} \tag{5.6}$$

where N_{Fe} = 8.47×10^{16} iron atoms per m^3, assuming the density of iron as 7.87 g/cm3. The bulk magnitude c corresponds to a coverage θ, which is responsible for fracture energy reduction, as will be shown in the next section. c and θ are related by means of the Langmuir- isotherm (Serebrinsky et al., 2004):

$$\theta = \frac{c}{c + \exp\left(-\frac{\Delta g_b^0}{RT}\right)} \tag{5.7}$$

The variation in Gibbs energy Δg_b^0 equals 30 kJ/mol (Serebrinsky et al., 2004). Even though this value was calculated for the segregation in grain boundaries, here it is used for a generic coverage.

Summing up, in the present Section two simplifications are made in the diffusion analysis:

- A Slow Strain Rate Test is simulated. Therefore, diffusion is supposed to occur faster than mechanical loading and hydrogen concentrations are considered in equilibrium. With this assumption, a steady state analysis is performed and the time-scale is meaningless for diffusion. Hence, C_L and C_T are determined just by the initial and boundary conditions and by the current stress-strain state. Even if transient effects are overlooked, mechanical load is not instantaneous so C_L and C_T do not remain constant over time.

- Hydrogen redistribution produced by crack tip propagation is not considered. This second simplification is not physically-based; however, due to numerical limitations in the coupling between diffusion and cohesive analysis, boundary conditions are not actualised with the crack propagation. Thus, a two-step analysis is carried out: a steady-state diffusion analysis is performed with the stress-strain coupling, but without crack propagation, and then hydrogen concentration and triaxiality are transferred to each cohesive element. This approach will be called informed Cohesive Zone Model, because it is not a truly simultaneous coupling between diffusion and fracture.

The flowchart is shown schematically in Figure 5-2, where the relationship between mechanical, diffusion and CZM analysis is depicted by means of input and output items. In Section 3.5.3 the dependence of TSL on triaxiality and hydrogen is detailed.

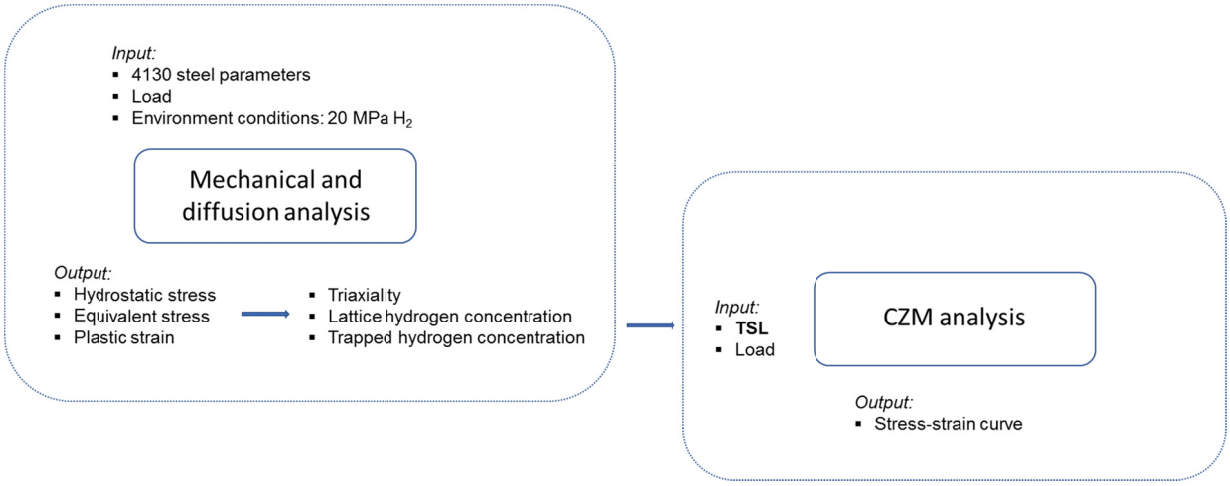

Figure 5-2. Scheme of the two-step simulation: firstly a mechanical and diffusion coupled analysis is performed and then an informed CZM analysis.

5.4 Results and discussion

The test is simulated in a displacement-controlled manner. The specimen is subjected to a ramped displacement, with a random rate since material behaviour is rate-independent and hydrogen is assumed to be in equilibrium. When load increases, hydrostatic stress peak is shifted from the notch root towards the centre of the specimen. Figure 5-3 shows the hydrostatic pressure distribution at the beginning of load for a notch radius of 0.25 mm. Mesh transition can also be appreciated.

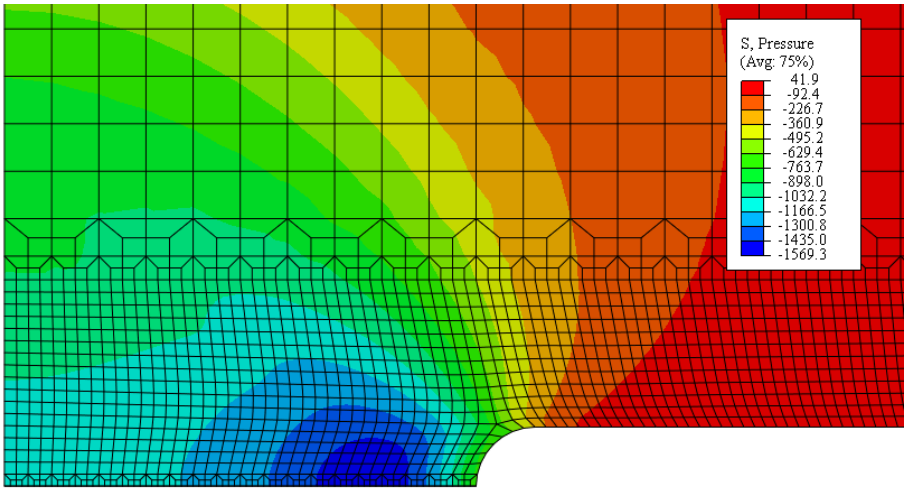

Figure 5-3. Hydrostatic pressure at the beginning of load for r = 0.25 mm. (note that $p = -\sigma_h$)

In Figure 5-4, the simulated axisymmetric quarter of the model is swept 180º and mirrored in the notch symmetry plane in order to show the distribution of the Von Mises equivalent stress in a whole specimen at the beginning of load for a notch radius of 0.25 mm. Dividing σ_h by σ_e, the local triaxiality H is found and then transferred to the cohesive elements. Both triaxiality and interstitial hydrogen depend on hydrostatic stress, so the peak will be an indicator of each. The evolution of H and θ can be shown in Figure 5-5.

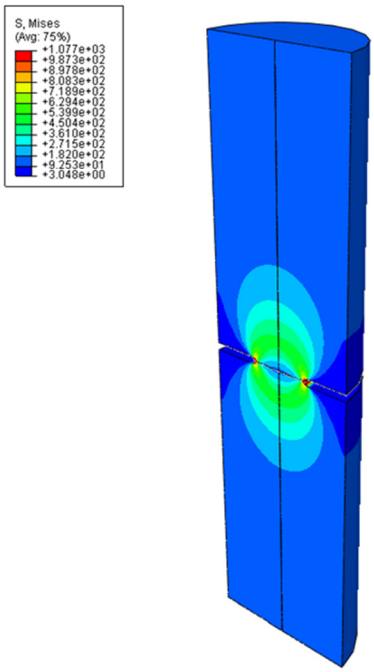

Figure 5-4. Equivalent stress at the beginning of load for r = 0.25 mm.

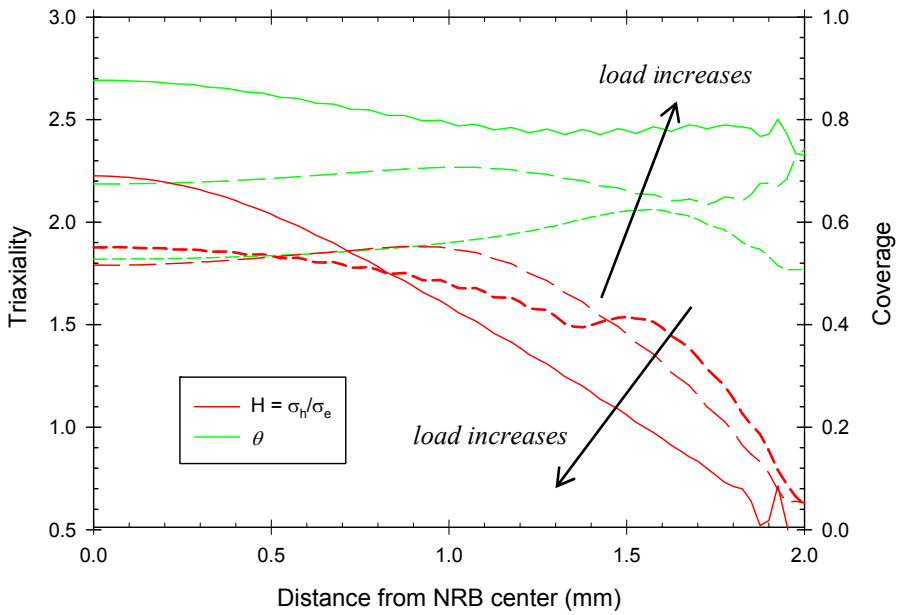

Figure 5-5. Triaxiality and coverage distribution in the notch root section with increasing load for r = 0.25 mm.

Coverage presents a peak in the notch root (x = 2 mm) for some stages of loading. This is due to the location of the plastic zone and the relationship between trapped hydrogen and plastic

strain expressed by Kumnick and Johnson expression. For higher binding energies, this coverage peak will be significant.

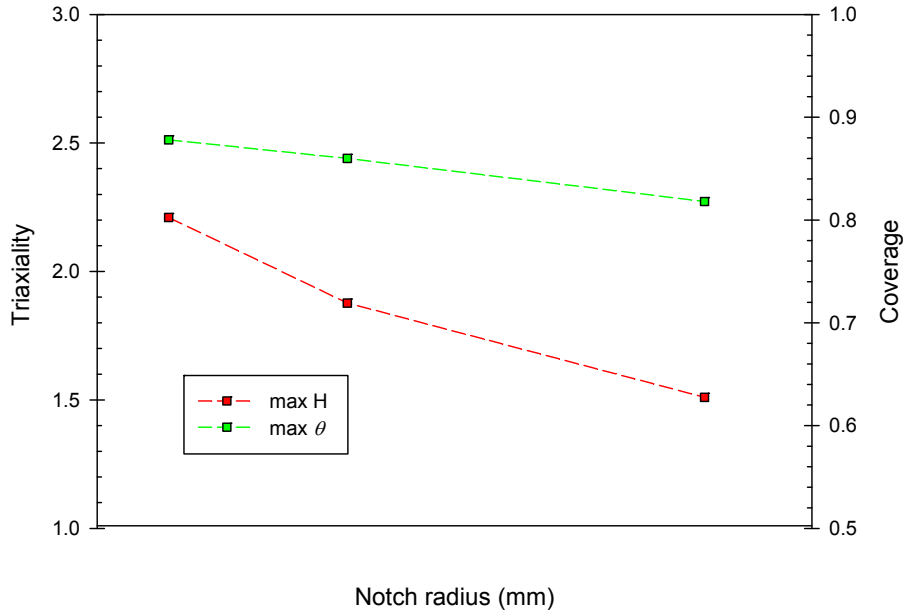

Figure 5-6. Notch radius effect on maximum triaxiality and hydrogen coverage.

Comparing maximum triaxiality and coverage reached in the centre of the specimen just before failure, it is demonstrated that for small notch radii, stress concentrations cause higher triaxialities and hydrogen content, as shown in Figure 5-6. Complete damage is achieved by the central elements because the local TSL has a lower cohesive energy due to the reduction caused by hydrogen (Equation (3.33)) and by triaxiality (Equation (3.38)).

The most important result of the NRB simulated test is the Force -Displacement curve, which can be translated to an Axial stress – strain curve. Tracking the reaction forces in top nodes $F_i(t)$, the current cross section at the notch root $A(t)$, and the current length $l(t)$:

$$\sigma = \frac{1}{A(t)} \sum_i F_i(t) \tag{5.8}$$

$$\varepsilon = \ln\left(\frac{l(t)}{l_0}\right) \tag{5.9}$$

First, the curve obtained in the static analysis performed with continuum elements, i.e. without crack initiation, is show in Figure 5-7. These simulations end at the beginning of unstable fracture, which corresponds to the final point of curves from Figure 5-7 to Figure 5-10. Last stage of fracture has not been modelled because of convergence problems.

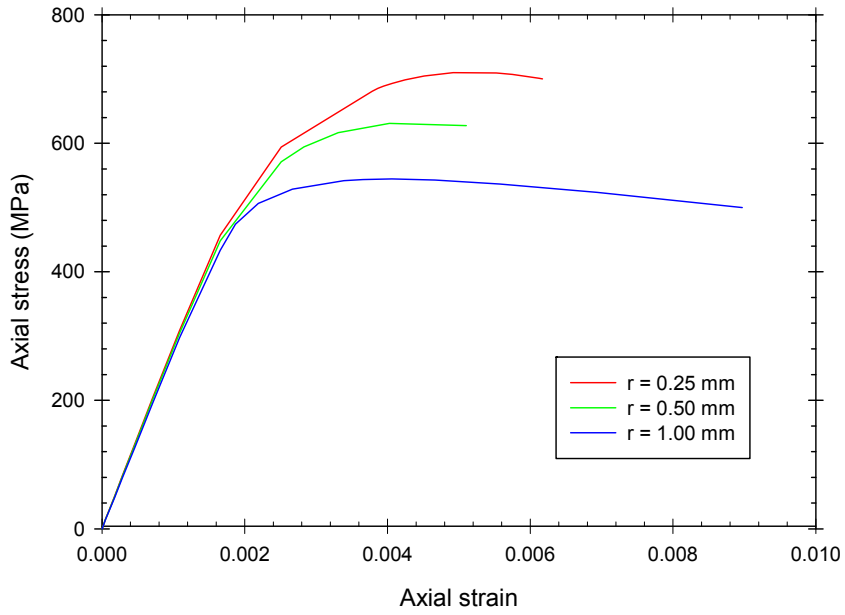

Figure 5-7. Stress-strain curve for different notch radii without cohesive elements.

Introducing the cohesive user elements in the notch plane, the fracture is simulated. It is demonstrated, and shown in Figure 5-8, that for small notch radii, a brittle behaviour is obtained. This can be explained not only by the higher stress concentration itself but also by the hydrogen concentration enhancement. Stress-strain curves almost coincide up to the beginning of damage. In that point, unstable fracture leads to convergence issues. Some strategies will be considered in future research, e.g. introducing dissipative or viscosity terms (Y. Gao & Bower, 2004; H. Yu, Olsen, Olden, et al., 2016), in order to improve convergence and simulate properly the crack propagation.

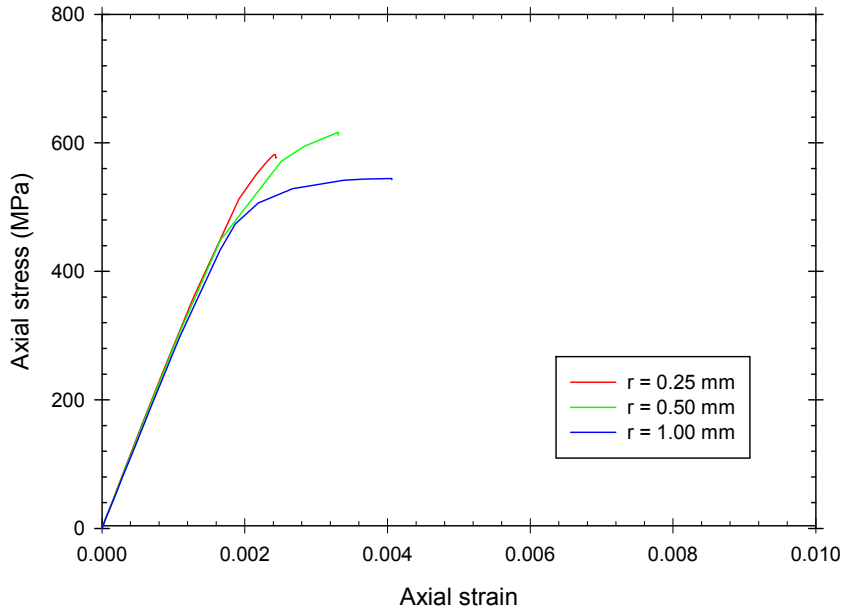

Figure 5-8. Stress-strain curve for different notch radii with cohesive elements

In order to differentiate the role of triaxiality and hydrogen embrittlement, fracture simulations have been carried out for notch radius r = 0.25 mm: (i) with both effects, plotted with a solid red line in Figure 5-9; (ii) only with triaxiality effect, plotted in green; (iii) and only with hydrogen effect, taking a constant triaxiality of 0.33 which corresponds to an uniaxial stress-state, plotted in blue.

Normal TSL has been considered with a shape parameter α = 2 in all of these simulations. As mentioned above, $\alpha > 2$ must be used for quasi-brittle materials while $\alpha < 2$ implies a plateau-type softening response, which is typical in ductile metals. The effect of this parameter in fracture simulation for r = 0.25 is shown in Figure 5-10. α = 1.01 is chosen because the unity produces numerical problems in equations (3.31) and (3.32).

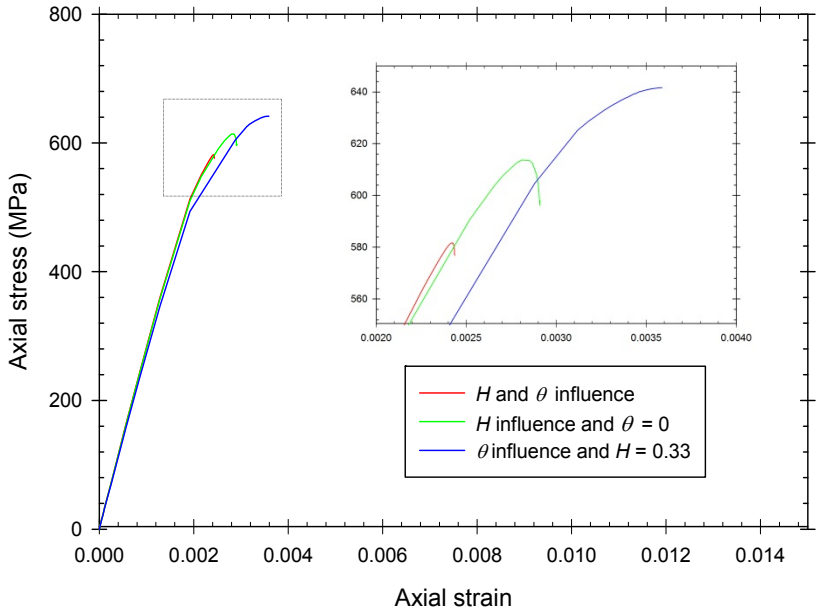

Figure 5-9. Stress-strain curve for r = 0.25 mm: triaxiality H, and coverage influence.

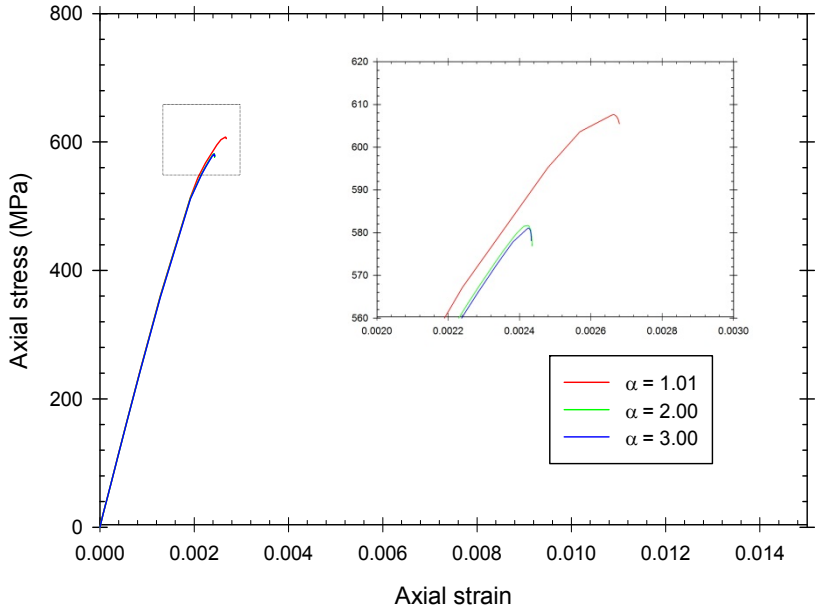

Figure 5-10. Stress-strain curve for r = 0.25 mm: α influence.

As expected, α = 1.01 causes a slight increase in ductility. However, for α > 2, embrittlement is not observed and results are practically unaffected. Keeping in mind that α is a ductility indicator in the TSL, and that hydrogen enhances local softening according to the HELP theory, a local variation $\alpha = \alpha(\theta)$ could be implemented in a more sophisticated hydrogen-informed Cohesive Zone Model.

5.5 Conclusions

A numerical procedure has been presented with the objective of combining hydrogen and triaxiality effects in Notch Fracture Mechanics. To do so, a two-step analysis has been performed: first hydrogen distribution is obtained with diffusion equations modified by the stress-strain state and then a Cohesive Model is included to model damage initiation. Results indicate that hydrogen is concentrated in the hydrostatic stress peak, so it is related to local triaxiality. The obtained stress-strain curves for the NRB simulated specimens in a 20 MPa of high-pressure H_2 environment show that ductility is limited at small notch radii. High concentrations of hydrogen are located in the same places than high triaxialities, at least for the selected trap binding energies; thus embrittlement effect, within a CZM approach, is multiplied when both effects are included in the TSL.

Chapter 6 Application to a pressure vessel considering cyclic loading

In this Chapter, a high pressure vessel storing H_2 is simulated. Cyclic loads are introduced to reproduce the fuel filling operations in a real tank. The objective is to assess how hydrogen concentrates near a stress concentrator and the influence of load amplitude and frequency. Diffusion model with the previously discussed relationship between boundary conditions, pressure and fugacity is implemented here.

6.1 Introduction

With the increasing interest in the use of hydrogen as an energy carrier, a better understanding of hydrogen embrittlement affecting materials is required. In addition, hydrogen tanks suffer fatigue processes due to stress variation in filling and refuelling operations. Models used by previous authors have been improved by implementing a stress state dependent concentration as boundary condition, based on the work of (Di Leo & Anand, 2013). Additionally, the relationship between fugacity, H_2 pressure, and hydrogen concentration in the surface is exposed and discussed. Once this numerical model is established and checked, a pressurized hydrogen vessel is simulated in this Chapter, assuming a defect in the inner wall and cyclic stresses. A metal vessel without liner and without reinforcement or wrapping is modelled, i.e. a Type I hydrogen tank. Usually these containers are made of austenitic stainless steels or aluminium alloys, but medium and high strength steels are being proposed in order to reduce thickness and total weight. Here, the AISI 4130 steel is selected for simulations. The problem of high strength steels is that they are very susceptible to hydrogen embrittlement. In addition, the filling and fuelling operations produce

cyclic loads that might cause fatigue. The initiation and subsequent fatigue propagation of cracks is influenced by the hydrogen concentration within the material. Therefore, the main objective of this Chapter is to find the hydrogen concentrations produced in a crack tip as a result of cyclic hydrogen pressure with a maximum of 70 MPa. The influence of internal pressure, load amplitude and frequency on hydrogen concentration near the crack tip is discussed.

6.2 Hydrogen diffusion model

Considering the implemented model described in Chapter 3, diffusion near a crack present in the simulated vessel with the following characteristics:

- A two-level model with hydrostatic stress and plastic strain influence is used for the diffusion simulation in the vessel. Governing Equation (3.15) is solved with the described subroutine UMATHT.
- Oriani's equilibrium is assumed, i.e. Equation (3.16) is applied.
- A term corresponding to the dilatation produced by hydrogen is added to the deformation rate tensor in the constitutive equation.
- The boundary condition is a stress-dependent concentration (Section 3.6.3) in which the fugacity also depends on the cyclic pressure through the Abel-Nobel expression (Equation (7.2)).

6.3 Modelling

6.3.1 Material characterization

The AISI 4130 steel has been chosen for the simulated vessel. Its chemical composition is shown in Table 6-1:

Table 6-1. Allowable composition range (wt%) for AISI 4130 steel (San Marchi & Somerday)

Component	Cr	Mo	C	Mn	Si	P	S	Other
min wt%	0.80	0.15	0.28	0.40	0.15	-	-	-
max wt%	1.10	0.25	0.33	0.60	0.35	0.035	0.040	-

Yield strength σ_0 and ultimate tensile strength σ_u are extracted from reference (Song & Shieh, 2004) where steel AISI 4130 was quenched in oil to room temperature and then tempered at 450ºC for 1.5 hours obtaining thus a tempered martensite microstructure. Young's modulus E, Poisson's coefficient ν and hardening exponent n are chosen as usual for steels.

Table 6-2. Mechanical parameters for AISI 4130 steel.

E (MPa)	210000
ν	0.3
σ_0 (MPa)	1186
σ_u (MPa)	1289
n	0.2

6.3.2 Diffusion parameters

For quenched and tempered 4130 steel, Arrhenius-type expressions of diffusivity D and solubility K have been found in references (Nelson & Williams, 1973; San Marchi & Somerday). Although permeation tests were performed at high temperatures, values are extrapolated to room temperature (298 K). Apparent diffusivity from (Nelson & Williams, 1973) is assumed as lattice coefficient D_L because its value is very close to that found for pure iron (A. H. M. Krom, R. W. J. Koers, & A. Bakker, 1999), showing a little trapping influence in these permeation tests. Partial molar volume $\bar{V}_H$ of hydrogen in steel is taken as $2{\cdot}10^{-6}$ m^3/mol (A. H. M. Krom et al., 1999). Number of lattice sites N_L is obtained assuming

a bcc structure for martensite (for carbon content less than 0.6 mass % (Sherby, Wadsworth, Lesuer, & Syn, 2008)) and tetrahedral preferred occupancy (A. H. Krom & A. Bakker, 2000).

The binding energy E_b of traps is taken from (F.-G. Wei & Tsuzaki, 2005) as the corresponding energy of a dislocation in tempered martensite. The number of trapping sites is related with equivalent plastic strain through the expression found by Kumnick and Johnson (A. Kumnick & H. Johnson, 1980).

Regarding the hydrogen induced dilatation, Δv and Ω are obtained assuming the usual density and atomic weight of iron. ξ parameter is equal to zero since there is no evidence of local softening or hardening in 4130 steel. All parameters are shown in Table 6-3:

Table 6-3. Diffusion parameters for AISI 4130 steel.

D_L (mm^2/s)	0.0141
K (atH·mm^{-3}MPa$^{-1/2}$)	2.09×10^{12}
N_L (sites/mm^3)	5.09×10^{20}
$\bar{V}_H$ (mm^3/mol)	2000
E_b (kJ/mol)	33.9
$\lambda = \Delta v/\Omega$	0.2834
ξ	0

6.3.3 Thickness design

The two set values are: maximum internal working pressure p_w of 70 MPa and inner radius r_i of 500 mm. The BPVC ("Boiler and Pressure Vessel Code. Section VIII Division 1. ASME ", 2010), gives a value of thickness t_w assuming thin (7.1) or thick (7.2) or thick wall:

$$t_w \geq \frac{p\, r_i}{SE - 0.6p} \tag{6.1}$$

$$t_w \geq r_i \left[\sqrt{\frac{SE + p}{SE - p}} - 1 \right] \tag{6.2}$$

p is the internal pressure. However, type I vessels must resist not only the working pressure; they are designed for a proof load (p = 1.5 p_w) and a burst load (p = 2.25 p_w). S is the material strength (σ_0 for proof load and σ_u for burst load). E is a parameter that introduces the welding efficiency in the vessel; in this case, welding influence is neglected, i.e. E = 1.

Another design option is to assume the analytical formulas for the stresses on a vessel. Hoop and radial maximal stresses ($\sigma_{\theta,max}$, $\sigma_{r,max}$) are obtained from the force equilibrium in a cylindrical wall with closed ends. Assuming plane strain conditions, longitudinal stress $\sigma_{z,\max}$ might also be obtained:

$$\sigma_{\theta,max} = p \left[\frac{2r_i^2}{2r_i t_w + t_w^2} + 1 \right] \tag{6.3}$$

$$\sigma_{r,max} = -p \tag{6.4}$$

$$\sigma_{z,max} = \nu(\sigma_{\theta,max} + \sigma_{r,max}) \tag{6.5}$$

If $t_w \ll r_i$, hoop stresses might be found with the thin wall formula:

$$\sigma_{\theta,max} = p \frac{r_i}{t_w} \tag{6.6}$$

Hoop stresses are often taken as the critical stresses. However, in order to refine the thickness design, the equivalent von Mises stress can be compared with the strength of the material. Considering the obtained design values shown in Table 4, a thickness of 66 mm is modelled. Being r_i/t_w = 7.57, the condition of thin wall (r_i/t_w> 10) is not satisfied.

Table 6-4. Minimum thickness required considering different approaches.

	ASME		Analytical (hoop stress)		Analytical (von Mises stress)	
	Thin Wall	Thick Wall	Thin Wall	Thick Wall	Thin Wall	Thick wall
Proof load	46.75	46.41	44.26	46.41	42.36	44.32
Burst load	65.93	65.33	61.09	65.33	60.25	64.35

6.3.4 Vessel

A half of the vessel cross section is modelled in 2D considering symmetry and assuming plane strain conditions (Figure 6-2). With the purpose of analysing the stress state influence on hydrogen diffusion, a crack with a length of 5% of the thickness and 0.5 mm of root radius is introduced in the plane of symmetry.

6.3.5 Cyclic load

The filling time of the tank is supposed to be 5 minutes in which there is a ramp pressure from 0 to 70 MPa. Since then, a cosine periodic charge is introduced, varying the amplitude and the frequency. Four situations are simulated:

- non-cyclic pressure of 70 MPa (Figure 6-3)
- 70 to 50 MPa and a cycle time of 300 s (Figure 6-4)
- 70 to 35 MPa and a cycle time of 300 s (Figure 6-5)
- 70 to 35 MPa and a cycle time of 30 s (Figure 6-6)

6.4 Results and discussion

Dashed blue line in Figure 6-1 represents C_L at 300 s, when hydrogen pressure has reached its maximum of 70 MPa. Peak concentration is located at the boundary at that moment. As

hydrogen diffuses, hydrostatic stress peak drifts C_L maximum towards the bulk material, and the solid line shown in Figure 1 is achieved at steady state when chemical potential gradients have disappeared. C_L maximum at steady state is approximately 0.013 wppm. This value represent the $C_{L,max}$ asymptote in transient analysis for long times.

Hydrogen concentration in trapping sites C_T is always two or three orders of magnitude less than C_L since there is no a significant level of plastic strain and dislocations have a low binding energy. As a consequence, total hydrogen concentration might be identified with C_L.

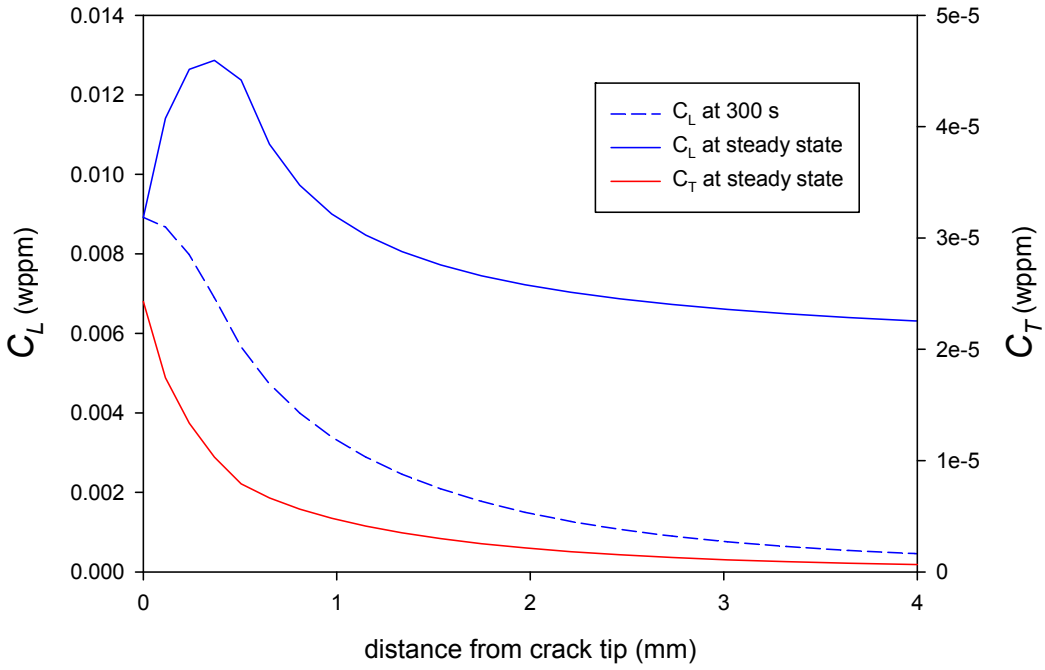

Figure 6-1. Hydrogen distribution C_L and C_T in the symmetry axis.

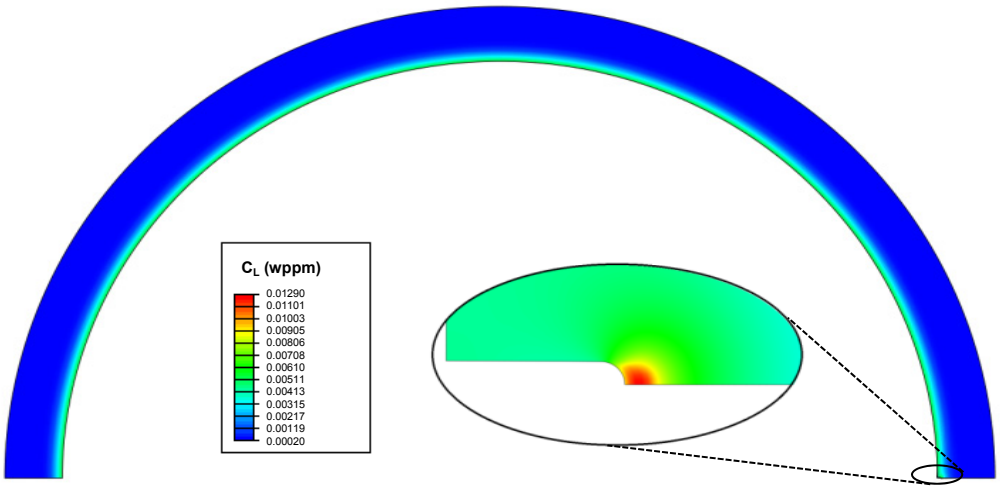

Figure 6-2. Hydrogen distribution in lattice sites near the notch tip.

When pressure is maintained constant after the initial ramp (Figure 6-3), maximum hydrogen concentration is reached at the boundary, i.e. $C_{L,b} = C_{L,max}$. Since approximately 1400 s, $C_{L,max}$ increases because a peak is appearing at a certain distance from crack tip.

As load amplitude is increased, i.e. $R = p_{min}/p_{max}$ is reduced, $C_{L,max}$ rises slower because of the boundary condition influence. At 3300 s, $C_{L,max}$ reaches 0.0119 wppm for R = 1 (Figure 6-3), whereas for R = 0.714 only reaches 0.0110 wppm (Figure 6-4), and for R = 0.5 only 0.00998 wppm (Figure 6-5). The range of $C_{L,b}$ is associated also with this amplitude.

$C_{L,max}$ peaks are slightly delayed respect those of $C_{L,b}$; this represents the times it takes hydrogen to diffuse from the crack tip to the region of high hydrostatic stress. Nonetheless, when frequency is increased (t_{cycle} = 30 s in Figure 6-6), hydrogen does not have time to diffuse in such a short cycle time and thus the $C_{L,max}$ peak coincides with that of $C_{L,b}$ at the moment in which the pressure is 70 MPa. Therefore, C_L peaks of 0.00938 wppm never rise.

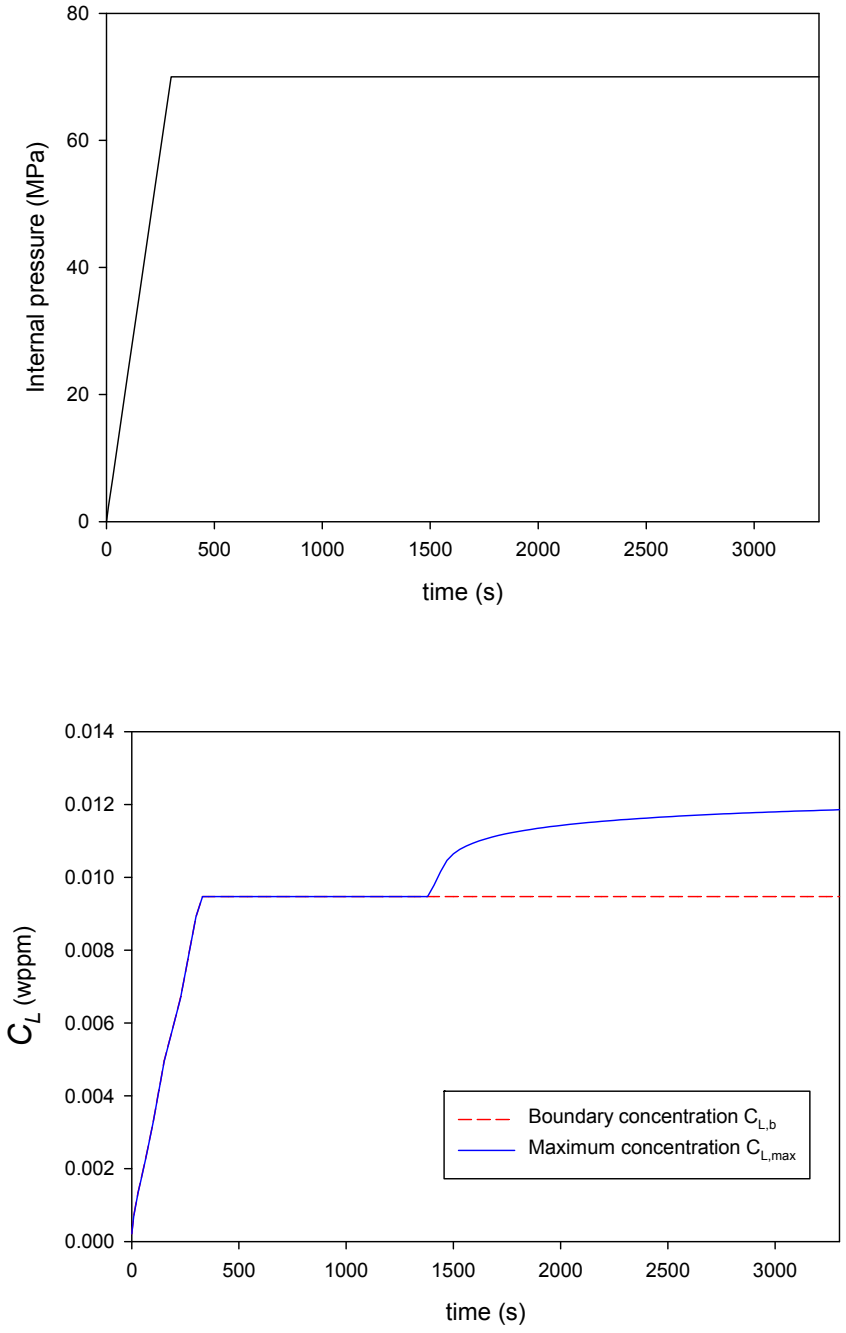

Figure 6-3. C_L at crack tip boundary (dashed red line) and maximum C_L (solid blue line) for R = 1.0

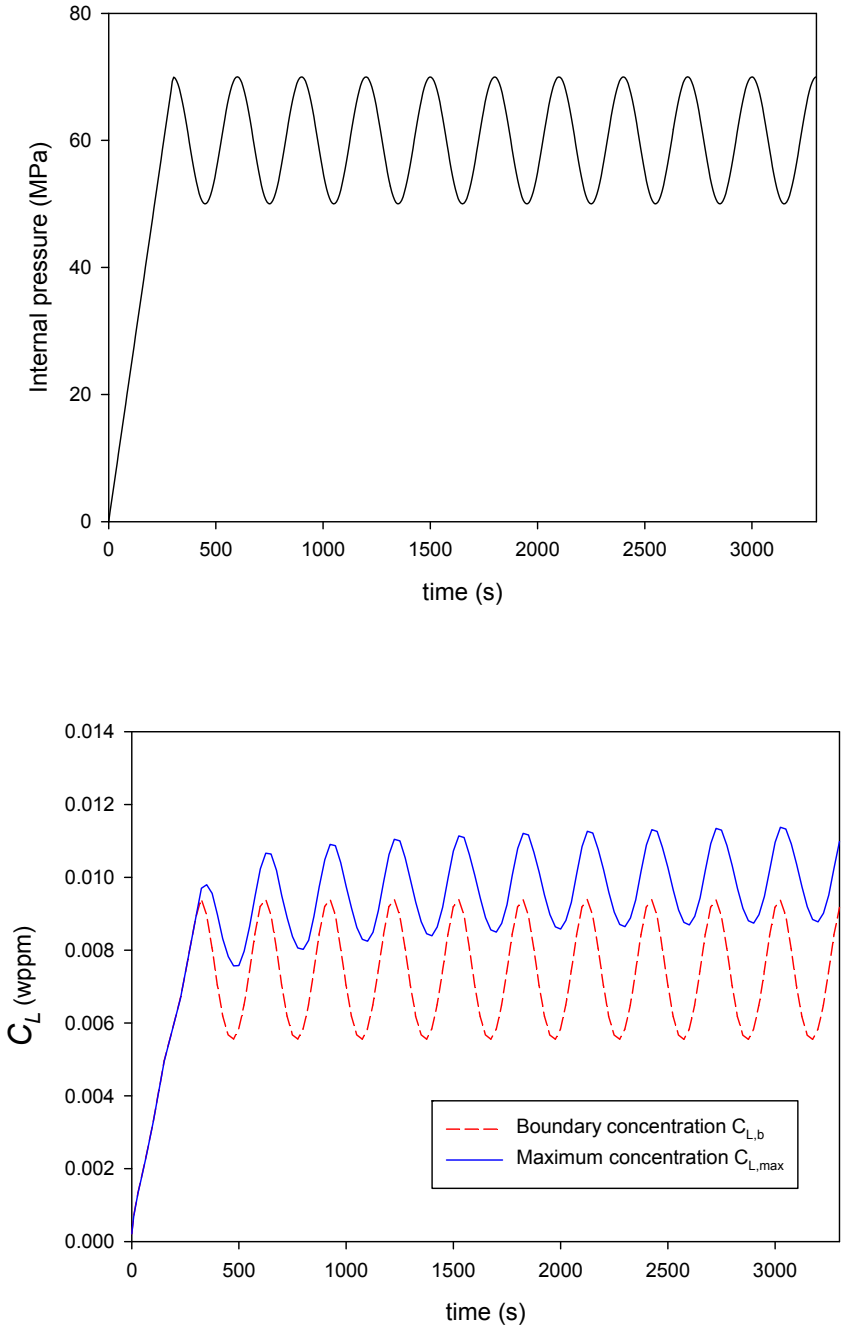

Figure 6-4. C_L at crack tip boundary (dashed red line) and maximum C_L (solid blue line) for R = 0.714 and t_{cycle} = 300 s

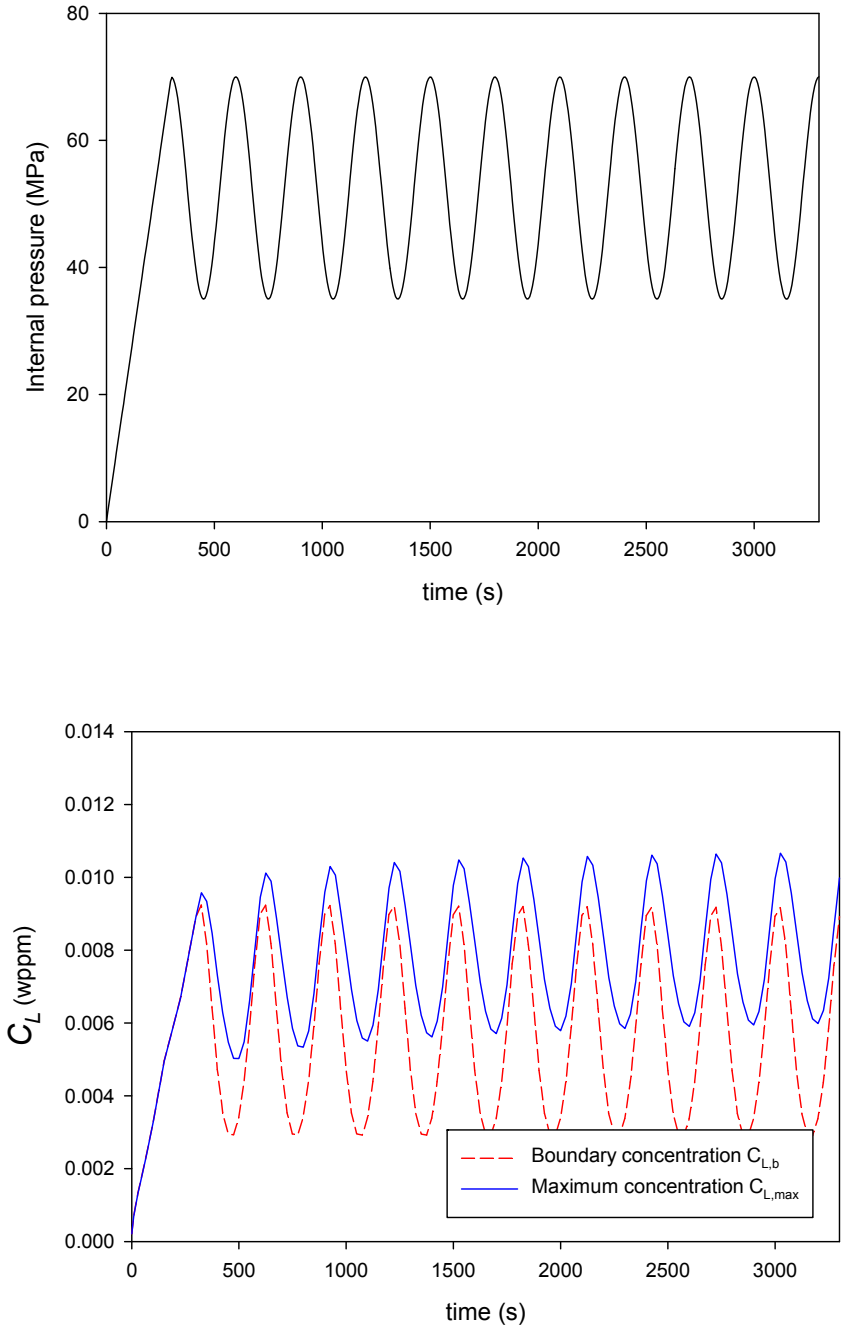

Figure 6-5. C_L at crack tip boundary (dashed red line) and maximum C_L (solid blue line) for R = 0.5 and t_{cycle} = 300 s

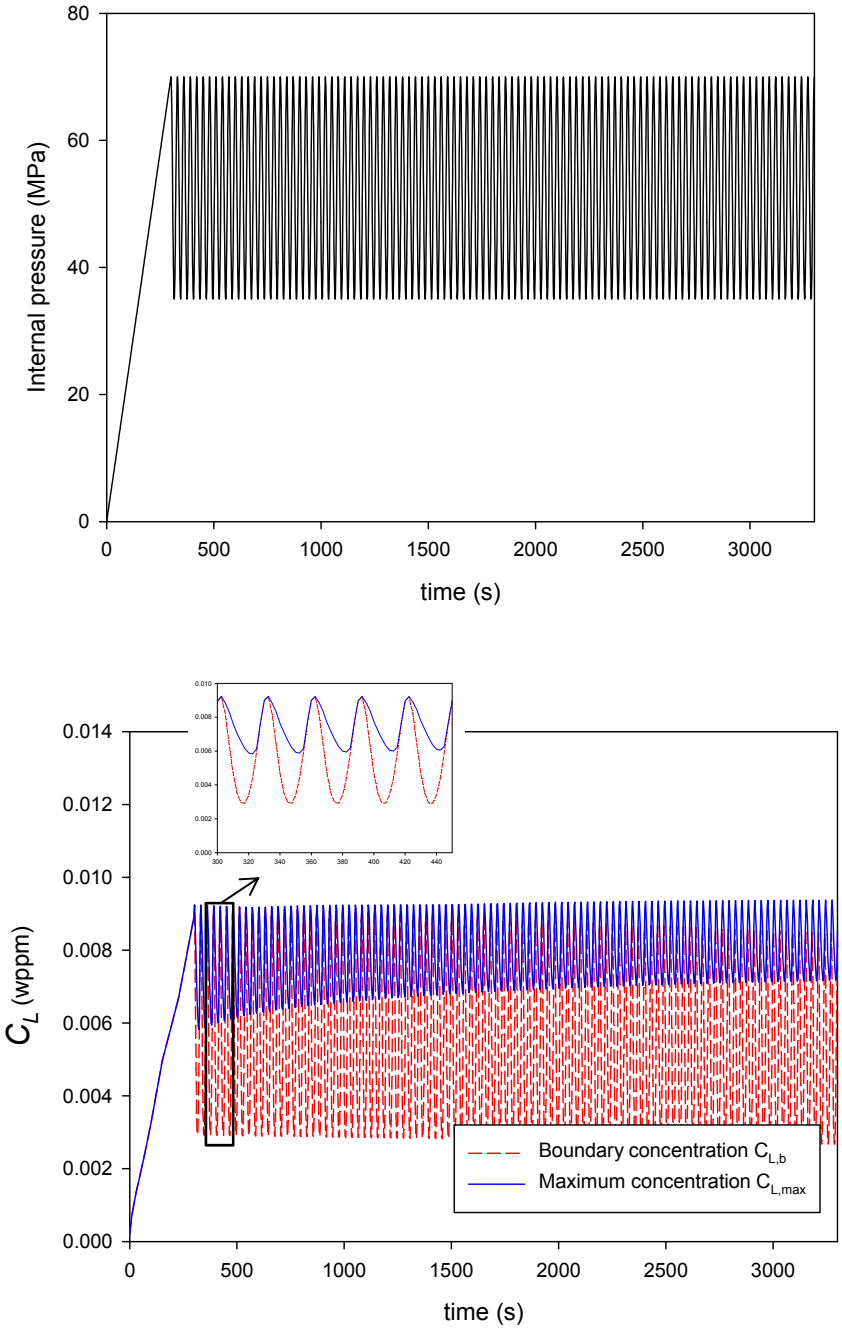

Figure 6-6. C_L at crack tip boundary (dashed red line) and maximum C_L (solid blue line) for R = 0.5 and t_{cycle} = 30 s

6.5 Conclusions

During their lifetime, pressure vessels containing hydrogen experience cyclic loads. When internal pressure p is a cyclic load, it influences the hydrogen distribution in two senses: through the fugacity and through the stress state produced in the vessel. In order to analyse the crack initiation and propagation it is essential to know how hydrogen is redistributed when stress state, and thus boundary condition, is not constant.

When hydrogen transport evolves, a concentration peak appears due to the hydrostatic stress distribution. In the simulated tank, the maximum concentration at steady state is equal to 0.013 wppm. This value is a consequence of the low solubility of hydrogen in steel. However, embrittlement might occur in high strength steels with small concentrations.

In this Chapter, trapping influence is implemented in diffusion equations. However, hydrogen is hardly retained in traps because of the low binding energy found for dislocations in tempered martensite. Other kind of traps should be better characterized by different tests in AISI 4130 steel since, in many cases, C_T could be not negligible.

Chapter 7 Assessment of residual stress effects in a pressure vessel

In this Chapter, a high pressure vessel storing H_2 is simulated again. Here, a monotonic working pressure of 70 MPa is considered. However, a residual stress-strain state is introduced in order to reproduce an autofrettage process; thus, final hydrogen concentrations in lattice sites will be modified by the compressive residual stress whereas hydrogen in trapping sites might be affected by the plasticisation of the inner layer of the vessel.

7.1 Introduction

The introduction of compressive residual stresses, e.g. by means of an autofrettage process, is a common strategy in industry for the improvement in fatigue life of high-pressure vessels. The application of autofrettage process in a vessel, storing hydrogen at 70 MPa, is evaluated here. Compressive stresses make difficult the entry of hydrogen in the metal lattice, however the produced plastic strain might be related to the creation of trapping sites for hydrogen. The balance between these two phenomena is analysed. In addition, the likely presence of notches is considered since stress concentrators increase the level of hydrostatic stress and plastic deformation, thus rising hydrogen content in the vicinity of the notch. A pressure vessel is simulated with the Finite Element method combining a static stress-strain analysis with a steady-state hydrogen diffusion analysis. Both autofrettage process and service life are simulated, and a notch is introduced in the inner surface of the vessel. Results indicate that, for each of the considered notch depths, autofrettage pressure must be limited in order to avoid high hydrogen concentrations, thus reducing the efficiency of the autofrettage process.

This phenomenon is strongly dependent on the binding energy of trapping sites created by plastic strain.

Chromium-Molybdenum (Cr-Mo) steels have been proposed as possible candidates for metallic pressure vessels, as mentioned in 0. A high yield stress allows the reduction of the thickness and thus the weight of the vessel. However, it has been proved that the higher the steel strength, the higher the hydrogen embrittlement susceptibility. Here a 4130 steel is chosen because its behaviour in hydrogen environments has been extensively studied.

From a quantitative and macroscopic point of view, hydrogen damage is characterised by a decrease in toughness, an increase in crack growth rate, a modification in the yield strength, etc. The ratio between these material resistance parameters in air and those in a hydrogen atmosphere will depend on the aggressiveness of the environment. Undoubtedly, gaseous H_2 at 2 MPa will be less deleterious than at 20 MPa; likewise, a cathodic charging at 0.1 V will be less damaging that at 1 V. Those external variables are related with adsorption and absorption phenomena at the metal surface, but the variable expected to govern embrittlement independently of the environment is hydrogen concentration. In the present work, durability is analysed in the long term so the steady-state distribution is sought.

In the traditional approach, Fick's Laws consider that at steady state hydrogen distribution will be uniform and equal to the equilibrium concentration. However, the stress state can shift the maximum concentration at a certain distance from surface because of the presence of a hydrostatic stress peak. In addition, hydrogen might be retained in lattice defects in which the potential energy is lower than in the perfect lattice, i.e. in trapping sites. The enhancement of hydrogen concentration caused by tensile hydrostatic stress and traps has been empirically demonstrated by Nagao et al. (Nagao, Kuramoto, Ichitani, & Kanno, 2001). On the other hand, when residual compressive stresses are present the lattice is compressed and the chemical potential is higher than in the unstressed lattice. The effect is a reduction in hydrogen concentration in lattice sites.

Takakuwa et al. (Takakuwa, Nishikawa, & Soyama, 2012) have simulated hydrogen diffusion near a crack tip in the presence of compressive residual stress, however they do not include trapping effects. Few attempts to introduce residual stresses in order to mitigate

hydrogen embrittlement have been carried out. For example, Takakuwa et al. (Takakuwa & Soyama, 2012) demonstrate the beneficial effect of cavitation peening to reduce the hydrogen-assisted crack growth.

Moreover, permeation tests in iron and various steels have revealed that the number of trapping sites is related with plastic strain (A. J. Kumnick & H. H. Johnson, 1980). This has been discussed in 2.5.4. As a consequence, autofrettage will certainly increase the number of traps as the vessel surface yields and dislocations are created. Thus, there is a competition between plastic strain creating traps for hydrogen and compressive residual stress reducing hydrogen concentration in lattice sites. The competition will be discussed in order to optimise the autofrettage process for hydrogen storage vessels. In addition, the role of compressive stresses will be analysed considering different notches in the inner surface of the vessel. Numerical assessment of the hydrogen content is carried out by means of surface responses where the variables are the notch depth and the autofrettage pressure.

7.2 Hydrogen diffusion model

The aim of diffusion models is to find hydrogen concentrations for different times and thickness locations, i.e. $C(x,t)$, where x is a material point in the bulk metal and t is the service time. Due to the presence of compressed stored hydrogen in the inner surface, there is a concentration gradient in the vessel thickness so a flux is established and hydrogen permeates from the inner to the outer surface. In addition, stress-strain state drifts the diffusion equations.

7.2.1 Parameters and boundary concentration

In the present Chapter a steady state analysis is carried out so the time-scale is meaningless. This does not imply that concentration is constant along the thickness because there is a non-uniform stress-strain distribution due to the internal pressure history. In addition, hydrogen pressure will affect directly to the H_2 dissociation process and hence to the boundary conditions of diffusion. Following the same mathematical procedure explained in Section 3.3:

$$C_L(x \in \mathcal{B}) = K \exp\left(\frac{\bar{V}_H \sigma_h(x \in \mathcal{B})}{RT}\right)\sqrt{f_{H_2}} \tag{7.1}$$

It can be seen that boundary concentration will be explicitly related to the hydrostatic stress in the entry surface $\sigma_h(x \in \mathcal{B})$. Fugacity is a measure of chemical activity which is related with pressure p_{H_2} by means of the Abel-Nobel equation (Marchi et al., 2007):

$$f_{H_2} = p_{H_2} \exp\left(b\frac{p_{H_2}}{RT}\right) \tag{7.2}$$

The b constant accounts for the non-ideal behaviour of gases. At low pressures $f_{H_2} \to p_{H_2}$, but for the present situation (p_{H_2}= 70 MPa) fugacity is 1.238 times the pressure (f_{H_2}= 121 MPa). In the performed simulations p_{H_2} corresponds to the working pressure during service ($p_{H_2} = p_w$).

Diffusivity D_L and solubility K have been obtained in references (Nelson & Williams, 1973; San Marchi & Somerday) for a quenched and tempered 4130 steel. They follow Arrhenius-type expressions, i.e. with a pre-exponential factor and activation energy as fitted magnitudes. Although permeation tests were performed at high temperatures, values are extrapolated to room temperature (298 K). Apparent diffusivity from (Nelson & Williams, 1973) is assumed as lattice coefficient D_L because its value is very close to that found for pure iron (A. H. M. Krom et al., 1999), showing a little trapping influence in these permeation tests. Partial molar volume $\bar{V}_H$ of hydrogen in steel is taken as $2 \cdot 10^{-6}$ m^3/mol (A. H. M. Krom et al., 1999). Number of lattice sites N_L is obtained assuming a bcc structure for martensite (for carbon content less than 0.6 mass % (Sherby et al., 2008)) and tetrahedral preferred occupancy (A. H. Krom & A. Bakker, 2000). All parameters are shown in Table 7-1:

Table 7-1. Diffusion parameters for AISI 4130 steel.

D_L (mm^2/s)	0.0141
K (atH·mm^{-3}MPa$^{-1/2}$)	2.09×10^{12}
N_L (sites/mm^3)	5.09×10^{20}
$\bar{V}_H$ (mm^3/mol)	2000

7.2.2 Hydrogen trapping

The amount of trapped hydrogen is obtained considering the equilibrium between the two sites, which means that hydrogen concentration in trapping sites can be found explicitly once C_L is known. Assuming, as before, low lattice occupancy:

$$C_T = \frac{N_T}{1 + \frac{N_L}{C_L \exp\left(\frac{E_b}{RT}\right)}} \tag{7.3}$$

Results shown in following simulations consider the expression obtained by Kumnick and Johnson for pure iron (A. J. Kumnick & H. H. Johnson, 1980). However, an important matter of discuss is the trapping behaviour with compressive and reverse yielding. In the present work, isotropic hardening is considered so the occurrence of reverse yielding (during unloading) is difficult to happen. However, if Bauschinger effect is taken into account, yield limit in compression will be lower so a reverse yielding is likely to occur. In this case, asymmetry of dislocation behaviour in tension-compression also might affect hydrogen diffusion and embrittlement and should be better understood to assess hydrogen enhanced fatigue.

As the objective of the present Chapter is to study how plastic strain in autofrettage can influence the hydrogen uptake and diffusion, binding energy is taken as the binding energy of a dislocation. Kumnick and Johnson found a binding energy of trapping sites in bcc iron equal to 61 kJ/mol (A. J. Kumnick & H. H. Johnson, 1980). This high value contrasts with values found by other authors for the binding energy of a dislocation. There is a lot of discrepancy between the binding energies for traps in cold-worked ferrous alloys, ranging from 20 kJ/mol up to 60 kJ/mol (Michihiko Nagumo, 2016). Even a small variation in the binding energy promotes a huge variation in trapping concentration because the exponential term appearing in the equilibrium constant K_T.

For a tempered martensite, the predominant phase in the chosen AISI 4130 steel, a E_b of 33.9 kJ/mol has been found (F.-G. Wei & Tsuzaki, 2005). However, due to the uncertainty in

the binding energy of traps, simulations are carried out with three different values (30, 45 and 60 kJ/mol) in order to evaluate the influence of this factor.

7.3 Vessel modelling

A full metal vessel (Type I) is proposed as stationary system for hydrogen storage. Its geometry consists of a cylindrical tank which closuring end caps have not been modelled. A 4130 steel is selected with the following mechanical parameters:

Yield strength σ_0 and ultimate tensile strength σ_u have been obtained in reference (Song & Shieh, 2004) where steel AISI 4130 was quenched in oil to room temperature and then tempered at 450ºC for 1.5 hours obtaining thus a tempered martensite microstructure. Young's modulus E, Poisson's coefficient ν and hardening exponent n are chosen as usual for steels. The hardening behaviour will be modelled with a power law, as shown in equation (3.59).

Table 7-2. Mechanical parameters for AISI 4130 steel.

E (MPa)	210000
ν	0.3
σ_0 (MPa)	1186
σ_u (MPa)	1289
n	0.2

Optionally, hoop stresses might be taken as the design stress for the thickness selection. More precise calculations consider the von Mises equivalent stress. Here the design criteria indicated in the BPVC, ("Boiler and Pressure Vessel Code. Section VIII Division 1. ASME ", 2010) are followed. The thickness t must be chosen to resist the working pressure p_w as well as the pressure test which is 1.5 times the working pressure; for the proof load, the thickness must fulfil the next condition:

$$t_w \geq r_i \left[\sqrt{\frac{\sigma_0 + 1.5\, p_w}{\sigma_0 - 1.5\, p_w}} - 1 \right] \tag{7.4}$$

As previously mentioned, a working pressure p_w of 70 MPa has been chosen. Fixing the inner radius r_i = 500 mm, thickness must be greater than 46.41 mm for the proof load and greater than 65.33 for the burst load. Vessel is thus designed with a 66 mm thickness. Load history is the fundamental input parameter as it governs stress-strain distribution and also the hydrogen fugacity during storage stage, as seen in the previous Chapter.

Material behaviour is considered as rate-independent and hydrogen is analysed after the steady state is reached so the time scale is neglected. The slopes in pressure history are just introduced in the simulations due to convergence issues and depicted in Figure 1 with illustrative purposes. The scheme just tries to represent the loading-unloading-service sequence. It must be noted that neither a pressure test nor a burst test are simulated even if they could produce significant residual stresses.

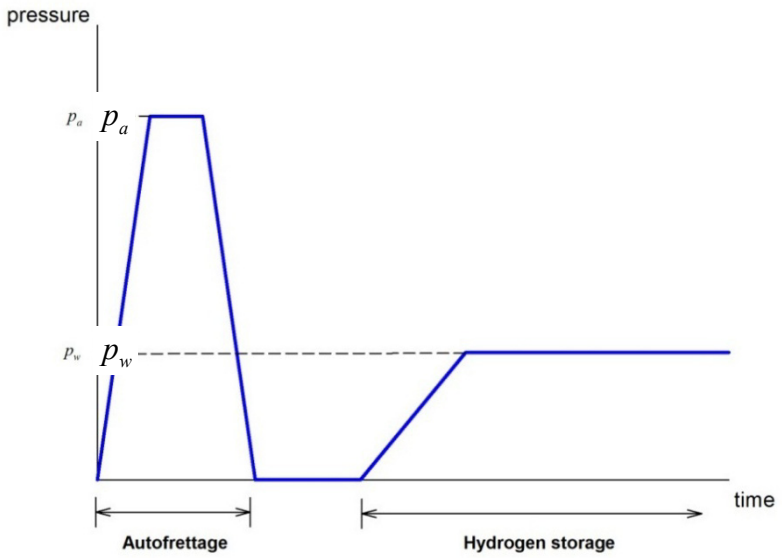

Figure 7-1. Internal pressure history.

7.3.1 Vessel without defects

In many cases, pressure vessel design still relies in the use of analytical formulas for cylindrical tubes. An internal pressure is considered which might be the autofrettage pressure in the manufacturing process p_a or the hydrogen pressure during storage, named as working pressure p_w. In both cases an outer pressure is zero. Analytical expressions of the stress-strain field will depend on whether the internal pressure produces yielding or not. For the elastic case, i.e. not yielding, the radial, hoop and axial stress in the vessel, σ_θ^*, σ_r^* and σ_z^*, respectively, are:

$$\sigma_\theta^* = \frac{p_a}{r_o^2 - r_i^2} r_i^2 \left(1 + \frac{r_o^2}{r^2}\right) \tag{7.5}$$

$$\sigma_r^* = \frac{p_a}{r_o^2 - r_i^2} r_i^2 \left(1 - \frac{r_o^2}{r^2}\right) \tag{7.6}$$

$$\sigma_z^* = \frac{p_a}{r_o^2 - r_i^2} r_i^2 \tag{7.7}$$

Those equations give a stress distribution depending on the distance r to the centre of the cylinder, where r_o is the outer radius and r_i is the inner radius. However, autofrettage pressure p_a is high enough to always produce yielding in an inner layer of the vessel; as a consequence, the elastic equations have to be modified in this plastic region. Some attempts have been made to obtain analytical expressions of residual stresses in different situation. However, the mathematical process is long and the analytical stresses are complex. Thus some simplifications are taken. For instance, Alegre et al. take the Tresca yielding criterion and consider an elastic-perfectly plastic material (Alegre et al., 2007). In contrast, Huang (Huang, 2005) uses Von Mises criterion and take into account a power law hardening, but he assumes incompressible volume, which may not be a good approach for steels. Gao et al. (X.-L. Gao, 1993) have obtained autofrettage residual stress distributions for large strains and with different assumptions: open and close ends, spherical and cylindrical tanks. They even have included Strain Gradient Plasticity (SGP) theories of plasticity in the elasto-plastic analysis (X. L. Gao, 2003) but the assumption there is also incompressibility. SGP theories predict that hydrogen concentration dramatically increases in the crack tip so there must be

consider in future works. Here, the Von Mises yielding criterion is used. Hardening is modelled with a power law:

$$\sigma_{ys} = \sigma_0 \left(1 + \frac{E}{\sigma_0}\varepsilon^p\right)^n \tag{7.8}$$

where σ_{ys} is the yield stress correspondent to each level of equivalent plastic strain ε^p. Because of unloading, the inner layer that has yielded before enters in a compressive stress state. Whether unloading produces yielding or not will depend on the yield stress on compression. The hardening behaviour is classified in isotropic or kinematic, or a combination of both, and has a great influence in this reversible yielding. In a high-pressure vessel designed to store gaseous hydrogen, the working pressure is around 70 MPa, so the autofrettage pressure does not need to be extremely high, and unloading is unlikely to cause reverse yielding. Thus, in this autofrettage simulation it is supposed that unloading stresses are elastic along the thickness and the residual stresses are:

$$\boldsymbol{\sigma}^{res} = \boldsymbol{\sigma}^{load}(p_a) + \boldsymbol{\sigma}^*(-p_a) \tag{7.9}$$

where $\boldsymbol{\sigma}^*(-p_a)$ is an elastic stress state, which components are shown in Equations (7.5), (7.6) and (7.7), due to the unload process, i.e. correspondent to a negative pressure. Stress produced during loading, $\boldsymbol{\sigma}^{load}(p_a)$, causes plasticization of an inner layer which is usually called yield radius. Because thickness is chosen to avoid yielding during service life, the final stress state of the hydrogen vessel is the sum of the residual stresses and those elastic produced by the working pressure:

$$\boldsymbol{\sigma} = \boldsymbol{\sigma}^{res} + \boldsymbol{\sigma}^*(p_w) \tag{7.10}$$

Simulations of autofrettage and hydrogen storage have been performed with the commercial Finite Element code ABAQUS. Results of hoop and hydrostatic stress are plotted in Figure 2 and Figure 3, respectively. In both figures, dashed lines represent the residual stress distribution while solid lines show the stress state during service life. The latter is directly related to hydrogen distribution in the steady state.

It is also possible to consider the softening induced by hydrogen, by means of a coupling parameter between local plastic flow and hydrogen concentration (Kotake et al., 2008). However, yielding occurs mainly during autofrettage process when steel is not in a hydrogen environment, so this local softening is not included here.

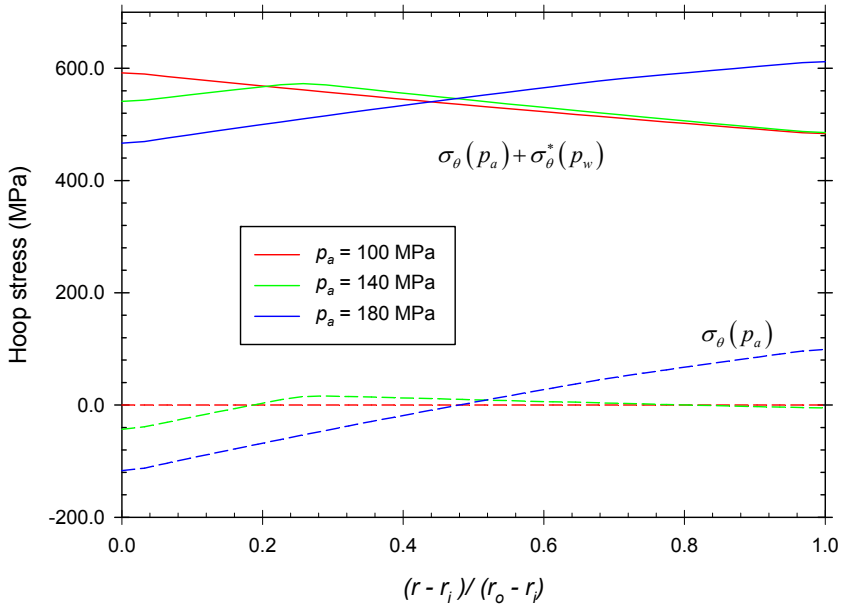

Figure 7-2. Hoop stress σ_θ along the vessel thickness depending on the autofrettage pressure. Dashed lines represent residual stress and solid lines represent the hoop stress during the service life.

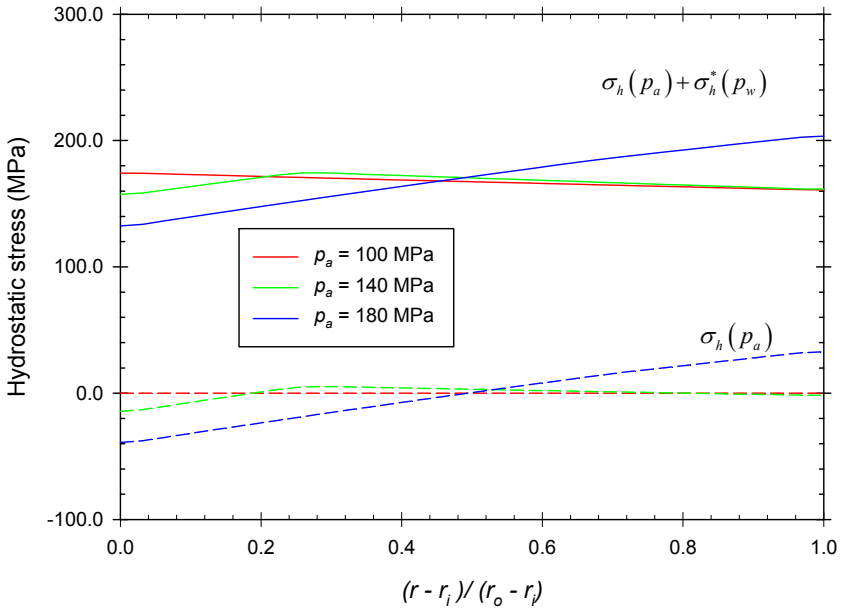

Figure 7-3. Hydrostatic stress σ_h along the vessel thickness depending on the autofrettage pressure. Dashed lines represent residual stress and solid lines represent the hoop stress during the service life.

7.3.2 Notched vessel

Residual stresses might deviate severely from the predictions made by analytical expressions in which most of design procedures still rely; in these cases, a numerical simulation is needed. This is especially critical in both analysed phenomena: during autofrettage-induced residual stress and plastic strain modelling, and in the process of calculating hydrogen concentration near a notch. The beneficial effect of autofrettage on the tensile stress concentration, and thus on fatigue life, has been studied for cracked spherical vessels (Perl & Steiner, 2016) , for evacuators in tubes (Parker & Underwood, 1996), for cross-bores in cylinders (Hameed, Brown, & Hetherington, 2004), etc. Even without bores or evacuators, minor defects are always present in pressure vessels due to welding or to other manufacturing processes. These stress concentrators might affect fracture and fatigue behaviour. The expected presence of these defects is here considered with the introduction of semi-circular notches in the inner surface of the vessel; the semi-circular notch in the 2D model represents a semi-cylindrical stress concentrator along the longitudinal axis of the 3D vessel. Three

notch depths L_n (or, equivalently, notch radius) are analysed: 0.1 mm, 0.5 mm and 0.9 mm of the vessel thickness. The geometry of the Finite Element model is shown in Figure 4.

7.4 Results and discussion

The influence of autofrettage pressure and notch depth on hydrogen content is analysed. In order to evaluate a proper range of values and optimise the number of simulations performed, a design of experiments based on response surfaces is created (Cuesta, Lorenzo, & Alegre, 2014). Each "experiment" corresponds here to a Finite Element simulation with a given geometry (L_n) and input parameters (p_a, E_b). The response surface is then analysed with the purpose of finding an optimum autofrettage pressure for each specific situation.

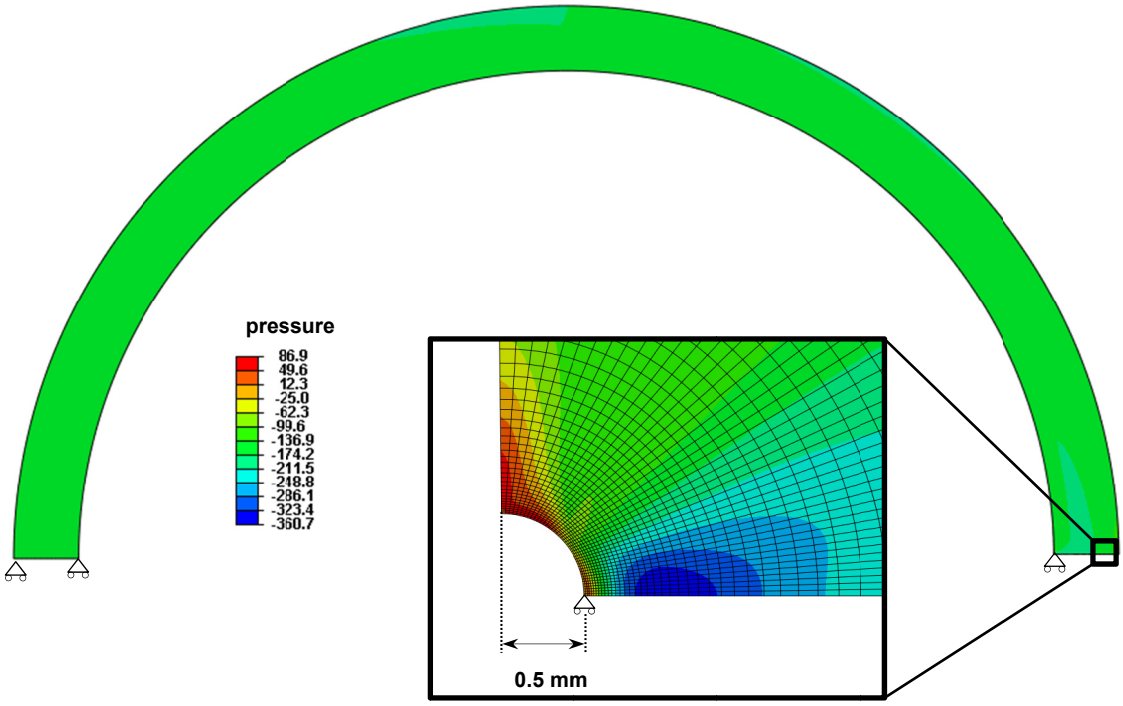

Figure 7-4. Geometry and hydrostatic stress during service for p_a = 140 MPa. Detail shows notch geometry and mesh for L_n = 0.5 mm. Note that here compressive stresses are positive (i.e. $p = -\sigma_h$)

The variable governing damage is assumed as the maximum concentration in the vicinity of the notch. Some authors consider that decohesion is triggered by interstitial hydrogen and thus the C_L should be the critical variable. However, trapped hydrogen in grain boundaries

might also affect grain boundary decohesion; in addition, hydrogen near a dislocation enhances its mobility and might cause fracture due to strain localization. Therefore, the implementation of each concentration in Damage models, e.g. Cohesive Zone Models modified by hydrogen, is not straightforward. In the present work two peaks are analysed: maximum lattice hydrogen concentration C_L^{max} and maximum hydrogen total concentration C_{tot}^{max}. Depending on the character of the trapping sites the influence of each concentration on fracture should be discussed in further detail. For instance, Dadfarnia et al. (M. Dadfarnia et al., 2011) studied hydrogen interaction with multiple traps analysing their beneficial or detrimental effect, concluding that traps can act as sources or sinks depending on their irreversibility.

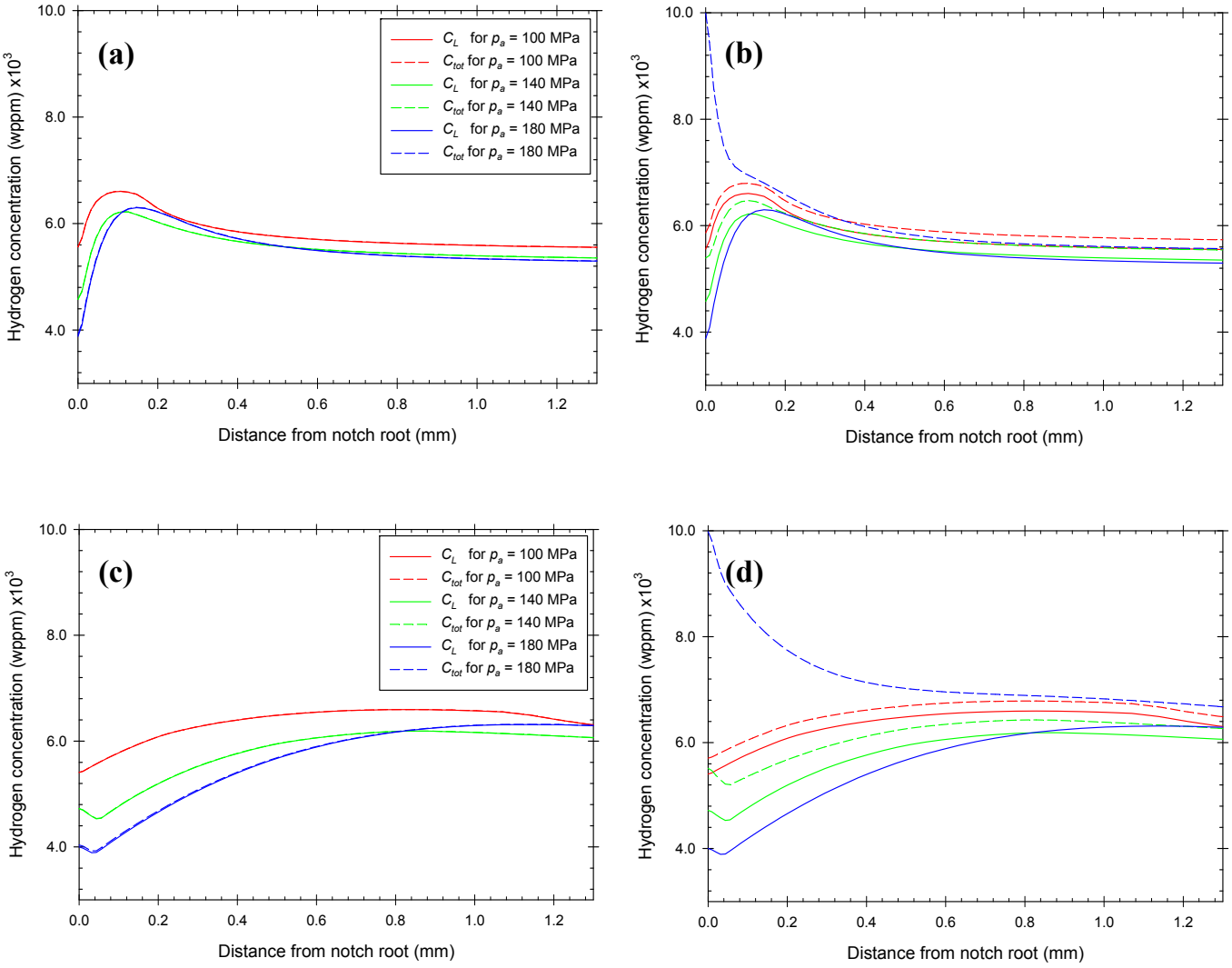

Figure 7-5. Lattice hydrogen concentration and total hydrogen concentration near the notch root for: (a) L_n = 0.1 mm and E_b = 30 kJ/mol; (b) L_n = 0.1 mm and E_b = 60 kJ/mol; (c) L_n = 0.9 mm and E_b = 30 kJ/mol; (d) L_n = 0.9 mm and E_b = 60 kJ/mol.

The designed experiment consists of two response surfaces (C_L^{max} and C_{tot}^{max}) and two variable parameters (L_n and p_a). The range of variation of $L_n$and p_a is shown in Table 3, and those limits are coded into the [-1,1] range in order to normalise the design of experiments. For a cubic domain, the coding of X_i (real values) into x_i (in the [-1,1] range) might be expressed as:

$$x_i = \frac{2\left(X_i - \tilde{X}\right)}{X_{iNSup} - X_{iNInf}} \qquad i = L_n^*, p_a^* \tag{7.11}$$

where X_{iNInf} is the lower real limit, X_{iNSup} is the upper real limit and $\tilde{X}$ is the mean of the lower and upper limits, corresponding to each variable i.

Table 7-3. Variable parameter range in the interval [-1, 1].

Variable	**Range**
L_n (mm)	[0.1, 0.9]
p_a (MPa)	[100, 180]

The two response surfaces C_L^{max} and C_{tot}^{max}, are thus determined by the parameters L_n and p_a, Those responses are extracted from the hydrogen distribution near the notch obtained in the Finite Element simulation and shown in Figure 5 for the range limits. The relationship that exists among the two parameters and the values of the response surfaces can be expressed as $f(L_n, p_a)$, where f is postulated as a quadratic model of the form expressed in the follwing equation:

$$f(L_n, p_a) = b_0 + b_1 L_n + b_2\, p_a + b_{11} L_n^2 + b_{22}\, p_a^2 + b_{12} L_n\, p_a \tag{7.12}$$

The coefficients of the function $f(L_n, p_a)$ for each simulation result (C_L^{max} and C_{tot}^{max}) are estimated by means of a design experiment analysis using Statgraphics XVII software ("Statgraphics Centuron XVII," 2014). The main features of this design are:

- The use of two experimental factors, in this case the input simulation parameters L_n and p_a.
- A cubic domain.
- The coding of the value of intervals for the two factors listed in Table 7-3 using expression (7.11).
- The cubic experiment matrix with three levels for each factor

The use of expression (7.12) to fit the two response surfaces.Table 7-4, Table 7-5 and Table 7-6 show both the experiment matrix with the coded variables and the matrix for the experimentation plan with the values of the experiment design factors proposed for determining the coefficients of the function $f(L_n, p_a)$. Performed simulations, following the methodology exposed in previous sections, give the responses $C_L^{max}$and C_{tot}^{max} which correspond to $f(L_n, p_a)_{C_L^{max}}$ and $(L_n, p_a)_{C_{tot}^{max}}$, respectively. The fitted coefficients are show in Table 7-7.

Table 7-4. Design of experiments performed for E_b = 30 kJ/mol.

Experiment NUM.	Experiment Matrix		Experimentation Plan		Responses	
	L_n^*	p_a^*	L_n (mm)	p_a (MPa)	C_L^{max} (wppm)	C_{tot}^{max} (wppm)
1	-1	-1	0.1	100	6.604×10^{-3}	6.606×10^{-3}
2	-1	0	0.1	140	6.220×10^{-3}	6.222×10^{-3}
3	-1	1	0.1	180	6.299×10^{-3}	6.304×10^{-3}
4	0	-1	0.5	100	6.601×10^{-3}	6.603×10^{-3}
5	0	0	0.5	140	6.203×10^{-3}	6.205×10^{-3}
6	0	1	0.5	180	6.309×10^{-3}	6.313×10^{-3}
7	1	-1	0.9	100	6.595×10^{-3}	6.597×10^{-3}
8	1	0	0.9	140	6.188×10^{-3}	6.191×10^{-3}
9	0	1	0.9	180	6.313×10^{-3}	6.317×10^{-3}

Table 7-5. Design of experiments performed for E_b = 45 kJ/mol.

Experiment NUM.	Experiment Matrix		Experimentation Plan		Responses	
	L_n^*	p_a^*	L_n (mm)	p_a (MPa)	C_L^{max} (wppm)	C_{tot}^{max} (wppm)
1	-1	-1	0.1	100	6.604×10^{-3}	6.757×10^{-3}
2	-1	0	0.1	140	6.220×10^{-3}	6.422×10^{-3}
3	-1	1	0.1	180	6.299×10^{-3}	8.225×10^{-3}
4	0	-1	0.5	100	6.601×10^{-3}	6.753×10^{-3}
5	0	0	0.5	140	6.203×10^{-3}	6.398×10^{-3}
6	0	1	0.5	180	6.309×10^{-3}	8.450×10^{-3}
7	1	-1	0.9	100	6.595×10^{-3}	6.747×10^{-3}
8	1	0	0.9	140	6.188×10^{-3}	6.381×10^{-3}
9	0	1	0.9	180	6.313×10^{-3}	8.290×10^{-3}

Table 7-6. Design of experiments performed for E_b = 60 kJ/mol.

Experiment NUM.	Experiment Matrix		Experimentation Plan		Responses	
	L_n^*	p_a^*	L_n (mm)	p_a (MPa)	C_L^{max} (wppm)	C_{tot}^{max} (wppm)
1	-1	-1	0.1	100	6.604×10^{-3}	6.794×10^{-3}
2	-1	0	0.1	140	6.220×10^{-3}	6.473×10^{-3}
3	-1	1	0.1	180	6.299×10^{-3}	9.991×10^{-3}
4	0	-1	0.5	100	6.601×10^{-3}	6.790×10^{-3}
5	0	0	0.5	140	6.203×10^{-3}	6.447×10^{-3}
6	0	1	0.5	180	6.309×10^{-3}	1.021×10^{-2}
7	1	-1	0.9	100	6.595×10^{-3}	6.784×10^{-3}
8	1	0	0.9	140	6.188×10^{-3}	6.430×10^{-3}
9	0	1	0.9	180	6.313×10^{-3}	9.981×10^{-3}

Table 7-7. Coefficients of the functions $f(L_n, p_a)$.

	C_L^{max}	C_{tot}^{max} for E_b = 30 kJ/mol	C_{tot}^{max} for E_b = 45 kJ/mol	C_{tot}^{max} For E_b = 60 kJ/mol
Coefficient	Value	Value	Value	Value
b_0	9.794×10^{-3}***	9.819×10^{-3}***	1.761×10^{-2}***	2.487×10^{-2}***
b_1	-3.020×10^{-5}	-7.396×10^{-5}	2.292×10^{-4}	4.331×10^{-4}
b_2	-4.749×10^{-5}***	-4.765×10^{-5}***	-1.8×10^{-4}***	-3.047×10^{-4}***
b_{11}	0.0	0.0	-3.958×10^{-4}	-4.593×10^{-4}
b_{22}	1.5625×10^{-7}***	1.5625×10^{-7}***	7.10417×10^{-7}***	1.234×10^{-6}***
b_{12}	1.5625×10^{-7}	4.6875×10^{-7}	1.25×10^{-6}	0.0

99% confidence level: * If the number is <5; ** If the number is <1; *** If the number is <0.1

Once the coefficients have been found, response surfaces might be plotted in 3D with coloured contours. Horizontal x-axis represents the notch size L_n, horizontal y-axis represents the autofrettage pressure p_a, and the vertical z-axis corresponds to the maximum total concentration C_{tot}^{max}. Maximum lattice concentration is not shown because, being unclear which variable plays a more important role in hydrogen-assisted fracture, total concentration is analysed. Contours show that there is a minimum region, tending to dark blue, for every considered binding energy. Therefore, an optimum autofrettage pressure might be found between 120 and 140 MPa. Binding energy has a strong effect on hydrogen trapping and so in maximum concentration: for weak defects (E_b = 30 kJ/mol) autofrettage pressure can be higher, optimising thus the fatigue life improvement while for irreversible traps (E_b = 60 kJ/mol) concentrations will be higher and the optimum autofrettage pressure is lower. On the other hand, it can be concluded that the notch depth has little influence on maximum concentration, at least for the considered semi-circular shape.

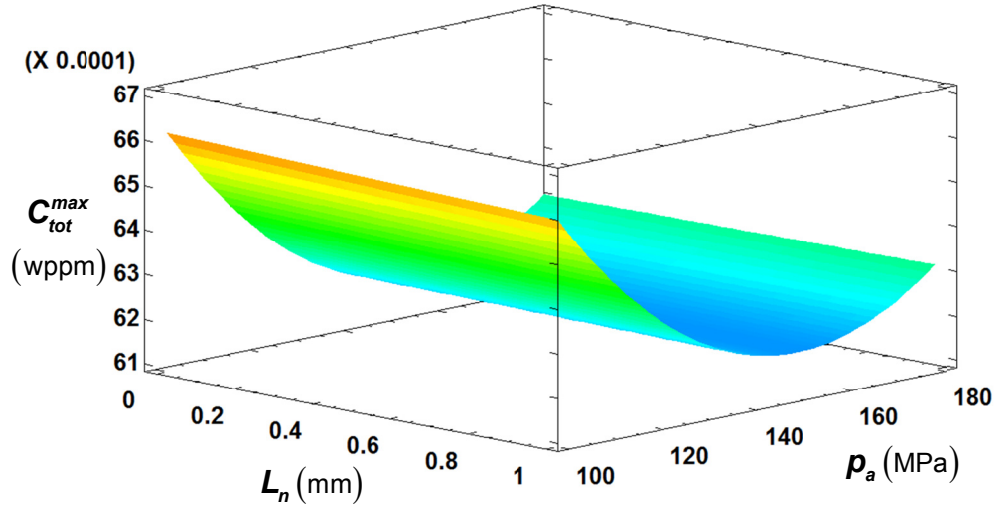

Figure 7-6. C_{tot}^{max} response surface for E_b = 30 kJ/mol.

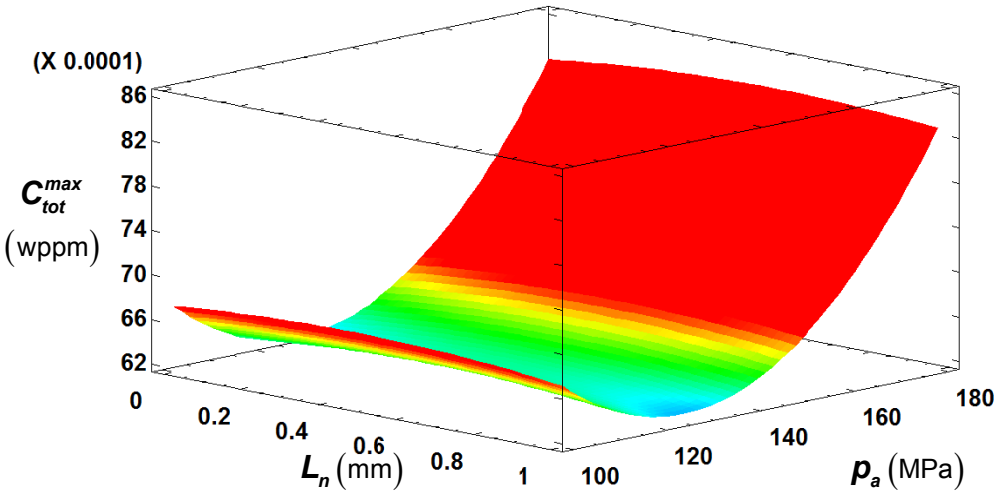

Figure 7-7. C_{tot}^{max} response surface for E_b = 45 kJ/mol.

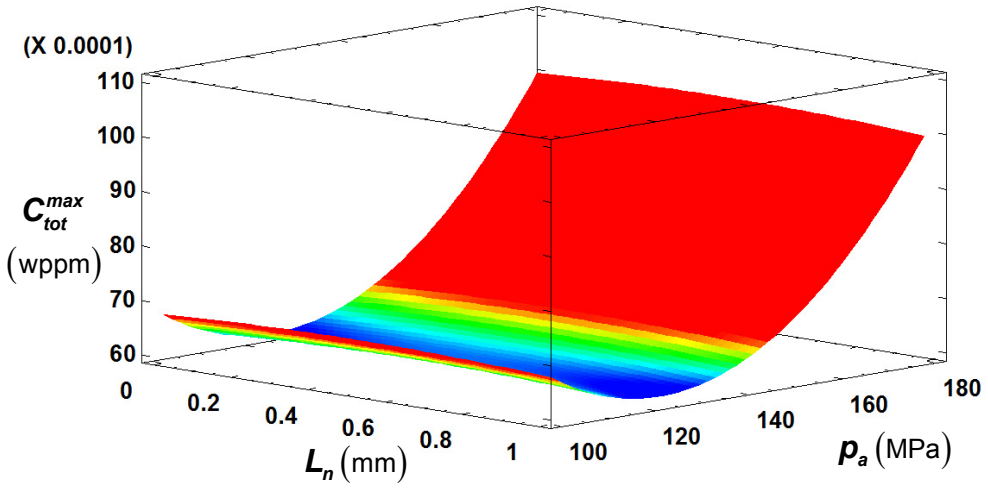

Figure 7-8. C_{tot}^{max} response surface for E_b = 60 kJ/mol.

7.5 Conclusions

The beneficial effect of introducing compressive residual stresses has been demonstrated numerically. The physical phenomenon underlying this effect is the increase in lattice chemical potential due to compressive hydrostatic stress. In addition, trapping effects have been considered and a parametric study has been performed. Results show, as expected, that total concentration is higher for irreversible traps with 60 kJ/mol.

The presence of notches has been considered as hydrogen tends to be located in regions of stress concentration. In addition, the plastic strain produced in the notch tip will affect the creation of traps. A semi-circular notch is introduced with three different notch depths. Results of response surfaces indicate that depth, i.e. notch radius, it is not a significant parameter for this notch shape.

The methodology of response surface is also a useful tool for finding an optimum autofrettage pressure. Here, “optimum” means the pressure which produces a lower hydrogen concentration; it is difficult to establish which location of hydrogen, i.e. in lattice sites, in trapping sites or in both, is the most detrimental for fracture. If lattice hydrogen is the

responsible of decohesion and embrittlement, autofrettage pressure might be higher because plastic strain does not increase this concentration. On the contrary, if total hydrogen damages the material, traps created by dislocations are multiplied with autofrettage and the optimum pressure will be lower. In the latter case, an optimum pressure between 120 MPa (for strong traps) and 140 MPa (for weak traps) has been found, as shown in the response surfaces plotted in Figure 7-6, Figure 7-7 and Figure 7-8.

Chapter 8 Conclusions and future work

In this Chapter, some conclusions are summarised related to hydrogen diffusion modelling, fracture simulations, and the practical application to pressure vessels. Finally, future research, on numerical modelling and the associated experimental work, is foreseen here.

8.1 Conclusions

Although hydrogen embrittlement in different materials has been documented and studied for a century, mechanisms by which it is produced are not yet entirely clear. Therefore, the hydrogen-metal interaction should be best described to elucidate these mechanisms and to predict possible failures. The emerging technologies of hydrogen as an energy carrier require a qualitative and quantitative modelling in order to optimise the use of fuel cells and hydrogen storage vessels. In this context, combining modelling with experimental results will allow the selection of less susceptible alloys.

As a first stage in the prognosis and mitigation of hydrogen-related failure of metals, this thesis has focused on hydrogen diffusion modelling near a crack tip. In particular, a consistent numerical methodology has been presented with the purpose of collecting, implementing and critically discussing the existent models for hydrogen diffusion in metals. From the results presented, some particular conclusions might be summarised:

8.1.1 Hydrogen diffusion near a crack tip

- Simulations of hydrogen transport in a crack tip must include the hydrostatic stress as a driving variable, since it modifies the chemical potential. Two consequence of this drift diffusion term have been observed:
  - The appearance of a peak in hydrogen concentration in lattice sites shifted some micro-meters from the surface. This fact could be associated to the location of the Fracture Process Zone in hydrogen-related failures.
  - At boundaries, constant concentration given by Sievert's law must be modified in order to account for the superficial lattice expansion when hydrostatic stress is not zero.

- Level of plastic strain is always associated with an increase in the number of traps, causing the creation of defects in the form of dislocations. Including equivalent plastic strain as an internal state variable within diffusion equations, strain field in the crack tip predicts a peak in trapped hydrogen concentrations. This maximum is always located in the surface, in contrast with lattice hydrogen peak.

- The concept of trap comprises many defect types in a metal lattice (e.g. grain boundaries, inclusions, vacancies, etc.) that are not a direct consequence of plastic deformation. In addition, each trap has a different associated binding energy. Both the concentration of each type of trap within the bulk material and its corresponding energy characteristics should be better studied at some point in the future.

- Thermodynamic equilibrium firstly proposed by Oriani is usually assumed in literature on hydrogen diffusion modelling near a crack tip. McNabb and Foster kinetic formulation is usually relegated to TDS simulations, in which the heating rate promotes a faster capture and release processes. However, it has been demonstrated in the present work that for some values of trap energies, trap densities or hop frequencies, results differ substantially between equilibrium and non-equilibrium predictions near a crack tip at constant temperature.

- Commercial Finite Element codes usually possess a wider range of capabilities for heat transfer than for mass diffusion; thus, as a strategy for the numerical implementation of diffusion equations, the analogy between transport phenomena, in this case between mass diffusion and heat transfer, has been exploited.

- Inserted hydrogen causes a dilatation that can be modelled through and imposed volumetric deformation. It has been shown how this effect can be neglected for steels. Nevertheless, for other crystalline structures might be critical.

- Milestones in hydrogen diffusion modelling have been revisited. Starting from Sofronis and McMeeking, 1989, a Modified Boundary Layer approach has been revisited by many authors. It can be concluded that this progressive benchmarking over decades has been fundamental for the advances in hydrogen diffusion modelling, especially since experimental verification is hard to be performed.

- The consideration of local softening or hardening has some influence on diffusion, i.e. on the hydrogen concentration distributions near the crack tip. However, quantifying this effect is tricky since the concentration-dependent hardening law is phenomenological and has not been verified.

8.1.2 Hydrogen Assisted Fracture modelling

- Cohesive Zone Models have been demonstrated to be a powerful tool for fracture simulations. In the case of hydrogen embrittlement, transition from ductile to brittle behaviour is implemented by means of a modification in the Traction Separation Law (TSL). In the present work, a reduction in the cohesive energy (area under the curve) has been considered. In addition, local triaxiality effects have been implemented.

- Force – displacement curves, or stress – strain curves, have shown how a locally-informed cohesive model is able to account for hydrogen and triaxiality effects also in a macroscopic scale, i.e. in the simulated notched tensile test.

- In relation to the local softening/ hardening promoted by hydrogen, more efforts should be made to link hardening curves with the interaction between hydrogen and dislocation behaviour. The theory known as Hydrogen Enhanced Localised Plasticity (HELP) could be connected to a modification in plastic laws, leading to plastic instabilities, a void growth acceleration or an enhanced void coalescence.

- In order to introduce a physical-based fracture energy reduction, an expression that consider hydrogen enhanced decohesion from first principles has been taken from literature and implemented. Therefore, a competition between plasticity enhancement (HELP theory) and decohesion (HEDE) can be investigated with the present approach.

8.1.3 Diffusion in high pressure vessels for H_2 storage

- In high pressure vessels storing H_2, load amplitude is a crucial magnitude in hydrogen diffusion: the smaller is the amplitude, the faster the maximum steady state concentration is achieved for a fixed maximum pressure. Frequency is also an important parameter: as shown in some fatigue tests (Matsuoka, Tanaka, Homma, & Murakami, 2011), steels are less embrittled at high frequencies because there is not enough time for hydrogen to diffuse towards the Fracture Process Zone. Results also indicate that the higher the frequency, the lower the maximum concentration reached.
- Hydrogen storage may be enhanced by those manufacturing technologies that introduce compressive residual stresses, since hydrogen diffusion will be prevented and embrittlement might be mitigated. Autofrettage is a common process in industry which allows the improvement of fatigue life: vessels are subjected to a certain pressure, greater than the working pressure, and the plasticization of an inner layer produces a residual compressive stress state. Therefore, the use of autofrettage to the manufacturing of hydrogen storage tanks of Type I has been validated.

- Storing H_2 at 70 MPa is a challenging process since very high strength steel should be introduced in order to reduce vessel thickness and weight. An AISI 4130 steel has been simulated. However, the characterization of trapping sites is really complex and there is uncertainty in the binding energy of traps.
- The lack of empirical data on the interaction between autofrettage and hydrogen diffusion is one of the limitations of the present work. Additionally, results are difficult to extrapolate to other vessel types or geometries. However, the numerical methodology shown has the purpose of linking an industrial process in vessel manufacturing with the basics of hydrogen diffusion and embrittlement.

8.2 Future work

Future work is intended to improve the current models by both implementing better FEM codes and carrying out laboratory tests.

8.2.1 Numerical implementation

Regarding hydrogen diffusion modelling, in future research:

- hydrogen entry will be modelled more realistically, considering both gaseous and electrochemical conditions. Mainly, generalised boundary conditions will be investigated and linked to absorption/desorption reactions. For electrochemical hydrogen charging, the objective is to correlate charging parameters, e.g. current density and/or overpotential, with boundary conditions in diffusion equations. In the more general case, a flux including all these phenomena will be imposed as a Neumann boundary condition.
- a better integration scheme will be developed for the implementation of McNabb and Foster equation in order to reduce numerical instabilities. In addition, Thermal Desorption curves will be analysed with the improved model and the influence of kinetic parameters, e.g. capture and release rates, will be evaluated.

- subroutines used for 2D (both for plane strain and plane stress) and axisymmetric elements in the present work will be extended to 3D situations. This extension is expected to be relatively undemanding.
- hydrogen diffusion in polycrystalline structures will be investigated. By means of Voronoi tessellations, grains will be reproduced in a FEM simulation. Using the models presented in this thesis, dependence of diffusivity parameters on crystal orientation might be analysed and trapping effects can be implemented locally at grain boundaries.
- taking into consideration that hydrogen diffusion strongly depends on the implemented plasticity model, modern plasticity theories are intended to be implemented. For instance, Strain Gradient Plasticity is one of the promising fields that could clarify scale-effects and critical distances in hydrogen-metal interaction near the crack tip.
- considering the disadvantage that heat transfer subroutines presented here are only valid for isothermal models because hydrogen concentration is allocated within the "Temperature" variable, models considering thermophoresis, i.e. how temperature gradients affect hydrogen diffusion, will need an additional field and the inclusion of heat transfer equations, or even more complex subroutines like UEL.

Concerning hydrogen-assisted fracture modelling, in future research:

- a simultaneous analysis will be made, e.g. combining the UMATHT for diffusion with a UEL including Cohesive behaviour. In fracture simulations presented in Chapter 5, a procedure limitation is that triaxiality and hydrogen values have been obtained in a continuum elasto-plastic analysis; this is a simplification since including the traction-separation response will change local stress state.

- keeping in mind that cohesive modelling is essentially a phenomenological approach, Traction – Separation curves will be obtained through "Unit Cell" simulations. These "Unit Cell" simulations must reproduce void behaviour, explicitly in a voided cell or implicitly with a porosity-based damage model. In addition, hydrogen redistribution

around a void and the inclusion of a concentration-dependent softening could give hydrogen-dependent Traction – Separation Law.

- analogies between heat transfer and hydrogen diffusion will be extended to damage modelling; the inclusion of temperature-dependencies in laws of damage, e.g. Traction Separation Law in the Cohesive Zone Model, might be included in ABAQUS analogically to the hydrogen-dependencies of damage parameters. This might be a regarded as an alternative to the more advanced UEL writing.

Finally, in future work on vessel modelling:

- the possibility of crack initiation and propagation will be considered by means of damage models. Because cohesive modelling requires a predefined crack path, stress concentrators, notches and surface defects in the vessel will be evaluated as likely crack initiation places.

- in addition to autofrettage, different techniques will be simulated for the generation of compressive residual stresses: swaging, wire-winding, deep rolling, etc. Industrial application of each method will be discussed. Summing crack propagation modelling to cyclic diffusion, already analysed in the present work, fatigue life of a vessel can be numerically predicted in future works.

- More complex plasticity models must be implemented. In addition to SGP theories, mentioned above, kinematic hardening models must be considered in order to simulate cyclic plasticity, reverse yielding and the Bauschinger effect.

- whole vessels will be simulated, including manufacturing processes to consider residual stresses from welding and compressive stresses from fatigue-improvement techniques. Thus, computationally expensive models must be created. These simulations have the purpose of analysing 3D effects, border effects, realistic stress concentrators, e.g. nozzles, weldments, bores, etc..

8.2.2 Experimental work

This work follows a numerical approach; consequently, empirical conclusions cannot be drawn and experimental validation must be performed in future research. In particular:

- empirical diffusion tests will be performed. In particular, as an alternative to permeation tests, desorption tests will be carried out to find diffusion parameters, e.g. apparent diffusivity, trap density, etc. A numerical fitting procedure will be needed to obtain those parameters. Moreover, trapping influence implemented in the numerical models exposed in the present work will be verified.

- Relationship between plastic strain and trapping effects will be analysed. Specimens pre-deformed plastically will be subjected to diffusion tests mentioned above.

- Thermal Desorption Spectroscopy tests will be used for characterising activation energies for diffusion and trapping. Evaluating desorption peaks at various heating rates, binding energies for different kind of defects will be found. With the ramping temperature, kinetic formulation implemented in the present thesis might be confirmed and improved. Influence of thermal gradients on diffusion might also be studied.

- Tensile tests of notched specimens must be made for verification purposes. Cohesive Zone Models require an empirical fitting for the Traction Separation Law parameters. Moreover, performing these tests with different hydrogen concentrations, i.e. at different charging conditions, the cohesive model informed by hydrogen might be empirically enriched.

- The interaction between residual stresses and hydrogen diffusion and embrittlement will be studied. After the introduction of compressive residual stresses in a specimen, e.g. through a cyclic load, the stress distribution will be measured with the Hole-Drilling method and correlated with diffusion and hydrogen-related fracture parameters.

References

Ahn, D. C., Sofronis, P., & Dodds, R. (2007). Modeling of hydrogen-assisted ductile crack propagation in metals and alloys. *International Journal of Fracture, 145*(2), 135-157. doi: 10.1007/s10704-007-9112-3

Alegre, J. M., Bravo, P., & Preciado, M. (2007). Fatigue behaviour of an autofrettaged high-pressure vessel for the food industry. *Engineering Failure Analysis, 14*(2), 396-407. doi: https://doi.org/10.1016/j.engfailanal.2006.02.015

Alex, K., & McLellan, R. B. (1970). A zeroth order mixing treatment of interstitial solid solutions. *Journal of Physics and Chemistry of Solids, 31*(12), 2751-2753. doi: http://dx.doi.org/10.1016/0022-3697(70)90273-8

Altenberger, A. R. (1978). On the theory of generalized diffusion processes in many-particle systems. *Physica A: Statistical Mechanics and its Applications, 92*(3), 391-409. doi: http://dx.doi.org/10.1016/0378-4371(78)90139-5

Alvaro, A., Thue Jensen, I., Kheradmand, N., Løvvik, O. M., & Olden, V. (2015). Hydrogen embrittlement in nickel, visited by first principles modeling, cohesive zone simulation and nanomechanical testing. *International Journal of Hydrogen Energy, 40*(47), 16892-16900. doi: https://doi.org/10.1016/j.ijhydene.2015.06.069

Anderson, D. L. (1989). *Theory of the Earth*: Blackwell scientific publications.

Anvari, M., Scheider, I., & Thaulow, C. (2006). Simulation of dynamic ductile crack growth using strain-rate and triaxiality-dependent cohesive elements. *Engineering Fracture Mechanics, 73*(15), 2210-2228. doi: https://doi.org/10.1016/j.engfracmech.2006.03.016

Asaoka, T., Lapasset, G., Aucouturier, M., & Lacombe, P. (1978). Observation of Hydrogen Trapping in Fe-0.15 Wt% Ti Alloy by High Resolution Autoradiography. *CORROSION, 34*(2), 39-47. doi: 10.5006/0010-9312-34.2.39

Barnoush, A. (2011). Hydrogen embrittlement. *Saarland University*.

Barnoush, A., & Vehoff, H. (2010). Recent developments in the study of hydrogen embrittlement: Hydrogen effect on dislocation nucleation. *Acta Materialia, 58*(16), 5274-5285. doi: http://dx.doi.org/10.1016/j.actamat.2010.05.057

Barrera, O., Tarleton, E., Tang, H. W., & Cocks, A. C. F. (2016). Modelling the coupling between hydrogen diffusion and the mechanical behaviour of metals. *Computational Materials Science, 122*, 219-228. doi: http://dx.doi.org/10.1016/j.commatsci.2016.05.030

Beachem, C. (1972). A new model for hydrogen-assisted cracking (hydrogen "embrittlement"). *Metallurgical transactions, 3*(2), 441-455.

Beck, W., Bockris, J. M., McBreen, J., & Nanis, L. (1966). *Hydrogen permeation in metals as a function of stress, temperature and dissolved hydrogen concentration.* Paper presented at the Proceedings of the Royal Society of London A: Mathematical, Physical and Engineering Sciences.

Bernstein, I. (1970). The role of hydrogen in the embrittlement of iron and steel. *Materials Science and Engineering, 6*(1), 1-19.

Bird, R. B., Stewart, W. E., & Lightfoot, E. N. (2007). *Transport Phenomena*: Wiley.

Birnbaum, H. K., & Sofronis, P. (1994). Hydrogen-enhanced localized plasticity—a mechanism for hydrogen-related fracture. *Materials Science and Engineering: A, 176*(1–2), 191-202. doi: http://dx.doi.org/10.1016/0921-5093(94)90975-X

Bockris, J. M., & Subramanyan, P. (1971). The equivalent pressure of molecular hydrogen in cavities within metals in terms of the overpotential developed during the evolution of hydrogen. *Electrochimica Acta, 16*(12), 2169-2179.

Boellinghaus, T., Holtappels, K., Mair, G. W., & Grunewald, T. (2014). Explosion of iron hydrogen storage containers – Investigations from 120 years ago revisited. *Engineering Failure Analysis, 43*, 47-62. doi: http://dx.doi.org/10.1016/j.engfailanal.2014.03.017

Boiler and Pressure Vessel Code. Section VIII Division 1. ASME (2010).

Brass, A. M., Chene, J., & Boutry-Forveille, A. (1996). Measurements of deuterium and tritium concentration enhancement at the crack tip of high strength steels. *Corrosion Science, 38*(4), 569-585. doi: http://dx.doi.org/10.1016/0010-938X(95)00146-B

Bueno, A. H. S., Moreira, E. D., & Gomes, J. A. C. P. (2014). Evaluation of stress corrosion cracking and hydrogen embrittlement in an API grade steel. *Engineering Failure Analysis, 36*, 423-431. doi: http://dx.doi.org/10.1016/j.engfailanal.2013.11.012

Coleman, B., & Noll, W. (1963). The thermodynamics of elastic materials with heat conduction and viscosity. *Archive for Rational Mechanics and Analysis, 13*(1), 167-178. doi: 10.1007/BF01262690

Cornec, A., Scheider, I., & Schwalbe, K.-H. (2003). On the practical application of the cohesive model. *Engineering Fracture Mechanics, 70*(14), 1963-1987. doi: https://doi.org/10.1016/S0013-7944(03)00134-6

Crank, J. (1979). *The mathematics of diffusion*: Oxford university press.

Cuesta, I. I., Lorenzo, M., & Alegre, J. M. (2014). Response surface application for estimating failure time and other creep properties using the Small Punch Creep Test. *Engineering Failure Analysis, 45*, 49-58. doi: https://doi.org/10.1016/j.engfailanal.2014.06.023

Choo, W. Y., & Lee, J. Y. (1982). Thermal analysis of trapped hydrogen in pure iron. *Metallurgical Transactions A, 13*(1), 135-140. doi: 10.1007/bf02642424

Chornet, E., & Coughlin, R. W. (1972). Chemisorption of hydrogen on iron. *Journal of Catalysis, 27*(2), 246-265. doi: https://doi.org/10.1016/0021-9517(72)90266-7

Choudhury, S., Barnard, L., Tucker, J. D., Allen, T. R., Wirth, B. D., Asta, M., & Morgan, D. (2011). Ab-initio based modeling of diffusion in dilute bcc Fe–Ni and Fe–Cr alloys and implications for radiation induced segregation. *Journal of Nuclear Materials, 411*(1–3), 1-14. doi: http://dx.doi.org/10.1016/j.jnucmat.2010.12.231

Christensen, O. B., Stoltze, P., Jacobsen, K. W., & Nrskov, J. K. (1990). Effective-medium calculations for hydrogen in Ni, Pd, and Pt. *Physical Review B, 41*(18), 12413-12423.

Dadfarnia, M., Martin, M. L., Nagao, A., Sofronis, P., & Robertson, I. M. (2015). Modeling hydrogen transport by dislocations. *Journal of the Mechanics and Physics of Solids, 78*, 511-525. doi: http://dx.doi.org/10.1016/j.jmps.2015.03.002

Dadfarnia, M., Sofronis, P., & Neeraj, T. (2011). Hydrogen interaction with multiple traps: Can it be used to mitigate embrittlement? *International Journal of Hydrogen Energy, 36*(16), 10141-10148. doi: https://doi.org/10.1016/j.ijhydene.2011.05.027

Danielewski, M., & Wierzba, B. (2010). Thermodynamically consistent bi-velocity mass transport phenomenology. *Acta Materialia, 58*(20), 6717-6727. doi: http://dx.doi.org/10.1016/j.actamat.2010.08.037

Daw, M. S., & Baskes, M. I. (1983). Semiempirical, quantum mechanical calculation of hydrogen embrittlement in metals. *Physical Review Letters, 50*(17), 1285.

Daw, M. S., & Baskes, M. I. (1984). Embedded-atom method: Derivation and application to impurities, surfaces, and other defects in metals. *Physical Review B, 29*(12), 6443.

Dayal, R. K., & Parvathavarthini, N. Hydrogen embrittlement in power plant steels. *Sadhana, 28*(3), 431-451. doi: 10.1007/bf02706442

Delafosse, D., & Magnin, T. (2001). Hydrogen induced plasticity in stress corrosion cracking of engineering systems. *Engineering Fracture Mechanics, 68*(6), 693-729. doi: http://dx.doi.org/10.1016/S0013-7944(00)00121-1

Devanathan, M., Stachurski, Z., & Beck, W. (1963). A technique for the evaluation of hydrogen embrittlement characteristics of electroplating baths. *Journal of the electrochemical society, 110*(8), 886-890.

Di Leo, C. V., & Anand, L. (2013). Hydrogen in metals: A coupled theory for species diffusion and large elastic–plastic deformations. *International Journal of Plasticity, 43*(0), 42-69. doi: http://dx.doi.org/10.1016/j.ijplas.2012.11.005

Díaz, A., Alegre, J. M., & Cuesta, I. I. A review on diffusion modelling in hydrogen related failures of metals. *Engineering Failure Analysis*. doi: http://dx.doi.org/10.1016/j.engfailanal.2016.05.019

Díaz, A., Alegre, J. M., & Cuesta, I. I. (2016). Coupled hydrogen diffusion simulation using a heat transfer analogy. *International Journal of Mechanical Sciences, 115–116*, 360-369. doi: https://doi.org/10.1016/j.ijmecsci.2016.07.020

Dietzel, W., Pfuff, M., & Juilfs, G. G. (2006). Hydrogen permeation in plastically deformed steel membranes. *Materials Science, 42*(1), 78-84. doi: 10.1007/s11003-006-0059-8

Ebihara, K.-i., Kaburaki, H., Suzudo, T., & Takai, K. (2009). A numerical study on the validity of the local equilibrium hypothesis in modeling hydrogen thermal desorption spectra. *ISIJ international, 49*(12), 1907-1913.

Einstein, A. (1906). On the theory of the Brownian movement. *Annalen der physik, 4*(19), 371-381.

Elices, M., Guinea, G. V., Gómez, J., & Planas, J. (2002). The cohesive zone model: advantages, limitations and challenges. *Engineering Fracture Mechanics, 69*(2), 137-163. doi: http://dx.doi.org/10.1016/S0013-7944(01)00083-2

Estrin, Y. (1996). Dislocation-density-related constitutive modeling. *Unified constitutive laws of plastic deformation, 1*, 69-106.

Falkenberg, R., Brocks, W., Dietzel, W., & Scheider, I. (2010). Modelling the effect of hydrogen on ductile tearing resistance of steels: Dedicated to Professor Dr. Hermann

Riedel on the occasion of his 65th birthday. *International Journal of Materials Research, 101*(8), 989-996.

Ferro, A. (1957). Theory of diffusion constants in interstitial solid solutions of bcc metals. *Journal of Applied Physics, 28*(8), 895-900.

Fleck, N. A., & Hutchinson, J. W. (1993). A phenomenological theory for strain gradient effects in plasticity. *Journal of the Mechanics and Physics of Solids, 41*(12), 1825-1857. doi: http://dx.doi.org/10.1016/0022-5096(93)90072-N

Fukai, Y. (2006). *The metal-hydrogen system: basic bulk properties* (Vol. 21): Springer Science & Business Media.

Gangloff, R. P., & Somerday, B. P. (2012). *Gaseous Hydrogen Embrittlement of Materials in Energy Technologies: Mechanisms, modelling and future developments* (Vol. 2): Elsevier.

Gao, X.-L. (1993). An exact elasto-plastic solution for a closed-end thick-walled cylinder of elastic linear-hardening material with large strains. *International Journal of Pressure Vessels and Piping, 56*(3), 331-350. doi: http://dx.doi.org/10.1016/0308-0161(93)90004-D

Gao, X. L. (2003). Elasto-plastic analysis of an internally pressurized thick-walled cylinder using a strain gradient plasticity theory. *International Journal of Solids and Structures, 40*(23), 6445-6455. doi: https://doi.org/10.1016/S0020-7683(03)00424-4

Gao, Y., & Bower, A. (2004). A simple technique for avoiding convergence problems in finite element simulations of crack nucleation and growth on cohesive interfaces. *Modelling and Simulation in Materials Science and Engineering, 12*(3), 453.

Gerberich, W. W., & Chen, Y. T. (1975). Hydrogen-controlled cracking—An approach to threshold stress intensity. *Metallurgical Transactions A, 6*(2), 271-278. doi: 10.1007/BF02667281

Gobbi, G., Colombo, C., & Vergani, L. (2016). A cohesive zone model to simulate the hydrogen embrittlement effect on a high-strength steel. *Frattura ed Integritá Strutturale*(35), 260.

Gorban, A., Sargsyan, H., & Wahab, H. (2011). Quasichemical models of multicomponent nonlinear diffusion. *Mathematical Modelling of Natural Phenomena, 6*(05), 184-262.

Grabert, H., & Wipf, H. (1990). Tunneling of hydrogen in metals. In U. Rössler (Ed.), *Festkörperprobleme 30* (Vol. 30, pp. 1-23): Springer Berlin Heidelberg.

Grange, M., Besson, J., & Andrieu, E. (2000). An anisotropic Gurson type model to represent the ductile rupture of hydrided Zircaloy-4 sheets. *International Journal of Fracture, 105*(3), 273-293.

Guggenheim, E., & McGlashan, M. (1951). *Statistical mechanics of regular mixtures.* Paper presented at the Proceedings of the Royal Society of London A: Mathematical, Physical and Engineering Sciences.

Gurson, A. L. (1977). Continuum theory of ductile rupture by void nucleation and growth: Part I—Yield criteria and flow rules for porous ductile media. *Journal of engineering materials and technology, 99*(1), 2-15.

Gurtin, M. E., Fried, E., & Anand, L. (2010). *The mechanics and thermodynamics of continua*: Cambridge University Press.

Hadianfard, M. (2010). Failure in a high pressure feeding line of an oil refinery due to hydrogen effect. *Engineering Failure Analysis, 17*(4), 873-881.

Hameed, A., Brown, R. D., & Hetherington, J. (2004). A Study of the Residual Stress Distribution in an Autofrettaged, Thick-Walled Cylinder With Cross-Bore. *Journal of Pressure Vessel Technology, 126*(4), 497-503. doi: 10.1115/1.1811111

Hao, P., Fang, Y., Sun, J., Csonka, G. I., Philipsen, P. H. T., & Perdew, J. P. (2012). Lattice constants from semilocal density functionals with zero-point phonon correction. *Physical Review B, 85*(1), 014111.

Hardie, D., Charles, E. A., & Lopez, A. H. (2006). Hydrogen embrittlement of high strength pipeline steels. *Corrosion Science, 48*(12), 4378-4385. doi: http://dx.doi.org/10.1016/j.corsci.2006.02.011

Harper, P. W., & Hallett, S. R. (2008). Cohesive zone length in numerical simulations of composite delamination. *Engineering Fracture Mechanics, 75*(16), 4774-4792. doi: https://doi.org/10.1016/j.engfracmech.2008.06.004

Hill, M., & Johnson, E. (1959). Hydrogen in cold worked Iron-Carbon alloys and the mechanism of hydrogen embrittlement. *Transactions of the metallurgical society of AIME, 215*, 717-725.

Hirth, J. (1980). Effects of hydrogen on the properties of iron and steel. *Metallurgical Transactions A, 11*(6), 861-890. doi: 10.1007/BF02654700

Horstemeyer, M. F. (2010). Multiscale modeling: a review *Practical aspects of computational chemistry* (pp. 87-135): Springer.

Huang, X. (2005). A general autofrettage model of a thick-walled cylinder based on tensile-compressive stress-strain curve of a material. *The Journal of Strain Analysis for Engineering Design, 40*(6), 599-607.

Hutchinson, J. W. (2000). Plasticity at the micron scale. *International Journal of Solids and Structures, 37*(1), 225-238.

Jiang, D., & Carter, E. A. (2004). First principles assessment of ideal fracture energies of materials with mobile impurities: implications for hydrogen embrittlement of metals. *Acta Materialia, 52*(16), 4801-4807.

Juilfs, G. (2002). *Das Diffusionsverhalten von Wasserstoff in einem niedriglegierten Stahl unter Berücksichtigung des Verformungsgrades*: GRIN Verlag.

Kanayama, H., Ndong-Mefane, S., Ogino, M., & Miresmaeili, R. (2009). Reconsideration of the Hydrogen Diffusion Model Using the McNabb-Foster Formulation. *Memoirs of the Faculty of Engineering, Kyushu University, 69*(4), 149-161.

Katzarov, I. H., Pashov, D. L., & Paxton, A. T. (2013). Fully quantum mechanical calculation of the diffusivity of hydrogen in iron using the tight-binding approximation and path integral theory. *Physical Review B, 88*(5), 054107.

Kawamoto, K., Oda, Y., Noguchi, H., Fujii, H., Izumi, T., & Itoh, G. (2009). Investigation of Local Hydrogen Distribution Around Fatigue Crack Tip of a Type 304 Stainless Steel with Secondary Ion Mass Spectrometry and Hydrogen Micro-Print Technique. *Journal of Solid Mechanics and Materials Engineering, 3*(6), 898-909.

Kehr, K. (1978). Theory of the diffusion of hydrogen in metals *Hydrogen in Metals I* (pp. 197-226): Springer.

Kim, N.-H., Oh, C.-S., Kim, Y.-J., Yoon, K.-B., & Ma, Y.-W. (2012). Hydrogen-assisted stress corrosion cracking simulation using the stress-modified fracture strain model. *Journal of mechanical science and technology, 26*(8), 2631-2638.

Kimura, H., & Matsui, H. (1987). Mechanism of hydrogen-induced softening and hardening in iron. *Scripta Metallurgica, 21*(3), 319-324. doi: http://dx.doi.org/10.1016/0036-9748(87)90221-3

Kirchheim, R. (1982). Solubility, diffusivity and trapping of hydrogen in dilute alloys. Deformed and amorphous metals—II. *Acta Metallurgica, 30*(6), 1069-1078.

Kirchheim, R. (1987). Monte-carlo simulations of interstitial diffusion and trapping—I. One type of traps and dislocations. *Acta Metallurgica, 35*(2), 271-280. doi: http://dx.doi.org/10.1016/0001-6160(87)90235-5

Kirchheim, R. (1988). Hydrogen solubility and diffusivity in defective and amorphous metals. *Progress in Materials Science, 32*(4), 261-325.

Kirchheim, R., & Stolz, U. (1987). Monte-carlo simulations of interstitial diffusion and trapping—II. Amorphous metals. *Acta Metallurgica, 35*(2), 281-291. doi: http://dx.doi.org/10.1016/0001-6160(87)90236-7

Kittel, J., Smanio, V., Fregonese, M., Garnier, L., & Lefebvre, X. (2010). Hydrogen induced cracking (HIC) testing of low alloy steel in sour environment: Impact of time of exposure on the extent of damage. *Corrosion Science, 52*(4), 1386-1392. doi: http://dx.doi.org/10.1016/j.corsci.2009.11.044

Kotake, H., Matsumoto, R., Taketomi, S., & Miyazaki, N. (2008). Transient hydrogen diffusion analyses coupled with crack-tip plasticity under cyclic loading. *International Journal of Pressure Vessels and Piping, 85*(8), 540-549. doi: http://dx.doi.org/10.1016/j.ijpvp.2008.02.002

Krom, A. H., & Bakker, A. (2000). Hydrogen trapping models in steel. *Metallurgical and materials transactions B, 31*(6), 1475-1482.

Krom, A. H. M., Koers, R. W. J., & Bakker, A. (1999). Hydrogen transport near a blunting crack tip. *Journal of the Mechanics and Physics of Solids, 47*(4), 971-992. doi: http://dx.doi.org/10.1016/S0022-5096(98)00064-7

Krom, A. M., & Bakker, A. (2000). Hydrogen trapping models in steel. *Metallurgical and Materials Transactions B, 31*(6), 1475-1482. doi: 10.1007/s11663-000-0032-0

Kumnick, A., & Johnson, H. (1980). Deep trapping states for hydrogen in deformed iron. *Acta Metallurgica, 28*(1), 33-39.

Kumnick, A. J., & Johnson, H. H. (1980). Deep trapping states for hydrogen in deformed iron. *Acta Metallurgica, 28*(1), 33-39. doi: http://dx.doi.org/10.1016/0001-6160(80)90038-3

Lacher, J. R. (1937). The Statistics of the Hydrogen-Palladium System. *Mathematical Proceedings of the Cambridge Philosophical Society, 33*(04), 518-523. doi: doi:10.1017/S0305004100077641

Lacher, J. R. (1937). A Theoretical Formula for the Solubility of Hydrogen in Palladium. *Proceedings of the Royal Society of London. Series A, Mathematical and Physical Sciences, 161*(907), 525-545. doi: 10.2307/96937

Leblond, J. B., & Dubois, D. (1983a). A general mathematical description of hydrogen diffusion in steels—I. Derivation of diffusion equations from boltzmann-type transport equations. *Acta Metallurgica, 31*(10), 1459-1469. doi: http://dx.doi.org/10.1016/0001-6160(83)90142-6

Leblond, J. B., & Dubois, D. (1983b). A general mathematical description of hydrogen diffusion in steels—II. Numerical study of permeation and determination of trapping

parameters. *Acta Metallurgica, 31*(10), 1471-1478. doi: http://dx.doi.org/10.1016/0001-6160(83)90143-8

Lee, H. G., & Lee, J.-Y. (1984). Hydrogen trapping by TiC particles in iron. *Acta Metallurgica, 32*(1), 131-136. doi: https://doi.org/10.1016/0001-6160(84)90210-4

Lee, J.-L., & Lee, J.-Y. (1986). The interaction of hydrogen with the interface of AI2O3 particles in iron. *Metallurgical Transactions A, 17*(12), 2183-2186. doi: 10.1007/bf02645916

Lee, J. L., & Lee, J. Y. (1983). Hydrogen trapping in AISI 4340 steel. *Metal Science, 17*(9), 426-432. doi: 10.1179/030634583790420619

Lee, K. Y., Lee, J.-Y., & Kim, D. R. (1984). A study of hydrogen-trapping phenomena in AISI 5160 spring steel. *Materials Science and Engineering, 67*(2), 213-220. doi: https://doi.org/10.1016/0025-5416(84)90053-3

Liang, Y., Ahn, D. C., Sofronis, P., Dodds Jr, R. H., & Bammann, D. (2008). Effect of hydrogen trapping on void growth and coalescence in metals and alloys. *Mechanics of Materials, 40*(3), 115-132. doi: https://doi.org/10.1016/j.mechmat.2007.07.001

Liang, Y., & Sofronis, P. (2003). Toward a phenomenological description of hydrogen-induced decohesion at particle/matrix interfaces. *Journal of the Mechanics and Physics of Solids, 51*(8), 1509-1531. doi: http://dx.doi.org/10.1016/S0022-5096(03)00052-8

Liang, Y., Sofronis, P., & Aravas, N. (2003). On the effect of hydrogen on plastic instabilities in metals. *Acta Materialia, 51*(9), 2717-2730. doi: http://dx.doi.org/10.1016/S1359-6454(03)00081-8

Liu, Q., Atrens, A. D., Shi, Z., Verbeken, K., & Atrens, A. (2014). Determination of the hydrogen fugacity during electrolytic charging of steel. *Corrosion Science, 87*, 239-258.

Lufrano, J., Sofronis, P., & Birnbaum, H. K. (1996). Modeling of hydrogen transport and elastically accommodated hydride formation near a crack tip. *Journal of the Mechanics and Physics of Solids, 44*(2), 179-205. doi: http://dx.doi.org/10.1016/0022-5096(95)00075-5

Lufrano, J., Sofronis, P., & Birnbaum, H. K. (1998). Elastoplastically accommodated hydride formation and embrittlement. *Journal of the Mechanics and Physics of Solids, 46*(9), 1497-1520. doi: http://dx.doi.org/10.1016/S0022-5096(98)00054-4

Lumsden, J. (1952). *Thermodynamics of Alloys*: Inst. of Metals.

Lupis, C. H. P., & Elliott, J. F. (1967). Prediction of enthalpy and entropy interaction coefficients by the "central atoms" theory. *Acta Metallurgica, 15*(2), 265-276. doi: http://dx.doi.org/10.1016/0001-6160(67)90202-7

Lynch, S. (2007). *Progress towards understanding mechanisms of hydrogen embrittlement and stress corrosion cracking.* Paper presented at the CORROSION 2007.

Mao, S. X., & Li, M. (1998). Mechanics and thermodynamics on the stress and hydrogen interaction in crack tip stress corrosion: experiment and theory. *Journal of the Mechanics and Physics of Solids, 46*(6), 1125-1137. doi: http://dx.doi.org/10.1016/S0022-5096(97)00054-9

Marchi, C. S., Somerday, B. P., & Robinson, S. L. (2007). Permeability, solubility and diffusivity of hydrogen isotopes in stainless steels at high gas pressures. *International Journal of Hydrogen Energy, 32*(1), 100-116. doi: http://dx.doi.org/10.1016/j.ijhydene.2006.05.008

Maroef, I., Olson, D., Eberhart, M., & Edwards, G. (2002). Hydrogen trapping in ferritic steel weld metal. *International Materials Reviews, 47*(4), 191-223.

Martínez-Pañeda, E., del Busto, S., Niordson, C. F., & Betegón, C. (2016). Strain gradient plasticity modeling of hydrogen diffusion to the crack tip. *International Journal of Hydrogen Energy, 41*(24), 10265-10274. doi: https://doi.org/10.1016/j.ijhydene.2016.05.014

Martínez-Pañeda, E., & Niordson, C. F. (2016). On fracture in finite strain gradient plasticity. *International Journal of Plasticity, 80*, 154-167. doi: https://doi.org/10.1016/j.ijplas.2015.09.009

Matsui, H., Kimura, H., & Moriya, S. (1979). The effect of hydrogen on the mechanical properties of high purity iron I. Softening and hardening of high purity iron by hydrogen charging during tensile deformation. *Materials Science and Engineering, 40*(2), 207-216. doi: http://dx.doi.org/10.1016/0025-5416(79)90191-5

Matsuoka, S., Tanaka, H., Homma, N., & Murakami, Y. (2011). Influence of hydrogen and frequency on fatigue crack growth behavior of Cr-Mo steel. *International Journal of Fracture, 168*(1), 101-112.

McLellan, A. G. (1970). *Non-Hydrostatic Thermodynamics of Chemical Systems* (Vol. 314).

McLellan, R. B. (1972). Invited review: Thermodynamics of solid solutions. *Materials Science and Engineering, 9*, 121-140.

McLellan, R. B., & Dunn, W. W. (1969). A quasi-chemical treatment of interstitial solid solutions: It application to carbon austenite. *Journal of Physics and Chemistry of Solids, 30*(11), 2631-2637.

McNabb, A., & Foster, P. K. (1963). A new analysis of the diffusion of hydrogen in iron and ferritic steels. *Transactions of the metallurgical society of AIME, 227*, 618-627. doi: citeulike-article-id:4956272

Mecking, H., & Kocks, U. F. (1981). Kinetics of flow and strain-hardening. *Acta Metallurgica, 29*(11), 1865-1875. doi: http://dx.doi.org/10.1016/0001-6160(81)90112-7

Mehrer, H., & Stolwijk, N. A. (2009). Heroes and Highlights in the History of Diffusion.

Miresmaeili, R., Ogino, M., Nakagawa, T., & Kanayama, H. (2010). A coupled elastoplastic-transient hydrogen diffusion analysis to simulate the onset of necking in tension by using the finite element method. *International Journal of Hydrogen Energy, 35*(3), 1506-1514. doi: http://dx.doi.org/10.1016/j.ijhydene.2009.11.024

Moon, K. M., Lee, M. H., Kim, K. J., Kim, J. G., & Kim, S. J. (2003). A study on the post-weld heat treatment effect to mechanical properties and hydrogen embrittlement for heating affected zone of a RE 36 steel. *Corrosion Science and Technology, 2*(6), 283-288.

Moriconi, C., Hénaff, G., & Halm, D. (2014). Cohesive zone modeling of fatigue crack propagation assisted by gaseous hydrogen in metals. *International Journal of Fatigue, 68*, 56-66. doi: https://doi.org/10.1016/j.ijfatigue.2014.06.007

Nagao, A., Kuramoto, S., Ichitani, K., & Kanno, M. (2001). Visualization of hydrogen transport in high strength steels affected by stress fields and hydrogen trapping. *Scripta Materialia, 45*(10), 1227-1232. doi: https://doi.org/10.1016/S1359-6462(01)01154-X

Nagumo, M. (2016). *Fundamentals of hydrogen embrittlement*: Springer.

Nagumo, M., Takai, K., & Okuda, N. (1999). Nature of hydrogen trapping sites in steels induced by plastic deformation. *Journal of alloys and compounds, 293*, 310-316.

Nelson, H. G., & Williams, D. (1973). Quantitative observations of hydrogen-induced, slow crack growth in a low alloy steel.

Neumann, R. M. (1980). Entropic approach to brownian movement. *American Journal of Physics, 48*(5), 354-357.

Oh, C.-S., Kim, Y.-J., & Yoon, K.-B. (2010). Coupled analysis of hydrogen transport using ABAQUS. *Journal of Solid Mechanics and Materials Engineering, 4*(7), 908-917.

Olden, V., Thaulow, C., Johnsen, R., & Østby, E. (2007). Cohesive zone modeling of hydrogen-induced stress cracking in 25% Cr duplex stainless steel. *Scripta Materialia, 57*(7), 615-618. doi: http://dx.doi.org/10.1016/j.scriptamat.2007.06.006

Olden, V., Thaulow, C., Johnsen, R., Østby, E., & Berstad, T. (2008). Application of hydrogen influenced cohesive laws in the prediction of hydrogen induced stress cracking in 25%Cr duplex stainless steel. *Engineering Fracture Mechanics, 75*(8), 2333-2351. doi: https://doi.org/10.1016/j.engfracmech.2007.09.003

Ono, K., & Meshii, M. (1992). Hydrogen detrapping from grain boundaries and dislocations in high purity iron. *Acta Metallurgica et Materialia, 40*(6), 1357-1364. doi: https://doi.org/10.1016/0956-7151(92)90436-I

Onsager, L. (1931a). Reciprocal relations in irreversible processes. I. *Physical Review, 37*(4), 405.

Onsager, L. (1931b). Reciprocal relations in irreversible processes. II. *Physical Review, 38*(12), 2265.

Oriani, R. A. (1970). The diffusion and trapping of hydrogen in steel. *Acta Metallurgica, 18*(1), 147-157. doi: http://dx.doi.org/10.1016/0001-6160(70)90078-7

Oriani, R. A. (1978). Hydrogen Embrittlement of Steels. *Annual Review of Materials Science, 8*(1), 327-357. doi: doi:10.1146/annurev.ms.08.080178.001551

Oriani, R. A. (1983). The Hardening and Softening Induced by Hydrogen in Carbon Steels. In R. M. Latanision & J. R. Pickens (Eds.), *Atomistics of Fracture* (pp. 795-798): Springer US.

Oriani, R. A., & Josephic, P. H. (1974). Equilibrium aspects of hydrogen-induced cracking of steels. *Acta Metallurgica, 22*(9), 1065-1074. doi: http://dx.doi.org/10.1016/0001-6160(74)90061-3

Oudriss, A., Creus, J., Bouhattate, J., Conforto, E., Berziou, C., Savall, C., & Feaugas, X. (2012). Grain size and grain-boundary effects on diffusion and trapping of hydrogen in pure nickel. *Acta Materialia, 60*(19), 6814-6828. doi: https://doi.org/10.1016/j.actamat.2012.09.004

Oudriss, A., Creus, J., Bouhattate, J., Savall, C., Peraudeau, B., & Feaugas, X. (2012). The diffusion and trapping of hydrogen along the grain boundaries in polycrystalline nickel. *Scripta Materialia, 66*(1), 37-40. doi: https://doi.org/10.1016/j.scriptamat.2011.09.036

Owen, C. V., & Scott, T. E. (1972). Relation between hydrogen embrittlement and formation of hydride in group v transition-metals. *Metallurgical transactions, 3*(7), 1715-&. doi: 10.1007/bf02642552

Pardal, J. M., Tavares, S. S. M., Barbosa, B. A. R. S., Mainier, F. B., Corte, J. S., & Pardal, J. P. (2013). Investigation of hydrogen embrittlement failure in a steam separator by

field metallography. *Engineering Failure Analysis, 35*, 46-53. doi: http://dx.doi.org/10.1016/j.engfailanal.2012.11.001

Park, K., & Paulino, G. H. (2012). Computational implementation of the PPR potential-based cohesive model in ABAQUS: Educational perspective. *Engineering Fracture Mechanics, 93*, 239-262. doi: https://doi.org/10.1016/j.engfracmech.2012.02.007

Park, K., & Paulino, G. H. (2013). Cohesive Zone Models: A Critical Review of Traction-Separation Relationships Across Fracture Surfaces. *Applied Mechanics Reviews, 64*(6), 060802-060802-060820. doi: 10.1115/1.4023110

Park, K., Paulino, G. H., & Roesler, J. R. (2009). A unified potential-based cohesive model of mixed-mode fracture. *Journal of the Mechanics and Physics of Solids, 57*(6), 891-908. doi: https://doi.org/10.1016/j.jmps.2008.10.003

Parker, A. P., & Underwood, J. H. (1996). Stress Intensity, Stress Concentration, and Fatigue Crack Growth Along Evacuator Holes of Pressurized, Autofrettaged Tubes. *Journal of Pressure Vessel Technology, 118*(3), 336-342. doi: 10.1115/1.2842197

Paxton, A. T. (2014). From quantum mechanics to physical metallurgy of steels. *Materials Science and Technology, 30*(9), 1063-1070.

Peisl, H. (1978). Lattice strains due to hydrogen in metals *Hydrogen in metals I* (pp. 53-74): Springer.

Perl, M., & Steiner, M. (2016). 3-D Stress Intensity Factors due to Full Autofrettage for Inner Radial or Coplanar Crack Arrays and Ring Cracks in a Spherical Pressure Vessel. *Procedia Structural Integrity, 2*, 3625-3646. doi: http://dx.doi.org/10.1016/j.prostr.2016.06.452

Pineau, A., Benzerga, A. A., & Pardoen, T. (2016). Failure of metals I: Brittle and ductile fracture. *Acta Materialia, 107*, 424-483. doi: https://doi.org/10.1016/j.actamat.2015.12.034

Podgurski, H. H., & Oriani, R. A. (1972). Nitrogenation of Fe-Al alloys. III: Absorption of hydrogen in nitrogenated Fe-Al alloys. *Metallurgical transactions, 3*(8), 2055-2063. doi: 10.1007/bf02643214

Pressouyre, G., & Bernstein, I. (1978). A quantitative analysis of hydrogen trapping. *Metallurgical and Materials Transactions A, 9*(11), 1571-1580.

Pressouyre, G. M. (1980). Trap theory of Hydrogen embrittlement. *Acta Metallurgica, 28*(7), 895-911. doi: http://dx.doi.org/10.1016/0001-6160(80)90106-6

Risto, M. N. (2002). From atomistic simulation towards multiscale modelling of materials. *Journal of Physics: Condensed Matter, 14*(11), 2859.

Robertson, I. M. (2001). The effect of hydrogen on dislocation dynamics. *Engineering Fracture Mechanics, 68*(6), 671-692. doi: http://dx.doi.org/10.1016/S0013-7944(01)00011-X

San Marchi, C., & Somerday, B. P. Technical reference on hydrogen compatibility of materials.

San Marchi, C., & Somerday, B. P. (2008). Technical reference on hydrogen compatibility of materials. *SAND2008-1163), Sandia National Laboratories, Livermore CA*.

Schaumann, G., Völki, J., & Alefeld, G. (1970). The diffusion coefficients of hydrogen and deuterium in vanadium, niobium, and tantalum by gorsky-effect measurements. *physica status solidi (b), 42*(1), 401-413.

Schubert, E. F. (2005). *Doping in III-V semiconductors* (Vol. 1): Cambridge University Press.

Serebrinsky, S., Carter, E. A., & Ortiz, M. (2004). A quantum-mechanically informed continuum model of hydrogen embrittlement. *Journal of the Mechanics and Physics of Solids, 52*(10), 2403-2430. doi: http://dx.doi.org/10.1016/j.jmps.2004.02.010

Sherby, O. D., Wadsworth, J., Lesuer, D. R., & Syn, C. K. (2008). Revisiting the structure of martensite in iron-carbon steels. *Materials transactions, 49*(9), 2016-2027.

Shipilov, S. A., & Le May, I. (2006). Structural integrity of aging buried pipelines having cathodic protection. *Engineering Failure Analysis, 13*(7), 1159-1176. doi: http://dx.doi.org/10.1016/j.engfailanal.2005.07.008

Sofronis, P., & Birnbaum, H. K. (1995). Mechanics of the hydrogendashdislocationdashimpurity interactions—I. Increasing shear modulus. *Journal of the Mechanics and Physics of Solids, 43*(1), 49-90. doi: http://dx.doi.org/10.1016/0022-5096(94)00056-B

Sofronis, P., Liang, Y., & Aravas, N. (2001). Hydrogen induced shear localization of the plastic flow in metals and alloys. *European Journal of Mechanics - A/Solids, 20*(6), 857-872. doi: http://dx.doi.org/10.1016/S0997-7538(01)01179-2

Sofronis, P., & McMeeking, R. M. (1989). Numerical analysis of hydrogen transport near a blunting crack tip. *Journal of the Mechanics and Physics of Solids, 37*(3), 317-350. doi: http://dx.doi.org/10.1016/0022-5096(89)90002-1

Son, D.-S., & Chang, S.-H. (2012). Evaluation of modeling techniques for a type III hydrogen pressure vessel (70 MPa) made of an aluminum liner and a thick carbon/epoxy composite for fuel cell vehicles. *International Journal of Hydrogen Energy, 37*(3), 2353-2369. doi: https://doi.org/10.1016/j.ijhydene.2011.11.001

Son, D.-S., Hong, J.-H., & Chang, S.-H. (2012). Determination of the autofrettage pressure and estimation of material failures of a Type III hydrogen pressure vessel by using finite element analysis. *International Journal of Hydrogen Energy, 37*(17), 12771-12781. doi: https://doi.org/10.1016/j.ijhydene.2012.06.044

Song, P. S., & Shieh, Y. L. (2004). Fracture lifetime of hydrogen-charged AISI 4130 alloy steel under intermittent sustained overloads. *Engineering Fracture Mechanics, 71*(11), 1577-1584. doi: http://dx.doi.org/10.1016/S0013-7944(03)00213-3

Statgraphics Centuron XVII. (2014).

Steigerwald, E. A., Schaller, F. W., & Troiano, A. R. (1960). THE ROLE OF STRESS IN HYDROGEN INDUCED DELAYED FAILURE. *Journal Name: Trans. Met. Soc. AIME; Journal Volume: Vol: 218; Other Information: Orig. Receipt Date: 31-DEC-61*, Medium: X; Size: Pages: 832-841.

Stoneham, A. (1972a). Quantum theory of diffusion: temperature dependence of diffusion of light interstitials in Debye solids. *Journal of Physics F: Metal Physics, 2*(3), 417.

Stoneham, A. (1972b). Theory of the diffusion of hydrogen in metals. *Berichte der Bunsengesellschaft für physikalische Chemie, 76*(8), 816-823.

Stoneham, A. M. (1978). Non- classical diffusion processes. *Journal of Nuclear Materials, 69*, 109-116. doi: http://dx.doi.org/10.1016/0022-3115(78)90239-8

Taha, A., & Sofronis, P. (2001). A micromechanics approach to the study of hydrogen transport and embrittlement. *Engineering Fracture Mechanics, 68*(6), 803-837. doi: http://dx.doi.org/10.1016/S0013-7944(00)00126-0

Takai, K., Yamauchi, G., Nakamura, M., & Nagumo, M. (1998). Hydrogen trapping characteristics of cold-drawn pure iron and eutectoid steel evaluated by thermal

desorption spectrometry. *Journal of the Japan Institute of Metals(Japan), 62*(3), 267-275.

Takakuwa, O., Nishikawa, M., & Soyama, H. (2012). Numerical simulation of the effects of residual stress on the concentration of hydrogen around a crack tip. *Surface and Coatings Technology, 206*(11–12), 2892-2898. doi: https://doi.org/10.1016/j.surfcoat.2011.12.018

Takakuwa, O., & Soyama, H. (2012). Suppression of hydrogen-assisted fatigue crack growth in austenitic stainless steel by cavitation peening. *International Journal of Hydrogen Energy, 37*(6), 5268-5276. doi: https://doi.org/10.1016/j.ijhydene.2011.12.035

Tanner, G. (1992). Hydrogen Embrittlement Failure of Socket Head Cap Screws. *ASM International, Handbook of Case Histories in Failure Analysis., 1*, 332-334.

Thompson, A., Bernstein, I., & Swanson, R. (1982). Stress Corrosion Cracking of Wrought and P/M High Strength Aluminum Alloys: DTIC Document.

Toribio, J., & Kharin, V. (2015). A generalised model of hydrogen diffusion in metals with multiple trap types. *Philosophical Magazine*, 1-23. doi: 10.1080/14786435.2015.1079660

Tsallis, C., & Bukman, D. J. (1996). Anomalous diffusion in the presence of external forces: Exact time-dependent solutions and their thermostatistical basis. *Physical Review E, 54*(3), R2197.

Turnbull, A. (2015). Perspectives on hydrogen uptake, diffusion and trapping. *International Journal of Hydrogen Energy*. doi: http://dx.doi.org/10.1016/j.ijhydene.2015.06.147

Turon, A., Dávila, C. G., Camanho, P. P., & Costa, J. (2007). An engineering solution for mesh size effects in the simulation of delamination using cohesive zone models. *Engineering Fracture Mechanics, 74*(10), 1665-1682. doi: https://doi.org/10.1016/j.engfracmech.2006.08.025

Van Leeuwen, H. (1974). The kinetics of hydrogen embrittlement: a quantitative diffusion model. *Engineering Fracture Mechanics, 6*(1), 141-161.

Venturini, G., Wang, K., Romero, I., Ariza, M., & Ortiz, M. (2014). Atomistic long-term simulation of heat and mass transport. *Journal of the Mechanics and Physics of Solids, 73*, 242-268.

Wallaert, E., Depover, T., Arafin, M., & Verbeken, K. (2014). Thermal Desorption Spectroscopy Evaluation of the Hydrogen-Trapping Capacity of NbC and NbN Precipitates. *Metallurgical and Materials Transactions A, 45*(5), 2412-2420. doi: 10.1007/s11661-013-2181-1

Wang, M., Akiyama, E., & Tsuzaki, K. (2005). Effect of hydrogen and stress concentration on the notch tensile strength of AISI 4135 steel. *Materials Science and Engineering: A, 398*(1–2), 37-46. doi: https://doi.org/10.1016/j.msea.2005.03.008

Wei, F.-G., & Tsuzaki, K. (2005). Response of hydrogen trapping capability to microstructural change in tempered Fe–0.2C martensite. *Scripta Materialia, 52*(6), 467-472. doi: https://doi.org/10.1016/j.scriptamat.2004.11.008

Wei, F. G., Hara, T., & Tsuzaki, K. (2004). Precise determination of the activation energy for desorption of hydrogen in two Ti-added steels by a single thermal-desorption spectrum. *Metallurgical and Materials Transactions B, 35*(3), 587-597. doi: 10.1007/s11663-004-0057-x

Wen, M., Xu, X.-J., Fukuyama, S., & Yokogawa, K. (2001). Embedded-atom-method functions for the body-centered-cubic iron and hydrogen. *Journal of Materials Research, 16*(12), 3496-3502.

Wijmans, J., & Baker, R. (1995). The solution-diffusion model: a review. *Journal of membrane science, 107*(1), 1-21.

Wimmer, E., Wolf, W., Sticht, J., Saxe, P., Geller, C. B., Najafabadi, R., & Young, G. A. (2008). Temperature-dependent diffusion coefficients from ab initio computations: Hydrogen, deuterium, and tritium in nickel. *Physical Review B, 77*(13), 134305.

Yu, H., Olsen, J. S., Alvaro, A., Olden, V., He, J., & Zhang, Z. (2016). A uniform hydrogen degradation law for high strength steels. *Engineering Fracture Mechanics, 157*, 56-71. doi: https://doi.org/10.1016/j.engfracmech.2016.02.001

Yu, H., Olsen, J. S., Olden, V., Alvaro, A., He, J., & Zhang, Z. (2016). Viscous regularization for cohesive zone modeling under constant displacement: An application to hydrogen embrittlement simulation. *Engineering Fracture Mechanics, 166*, 23-42. doi: https://doi.org/10.1016/j.engfracmech.2016.08.019

Yu, K., & Klinger, M. I. (1974). Theory of quantum diffusion of atoms in crystals. *Journal of Physics C: Solid State Physics, 7*(16), 2791.

Zhang, T.-Y., & Hack, J. E. (1999). The equilibrium concentration of hydrogen atoms ahead of a mixed mode I-Mode III crack tip in single crystal iron. *Metallurgical and Materials Transactions A, 30*(1), 155-159. doi: 10.1007/s11661-999-0203-9

Zhang, X., Peng, Q., & Lu, G. (2010). Self-consistent embedding quantum mechanics/molecular mechanics method with applications to metals. *Physical Review B, 82*(13), 134120.

Zhao, Y., & Lu, G. (2011). QM/MM study of dislocation—hydrogen/helium interactions in α-Fe. *Modelling and Simulation in Materials Science and Engineering, 19*(6), 065004.

Zheng, J., Liu, X., Xu, P., Liu, P., Zhao, Y., & Yang, J. (2012). Development of high pressure gaseous hydrogen storage technologies. *International Journal of Hydrogen Energy, 37*(1), 1048-1057. doi: https://doi.org/10.1016/j.ijhydene.2011.02.125

Zhenqian, Z., Zhiling, T., Chun, Y., & Shuangping, L. (2015). Failure analysis of vessel propeller bolts under fastening stress and cathode protection environment. *Engineering Failure Analysis, 57*, 129-136. doi: http://dx.doi.org/10.1016/j.engfailanal.2015.07.013

Zhou, L. (2005). Progress and problems in hydrogen storage methods. *Renewable and Sustainable Energy Reviews, 9*(4), 395-408. doi: http://dx.doi.org/10.1016/j.rser.2004.05.005